CFD MODELLING AND VALIDATION OF A LARGE 2-STROKE MARINE DIESEL ENGINE

By

Wei Jin

A thesis submitted in fulfilment of the requirements for the degree of Doctor of Philosophy

Department of Naval Architecture, Ocean and Marine Engineering
Universities of Glasgow and Strathclyde
September 2014

Statement

Abstract

With the increasing understanding of the physical processes of the large 2-stroke marine engine and the corresponding numerical models as turbulence, injection, evaporation and chemical combustion, it has become realisable to investigate the whole working processes using Computational Fluid Dynamics (CFD). However, CFD itself needs to be validated to produce reliable results. The focus of this thesis is on the CFD validation of the large 2-stroke marine diesel engine working processes.

The turbulence models and the wall functions in the CFD solver were firstly tested using two basic 2D cases to obtain performance results in the modelling of turbulence flow and heat transferring near the wall. It was concluded that the RNG and the Realisable k-ε turbulence models predict the same best flow field and Non-Equilibrium wall function produces the best heat transfer results. Following this, the spray breakup models were evaluated through the constant volume spray chamber test. The Stochastic Secondary Droplet (SSD) model was verified as the best one for its generality and accuracy. During this process, the appropriate mesh for droplet calculation using Euler-Lagrange approach was determined.

Based on the obtained conclusions, the computation model of a large 2-stroke marine diesel engine MAN B&W S60MC-C6 was generated, with the proven best models, the RNG k-ε turbulence model, the Non-Equilibrium wall function and the SSD breakup models. In addition, different combustion models including the Finite Rate / Eddy Dissipation (FRED), the Non-Premixed Equilibrium, the Non-Premixed Steady Flamelet and the Non-Premixed Unsteady Flamelet Diesel were investigated at four engine loads (25%, 50%, 75% and 100% Maximum Continuous Revolution (MCR)). The obtained in-cylinder pressure traces were compared with the shop test data. It was proven that the Non-Premixed Equilibrium combustion model presented the best prediction performance at four loads.

The derived conclusions can be used as guidelines for CFD simulations of the large 2-stroke marine diesel engines working processes. It also provides the starting point for engine optimisation to increase engine efficiency and reduce pollutant emissions.

Acknowledgements

I would like to firstly express my greatest thanks to my supervisor, Professor Dracos Vassalos for his always kindest instructions, understandings, encouragement and support during the past four years, together with the Department's financial support nurturing this research to fruition, even though there is still a long way from his expectations to making contributions to humankind. I also would like to express my greatest gratitude to Mr Qiuxin Gao for his always best handling and instructing in every step of my research and most considerable care during the past four and a half years.

I would also thank Professor Atilla Incecik for his kindest and most generous financial support for the software licenses. My sincerest thanks also go to Professor Chengi Kuo, Dr. Gerasimos Theotokatos, Ms Thelma Will, Ms Linda Mickay, Dr. Qing Xiao, Professor Peilin Zhou, Professor Shan Huang and Dr. Mahdi Khorasanchi for their always kindest help throughout this process. Sincere thanks also go to Professor Decheng Wan in Shanghai Jiao Tong University for his lasting inculcation to help me be a respectful researcher.

Especially sincere thanks go to Mr Long Shen, Mr Fenghua Liu and Ms Zhaoxia Hu in Hudong Heavy Machinery, Co. Ltd. in Shanghai for providing the most valuable data and discussions at the most desperate moment in this research. Your kindest supports will be always remembered. Finally, the kindest and greatest efforts made by the following people are sincerely appreciated:

Professor Jie Ma (Shanghai Jiao Tong University)
Professor Song Zhou (Harbin Engineering University)
Professor Guoquan Xiao (South China University of Technology)
Professor Huaming Wang (Zhejiang Ocean University)
Dr. Zhijian Huang, Dr. Dan Sun (Shanghai Maritime University)
Dr. Youhong Xiao, Dr. Pingjian Ming, Dr. Yongfeng Liu

(Harbin Engineering University)
Xiaopeng Liu (AVIC International, Beijing)
Yongquan Chang (China Classification Society, Shanghai)
Chao Ye (China Classification Society, Nanjing)
Zhiying Wang (Guangzhou Automotive Engineering Institute)
Chunfeng Zhou (Wuchang Shipbuilding Industry Co. Ltd.)
Airong Li (China Shipping Industry Co. Ltd., Shanghai)
Honggui Xiang, Shixing Gan, Cheng Chen, Rui Zhang
(Guangzhou Shipyard International Co. Ltd.)
Haiqiang Guo (China International Marine Containers Ltd.)
Xiaoming Yi (Lloyd's Register, Fuzhou, China)
Zhenhai Gan, Hao Tang, Yongdong Yang
(MAN Diesel & Turbo, China)
Dig Vijay Singh (Norwegian University of Science and Technology)
Dr. Sajjad Haider (Technical University of Denmark)
Dr. Paul Hellier (University College London)

I also wish to express my sincerest gratitude to Dr. Zhiliang Gao, Dr. Shi He, Dr. Liang Shen, Dr. Jiqing He, Dr. Leilei Tang, Dr. Wei Shao and Yue Ma, Dr. Zhengqiang Xu, Dr. Xing Sun, and my SSRC group members Dimitrios Mermiris, Konstantinos Sfakianakis, Dimitrios Sfakianakis, Rastko Simic, Yu Bi, Lei Ju and other unlisted colleagues in NAOME, who are the best people I have ever worked together.

My deep thanks also give to Glasgow Chinese Christian Church and Tron Church, and every kindest Christian there. It is you all who gave me the most touching understanding, courage and love. Together with you, I witnessed, I have been influenced and would always remember the magic power of faith, hope, and love.

My last but most special thanks are for my parents and my beautiful wife Mi, for the always devoted love that built and light up my life.

Publications

1. Wei Jin, Qiuxin Gao, Dracos Vassalos, The Prediction of KCS Resistance and Self-Propulsion by RANS, 8th-10th, December, 2010, *Gothenburg 2010 A Worshop on CFD in Ship Hydrodynamics*, Gothenburg, Sweden

2. Qiuxin Gao, Wei Jin, Dracos Vassalos, Computation of Wave Diffraction by RANS Approach, 8th-10th, December, 2010, *Gothenburg 2010 A Worshop on CFD in Ship Hydrodynamics*, Gothenburg, Sweden

3. Qiuxin Gao, Wei Jin, Dracos Vassalos, Simulation of Roll Decay by RANS Approach, 8th-10th, December, 2010, *Gothenburg 2010 A Worshop on CFD in Ship Hydrodynamics*, Gothenburg, Sweden

4. Qiuxin Gao, Wei Jin, Dracos Vassalos, The Calculations of Propeller Induced Velocity by RANS and Momentum Theory, *Journal of Marine Science and Application*, 2012

5. Wei Jin, Qiuxin Gao, Dracos Vassalos, Numerical Simulation of Marine Diesel Engine Combustion by RANS Method, *International Conference on Maritime Technology 2012*, 25-28 June 2012, Harbin, Heilongjiang, China

6. Qiuxin Gao, Zhiliang Gao, Wei Jin, Dracos Vassalos, The Numerical Study of Robotic Fish Hydrodynamics, *International Conference on Maritime Technology 2012*, 25-28 June 2012, Harbin, Heilongjiang, China

7. Wei Jin, Dracos Vassalos, Energy Modelling of Large 2-Stroke Marine Diesel Engine using CFD, *Low Carbon Shipping Conference 2013*, September 10-11 2013, London, UK

8. Lei Ju, Dracos Vassalos, Wei Jin, Rolling motion of Newtonian and non-Newtonian fluids in a ship compartment, *5th International Maritime Conference on Design for Safety*, November 25-27 2013, Shanghai, China

9. Wei Jin, Gerasimos Theotokatos, Dracos Vassalos, Numerical Simulation of the Scavenging Process of a Large 2-Stroke Marine Diesel Engine, *International Conference on Maritime Technology 2014*, 7-9 July 2014, Glasgow, UK

10. Wei Jin, Gerasimos Theotokatos, Dracos Vassalos, Numerical Investigations of the Spray-Mesh Interaction and Droplet Breakup Models for Evaporating Spray, *International Conference on Maritime Technology 2014*, 7-9 July 2014, Glasgow, UK

11. Wei Jin, Gerasimos Theotokatos, Dracos Vassalos, 3D Combustion Process Simulation of a Large 2-Stroke Marine Diesel Engine, *International Conference on Maritime Technology 2014*, 7-9 July 2014, Glasgow, UK

Contents

List of Figures

List of Tables

Abbreviations

ARK (Aungier-Redlich-Kwong)

BDC (Bottom Dead Centre)

CAD (Crank Angle Degree)

CFD (Computational Fluid Dynamics)

CIMAC (International Council on Combustion Engines)

CMC (Conditional Moment Closure)

CNG (Compressed Natural Gas)

DEM (Dynamic Energy Model)

DNS (Direct Numerical Simulation)

DPM (Discrete Phase Model)

DTU (Technical University of Denmark)

DWI (Direct Water Injection)

ECA (Emission Control Area)

ECN (Engine Combustion Network)

EDC (Eddy-Dissipation-Concept)

EEDI (Energy Efficiency Design Index)

EEOI (Energy Efficiency Operational Index)

EGR (Exhaust Gas Recirculation)

EOS (Equation of State)

ERC (Engine Combustion Center (University of Wisconsin))

ETAB (Enhanced Taylor Analogy Breakup)

ETH (Swiss Federal Institute of Technology)

FIA (Fuel Ignition Analyser)

FRED (Finite-Rate/Eddy-Dissipation)

GI (Gas Injection)

HC (Hydrocarbon)

HELIOS (High Pressure Electronically Controlled gas injection for marine 2-stroke

diesel engines)

HERCULES (High Efficiency R&D on Combustion with Ultra Low Emissions for Ships)

HFO (Heavy Fuel Oil)

HPC (High Performance Computing)

HRR (Heat Release Rates)

HSVA (Hamburgische Schiffbau Versuchsanstalt GmbH)

KH (Kelvin-Helmholtz)

KHRT (Kelvin-Helmholtz Rayleigh-Taylor)

LDA (Laser Doppler Anemometry)

LDV (Laser Doppler Velocimetry)

LES (Large Eddy Simulation)

LHV (Lower Heating Value)

LNG (Liquefied Natural Gas)

MARPOL 73/78 (International Convention for the Prevention of Pollution from Ships, MARPOL is short for marine pollution and 73/78 for years 1973 and 1978)

MCR (Maximum Continuous Revolution)

NS (Navier-Stokes)

PDF (Probability Density Function)

PIV (Particle Image Velocimetry)

PM (Particulate Matter)

PR (Peng-Robinson)

RANS (Reynolds Averaged Navier-Stokes)

RK (Redlich-Kwong)

RNG (Renormalisation Group)

RSM (Reynolds Stress Model)

RT (Rayleigh-Taylor)

RTZF (Ricardo Two-Zone Flamelet)

SCC (Spray Combustion Chamber)

SCR (Selective Catalytic Reduction)

SEEMP (Ship Energy Efficiency Management Plan)

SFOC (Specific Fuel Oil Consumption)

SGS (Sub-Grid Scale)

SRK (Soave-Redlich-Kwong)

SSD (Stochastic Secondary Droplet)

SSE (Standard State Enthalpy)

TAB (Taylor Analogy Breakup)

TARGETS (Targeted Advanced Research for Global Efficiency of Transportation Shipping)

TDC (Top Dead Centre)

USB (Unified Spray Breakup)

VCVCC (Visual Constant Volume Combustion Chamber)

Chapter 1 Introduction

1.1 Background

The internal combustion engine is a plant which combusts the fuel in the combustion chamber to release the chemical energy into thermal energy. The thermal energy in the combustion chamber would then convert into mechanical energy. The first ICE was invented by Germany inventor Nikolaus Otto in 1876. The other Germany inventor Rudolf Diesel invented the compression ignition engine in 1892, which was named after him as diesel engine (Heywood, 1988). Twenty years after the invention of diesel engine, the first ocean going vessel Selandia installed with diesel engines began her maiden journey in 1912. Since then, the diesel engine has been enjoying a dominant position in merchant ship propulsion markets for more than 100 years (Woodyard, 2009).

The thermal efficiency of diesel engines in the early stages was very low. The adoption of turbochargers induced a major boost to engine output and reductions in size and weight (Woodyard, 2009). In the mid-1950s, most 2-stroke engine builders introduced turbocharged designs. Thanks to the application of cylinder lubricants, the heavy fuel oils could be burnt in diesel engines during this period as well. This allows cost reductions and strengthens the status of diesel engines used in marine propulsion (Woodyard, 2009). Figure 1.1 is the evolution of thermal efficiency of 2-stroke engine (Sher, 1990).

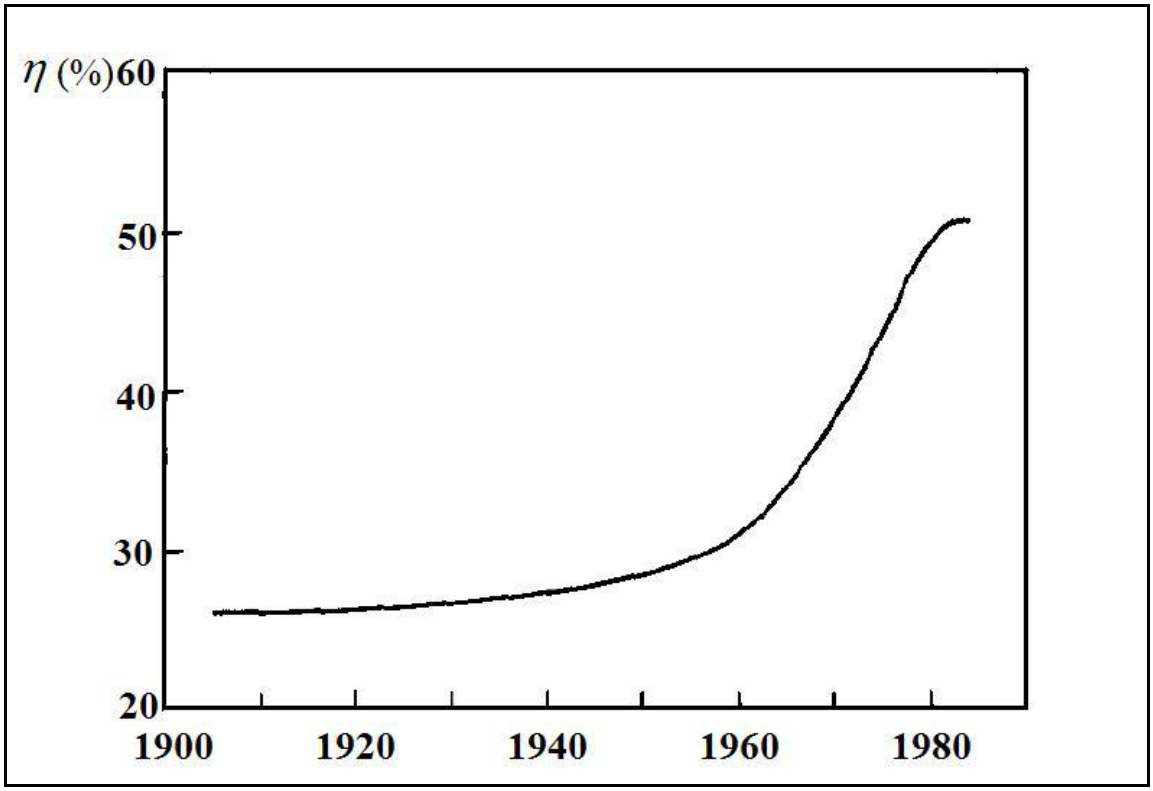

Figure 1.1 Evolution of thermal efficiency of 2-stroke engine

The most efficient large 2-stroke marine engines reach efficiencies up to 55% (Rasmussen, 2011) today. Even though the efficiency of diesel engines reaches nearly the maximum, engine companies still invest tremendous efforts to increase a tiny percentage to sustain their dominance. During the competition, a lot of contenders in low speed 2-stroke engines either no longer exist, or have become part of other brands. Such evolution also induces the survival of low speed engines sharing common basic configurations:

1) 2-stroke
2) Cross head
3) Constant scavenging pressure
4) Uniflow scavenging
5) Single exhaust valve in the cylinder head (Woodyard, 2009).

Today, only three low speed engine designers survive and contest the international marine engine market, namely MAN B&W, now part of MAN Diesel & Turbo, Wärtsilä and Mitsubishi. MAN B&W and Wärtsilä are two giants in this area, who share 98% of the global low speed marine engine market. Their market share in four quarters in 2013 is demonstrated in Figure 1.2 (Wärtsilä, 2014). Figure 1.3 is a typical large 2-stroke marine diesel engine manufactured by MAN B&W.

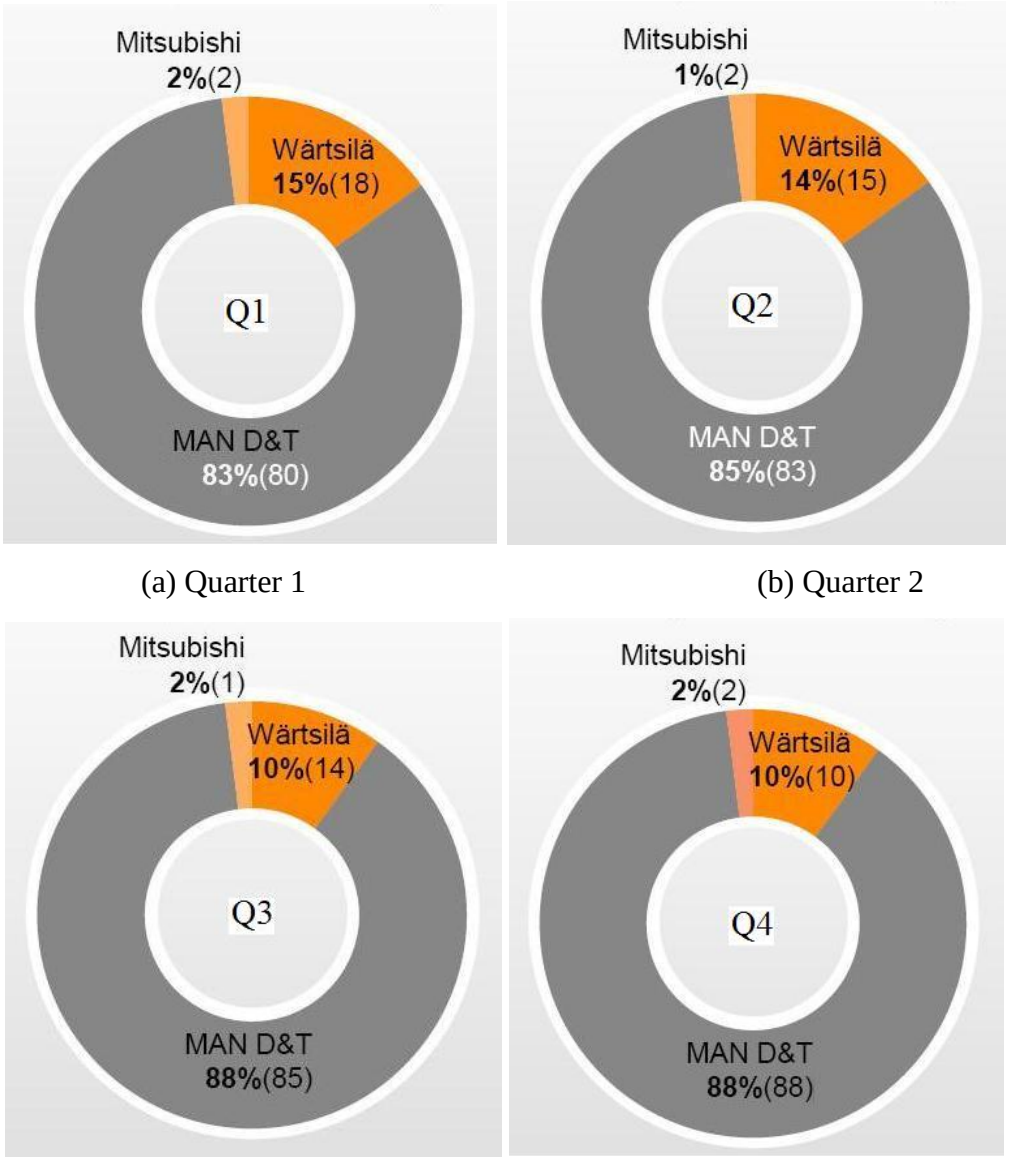

(a) Quarter 1 (b) Quarter 2

(c) Quarter 3 (d) Quarter 4

Figure 1.2 World market shares of low speed marine diesel engines in 2013

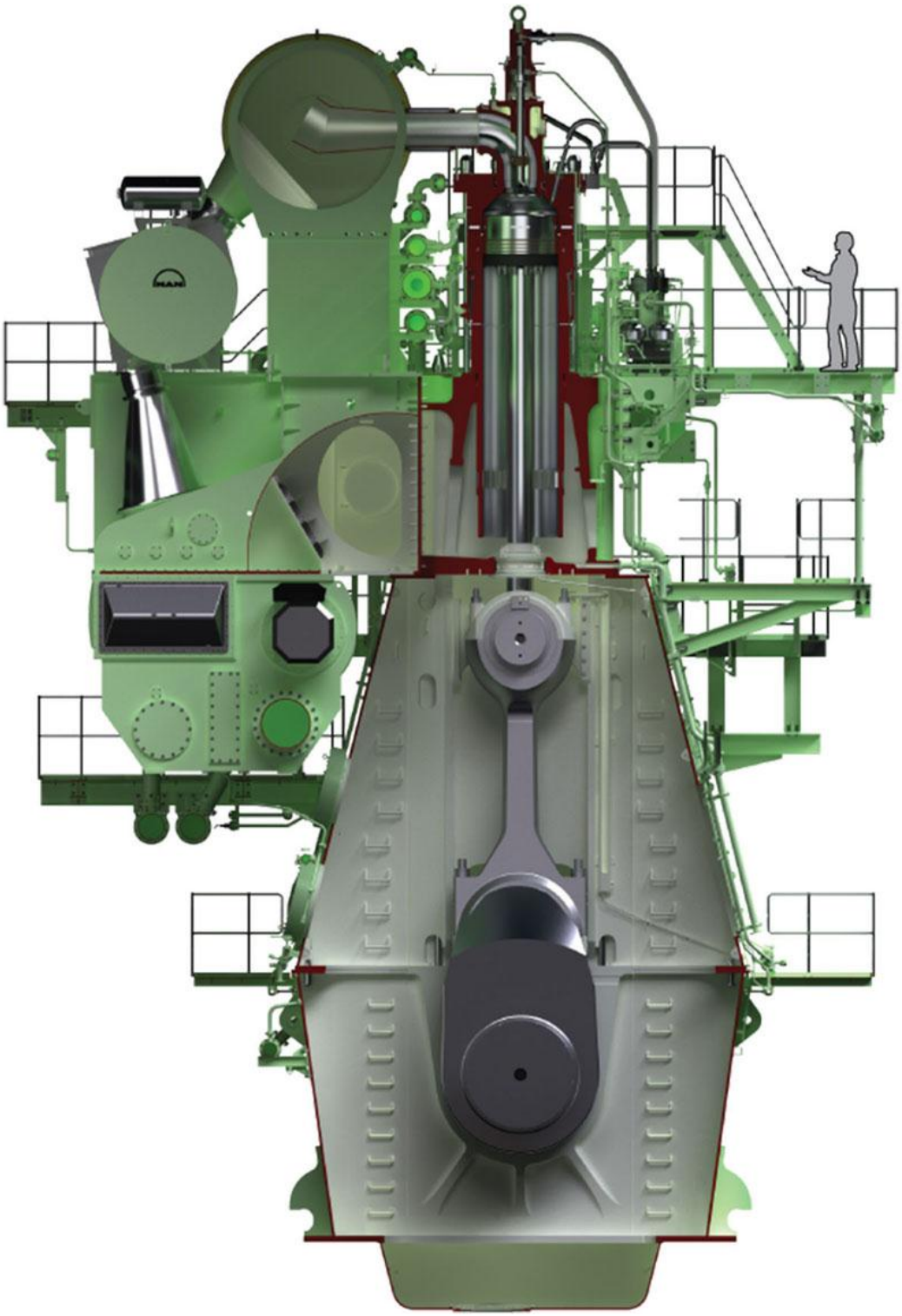

Figure 1.3 A large 2-stroke marine diesel engine made by MAN B&W

Another challenge for the engine designers is reducing the exhaust gas pollutants to meet increasing restrictions from IMO. The latest Annex VI of MARPOL 73/78 (International Convention for the Prevention of Pollution from Ships, MARPOL is short for Marine Pollution and 73/78 for years 1973 and 1978) contains a three-tier for NO_x regulations (IMO, 2009):

Tier I

For diesel engines installed on ships constructed from 1 January 2000 to 1 January 2011, the allowable NO_x emissions are:

17.0 g/kWh when n is less than 130 rpm

$45.0 \times n^{-0.2}$ g/kWh when n is 130 rpm or more but less than 2000 rpm

9.8 g/kWh when n is 2000 rpm or more

Tier II

For diesel engines installed on ships constructed on or after 1 January 2011, the allowable NO_x emissions are:

14.4 g/kWh when n is less than 130 rpm

$44.0 \times n^{-0.23}$ g/kWh when n is 130 rpm or more but less than 2000 rpm

7.7 g/kWh when n is 2000 rpm or more

Tier III

Ships constructed on or after 1 January 2016 will have additional limitations when operating in an Emission Control Area (ECA). No ECAs have yet been designated for NO_x emissions, but it is expected that both the Baltic Sea and North Sea will be designated as NO_x ECAs well ahead of 1 January 2016. For Tier III ships operating in the NO_x ECAs, the allowable NO_x emissions are:

3.4 g/kWh when n is less than 130 rpm

$9.0 \times n^{-0.2}$ g/kWh when n is 130 rpm or more but less than 2,000 rpm

2.0 g/kWh when n is 2,000 rpm or more

In-cylinder measures such as direct water injection and fuel emulsification can fulfil the Tier II limits. Selective Catalytic Reduction (SCR) can meet the toughest limits (Woodyard, 2009). Dual-fuel diesel and gas engine is also an alternative to address this problem. Both MAN B&W (GI-type) and Wärtsilä (DF-type) developed their dual-fuel engines.

To achieve greater fuel economy, engine designers have focused on combination of higher efficiency turbocharger, lower rotational speed and higher maximum combustion pressure. The latest developments include:

1) Engine thermal efficiency can be raised to over 54%.

2) Specific Fuel Oil Consumption (SFOC) can be as low as 155g/kWh.

3) Minimum engine speed can be reduced to as low as 55 rpm to improve the propeller efficiency (Woodyard, 2009).

The latest products launched by MAN B&W include G40/45/50ME-B9.3, G60/70/80ME-C9.2, S30ME-B9.3 and S90ME-C9.2. The naming of MAN B&W engines is shown in Figure 1.4. The G series engine of MAN B&W is a new generation of Green ultra-long-stroke type. Even though this may induce a new design of the aft ship to fully utilise the low engine revolutions, the market shows high interest to the new engines, including the newly variable exhaust valve timing ME-B9 engines (Kindt, 2013).

The electronically controlled fuel injection and exhaust valve systems would pave the way for the future “Intelligent Engine”, which monitors its own condition and adjusts the key parameters for optimum performance (Woodyard, 2009).

The terminologies and working processes of the large 2-stroke marine diesel engine would be out of the scope of this dissertation. Fundamental and encyclopaedic knowledge of these aspects can be found in Heywood (1988), Taylor (1996) and

Woodyard (2009).

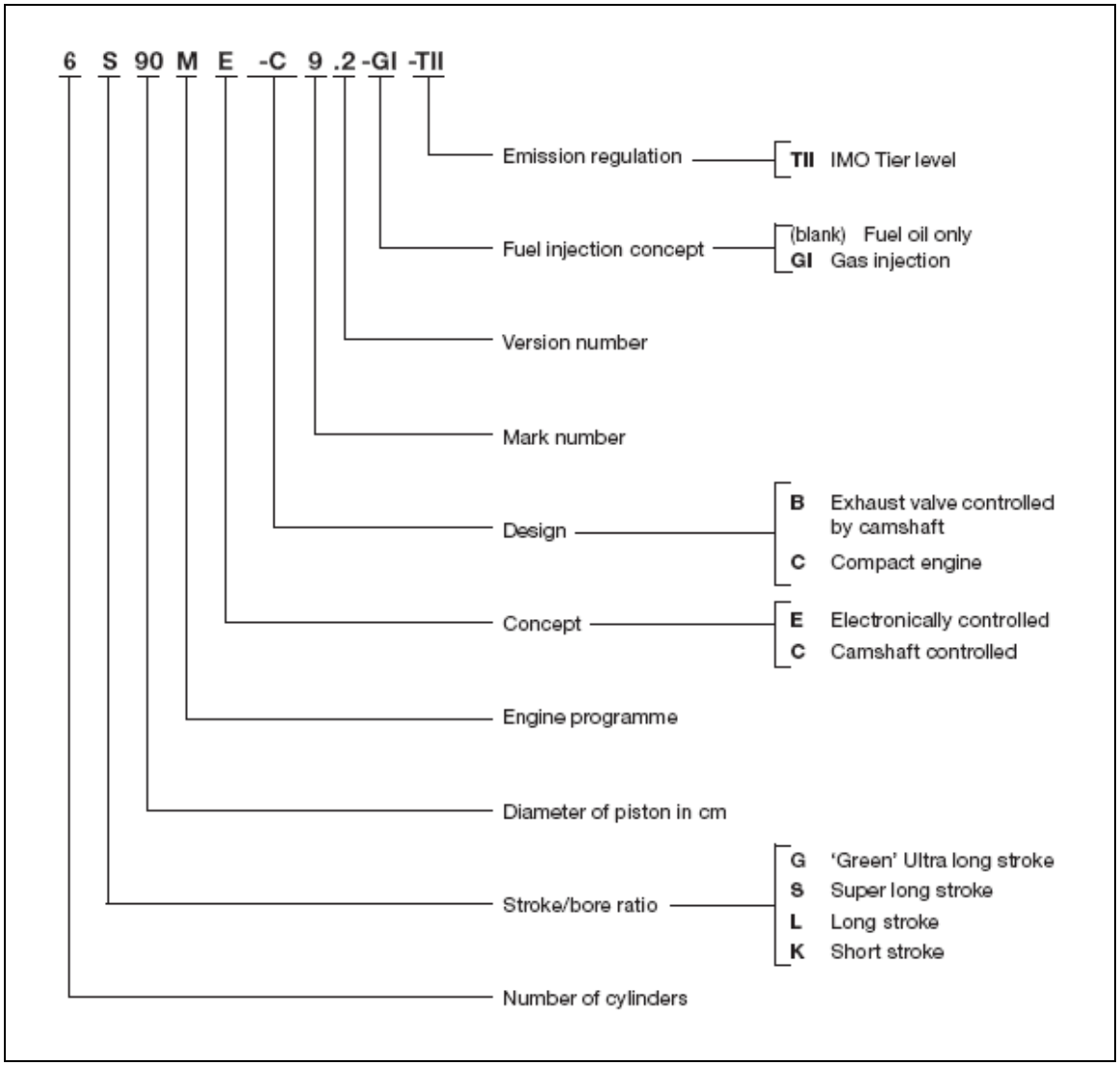

Figure 1.4 Naming of MAN B&W engines

1.2 CFD Applications to Marine Engines Research

With the enormously advancing of High Performance Computing (HPC) and Computational Fluid Dynamics (CFD), it became possible to simulate the engine combustion process in the late 1970s. The enhanced understandings of the engine combustion process and the numerical models related with the process as fluid dynamics, thermal dynamics and combustion chemistry make the engine combustion simulations more and more widely used in engine research. Even though the engine combustion CFD simulation is considered as one of the most challenging tasks, however, it becomes realisable to analyse this process quantitatively (Lakshminarayanan et al., 2010).

As the improvements of the fidelity and ease of use for CFD codes, it becomes gradually possible to use these with confidence in engine design. Two leading masterpieces come from Los Alamos National Laboratory, where KIVA was developed, and Imperial College in Great Britain where the STAR CD was born. Besides these two giants, some other commercial CFD software as AVL FIRE, ANSYS FLUENT, ANSYS CFX, VECTIS and CONVERGE are also the most preferred. Finally, the open source code OpenFOAM is attracting more and more interest from the engine developers. All of these are being continuously improved and boosting the innovation for engine research (Lakshminarayanan et al., 2010).

1.3 Research Aims

The overall aim is to develop and validate a numerical model of a 2-stroke marine engine with the view to utilise this capability to support wider scope research targeting the development and optimisation of integrated ship energy systems. To this end, specific objectives include:

1) To critically review state-of-the-art in the modelling of marine engines with the view to identifying best practice to be used and gaps to be targeted by this research.

2) To build a CFD engine model using ANSYS FLUENT to simulate the working processes of a large 2-stroke marine diesel engine MAN B&W S60MC-C6.

3) To validate the CFD models involved in the simulation of MAN B&W S60MC-C6 working process.

4) To provide reliable strategies for the CFD modelling of the working processes of the large 2-stroke marine diesel engines.

5) To offer recommendations for future research in this area.

1.4 Thesis Outline

The layout of the thesis is outlined next:

Chapter 2: Literature review of the large 2-stroke marine diesel engine research and development, which includes the key European Commission supported projects and a partial summary of the results from public engine research.

Chapter 3: This addresses numerical models involved in the simulation of the large 2-stroke marine diesel engine working processes, which include the dynamics mesh scheme, state equations, heat transfer modelling, turbulence modelling, spray modelling and combustion modelling.

Chapter 4: The basic cases tests to determine the mesh size, turbulence model, wall function and droplet breakup model, necessary for the modelling of the large 2-stroke marine diesel engine.

Chapter 5: The CFD modelling of a large 2-stroke marine diesel engine S60MC-C6 and the tests of the scavenging process at different load conditions.

Chapter 6: The compression and combustion validations of the large 2-stroke marine diesel engine S60MC-C6.

Chapter 7: Conclusions and discussion of the research undertaken and recommendations for further research.

Chapter 2 Critical Review

The research of the large 2-stroke marine diesel engine development is lagging behind that of the automotive engines. Almost the latest innovations in combustion would firstly be applied to automotive engines. The large 2-stroke marine engine is much more expensive than automotive engine and the fuel cost and facilities used by a large 2-stroke engine during the research would be much more costly than those for automotive engine. This makes the research of the large 2-stroke marine engine confined to the engine companies or agents who keep close relationships with them. The latest and most comprehensive development results presented in every three years' CIMAC (Congrès International des Monteurs a Combustion Interne, International Council on Combustion Engines) world congress. Regarding to the CFD research of the large 2-stroke marine diesel engines, for the reason that the CFD research goes hand in hand with the experiments, this induces less research results compared with automotive engines. In spite of this, tremendous efforts were, are and would be taken to investigate smart ways for the large 2-stroke engine research.

In this chapter, researches of the large 2-stroke marine diesel engine and related would be summarised.

2.1 Key European Commission Projects on Marine Engine R&D

Engine R&D is not only the tasks of engine companies, but is also under the umbrella of international supports for its great economy and environment benefits. The investments from national and international levels provide great financial supports for engine designers. As one of the key technology incubation bases of engines, European Union

keeps involving lasting financial and intellectual investments to the R&D of engines for car, bus, train, airplane and ship. Such projects greatly boost the development of modern engines. The following listed key projects relating with waterborne transport witness the footprints of the large 2-stroke marine diesel engines progress.

2.1.1 HERCULES-A

HERCULES (High Efficiency R&D on Combustion with Ultra Low Emissions for Ships) -A is a joint research project coordinated by MAN Diesel & Turbo and Wärtsilä with 40 other partners involved. It is within the European Commission's 6th Framework Program and aiming at developing marine diesel engines with technologies and components to achieve lower emissions and increase efficiency and reliability. HERCULES-A started in March 2004 and ended in September 2007.

The objectives of HERCULES-A are listed in Table 2.1.

Table 2.1 HERCULES-A objectives

Reduction of fuel consumption and CO_2 emissions	-1%
Reduction of NO_x (Relative to IMO 2000 standard)	-20%
Reduction of other emission components (PM, HC)	-5%
Improvement in engine reliability	10%
Reduction of time to market	-10%
Initial cost	0%
Fuel/lube-oil cost	-1%
Maintenance	-4%

HERCULES-A project followed the following lines:

1) Development of advanced process models and engineering software.

2) Manufacture and tests of prototype components.

3) Design of the experiment and assessment of the engine test bed data.

4) Test of full-scale engines on shipboard.

The detailed processes to realise these objectives are listed in Table 2.2.

Table 2.2 HERCULES-A innovations

Extreme design parameters	Engine components for extreme output operation
	Extreme value engine
Advanced Combustion Concepts	Combustion models
	Chemical kinetics models
	Full cycle simulation tools
Multistage/Intelligent turbocharging	Variable geometry turbocharger
	Power take-in, take-out systems
	Integration motor/generator/turbocharger
	Multistage inter-cooled turbocharger
Turbo-compound / hot engine	Composite structures for hot-engine
	Engine compounding systems and components
Emission reduction internal-water	Direct water injection system
	Inlet air humidification system
	Control systems for above
Emission reduction Internal-Exhaust Gas	Exhaust gas recirculation system
	PM measuring techniques
Emissions after treatment	In-service emissions monitoring system
	Non-Thermal Plasma Technology
	Wet Scrubber Technology
	Select-cylinder emission measurement technology
Reduced Friction	Low friction engine components
	In-service monitoring system for cylinder and

	lubricant feed rate adjustment
	Low friction engine
Adaptive engine	Onboard engine electronics

HERCULES-A project designed and manufactured several cutting-edge tests and the achievements by the end of the project are summarised in Table 2.3 (Kyrtatos, 2012).

Table 2.3 HERCULES-A achievements

	Targets	Achievements
Specific Fuel Oil Consumption	-1%	-1.4%
NO_x Emission	-20%	-50%
Other Emission Components	-20%	HC, -20%
		PM, -40%
		SO_x, -90%
Reliability	10%	>8000 Hours Testing
Time to Market (60 Months in 2004)	-10%	<42 Months

Link to http://www.ip-hercules.com/ for more details.

2.1.2 HERCULES-B

HERCULES-B is phase II of the whole HERCULES project. It is coordinated by MAN Diesel & Turbo and Wärtsilä with 30 other partners involved. It is within the European Commission's 7th Framework Program. Based on the results of HERCULES-A, the research area is narrowed down to focus on potential breakthroughs for lower specific fuel consumption and ultra-low emissions. HERCULES-B started in September 2008 and ended in December 2011.

The principal aim in HERCULES-B is to reduce fuel consumption of marine diesel

engines by 10%, to improve efficiency of marine diesel propulsion systems to a level of more than 60%. An additional aim is towards ultra low exhaust emissions (70% reduction of NO_x, 50% reduction of particulates) from marine engines by the year 2020.

Compared with HERCULES-A, HERCULES-B further developed the listed processes in Table 2.4.

Table 2.4 HERCULES-B innovations

Extreme Parameter Engines	2-Stroke engine, P_{MAX}: 220 bar Mean piston speed: 10 m/s
	4-Stroke engine, P_{MAX}: 300 bar Mean piston speed: 12 m/s
Combustion	Transparent cylinder cover with optical access 2-Stroke, 500 mm bore engine 4-Stroke, 320 mm bore engine firing conditions: 200 bar, 2000℃
	Measured injection and combustion full-scale spatial data for CFD engine simulation validation
Turbocharging	Multistage turbocharging with 8 bar charging pressure on test engine
Emission Reduction	EGR / CGR / Scrubbing for NO_x reduction >50%
	Engine application for SCR with fuel of high sulphur content.
Overall power train optimisation	High pressure boiler compounding system to achieve overall power plant efficiency 60% on test
Advanced materials, friction and wear	Reduction 25% in piston ring friction and guide shoe friction
Electronics and control	Installation on test engine of intelligent

	management system with self learning and fault tolerant capabilities and comparison with conventional systems

At the end of HERCULES-B in December 2011, most of the listed objectives were achieved. For 2-stroke extreme parameter tests, only 200 bar maximum pressure and 9m/s were carried out. The power train optimisation and intelligent management system were under testing as well.

Link to http://www.hercules-b.com/ for more details.

2.1.3 HERCULES-C

HERCULES-C is phase III of HERCULES program. It is still coordinated by MAN Diesel & Turbo and Wärtsilä with 20 other partners involved. It is within the European Commission's 7th Framework Program. HERCULES-C started in September 2012 and would last 3 years. The budget is 17 million Euros and 9 million of which funded by FP7.

The objective of phase III is firstly to achieve further reductions in fuel consumption through advanced engine developments in combustion, fuel injection and the optimisation of ship energy management and engine technologies supporting transport mission management. Secondly, near-zero emissions engine integrating the various technologies developed in the previous HERCULES-A and HERCULES-B Projects would be further developed. The third objective is to maintain the technical performance of engines throughout the operational lifetime. Its links with the first two stages is illustrated in Figure 2.1 (Kyrtatos et al., 2013).

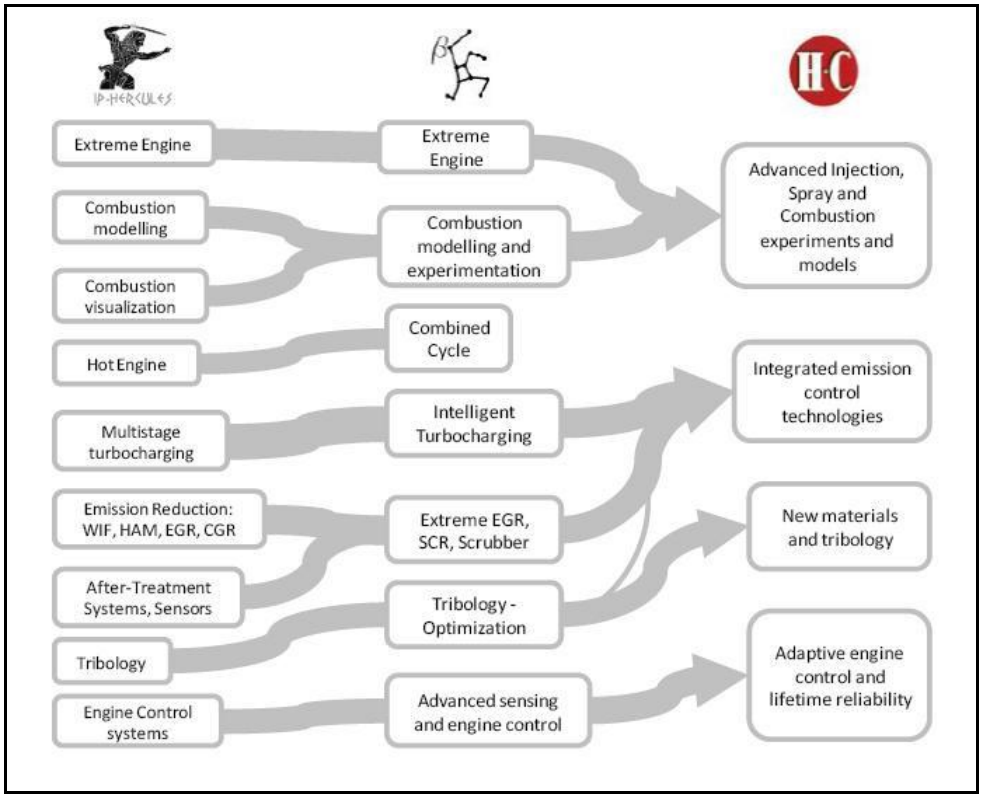

Figure 2.1 Links of HERCULES projects

The targets and approaches of HERCULES-C are demonstrated in Table 2.5.

Table 2.5 HERCULES-C objectives

Objectives	Targets	Approaches
Reduction of Fuel Consumption	3% Reduction	Optimisation of Power Production and Consumption
Reduction of Emissions	80% NO_x Reduction	Developments in Combustion and Best Practices in Phase I and II
Retain High Performance over Lifetime	20 Years	Developments in Sensors, Monitoring and Controlling
		Tribology Improvements
		Materials Improvements

The latest updates of HERCULES-C can be found at:
http://www.hercules-c.com/.

2.1.4 HELIOS

HELIOS (High Pressure Electronically Controlled gas injection for marine 2-stroke diesel engines) project is a cooperative research project coordinated by MAN Diesel & Turbo with eight other partners involved. It is within the European Commission's 7th Framework Program and aiming at developing the electronically controlled low speed 2-stroke marine diesel engines operating on Compressed Natural Gas (CNG) or Liquefied Natural Gas (LNG). What's more, the HELIOS project also bears the potential to retrofit of gas engine on existing ships in service without reinstalling of new engine. The HELIOS project started in February 2011 and ended in November 2013.

The HELIOS project experienced the following stages:
1) ME-GI world premiere demonstration tests
2) Optimisation of performance and reliability
3) Development and detailed design of S70ME-C-GI
4) Demonstration test at Hyundai and Mitsui
5) First vessels with ME-GI ordered
6) ME-GI + EGR test on 4T50ME-GI
7) Available for all ME engines

The most significant result of HELIOS project is the successful development of the ME-GI (Gas Injection) engine, which meet the Tier II limit. With EGR or SCR, Tier III standards can be reached as well. The environmental benefits are listed in Table 2.6.

Table 2.6 Improvements of HELIOS project

NO_x	24% Reduction

CO_2	23% Reduction
Methane “Slip”	0.2-0.3 g/kWh
PM	85% reduction
CO	Very Low
SO_2	Very Low
Smoke	Almost Eliminated
Thermal Efficiency	Very High

During the period from December 2012 to November 2013, the ordered GI engines reached 16. The assessment from MAN Diesel & Turbo to the potential for more orders is great.

Link to http://helios-fp7.eu/ for more details.

2.1.5 TARGETS

TARGETS (Targeted Advanced Research for Global Efficiency of Transportation Shipping) project is a joint research coordinated by HSVA (Hamburgische Schiffbau Versuchsanstalt GmbH) with 12 other partners involved. It is within the European Commission’s 7th Framework Program. TARGETS started in December 2010 and ended in March 2014.

TARGETS project is to globally analyse the most important causes of energy consumption on board of cargo ships in a comprehensive and holistic way. TARGETS project will contribute designing and operational guidelines for an energy efficient operation of cargo ships according to Energy Efficiency Design Index (EEDI), Energy Efficiency Operational Index (EEOI) and Ship Energy Efficiency Management Plan (SEEMP).

Ships are complex systems housing a variety of on-board installations consuming energy. The largest source of energy consumption is of course the main engine, which in case of large cargo ships almost exclusively is a two stroke diesel engine. Despite the remarkable developments in terms of engine technology over the past decades and the undisputed unparalleled efficiency of modern diesel engines, the overall efficiency of such engines is limited. Although the thermal efficiency of advanced diesel engines is about 50%, further improvements of the combustion process will be limited simply by physical constraints and additional gains will only be achieved through complementary measures such as advanced concepts for waste heat recovery. The focus of TARGETS lies on the efficient use of these 50% of energy consumption which are used to propel the ship. Compared with the other engine related projects, TARGETS would rather consider engine as one of the energy modules onboard than optimise the details of conventional engine (TARGETS, 2010). To improve EEDI, the ship hull form including the aft body and bulbous bow would be optimised. Thus the larger diameter propeller would possibly be installed. To obtain optimal propeller efficiency, the rotational speed of the propeller should be lower. Thus the ultra long stroke engine designing with lower-than-usual speed would meet the target. Or during the operation stage, the engine could be de-rated to improve EEOI. Through the introduction of EEDI and EEOI, the engine design would then be re-shaped as well.

After all the energy modules being finished, they are integrated into Dynamic Energy Model (DEM), which monitors the energy flow during the design, retrofitting and operating stages and provides with the optimal energy scheme (Marzi et al., 2011, Mermiris et al. 2011). The present research is the numerical validation of the main engine module of TARGETS project to provide reliable engine database for the comprehensive and holistic optimisation.

This research is financially supported by TARGETS project.

Link to http://www.targets-project.eu/ for more details.

2.2 Literature Review

In this section, the full cycle researches of the large 2-stroke engine are firstly reviewed. Except for the full cycle researches, two critical and controllable processes, thus scavenging and injection are also reviewed considering their directly relations to the full cycle researches.

2.2.1 Full Cycle

After decades of development of CFD using in the engine researches, Weisser et al. (1998) aimed to provide a status report of integrating CFD into the development process of the large diesel engines based on KIVA3 code. The models and setups are summarised below:

Engine type:	RTA58T
Produced by:	Wärtsilä
Engine speed:	103.0 rpm
Turbulence model:	RNG k-ε model
Fuel spray breakup:	Enhanced Taylor Analogy Breakup (ETAB) model
Ignition:	Weisser empirical model
Combustion:	Laminar and turbulent characteristic time combustion model
NO_x:	Enhanced Zeldovich mechanism

However, during the combustion process, the obvious discrepancy between the measured and calculated Heat Release Rates (HRR) made an objective review impossible. By demonstrating the investigations of interacting sprays results, it was concluded that even though CFD would not completely replace engine experiments, still it could contribute to a better understanding of in-cylinder processes. The then-still very

high computational expense made it was still time ahead for routine using.

Rodatz et al. (2000) utilised the same configurations of Weisser et al. (1998) to evaluate the predictive abilities at different injection pressure and duration combinations. By analysing the comparison of the results, it concluded that the computations results of cylinder pressure and heat release rate can adequately well match the measured data by adjusting the constant in the combustion model. For the reason that the scavenging process was not included, the trends of the temperature on the exhaust valve was not reproduced by the simulation. However, good trends were obtained for the predicted temperature distribution on the piston and cylinder cover. The trend of NO_x was adequately reflected but the absolute values were underestimated due to insufficient mesh resolution. The status review of CFD as the development tool was that it is able to reproduce the experimental trends and can be used to support the design process. But further sophisticated turbulence and combustion models should be developed to increase the accuracies.

Weisser et al. (2004) provided the latest reviews of to what extent CFD can be used for combustion development in terms of efficiency, emissions and reliability based on the commercial software STAR-CD. The models and setups are summarised below:

Engine type:	RTA58T-B & RT-flex58T-B
Produced by:	Wärtsilä
Ignition:	Multi-step involving various intermediate species
Combustion:	Extended coherent flame model
NO_x:	Enhanced Zeldovich mechanism
Soot:	Engine Combustion Centre (University of Wisconsin) (ERC) model

The scavenging and combustion processes of RTA58T-B were simulated and the measured in-cylinder pressure traces were very well reproduced. Then three different injectors with different hole numbers were calculated on RT-flex58T-B using the

validated models. The corresponding predicted pressure traces presented obvious discrepancies compared with the measured data. The NO_x and soot predictions were not so satisfactory either. It was emphasised that the models were not tuned or adapted during these investigations.

As a result, the conclusions obtained were:

1) There is still plenty of room to refine the models and develop the tools and methodologies to improve the accuracy.

2) CFD is regarded as an indispensable tool to get insight into the combustion and pollutant formations, even though great care has to be taken.

3) The CFD simulation of scavenging process reaches a certain level of maturity to be possibly extended to engine development in case of comprehensive validation.

Endo et al. (2001) focused their research on the heat transfer predictions using CFD code KIVA3. The models and setups are summarised below:

Engine type:	UEC85LSII
Produced by:	Mitsubishi Heavy Industries, Ltd
Engine speed:	76.0 rpm
Turbulence model:	RNG k-ε model
Fuel spray breakup:	Wave breakup model + Liquid core length
Fuel spray impingement:	Liquid film model
Ignition:	Livengood-Wu empirical model
Combustion:	Laminar and turbulent characteristic time combustion model
Heat transfer:	Launder & Spalding
Initial droplet diameter:	Nozzle hole diameter

For the reason that only the compression and combustion processes were calculated and the scavenging process was not included, the velocity distribution in the cylinder at the start of the simulation was initialised from the measured data using Laser Doppler Velocimetry (LDV). By converting the difference between the measured fuel injection

pressure and in-cylinder pressure, the fuel injection was obtained.

Firstly, the calculated in-cylinder pressure was compared with the experimental data. The calculated maximum in-cylinder pressure was overestimated by 6 bars (+4.5%). Secondly, in order to investigate the heat transfer, three different fuel injection directions (standard direction, +3 ° outward and +6 ° outward) were calculated. The heat transfers from the high temperature gas were transferred to the cylinder cover and piston. It was found that with increasing of the degree, the heat transfer to the cylinder cover and piston became higher as well. The absolute value of the heat transfer rate was compared with other researchers and was considered to be at the reasonable level. Finally, by integrating the predicted heat transfers on the cylinder cover and piston, the temperature on the cylinder cover and piston was compared with the measured data. It was found that the time integration of heat transfer rate on the cylinder cover coincided very well with the measured temperature on it. However, the prediction of the heat transfer on the piston was considered not so satisfactory. This reason was attributed to the inaccurate prediction of the flame behaviour.

Different from the work of Endo et al. (2001), Kim et al. (2001) focused their efforts on the reducing the pollutants emissions by varying the nozzle hole directions using the commercial software AVL FIRE. The models and setups are summarised below:

Engine type:	MAN B&W S70MC
Produced by:	MAN B&W
Engine speed:	91.0 rpm
Turbulence model:	k-ε
Fuel spray breakup:	Wave child breakup model + Diesel nozzle model
Ignition:	Auto-ignition model for diesel
Combustion:	Turbulence controlled combustion model
NO_x:	Equilibrium assumption + Enhanced Zeldovich mechanism

The calculated and measured in-cylinder pressure was firstly compared and very good

coincidence was obtained. The NO_x and soot prediction results were compared with different nozzle hole directions without validations. Finally, an improved hole configuration was determined by comparing the emission performance.

Andreadis et al. (2011) aimed at reducing the pollutants emissions by varying the nozzle injection profiles of the large 2-stroke marine diesel engine Wärtsilä RT-flex58T-B using KIVA3 code. Very good coincidence between the calculated and measured in-cylinder pressure guarantees the accuracy of the built model. By analysing the emission results predicted using different injection profiles obtained from the multi-objective engine optimisation in terms of the pilot and main injections, it was pointed out that the optimum solution could improve the NO_x emissions with the order of 15-20% and the Specific Fuel Oil Consumption (SFOC) with the order of 2%. Based on the analysis, it was concluded that only the optimisation of the injection profile would be impossible to fulfil the emission standards of Tier III.

Chryssakis et al. (2010(1)) introduced the air fumigation and Direct Water Injection (DWI) to the large 2-stroken marine diesel engine through KIVA3. The related SFOC, NO_x and soot emissions were investigated to get the corresponding effects. The computation models and setups are summarised as below:

Engine type:	RT-flex58T-B
Produced by:	Wärtsilä
Engine speed:	105rpm
Fuel spray breakup:	Kelvin-Helmholtz Rayleigh-Taylor (KHRT) model
Ignition:	Modified Shell model
Combustion:	Characteristic time combustion model
NO_x:	Enhanced Zeldovich mechanism
Soot:	Hiroyasu soot model

It was proven that the DWI was substantially more efficient in reducing NO_x emissions compared with the air fumigation. However, it was on the cost of significant penalties in

terms of soot emissions and SFOC. It was feasible via optimisation of water-addition to improve the large 2-stroke diesel engine performance. The analysis presented that the strictest Tier III NO_x emission standards could be met with water addition approaches.

Imamori et al. (2004) aimed at developing the simulator with CFD including the scavenging process based on the work of Endo et al. (2001) to eliminate the introduced error in the initialisation. The commercial software STAR-CD was used to calculate the scavenging process from exhaust valve open to exhaust valve close. Then KIVA3 code was used to deal with the compression and combustion processes. The data include velocity, pressure, temperature, species mass fraction and turbulence levels were transferred from STAR-CD to KIVA3 through data mapping. The models and setups are summarised below:

Engine type:	MHI UEC68LSE
Produced by:	Mitsubishi Heavy Industries, Ltd
Turbulence model:	RNG k-ε model
Fuel spray breakup:	Wave breakup model + Liquid core length
Fuel spray impingement:	Liquid film model
Ignition:	Livengood-Wu empirical model
Combustion:	Laminar and turbulent characteristic time combustion model
Heat transfer:	Launder & Spalding
NO_x:	Enhanced Zeldovich mechanism

In order to minimise the introduced error in the initialisation, three cycles coupling calculations of STAR-CD and KIVA3 were carried. It was found that it is necessary to experience at least three cycles calculation to stabilise the NO_x and heat release rate. Then two differently distributed nozzles were used to investigate the different effects. For both cases, the predicted maximum in-cylinder pressure was underestimated by about 7 bars (-5.7%). For the reason that the five-hole nozzle had slower spray evaporation, the later-combustion lasted longer and the heat release rate during this stage was higher than the four-hole nozzle. The CFD results duplicated these features and the

predicted NO_x and in-cylinder temperature were higher for the five-hole nozzle. By comparing the integrated the heat transfers of piston, cylinder cover, cylinder liner and the exhaust valve with the measured temperature, it finally concluded that the built model was capable of trend prediction.

To develop a platform for maintenance, Borkowski (2007) carried out the damaged injection nozzle hole investigations experimentally and numerically using the commercial CFD code Vectis. The models and setups are summarised below:

Engine type:	MAN B&W 7S50MC
Produced by:	MAN B&W
Turbulence model:	*k-ε*
Fuel spray breakup:	Huh-Gosman primary + Paterson-Reitz secondary model
Ignition:	Seven steps auto-ignition model
Combustion:	Ricardo Two-Zone Flamelet (RTZF) combustion model
Heat transfer:	Woschni correlation
Initial droplet diameter:	Nozzle hole diameter
NO_x:	Enhanced Zeldovich mechanism

In order to make the modelling as precise as possible, the following measures were adopted:

1) The intake and exhaust boundary conditions were obtained from the time dependent test-bed data processed Ricardo Wave code.

2) The temperature on the cylinder liner was specified piecewise.

3) The detailed geometries of the scavenging ports were modelled to consider the blow-by during the scavenging process.

4) The injection pressure was measured to specify the fuel mass flow rate profile.

To validate the CFD model, the predicted in-cylinder pressure in the normal injection condition at 100% and 25% loads was compared with the measured data. Comparing the results, very good agreement was obtained. Then the calculated in-cylinder pressure with

the damaged nozzle at 100% load was compared with the experimental pressure trace. It was noticed that the difference of the in-cylinder pressure of the simulation and measurement increased under the damaged nozzle situation. In spite of this, the trend of higher temperature producing higher NO_x was reproduced. At different loads (25%, 50%, 75% and 100%), the failure of one injection nozzle did not seriously affect the NO_x emission, which was proven both by the measured and computed results. However, the computation was not able to reproduce the measured NO_x emissions very well. The Enhanced Zeldovich with detailed mechanisms was required for better accuracy. It was pointed out that high standard quality facilities and experimental data were also critical for validations. One of the inaccuracy sources was also attributed to the inaccurate determination of fuel injection and cylinder pressure history.

Chryssakis et al. (2010(2)) applied their latest modelling of Heavy Fuel Oil (HFO) in Visual Constant Volume Combustion Chamber (VCVCC) and Fuel Ignition Analyser (FIA) to the large 2-stroken marine diesel engine through KIVA3. Except for the fuel properties were modified to those of HFO, the computation models and setups are summarised as below:

Engine type:	RT-flex58T-B
Produced by:	Wärtsilä
Fuel spray breakup:	ETAB model
Ignition:	Weisser empirical model
Combustion:	Laminar and turbulent characteristic time combustion model

Based on the satisfactory prediction results of spray structure and combustion development by the built model, HFO was used as fuel in the large 2-stroke marine engine RT-flex58T-B combustion simulations under five different injection timings. However, it was noticed that the predicted in-cylinder pressure traces with HFO were obviously lower than that of the diesel fuel during the expansion stroke. This was not the case for that the combustion features of HFO should not be significantly different from those of diesel fuel. By analysing the heat release rates, it was considered that such

errors should be induced by combustion model. As a result, further refinement of the combustion model was required.

Sencic (2010) aimed at investigating all the possible methods to reduce the pollutant emissions for the large 2-stroke marine diesel engine through OpenFOAM. A heavy fuel oil model was developed and a soot model was built into OpenFOAM. Different mesh scales were tested and the fuel spray parameters were calibrated to get good agreement with the measured data. The computation models and setups are summarised as below:

Engine type:	RT-flex50 and MAN B&W 6S50MC
Produced by:	Wärtsilä and MAN B&W
Fuel spray breakup:	Blob + KHRT model
NO_x:	Zeldovich mechanism
Soot:	Modified Fusco model

The validations were performed on the constant volume combustion chamber, the automotive engine and the large 2-stroke marine diesel engine. For the case of the large 2-stroke marine diesel engine, the predicted cylinder pressure and NO_x emissions were in good coincidence with the measured data. However, the predicted soot results were overestimated, even though the transient soot cloud positions were very well predicted. Based on the built model, several emission reduction specifications were tested to get the optimal strategy:

1) Reducing the scavenging temperature, which induced the soot and NO_x emissions lower without sacrificing the indicated power.

2) Exhaust gas recirculation, which induced obviously reduction NO_x emission and a minor reduction of soot emission but sacrificed a small indicated work.

3) Various injection strategies, which reduced the soot and NO_x emission. However, the engine efficiency was reduced by about 2% as well.

To get further insights of the working processes of the full scale large 2-stroke marine diesel engines, Mayer et al. (2013) equipped fully optical facilities and techniques into

MAN B&W test engine 4T50ME-X. As a result, the realistic working conditions of the engine would be fulfilled and can be recorded directly. The measured data includes detailed image of fuel spray propagation, ignition progress, in-cylinder flow fields and temperature distributions in the cylinder during scavenging. These obtained data can not only be used for CFD validation, but also for product development. To the author's best knowledge, this is the first time optical accessing to real size 2-stroke marine diesel engine.

2.2.2 Scavenging

The first CFD simulations of engine scavenging appeared in the 1980s. As to the scavenging process research of the large 2-stroke marine diesel engines, it mainly appears recently.

Nakagawa et al. (1990) used the LDV to experimentally investigate the scavenging process of a uniflow 2-stoke engine. They focused their interests on the scavenging efficiency and the scavenging-air swirl intensity during the scavenging and compression stroke with two different scavenging port configurations. Based on the obtained results, it was concluded that the air swirl at TDC during the compression stroke would be controlled by the scavenging port angle. The maximum tangential velocity was nearly proportional to sinusoidal value of scavenging port angle. The larger scavenging port angle would induce more axial flow velocity drops closing to the centre of the cylinder, thus poorer scavenging performance near the cylinder centre. The scavenging port made by the combination of a large angle port and a small angle port has higher scavenging ability and more sufficient swirl intensity.

Litke (1999) investigated the performances of the scavenging port schemes adopted by MAN B&W, Wärtsilä and Mitsubishi by mode tests using liquid. It was concluded that the difference of scavenging efficiency with inlet angle in the range of 15° to 20° are

negligible. The swirl speed in the cylinder increases proportionally with the scavenging port angle. The scavenging port scheme with differentiated angle adopted by Mitsubishi (Litke, 1999) presented better filling performance compared with that of the schemes adopted by MAN B&W, Wärtsilä at the same angle and delivery ratio.

Sher et al. (1991) investigated the steady state flow patterns inside a modified cylinder of a uniflow scavenged 2-stroke engine. A hot-wire anemometry was used to measure the velocity and turbulent kinetic energy and the obtained results were compared with the CFD results. The conclusion was that even though the model was simplified under steady state, it was still difficult to get very good coincidence between the calculation and measurement. The reasons were attributed to the measurement procedures and also the shortcomings of k-ε turbulence model.

The direct tests of the engine scavenging flows are not convenient. CFD is considered to be an ideal tool for any challenging flow research. However, the models of CFD itself need to be validated as well. The CFD investigations of Pergolesi (2009), Obeidat et al. (2010), Haider (2011) and Hemmingsen et al. (2013) were all based on the Technical University of Denmark (DTU) swirl rig, a simplified model of low speed 2-strok uniflow scavenged transparent facility by Particle Image Velocimetry (PIV) or Laser Doppler Anemometry (LDA). Even though very intensive experiments were carried out, however, the CFD results were still not so ideal for turbulence models investigation except the latest work of Hermmingsen et al. (2013). Using the latest updated experimental facilities, the obtained steady and transient axial and tangential velocities at different positions were compared with the results from CFD solver STAR CCM+. Spalart-Allmaras and SST k-ω turbulence models were adopted to capture the transient velocities and both of them can accurately predict the profiles.

Lamas et al. (2012) validated the predicted cylinder pressure during the scavenging process by CFD solver ANSYS FLUENT against the test bed measured data of the large 2-stroke marine diesel engine MAN B&W 7S50MC and the satisfactory results were

obtained. Sigurdsson et al. (2014) experimentally and numerically investigated the scavenging process of the MAN B&W test engine 4T50ME-X located in Copenhagen with combustion considered. 1/30 of the engine was modelled, meshed and computed using CFD software STAR CD. The computed in-cylinder pressure trace was compared with the measured data. It was noticed that good agreement can be obtained except the near TDC crank angle degrees, with the largest discrepancy about 14% at the TDC. The error was mainly attributed to the application of the ideal gas assumption. However, it was pointed out that the real gas Redlic-Kwong model can reduce this discrepancy to 6.5% and the remaining discrepancy was caused by the amount of the mass trapped in the cylinder during the compression stroke and the possible inaccuracy of the measured data. Nevertheless, the scavenging process was considered to be simulated very well.

2.2.3 Injection

In order to investigate the drop drag and breakup mechanisms of droplets, Hwang et al. (1996) performed the experimental and simulation study of liquid droplets injected into high velocity air jet. A range of tests were carried out and the obtained data were compared with the breakup models. It was concluded that the breakup would experience a series of process initiated from the flattening of the droplets. Taylor Analogy Breakup (TAB) model presented very good flattening time. Then the bag breakup would originate from the thinnest point of the flattened drop. As the increasing of Weber number, the catastrophic regime due to unstable growth of Rayleigh-Taylor (RT) or Kelvin-Helmholtz (KH) waves would be evoked. The temperature would influence the breakup mechanisms. Under the elevated temperature, the surface tension would be decreased. This would cause earlier bag disappearance and shorter ligament lengths. The obtained droplet diameter data were comparable to the computed KH wavelengths. The distortion of the droplet would significantly affect its drag coefficient. The dynamic drag model produced good agreement with the measured data.

Larmi et al. (2002) gave their efforts to get the predictive capabilities of the ETAB and Wave breakup models by comparing with the measured non-evaporating diesel sprays using KIVA3 code and commercial software STAR CD. All the adopted polar meshes were appropriate for spray predictions without obviously introduced uncertainties. The penetration predictions were considered in good agreement with the measured results. However, the Wave model presented better spray width than the ETAB model. As to the prediction of the droplet sizes, the viscosity seems to separate the performance of ETAB and Wave. The ETAB model gave excellent agreement for the light fuel oil case while the Wave model presented good coincidence for the marine fuel oil situation. It was emphasised that the model constants were kept original without tuning and concluded that the performance of both the tested models were rated as good considering the fact that the operating condition was quite different from that of the original reference. To further analyse the KHRT breakup model based on their former work, Larmi et al. (2003) investigated the Wave and KHRT breakup models on the same platform STAR CD. As for the prediction of the droplets diameter, the application of coalescence model made the results poor in both cases. The KHRT model presented its superiority over the Wave model on the prediction of droplet sizes if fuel viscosity effect was considered.

Lucchini et al. (2011) investigated the spray-mesh interaction for high pressure evaporating sprays using OpenFOAM. The SANDIA combustion chamber data was used to validate the air-fuel mixture formation process and the best mesh size was determined. It was noticed that the fuel vapour penetration and distribution presented less significant dependency on the mesh than the liquid phase. A mesh size with 2-10 times the nozzle diameter provided satisfactory results while mesh size with smaller than 2 times of the nozzle diameter would make the Eulerian-Lagrangian assumption invalid, inducing the inaccuracy.

Wang et al. (2010) successfully validated the mesh and time step size independent spray model using unsteady gas jet, vapour particle and influence radius droplet models. The models were applied together with KHRT model into KIVA code. The spray tip

penetration, local drop velocity and Sauter mean diameter of non-evaporating diesel sprays were compared with the experimental data. It was proven that the developed model gave very good mesh and time step size independent results by one order of magnitude in mesh cell and two orders of magnitude in time steps in non-evaporating and evaporating sprays.

In a summary work of n-heptane session of Engine Combustion Network (ECN), Hawkes (2011) summarised the results from nine groups on the non-reacting and reacting n-heptane spray performed in the Sandia constant volume chamber. For the non-reacting comparison, even though most of the results could reasonably match the experimental liquid length, however, nearly each group adopted a different definition. The selection of different percentages of the total liquid fuel mass would induce different values. In addition, the model coefficients were adjusted to achieve the agreement. As to the vapour penetration, almost every group adopted a different definition for vapour penetration as well. It was emphasised that the parametric studies were in need to better expose what is not working rather to simply make the coincidence by tuning. The comparison of the mixture fraction contour lines was good for the majority of the models, even though larger discrepancies were found closer to the nozzle and at the initial stages. This might be the reasons of grid or statistical convergence and different assumptions of the injection rate. Finally, it was suggested that a value of 0.0015 of local liquid volume fraction as the threshold of the liquid length. A value of 0.001 of local mixture fraction was suggested as the threshold of the vapour penetration length. To improve the models, a parametric study of the experiment should be much more helpful than just having one case. Blind simulations should be used to avoid parameter tuning. The research of the implementation of spray models into different codes was also suggested.

Dam (2007) gave an encyclopaedic summarisation of the theoretical and experimental findings on diesel sprays. The conclusion was that no complete theory was present and large challenges lie ahead. Even though there was good consensus on which physical

quantities would influence the spray characteristics, but there were some discrepancies. The nozzle layout would be very important and very small differences in setup would have large effects on the spray characteristics. Then the KIVA code was used to investigate the diesel sprays and concluded that the artificial diffusion of momentum is the most critical problem to be solved. The highlight of the work of Dam (2007) was to experimentally investigate the sprays at atmospheric conditions in an injection system same as the large 2-stroke marine diesel engines. Even though the condition was far from the combustion chamber, it was still expected to provide valuable insight to the atomisation process of the large 2-stroke marine diesel engines. The provided configurations and the related obtained experimental data as liquid penetration and spray shape can be used for CFD validation. It was also pointed out that care should be taken when using the spray angles in CFD simulations for that the spray was found to have a asymmetrical spray distribution.

Kyriakides et al. (2009) aimed at investigating the effect of fuel properties on spray atomisation using ETAB and Unified Spray Breakup (USB) modes based on their latest developed HFO model. A nozzle size representative of low speed marine engines had been considered for two different chamber pressures. It was shown that in comparison with a diesel spray, the HFO spray presented comparable values of penetration length but with larger droplet sized. When the HFO was used in the combustion of a large 2-stroke marine engine, the pressure trace of HFO was lower than that of diesel fuel oil for lower evaporation rates of HFO. However, it should be pointed out that, in another published paper of Chryssakis et al. (2010), variations in the cylinder pressure trace were considered should not be so significant based on experience from engine operation with HFO. Chryssakis et al. (2010) attributed the reason of pressure trace underestimation using HFO to the inaccurate combustion model.

As a part of research programs in HERCULES-A, B and C, a novel test Spray Combustion Chamber (SCC) was built by Swiss Federal Institute of Technology (ETH) to investigate the flow, spray, combustion and emissions at conditions typical of the

combustion system in the large 2-stroke marine diesel engines (Herrmann et al. 2007). The impacts of pressure, temperature, swirl and fuel quality could be adjusted corresponding to different working conditions of that in the large 2-stroke marine diesel engines. The diameter of the constant volume combustion chamber corresponded to the bore of a large marine diesel engine. A series of windows were equipped in the chamber walls, not only to generate the experimental data for CFD validations, but also for optimisation of actual combustion system. Schulz et al. (2010) visualised the spray propagation inside the chamber using shadow image method and the obtained spray and evaporation data were used to validate the models and setups in CFD software STAR CD. The prime and secondary breakups were simulated using Huh model and Reitz-Diwakar models. By adjusting the constants in Reitz-Diwakar secondary breakup model, perfectly good agreement of spray penetration and cone angles was obtained. Except for this, the ignition processes were also experimentally investigated and the internal nozzle flows were numerically simulated. Three different fuel oils, diesel, marine diesel oil and heavy fuel oil were numerically modelled using CFD to get their evaporation features. It was concluded that the least volatile component evaporated most slowly. More detailed setups and measured results based on the SCC can be found in Herrmann et al. (2010), Von Rotz et al. (2011) and Herrmann et al. (2011). Bolla et al. (2012) experimentally and numerically investigated the non-evaporating and evaporating penetration lengths using light fuel oil and heavy fuel oil under different temperature and pressure and very good coincidences were obtained. The grid sensitivity of penetration length under non-evaporating condition was carried out and the best mesh scale was determined as the 2mm, which was nearly 2 times of the injector hole diameter (0.875mm). Schulz et al. (2013) furthered the measurement with droplet size distribution, ignition and combustion included. Deeper insights into the engine combustion processes were obtained by the CFD models based on the measurements at the SCC. Finally, to further improve the combustion efficiency and reduce component temperature, the nozzle layouts were selected with Exhaust Gas Recirculation (EGR) based on the simulations. The most promising specifications were tested on the RTX-4 test engine (Schulz et al., 2013). It was noticed that in addition to the increasing of

efficiency, the temperatures of piston and exhaust valve reduced by about 20℃ while the temperatures of cylinder cover and liner maintained at their previous levels. Most recently, Bolla et al. (2014) carried out the joint experimental and numerical study to determine the influence of five nozzle diameters (from 0.2mm to 1.2mm) on ignition delay, lift-off length and flame evolution at the corresponding engine operating conditions. The experimental data confirmed that the injector diameter had a minor effect on the ignition delay and flame lift-off while the ambient temperature would have a significant influence on both quantities. As for the predictions, the ignition delay was slightly overestimated while the lift-off length was obviously underestimated. Even though the qualitative trends were reproduced, however, the impact of the injector diameter was clearly overestimated. The location of ignition and early flame spread were predicted fairly well. It was finally concluded that the Conditional Moment Closure (CMC) combustion model in STAR CD presented high potential for the prediction of auto-ignition for the large 2-stroke marine engines.

2.3 Closure

In this chapter, the research and development steps and results about the large 2-stroke marine diesel engines are reviewed. The latest research directions are still focused on the reduction of the pollutant emissions and the increasing of the engine efficiency. More innovative measures and facilities are developed to reach these aims, not only to optimise the engine itself, but also the whole propulsion system.

As to the numerical simulation, CFD is considered as a promising tool to support the engine development considering the currently obtained prediction results. However, it is never too prudent to validate the related models for its complexity. More sophisticated facilities are needed to get insight into the in-cylinder processes. Based on these high quality results, the existing models can be strictly validated and improved to apply to more general calculations for the development of large 2-stroke marine diesel engines.

Chapter 3 Numerical Models

3.1 Dynamic Mesh Theory

For modelling the movement of the piston and exhaust valve, it is necessary to use the dynamic mesh scheme. Considering the fact that the piston and exhaust valve would only move in the vertical direction, the dynamic layering method is selected as the best applicable way. To minimise the numerical error introduced from the mesh, the hexahedral prismatic grids are generated in the combustion chamber and cylinder domain. Using the dynamic layering method, the layer adjacent to the moving wall can be added or removed when the boundary wall is stretching or compressing the control volume, as shown in Figure 3.1.

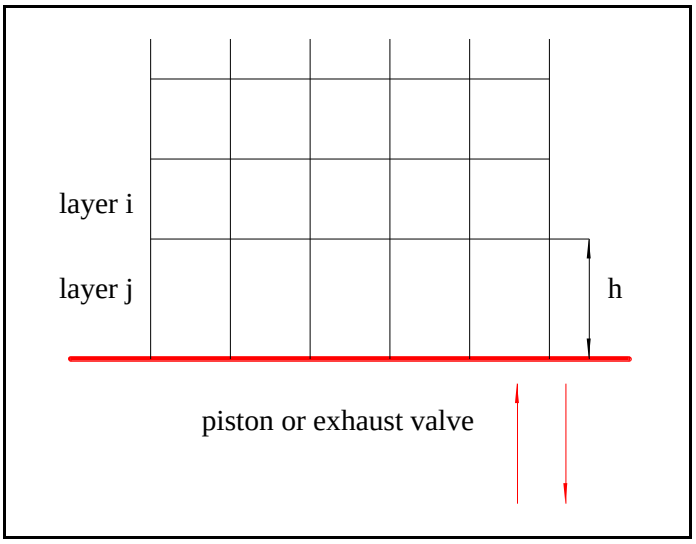

Figure 3.1 Dynamic layering method

In order to control the movement of the piston conveniently, ANSYS FLUENT (ANSYS, 2012) provides the In-Cylinder model. Through the In-Cylinder model, the position of the piston would be calculated according to the parameters related with the engine working configurations:

$$p_s = L + \frac{A}{2}(1-\cos\theta) - \sqrt{L^2 - \frac{A^2 \sin^2\theta}{4}} \tag{3.1}$$

p_s: the piston location. 0 means that the piston is at TDC and A at BDC.

L: the connecting rod length

A: the piston stroke

θ: the current crank angle.

As to controlling the movement of the exhaust valve, a separated profile file is generated to specify the exhaust valve lift to the crank angle. In order to avoid the "zero" volume mesh when the exhaust valve is in its closed position, the exhaust valve is considered to be closed as the crevice between the valve and its seat reaches a very small value (approximate 0.7mm in this thesis).

During the process of adding or removing of the layer mesh, the conservation equation of a general scalar ϕ can be computed as:

$$\frac{d}{dt}\int_V \rho\phi dV + \int_{\partial V} \rho\phi\left(\vec{u} - \vec{u}_g\right)\bullet d\vec{A} = \int_{\partial V} \Gamma\nabla\phi\bullet d\vec{A} + \int_V S_\phi dV \tag{3.2}$$

ρ: the fluid density

$\vec{u}$: the flow velocity

$\vec{u}_g$: the moving boundary velocity

Γ: the diffusion coefficient

∂V: the boundary of volume V

S_ϕ: the source term of ϕ

3.2 Equation of State (EOS)

In thermodynamics, an EOS is the mathematical description relates the state variables as P, V, T or internal energy for any physically homogeneous fluid under equilibrium state. In engine combustion simulation, EOS would be used to correlate P, T and V of the mixture system. Normally, homogeneous fluid can be classified as liquid and gas. However, as the temperature and pressure are above the critical points, the distinction of the physical properties cannot be clearly defined. The new phase characterised with some properties both of liquid and gas is named supercritical fluid. In supercritical fluid region, the liquid and gas phases become not distinguishable. Figure 3.2 is the PT diagram of a typical phase expression of a pure material existing at the corresponding conditions.

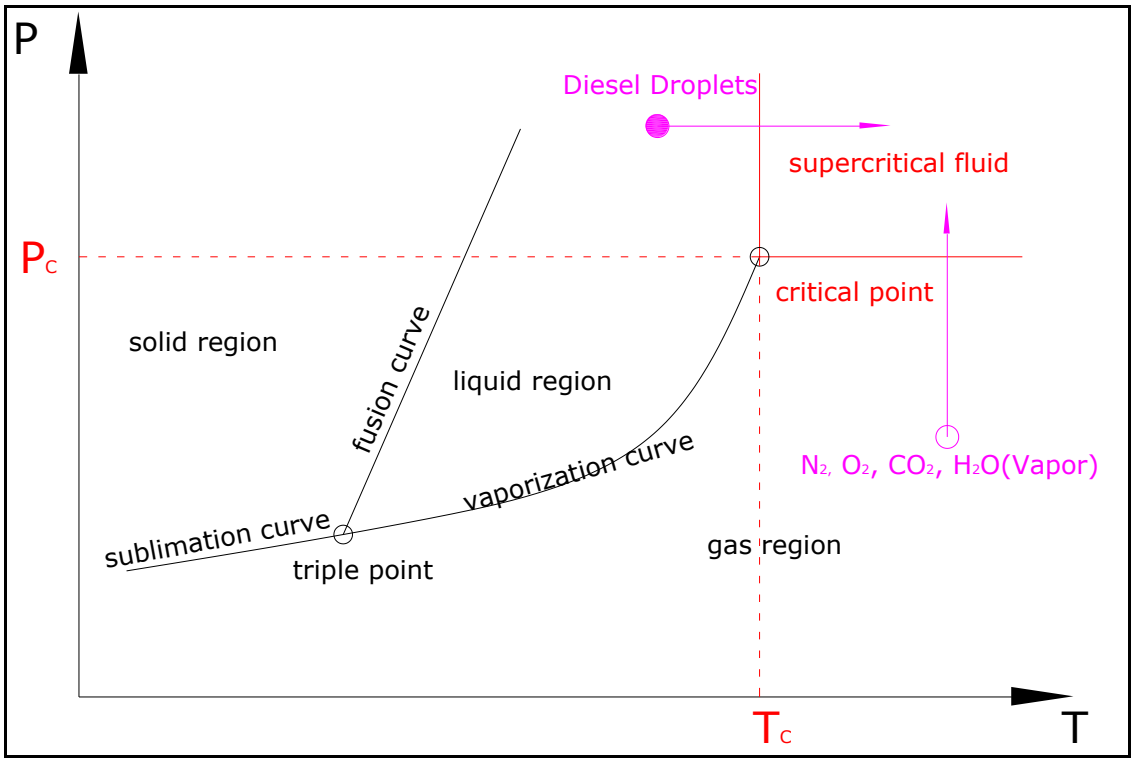

Figure 3.2 A typical phase diagram

The simplest and most frequently used EOS is the ideal gas law with the following form:

$$PV = nRT \tag{3.3}$$

P: the pressure of the mixture

V: the volume of the mixture

T: the temperature of the mixture

R: the ideal gas universal constant

n: the *amount of substance* of the mixture

Even based on hypothetical conditions, ideal gas law is still a good approximation under the following conditions:

$P \ll P_c$ or $T / T_c > 2$ and $P < P_c$

The diesel droplets and the surrounding gases in the current engine chamber would experience the phase change from liquid and gas to supercritical fluid respectively, as shown in Figure 3.2. As a result, the ideal gas law would be effective only for part of the engine cycle fulfilling the conditions listed above. As the working fluid behaves far from the listed conditions, the real gas EOS models would be accurate alternatives.

The first real gas model, Van der Waals equation, was discovered by Johannes Diderik van der Waals in 1873 and the Nobel Prize in physics 1910 was awarded to him for his work (Nobelprize.org, 2014). Van der Waals equation takes into account the molecular size and attraction forces between them with the following form:

$$p = \frac{RT}{v - b} - \frac{a}{v^2} \tag{3.4}$$

v: the volume of the container shared by each particle (m^3)

a: a measure of the particles attraction (N/m^4)

b: the volume excluded from v by a particle (m^3)

Van der Waals equation presents superiority to ideal gas law for lower pressure and temperature. However, it is not appropriate for rigorous quantitative calculations (Hill,

1960). Since then, many investigators have attempted to improve the accuracy. In 1949, the Redlich-Kwong equation of state (Poling et al., 2007) was developed and well known for its considerable improvement over other EOS of that time. The Redlich-Kwong equation (Redlich et al., 1949) and its following modified forms as Soave-Redlich-Kwong (Soave, 1972), Peng-Robinson (Peng et al., 1976) and Aungier-Redlich-Kwong (Aungier, 1995) state equations can be written as the below general form:

$$P = \frac{RT}{V - b + c} - \frac{a}{V^2 + \delta V + \varepsilon} \tag{3.5}$$

P : absolute pressure (Pa)

V : specific molar volume (m^3/kmol)

T : temperature (K)

R : universal gas constant

For each EOS, the coefficients as a , b , c , δ and ε are the functions of:

P_c : critical pressure

T_c : critical temperature

V_c : critical volume

ω : acentric factor

3.2.1 Redlich-Kwong Equation

In Redlich-Kwong equation, the expressions of a , b , c , δ and ε are:

$$a(T) = \frac{a_0}{(T / T_c)^{0.5}} \tag{3.6}$$

$$a_0 = \frac{0.42747 R^2 T_c^{\,2}}{P_c} \tag{3.7}$$

$$b = \delta = \frac{0.08664 R T_c}{P_c} \tag{3.8}$$

$$c = \varepsilon = 0 \tag{3.9}$$

Redlich-Kwong Equation requires only 2 parameters, P_c and T_c.

3.2.2 Soave-Redlich-Kwong Equation

In Soave-Redlich-Kwong equation, the expressions of a, b, c, δ and ε are:

$$a(T) = a_0[1 + n(1 - (T / T_c)^{0.5})]^2 \tag{3.10}$$

$$n = 0.48 + 1.574\omega - 0.176\omega^2 \tag{3.11}$$

$$a_0 = \frac{0.42747 R^2 T_c^{\,2}}{P_c} \tag{3.12}$$

$$b = \delta = \frac{0.08664 R T_c}{P_c} \tag{3.13}$$

$$c = \varepsilon = 0 \tag{3.14}$$

Soave-Redlich-Kwong Equation requires 3 parameters, ω, P_c and T_c.

3.2.3 Peng-Robinson Equation

In Peng-Robinson equation, the expressions of a, b, c, δ and ε are:

$$a(T) = a_0[1 + n(1 - (T / T_c)^{0.5})]^2 \tag{3.15}$$

$$n = 0.37464 + 1.54226\omega - 0.26992\omega^2 \tag{3.16}$$

$$a_0 = \frac{0.457247 R^2 T_c^{\,2}}{P_c} \tag{3.17}$$

$$b = \frac{0.0778 R T_c}{P_c} \tag{3.18}$$

$$\delta = 2b \tag{3.19}$$

$$\varepsilon = -b^2 \tag{3.20}$$

$$c = 0 \tag{3.21}$$

Peng-Robinson Equation requires 3 parameters, ω, P_c and T_c.

3.2.4 Aungier-Redlich-Kwong Equation

In Aungier-Redlich-Kwong equation, the expressions of a, b, c, δ and ε are:

$$a(T) = a_0 \left(\frac{T}{T_c} \right)^{-n} \tag{3.22}$$

$$n = 0.4986 + 1.1735\omega + 0.4754\omega^2 \tag{3.23}$$

$$a_0 = \frac{0.42747 R^2 T_c^{\,2}}{P_c} \tag{3.24}$$

$$b = \delta = \frac{0.08664 R T_c}{P_c} \tag{3.25}$$

$$c = \frac{RT_c}{P_c + \dfrac{a_0}{V_c(V_c + b)}} + b - V_c \tag{3.26}$$

$$\varepsilon = 0 \tag{3.27}$$

Peng-Robinson Equation requires 4 parameters, ω, V_c, P_c and T_c.

Under the real gas models, enthalpy, entropy and specific heat of each species are obtained using the departure functions, from the relevant ideal gas properties. Detailed descriptions can be found in Poling et al. (2007).

The critical constants ω, V_c, P_c and T_c for each component in the real gas models can be found in the open literature Poling et al. (2007), Owczarek et al. (2003), Owczarek et al. (2006), Sladkov (2001), Smith (1994), Somayajulu (1989) and Assael et al. (1996). The

properties of currently used diesel fuel have been set equal to those of n-heptane.

The above mentioned critical constants ω, V_c, P_c and T_c are for pure component. In the engine combustion simulation process, it is necessary to get the corresponding constants for the mixture system. The one-fluid van der Waals mixing rules (Redlich et al., 1949) would be an appropriate way to apply the EOS to mixtures by replacing a and b with composition-dependent expressions as:

$$\left(a_m\right)^{0.5} = \sum_i x_i \left(a_i\right)^{0.5} \tag{3.28}$$

$$b_m = \sum_i x_i b_i \tag{3.29}$$

The mixture critical constants ω_m can be solved by mole-weighted mixing law:

$$\omega_m = \sum_i x_i \omega_i \tag{3.30}$$

Thus, the results of the mixture critical constants can be computed as:

$$P_{cm} = \frac{T_{cm}}{\sum_i \frac{x_i T_{ci}}{P_{ci}}} \tag{3.31}$$

$$V_{cm} = \frac{T_{cm}}{P_{cm}} \sum_i \frac{x_i P_{ci} V_{ci}}{T_{ci}} \tag{3.32}$$

For Soave-Redlich-Kwong and Peng-Robinson models:

$$T_{cm} = \frac{\left[\sum_i \frac{x_i T_{ci}}{P_{ci}^{0.5}}\right]^2}{\sum_i \frac{x_i T_{ci}}{P_{ci}}} \tag{3.33}$$

For Redlich-Kwong model:

$$T_{cm} = \left[\frac{\left(\sum_i x_i \sqrt{\frac{T_{ci}^{2.5}}{P_{ci}}}\right)^2}{\sum_i \frac{x_i T_{ci}}{P_{ci}}}\right]^{\frac{1}{1.5}} \tag{3.34}$$

For Aungier-Redlich-Kwong model:

$$T_{cm} = \left[\frac{\left(\sum_i x_i \sqrt{\frac{T_{ci}^{2+n}}{P_{ci}}} \right)^2}{\sum_i \frac{x_i T_{ci}}{P_{ci}}} \right]^{\frac{1}{n+1}} \tag{3.35}$$

$$n = 0.4986 + 1.1735\omega + 0.4754\omega^2 \tag{3.36}$$

T_{cm} :mixture pseudo critical temperature (K)

P_{cm} :mixture pseudo critical pressure (Pa)

V_{cm} :mixture pseudo molar volume (m^3/kmol)

T_{ci} : critical temperature of component i (K)

P_{ci} : critical pressure of component i (Pa)

V_{ci} : critical molar volume of component i (m^3/kmol)

x_i : mole fraction of species i

The enthalpy, entropy and specific heat of the real gas can be computed through the introduction of the departure function which represents the properties departing from those of ideal gas condition. Refer to Aungier (1995) for more details.

3.3 Energy Equation

In engine combustion, there exist three ways for heat transfer: conduction, convection and radiation. Considering its insignificance, the radiation effect is out of the current research for simplicity. The thermal mixing and conduction would be considered in the modelling of heat transfer.

For the reason that the energy equation would be solved together with the combustion models, the forms of the energy equation would be different for the species transport and non-premixed combustion models. For the species transport combustion model, the energy equation can be written as (ANSYS, 2012):

$$\frac{\partial}{\partial t}(\rho E)+\nabla\bullet\left(\vec{v}\left(\rho E+p\right)\right)=\nabla\bullet\left(k_{eff}\nabla T-\sum_{j}h_{j}\vec{J}_{j}+\left(\tau_{eff}\bullet\vec{v}\right)\right)+S_{h} \tag{3.37}$$

E: the total energy

$$E=h-\frac{p}{\rho}+\frac{v^{2}}{2}$$

h: the enthalpy

k_{eff}: the effective conductivity

$$k_{eff}=k_{t}+k$$

k_t: the turbulent thermal conductivity

$\vec{J}_j$: the diffusion flux of species j

$k_{eff}\nabla T$: the heat transfer due to conduction

$-\sum_j h_j\vec{J}_j$: the heat transfer due to species diffusion

$\left(\tau_{eff}\bullet\vec{v}\right)$: the heat transfer due to viscous dissipation

S_h: the chemical reaction heat

As to the non-premixed combustion model, the energy equation would be in its total enthalpy form (ANSYS, 2012):

$$\frac{\partial}{\partial t}(\rho H)+\nabla\bullet(\rho\vec{v}H)=\nabla\bullet\left(\frac{k_t}{c_p}\nabla H\right)+S_h \tag{3.38}$$

H: the total enthalpy

$$H=\sum_j Y_j H_j$$

Y_j: the mass fraction of species j

$$H_j=\int_{T_{ref,j}}^{T} c_{p,j}dT+h_j^0\left(T_{ref,j}\right)$$

$h_j^0\left(T_{ref,j}\right)$: the formation enthalpy of species j at $T_{ref,j}$

In non-premixed combustion model, the diffusion coefficients for all species and enthalpy are equal. As a result, the heat transfer due to species diffusion and conduction can be combined together in the first term of the right side of equation (3.38). The heat transfer due to viscous dissipation would be considered in the source term.

3.4 Turbulence Models

3.4.1 General Turbulence Theory

Turbulence exists prevalently in the engineering fluid dynamics. It is a flow state characterised by random and rapid variation of pressure and velocity combined with irregular convection and diffusion of mass, energy and momentum. The theory of energy cascade advanced by Richardson (1922) is widely accepted for the description of turbulence structure in turbulence flows (Sreenivasan et al., 1995). With the concept of energy cascade, the turbulent flows can be regarded as an ensemble of hierarchy of eddies with wide range of length scales. The largest eddies are determined by the boundary of the domain and comparable with the scale of the flow field. The large eddies are unstable and they would transfer their energy to smaller ones through breakup of eddies. The smaller eddies would undergo the same process as that of the larger eddies and transfer their energy to the much smaller ones. And this process continues until the kinetic energy is dissipated by the viscosity of the fluid at small enough scales. The turbulence flow would be sustained by the dissipation which transfers the fluid kinetic energy into heat through viscous shear stress. This is a metaphoric description of the energy cascade.

Based on the work of Richardson, the hypotheses are introduced into energy cascade theory by Kolmogorov (Frisch, 1995):

1) If the Reynolds number is high enough, the small scales are statistically isotropic.

2) The statistical properties of the small isotropic scales are only dependent on their scale r, the viscosity ν and the mean kinetic energy dissipation rate ε.

Under these hypotheses, the Kolmogorov length η and the energy spectrum function $E(\kappa)$ can be expressed using dimensional analysis as:

$$\eta = \left(\frac{\nu^3}{\varepsilon} \right)^{1/4} \tag{3.39}$$

$$E(\kappa) = C\varepsilon^{2/3}\kappa^{-5/3} \tag{3.40}$$

C: universal constant

κ: wave number, $\kappa = 2\pi / r$

The Kolmogorov length η is the length scale at which kinetic energy converts into heat and the inertial and viscous forces are of the equal magnitude. Between the two extremes η and L (the largest eddy length scale in the flow field), an ensemble of eddies with the length scale of r are formed from the energy released from larger ones. These scales are much larger than Kolmogorov length scales but much smaller than the largest scales:

$$\eta \ll r \ll L \tag{3.41}$$

Since r is much larger than η, the dissipation from turbulence to heat would not happen in this range. Eddies with scale of r would only transfer the energy of larger eddies to smaller ones and the inertial force in this range is much larger than viscous force. So the r scale range is named inertial range.

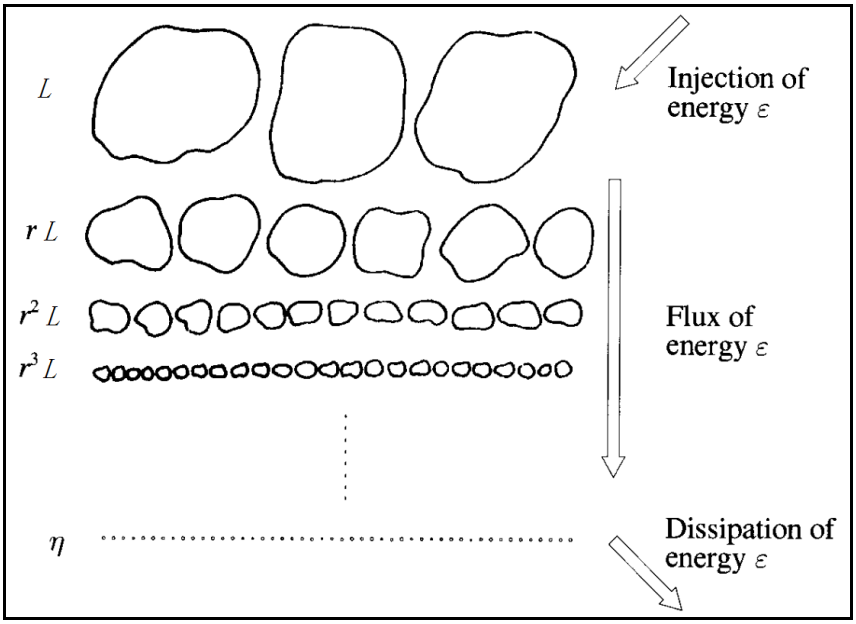

Figure 3.3 Energy cascade according to Kolmogorov 1941 theory

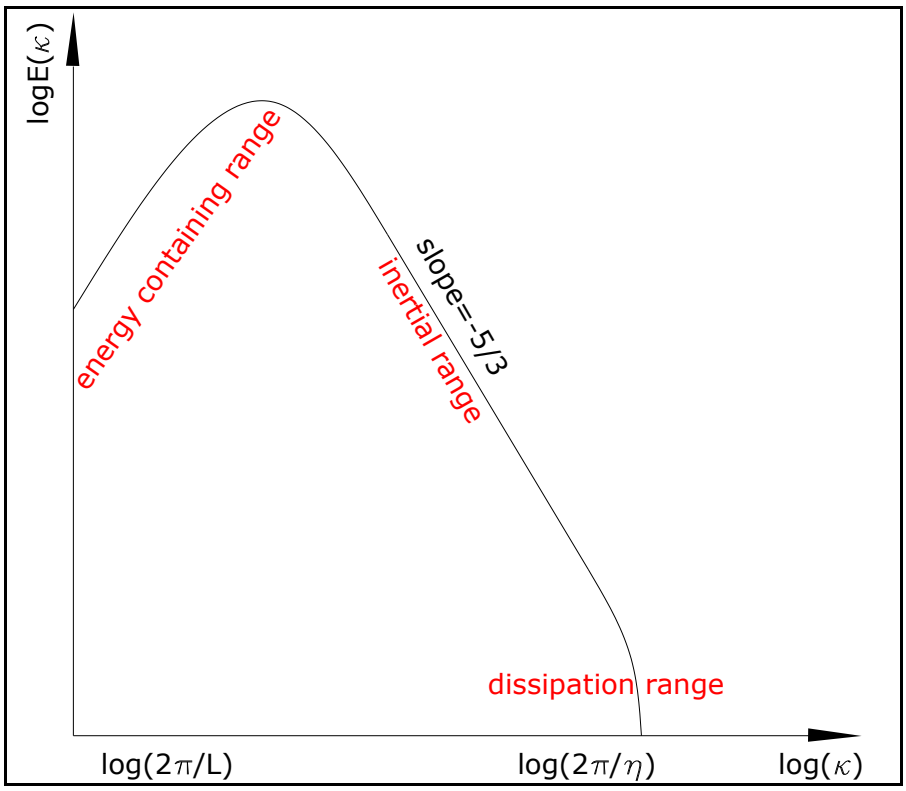

Figure 3.4 A typical relation of energy spectrum function and wave number

Figure 3.3 demonstrates the cascade according to the Kolmogorov theory (Frisch, 1995). Figure 3.4 is a typical relationship diagram of energy spectrum function $E(\kappa)$ and wave number κ. At large length scales, the eddy contains high kinetic energy and the turbulence is produced. On the contrary, at small length scales, the eddy dissipates and the energy decreases. The inertial range obeys the -5/3 law. Even though Kolmogorov theory is still under revision, generally, it is the cornerstone of turbulence research.

More profound background and mathematical derivation of the related theory can be found in (Frisch, 1995).

3.4.2 Navier-Stokes (NS) Equation

In fluid dynamics, NS equation is regarded as the strictly exact mathematical description of the fluid motions including turbulence. It is derived from the conservation law of mass and momentum (Newton's Second Law) with the following equivalent forms:

$$\frac{\partial \rho}{\partial t}+div\left(\rho\vec{u}\right)=0 \Leftrightarrow \frac{\partial \rho}{\partial t}+\frac{\partial}{\partial x_i}\left(\rho u_i\right)=0 \Leftrightarrow \frac{\partial \rho}{\partial t}+\frac{\partial\left(\rho u\right)}{\partial x}+\frac{\partial\left(\rho v\right)}{\partial y}+\frac{\partial\left(\rho w\right)}{\partial z}=0 \quad (3.42)$$

$$\rho\left(\frac{\partial \vec{u}}{\partial t}+\vec{u}\cdot\nabla\vec{u}\right)=-\nabla p+\mu\Delta\vec{u}+\left(\frac{1}{3}\mu+\zeta\right)\nabla div\vec{u}+\vec{f} \Leftrightarrow \quad (3.43)$$

$$\rho\left(\frac{\partial u_i}{\partial t}+u_j\frac{\partial u_i}{\partial x_j}\right)=-\frac{\partial p}{\partial x_i}+\frac{\partial}{\partial x_j}\left[\mu\left(\frac{\partial u_i}{\partial x_j}+\frac{\partial u_j}{\partial x_i}-\frac{2}{3}\delta_{ij}\frac{\partial u_l}{\partial x_l}\right)\right]+\frac{\partial}{\partial x_i}\left(\zeta\frac{\partial u_l}{\partial x_l}\right)+f_i \Leftrightarrow$$

$$\begin{cases}\rho\left(\dfrac{\partial u}{\partial t}+u\dfrac{\partial u}{\partial x}+v\dfrac{\partial u}{\partial y}+w\dfrac{\partial u}{\partial z}\right)=-\dfrac{\partial p}{\partial x}+\mu\left(\dfrac{\partial^2 u}{\partial x^2}+\dfrac{\partial^2 u}{\partial y^2}+\dfrac{\partial^2 u}{\partial z^2}\right)+\left(\dfrac{1}{3}\mu+\zeta\right)\left(\dfrac{\partial^2 u}{\partial x^2}+\dfrac{\partial^2 v}{\partial x\partial y}+\dfrac{\partial^2 w}{\partial x\partial z}\right)+f_x \\ \rho\left(\dfrac{\partial v}{\partial t}+u\dfrac{\partial v}{\partial x}+v\dfrac{\partial v}{\partial y}+w\dfrac{\partial v}{\partial z}\right)=-\dfrac{\partial p}{\partial y}+\mu\left(\dfrac{\partial^2 v}{\partial x^2}+\dfrac{\partial^2 v}{\partial y^2}+\dfrac{\partial^2 v}{\partial z^2}\right)+\left(\dfrac{1}{3}\mu+\zeta\right)\left(\dfrac{\partial^2 u}{\partial x\partial y}+\dfrac{\partial^2 v}{\partial y^2}+\dfrac{\partial^2 w}{\partial y\partial z}\right)+f_y \\ \rho\left(\dfrac{\partial w}{\partial t}+u\dfrac{\partial w}{\partial x}+v\dfrac{\partial w}{\partial y}+w\dfrac{\partial w}{\partial z}\right)=-\dfrac{\partial p}{\partial z}+\mu\left(\dfrac{\partial^2 w}{\partial x^2}+\dfrac{\partial^2 w}{\partial y^2}+\dfrac{\partial^2 w}{\partial z^2}\right)+\left(\dfrac{1}{3}\mu+\zeta\right)\left(\dfrac{\partial^2 u}{\partial x\partial z}+\dfrac{\partial^2 v}{\partial y\partial z}+\dfrac{\partial^2 w}{\partial z^2}\right)+f_z\end{cases}$$

μ: the constant, dynamic viscosity

ζ: the constant, volume viscosity

f: the body forces, such as gravity and centrifugal force

δ_{ij}: Kronecker delta, if $i=j$, δ_{ij}=1 and if $i\neq j$, δ_{ij}=0.

Equation (3.43) is the general form of NS equation with compressibility effects. NS equation would be simplified in incompressible fluid field as the divergence of the flow is zero. If fluid viscosity is not considered, NS equation would be degenerated into Euler equation.

3.4.3 Turbulence Modelling

The turbulence could be predicted through specific mathematical expressions. NS equation is the strict governing equation for the fluid motions including turbulence, even though the existence and smoothness of its solution in three dimensions have not been proved as one of the six unsolved Millennium Prize Problems. Combining with the continuity equation (3.42), NS equation closes itself and no additional mathematical parameters need to be introduced. For some simplified flows, the exact analytical solutions for NS equations do exist under rigorous conditions. However, for the highly non-linear engineering fluids, the numerical discretisation of NS equation in spatial and temporal domain was proved to be the only feasible way.

The most direct but computational costly numerical method for turbulence modelling is Direct Numerical Simulation (DNS). It solves a wide range of every time and length scales in turbulent flow and provides most detailed information of the flow including turbulence. This means that the spatial and temporal discretisation should be fine enough to resolve such small scales. The computational cost of DNS scales as Re^3 (Gatski et al., 1996) and this makes the method be prohibitive for most practical fluid engineering problems, even with the help of the most powerful computers available in the foreseeable decades. However, DNS is applicable at low Reynolds numbers and is regarded as a promising tool to study the physics of turbulence and to develop turbulence models.

The second method to preserve the turbulence information at best is Large Eddy Simulation (LES). LES abandons the complete range capture of every scale through a filtering operation. The selected filtering function would separate any field scalar into a filtered and sub-filtered portion. The large scale eddies would be solved explicitly and the effect of smaller scales on large scales would be considered by Sub-Grid Scale (SGS) model. Through such treatment, the computational cost of LES is much lower than that of DNS. Even though LES is now widely used in engineering application including

combustion, however, in the current context of large dimension engine simulation, the computational cost of LES is still prohibitively expensive. As a result, further detailed descriptions of this model would not be list here.

The turbulence models based on Reynolds Averaged Navier-Stokes (RANS) equation are dominantly used in most engineering fluid simulations for their economic computational cost and reliable precision. According to the idea of Reynolds averaging, the instantaneous scalar quantities can be decomposed into the ensemble-averaged mean component and fluctuating component:

$$\phi = \bar{\phi} + \phi' \tag{3.44}$$

The ensemble-averaging operation obeys the following rules:

$$\begin{array}{lllll} \bar{\phi}' = 0 & \bar{\bar{\phi}} = \bar{\phi} & \overline{\bar{\phi} + \phi'} = \bar{\phi} & \overline{\bar{\phi}\,\bar{f}} = \bar{\phi}\,\bar{f} & \overline{\bar{\phi}\,f'} = 0 \quad \overline{\bar{\phi}\,f} = \bar{\phi}\,\bar{f} \\ \dfrac{\overline{\partial\phi}}{\partial x_i} = \dfrac{\partial\bar{\phi}}{\partial x_i} & \dfrac{\overline{\partial\phi}}{\partial t} = \dfrac{\partial\bar{\phi}}{\partial t} & \dfrac{\overline{\partial^2\phi}}{\partial x_i^{\,2}} = \dfrac{\partial^2\bar{\phi}}{\partial x_i^{\,2}} & \dfrac{\overline{\partial^2\phi'}}{\partial x_i^{\,2}} = 0 & \dfrac{\overline{\partial\phi'}}{\partial x_i} = 0 \end{array} \tag{3.45}$$

Substitute the instantaneous scalar quantities with the form of equation (3.44) and take an ensemble average to NS equation (3.43) using the ensemble-averaging operation rules in equation (3.45):

$$\frac{\partial\rho}{\partial t} + \frac{\partial}{\partial x_i}\left(\rho\bar{u}_i\right) = 0 \tag{3.46}$$

$$\frac{\partial}{\partial t}\left(\rho\bar{u}_i\right) + \frac{\partial}{\partial x_j}\left(\rho\bar{u}_i\bar{u}_j\right) = -\frac{\partial\bar{p}}{\partial x_i} + \frac{\partial}{\partial x_j}\left[\mu\left(\frac{\partial\bar{u}_i}{\partial x_j} + \frac{\partial\bar{u}_j}{\partial x_i} - \frac{2}{3}\delta_{ij}\frac{\partial\bar{u}_l}{\partial x_l}\right)\right] + \frac{\partial}{\partial x_j}\left(-\rho\overline{u_i'u_j'}\right) + \bar{f}_i \tag{3.47}$$

Equations (3.46) and (3.47) are called RANS equations. The turbulence effects are represented through the additional Reynolds stress terms $-\rho\overline{u_i'u_j'}$. As a result, additional equations are needed to make the RANS equations closed. There are two approaches to build the closure equations. The first is based on the Boussinesq hypothesis, which connects the Reynolds stresses with the mean velocity gradients (ANSYS, 2012). The second approach is to build the transport equations for every Reynolds stress component and the turbulence models obtained through this way are named Reynolds Stress Model

(RSM). In the context of engine simulation, RSM is used very seldom. RSM is expensive to solve 7 transport equations in three dimensional simulations. Moreover, the stability of RSM is problematic. These issues would become more intensive when RSM is combined with the complex models involved in engine combustion simulation. All these make RSM not worthy to be considered, in spite of the fact that certain improvement is confirmed in some turbulent flows (Durbin, 1993). As a result, RSM is beyond the investigation of the current research.

Based on Boussinesq hypothesis, the Reynolds stresses can be computed with the mean velocity gradients:

$$-\rho\overline{u_i'u_j'} = \mu_t\left(\frac{\partial\overline{u}_i}{\partial x_j}+\frac{\partial\overline{u}_j}{\partial x_i}\right)-\frac{2}{3}\left(\rho k+\mu_t\frac{\partial\overline{u}_i}{\partial x_i}\right)\delta_{ij} \tag{3.48}$$

k: the turbulent kinetic energy

$$k=\frac{\overline{u_i'u_i'}}{2}=\frac{1}{2}\left(\overline{u'^2}+\overline{v'^2}+\overline{w'^2}\right) \tag{3.49}$$

Thus:

$$\overline{u'^2}=\overline{v'^2}=\overline{w'^2}=\frac{2}{3}k \tag{3.50}$$

This means that the Boussinesq hypothesis would introduce error of isotropic assumption, which is not strictly true.

μ_t: the turbulent viscosity (eddy viscosity)

According to the equations introduced to solve μ_t, the eddy viscosity turbulence models can be classified as:

0-equation models

1-equation models

2-equation models, which include

High Reynolds number $k-\varepsilon$

High Reynolds number $k-\omega$

Low Reynolds number $k-\varepsilon$

Transition $k-\omega$

3-equation models

4-equation models

Generally, it could be concluded that:

1) 0-equation models cannot get acceptable accuracy in complex three dimension simulations (Wilcox, 1998).

2) Spalart-Allmaras model could get reasonable prediction results for aerodynamics wall-bounded flows and boundary flows subjected to adverse pressure gradients (ANSYS, 2012).

3) High Reynolds number $k-\varepsilon$ and $k-\omega$ models are widely used in industrial turbulent flows for their acceptable computational cost and reasonable accuracy (ANSYS, 2012).

4) Low Reynolds number $k-\varepsilon$ and $k-\omega$ and 3, 4-equation models are the transitional turbulence models. These models are believed to be promising for accurately predicting boundary layer development and transition from laminar to turbulent flows (ANSYS, 2012).

High Reynolds number $k-\varepsilon$ turbulence models, especially the RNG $k-\varepsilon$ model and its variants are dominantly adopted in combustion simulations (Lakshminarayanan et al., 2010). As a result, the high Reynolds number $k-\varepsilon$ turbulence models would be selected and investigated in the following calculations. The original Standard (STD) $k-\varepsilon$ model is referenced as the baseline model and Realisable (REA) $k-\varepsilon$ model would be tested as well for its reasonable theoretical background and good reputation in applications (ANSYS, 2012). In these three models, the turbulence dissipation rate and turbulent viscosity are defined as:

$$\varepsilon = \frac{\mu}{\rho}\overline{\left(\frac{\partial u_i'}{\partial x_k}\right)\left(\frac{\partial u_i'}{\partial x_k}\right)} \tag{3.51}$$

$$\mu_t = \rho C_\mu \frac{k^2}{\varepsilon} \tag{3.52}$$

3.4.4 STD *k*-ε model

During the derivation of STD $k-\varepsilon$ model, it assumes that the flow is fully developed and the molecular viscosity effects are neglected. The transport equation of k is derived from its exact equation and the transport equation of ε is based on physical deduction (ANSYS, 2012). k and ε are derived from their transport equations (ANSYS, 2012):

$$\frac{\partial(\rho k)}{\partial t} + \frac{\partial(\rho k \bar{u}_i)}{\partial x_i} = \frac{\partial}{\partial x_i}\left[\left(\mu + \frac{\mu_t}{\sigma_k}\right)\frac{\partial k}{\partial x_i}\right] + G_k + G_b - \rho\varepsilon - Y_M \tag{3.53}$$

$$\frac{\partial(\rho \varepsilon)}{\partial t} + \frac{\partial(\rho \varepsilon \bar{u}_i)}{\partial x_i} = \frac{\partial}{\partial x_i}\left[\left(\mu + \frac{\mu_t}{\sigma_\varepsilon}\right)\frac{\partial \varepsilon}{\partial x_i}\right] + C_{1\varepsilon}\frac{\varepsilon}{k}(G_k + C_{3\varepsilon}G_b) - C_{2\varepsilon}\rho\frac{\varepsilon^2}{k} \tag{3.54}$$

G_k: production of k due to mean velocity gradients:

$$G_k = -\rho\overline{u_i' u_j'}\frac{\partial \bar{u}_j}{\partial x_i} = \mu_t\left(\frac{\partial \bar{u}_i}{\partial x_j} + \frac{\partial \bar{u}_j}{\partial x_i}\right)\frac{\partial \bar{u}_j}{\partial x_i} \tag{3.55}$$

G_b: production of k due to buoyancy:

$$G_b = -\frac{g_i}{\rho}\left(\frac{\partial \rho}{\partial T}\right)_p \frac{\mu_t}{\mathrm{Pr}_t}\frac{\partial T}{\partial x_i} \tag{3.56}$$

g_i: gravity in i direction

Pr_t: turbulent Prandtl number, 0.85

The subscript p means the pressure is held constant. This is important in the case of gas for that the density of which would vary appreciably with pressure and temperature during the expansion process.

Y_M: effect of fluctuating dilatation on the overall dissipation rate in compressible turbulence

$$Y_M = \frac{2\rho k \varepsilon c_v}{c_p RT} \tag{3.57}$$

c_v : heat capacity at constant volume

c_p : heat capacity at constant pressure

σ_k : turbulent Prandtl number of k , σ_k =1.0

σ_ε : turbulent Prandtl number of ε , σ_ε =1.3

$C_{1\varepsilon}$ =1.44

$C_{2\varepsilon}$ =1.92

$$C_{3\varepsilon} = \tanh\left|\frac{V}{U}\right| = \frac{e^{\left|\frac{V}{U}\right|} - e^{-\left|\frac{V}{U}\right|}}{e^{\left|\frac{V}{U}\right|} + e^{-\left|\frac{V}{U}\right|}} \tag{3.58}$$

V : flow velocity component parallel to the gravity vector

U : flow velocity component perpendicular to the gravity vector

C_μ =0.09

The above constants are determined through comparison with some fundamental turbulent flow experimental data and are generally acceptable for a wide range of wall-bounded and free shear applications. In early engine combustion studies, the standard $k-\varepsilon$ turbulence model was widely used in engine CFD code (Lakshminarayanan et al., 2010).

3.4.5 RNG *k-ε* model

The RNG $k-\varepsilon$ turbulence model was developed analytically by Yakhot and Orszag (Yakhot et al., 1986) from NS equations using the statistical Renormalisation Group (RNG) theory. RNG theory is a numerical method used in *theoretical physics*. It is a mathematical treatment which allows systematic investigation of the changes of physical system as view at different distance scales, as turbulent flows More theoretical backgrounds can be found in Wilson (1975) and Rosten (2012).

Compared with the standard $k-\varepsilon$ turbulence model, RNG $k-\varepsilon$ model includes the following refinements:

1) An additional term is added in the transport equation of ε to account for the rapid strain flows.

2) The swirl effect on turbulence is considered for swirl dominated flows.

3) The turbulent Prandtl number is analytically calculated using RNG theory.

4) Low-Reynolds number effect can be included through an analytical differential expression of effective viscosity using RNG theory.

The transport equations for k and ε according ot RNG $k-\varepsilon$ model are given below:

$$\frac{\partial(\rho k)}{\partial t}+\frac{\partial(\rho k\bar{u}_i)}{\partial x_i}=\frac{\partial}{\partial x_i}\left[\alpha_k\mu_{eff}\frac{\partial k}{\partial x_i}\right]+G_k+G_b-\rho\varepsilon-Y_M \tag{3.59}$$

$$\frac{\partial(\rho\varepsilon)}{\partial t}+\frac{\partial(\rho\varepsilon\bar{u}_i)}{\partial x_i}=\frac{\partial}{\partial x_i}\left[\alpha_\varepsilon\mu_{eff}\frac{\partial\varepsilon}{\partial x_i}\right]+C_{1\varepsilon}\frac{\varepsilon}{k}\left(G_k+C_{3\varepsilon}G_b\right)-C_{2\varepsilon}\rho\frac{\varepsilon^2}{k}-R_\varepsilon \tag{3.60}$$

μ_{eff} : effective viscosity

Effective viscosity could be computed by solving a differential equation obtained from the scale elimination in RNG theory.

$$\delta\left(k\sqrt{\frac{\rho}{\varepsilon\mu}}\right)=1.72\frac{\hat{\nu}}{\sqrt{\hat{\nu}^3-1+C_\nu}}\delta\hat{\nu} \tag{3.61}$$

$\hat{\nu}=\mu_{eff}/\mu$

$C_\nu\approx 100$

μ : dynamic viscosity

This bridges the near-wall low-Reynolds number flows with the fully developed high-Reynolds number flows. In the high-Reynolds number region ($\mu_{eff}\gg\mu$):

$$\mu_t=\mu_{eff}-\mu=\rho C_\mu\frac{k^2}{\varepsilon} \tag{3.62}$$

μ_t : turbulent viscosity

$C_\mu = 0.0845$

G_k : production of k due to mean velocity gradients:

$$G_k = -\rho\overline{u_i' u_j'}\frac{\partial \overline{u}_j}{\partial x_i} = \mu_t\left(\frac{\partial \overline{u}_i}{\partial x_j} + \frac{\partial \overline{u}_j}{\partial x_i}\right)\frac{\partial \overline{u}_j}{\partial x_i} \tag{3.63}$$

G_b : production of k due to buoyancy:

$$G_b = -\frac{g_i}{\rho}\left(\frac{\partial \rho}{\partial T}\right)_p \frac{\mu_t}{\mathrm{Pr}_t}\frac{\partial T}{\partial x_i} \tag{3.64}$$

Pr_t : turbulent Prandtl number and is obtained from:

$$\left|\frac{\frac{1}{\mathrm{Pr}_t} - 1.3929}{\frac{k}{\mu c_p} - 1.3929}\right|^{0.6321}\left|\frac{\frac{1}{\mathrm{Pr}_t} + 2.3929}{\frac{k}{\mu c_p} + 2.3929}\right|^{0.3679} = \frac{\mu}{\mu_{eff}} \tag{3.65}$$

Y_M : effect of fluctuating dilatation on the overall dissipation rate in compressible turbulence

$$Y_M = \frac{2\rho k \varepsilon c_v}{c_p RT} \tag{3.66}$$

c_v : heat capacity at constant volume

α_k : inverse effective Prandtl number of k

α_ε : inverse effective Prandtl number of ε

α_k and α_ε can be obtained by solving:

$$\left|\frac{\alpha - 1.3929}{\alpha_0 - 1.3929}\right|^{0.6321}\left|\frac{\alpha + 2.3929}{\alpha_0 + 2.3929}\right|^{0.3679} = \frac{\mu}{\mu_{eff}} \tag{3.67}$$

$\alpha = \alpha_k = \alpha_\varepsilon$

$\alpha_0 = 1$

In the high-Reynolds number region ($\mu_{eff} \gg \mu$), $\alpha_k = \alpha_\varepsilon \approx 1.393$

Swirl Modification

To account for the swirl flows effect on turbulence, the turbulent viscosity can be updated using:

$$\mu_t = \mu_{t0} f\left(\alpha_S,\ \Omega,\ \frac{k}{\varepsilon}\right) \tag{3.68}$$

μ_{t0}: turbulent viscosity computed using equation (3.61) without swirl modification.

α_S: swirl constant.

Ω: characteristic swirl number.

For mildly swirling flows, α_S =0.07. A higher value should be specified for strong rotating flows.

$$R_\varepsilon = \frac{C_\mu \rho \eta^3 \left(1-\eta/\eta_0\right)}{1+\beta\eta^3}\frac{\varepsilon^2}{k} \tag{3.69}$$

$$\eta = Sk/\varepsilon \tag{3.70}$$

$$S = \sqrt{2S_{ij}S_{ij}} \tag{3.71}$$

$$S_{ij} = \frac{1}{2}\left(\frac{\partial \overline{u}_i}{\partial x_j} + \frac{\partial \overline{u}_j}{\partial x_i}\right) \tag{3.72}$$

$\eta_0 = 4.38$

$\beta = 0.012$

Rearrange the transport equation of ε:

$$\frac{\partial(\rho\varepsilon)}{\partial t} + \frac{\partial(\rho\varepsilon\overline{u}_i)}{\partial x_i} = \frac{\partial}{\partial x_j}\left[\alpha_\varepsilon \mu_{eff}\frac{\partial \varepsilon}{\partial x_j}\right] + C_{1\varepsilon}\frac{\varepsilon}{k}\left(G_k + C_{3\varepsilon}G_b\right) - C_{2\varepsilon}^*\rho\frac{\varepsilon^2}{k} \tag{3.73}$$

$$C_{2\varepsilon}^* = C_{2\varepsilon} + \frac{C_\mu \eta^3\left(1-\eta/\eta_0\right)}{1+\beta\eta^3} \tag{3.74}$$

$C_{1\varepsilon}$ =1.42

$C_{2\varepsilon}$ =1.68

$$C_{3\varepsilon} = \tanh\left|\frac{V}{U}\right| = \frac{e^{\left|\frac{V}{U}\right|} - e^{-\left|\frac{V}{U}\right|}}{e^{\left|\frac{V}{U}\right|} + e^{-\left|\frac{V}{U}\right|}} \tag{3.75}$$

In regions where $\eta < \eta_0$, R_ε plays a positive role and $C_{2\varepsilon}^* > C_{2\varepsilon}$. For example, in log-law region, $\eta \approx 3$, thus $C_{2\varepsilon}^* \approx 2.0$, which is very close to $C_{2\varepsilon}$ (=1.92). As a result, in weak or moderate strain rate flows, RNG $k-\varepsilon$ does not show obvious superiority over standard $k-\varepsilon$ model.

In regions where $\eta > \eta_0$, the contribution of R_ε would be negative and thus a lower turbulent viscosity is produced by RNG $k-\varepsilon$ model compared with standard $k-\varepsilon$ model. As a result, the introduction of R_ε makes RNG $k-\varepsilon$ model be more responsive to the large strain rate flows (where $\eta > \eta_0$) than standard $k-\varepsilon$ model (ANSYS, 2012).

The above models constants are derived analytically using RNG theory, contrary to those obtained by experimental adjustment in standard $k-\varepsilon$ model (ANSYS, 2012). With the above improvements, RNG $k-\varepsilon$ model has been applied to a wide class of turbulent flows with great success since its appearance (ANSYS, 2012).

3.4.6 Realisable *k*-*ε* model

The term "realisable" means that this model fulfils the following two mathematical constrains:

1) The normal Reynolds stresses should be always positive, thus:

$$\overline{u_i'^2} > 0 \tag{3.76}$$

2) The shear stresses should satisfy Schwarz inequality, thus:

$$\overline{u_\alpha'^2 u_\beta'^2} \geq \left(\overline{u_\alpha' u_\beta'}\right)^2 \quad (\alpha \neq \beta) \tag{3.77}$$

To meet the positive normal Reynolds stresses condition:

$$\overline{u'^2} = \frac{2}{3}k - 2\nu_t \frac{\partial \bar{u}}{\partial x} = \frac{2}{3}k - 2\left(C_\mu \frac{k^2}{\varepsilon}\right)\frac{\partial \bar{u}}{\partial x} \geq 0 \tag{3.78}$$

Thus, the mean strain rate must satisfy:

$$\frac{k}{\varepsilon}\frac{\partial \bar{u}}{\partial x} \leq \frac{1}{C_\mu} \approx 3.7 \tag{3.79}$$

This means that, if the mean strain rate of the flow is large enough, the model would be inconsistent with the turbulent flow physics. Similarly, it can be proven that if the mean strain rates exceed the limits, the Schwarz inequality of shear stresses would be violated as well.

The most straightforward way to make the realisable constraint satisfied is to set C_μ variable and related it with k, ε and strain rate. Shih et al. (1995) introduced a new turbulent viscosity formula which makes C_μ a variable dependent on k, ε and strain rate.

As to the standard $k-\varepsilon$ model, the transport equation of k is derived from the exact equation (ANSYS, 2012). However, the construction of the transport equation of ε is only based on physical reasoning and the structure of the transport equation of ε is far away from its exact mathematical form. This is the weakness of the standard $k-\varepsilon$ model (ANSYS, 2012). To address this deficiency, a new transport equation of ε is built up based on the dynamic equation of the mean-square vorticity fluctuation (ANSYS, 2012).

The transport equations of realisable $k-\varepsilon$ model are:

$$\frac{\partial(\rho k)}{\partial t} + \frac{\partial(\rho k \bar{u}_i)}{\partial x_i} = \frac{\partial}{\partial x_i}\left[\left(\mu + \frac{\mu_t}{\sigma_k}\right)\frac{\partial k}{\partial x_i}\right] + G_k + G_b - \rho\varepsilon - Y_M \tag{3.80}$$

$$\frac{\partial(\rho\varepsilon)}{\partial t}+\frac{\partial(\rho\varepsilon\overline{u}_i)}{\partial x_i}=\frac{\partial}{\partial x_i}\left[\left(\mu+\frac{\mu_t}{\sigma_\varepsilon}\right)\frac{\partial\varepsilon}{\partial x_i}\right]+\rho C_1 S\varepsilon-\rho C_2\frac{\varepsilon^2}{k+\sqrt{\nu\varepsilon}}+C_{1\varepsilon}\frac{\varepsilon}{k}C_{3\varepsilon}G_b \tag{3.81}$$

G_k is the production of k due to mean velocity gradients:

$$G_k=-\rho\overline{u_i'u_j'}\frac{\partial\overline{u}_j}{\partial x_i}=\mu_t\left(\frac{\partial\overline{u}_i}{\partial x_j}+\frac{\partial\overline{u}_j}{\partial x_i}\right)\frac{\partial\overline{u}_j}{\partial x_i} \tag{3.82}$$

G_b is the production of k due to buoyancy:

$$G_b=-\frac{g_i}{\rho}\left(\frac{\partial\rho}{\partial T}\right)_p\frac{\mu_t}{\mathrm{Pr}_t}\frac{\partial T}{\partial x_i} \tag{3.83}$$

Pr_t : turbulent Prandtl number, 0.85

Y_M is the effect of fluctuating dilatation on the overall dissipation rate in compressible turbulence

$$Y_M=\frac{2\rho k\varepsilon c_v}{c_p RT} \tag{3.84}$$

$$C_1=\max\left[0.43,\frac{\eta}{\eta+5}\right] \tag{3.85}$$

$$\eta=S\frac{k}{\varepsilon}$$

$$S=\sqrt{2S_{ij}S_{ij}}$$

$$S_{ij}=\frac{1}{2}\left(\frac{\partial\overline{u}_i}{\partial x_j}+\frac{\partial\overline{u}_j}{\partial x_i}\right)$$

$C_{1\varepsilon}$ =1.44 (3.86)

C_2 =1.9 (3.87)

$$C_{3\varepsilon}=\tanh\left|\frac{V}{U}\right|=\frac{e^{\left|\frac{V}{U}\right|}-e^{-\left|\frac{V}{U}\right|}}{e^{\left|\frac{V}{U}\right|}+e^{-\left|\frac{V}{U}\right|}} \tag{3.88}$$

σ_k : turbulent Prandtl number of k , σ_k =1.0

σ_ε : turbulent Prandtl number of ε , σ_ε =1.2

μ_t : turbulent viscosity

$$\mu_t = \rho C_\mu \frac{k^2}{\varepsilon} \tag{3.89}$$

$$C_\mu = \frac{1}{A_0 + A_S U^* k / \varepsilon} \tag{3.90}$$

$$U^* = \sqrt{S_{ij} S_{ij} + \Omega_{ij} \Omega_{ij}} \tag{3.91}$$

Ω_{ij} : the mean rate-of-rotation tensor

$A_0 = 4.04$

$A_s = \sqrt{6} \cos\phi$

$\phi = \frac{1}{3} \arccos\left(\sqrt{6} W\right)$

$W = \frac{S_{ij} S_{jk} S_{ki}}{\tilde{S}^3}$

$\tilde{S} = \sqrt{S_{ij} S_{ij}}$

3.5 Near-Wall Turbulent Flows

The turbulence models described in Section 3.4 can only be used in the fully-developed turbulent flows. As to the flows in the near wall regions, the presence of the wall would play a pivotal role to the development of the turbulence. The fact that the wall is one of the main sources of turbulence and large mean velocity gradients exist near it makes the near-wall turbulent simulation critical. It is substantiated by experiments that the near-wall region can be generally separated into three layers (ANSYS, 2012). The most inner layer is viscosity-dominated and the flow in this layer presents the characteristics as that of laminar flow. The most outer region is the fully-developed turbulent flow field and turbulence plays a dominant role in the mass, energy and momentum transfer. Between these two layers, a transition layer exists, in which turbulence and viscosity co-effect the transfers. To numerically simulate the near-wall turbulent flow, it is necessary to make the resolution of the boundary layer sufficient. There are two approaches to solve this. The first one is termed the "wall function" which uses empirical expressions to link the innermost viscous sub-layer with the outermost fully-developed turbulent region, and the interim buffer layer between them is not solved. Another approach is to solve the near-wall regions down to the wall. This needs the turbulence model be valid throughout the three layers (ANSYS, 2012). Considering the fact that the latter treatment would require the resolution of the viscous sub-layer be enough, and thus would increase the computational cost, the wall functions are used in the present context. The wall functions would provide the mathematical expressions for momentum, energy, species and turbulence transfers in the near-wall region. The following three different wall functions are investigated:

Standard (STD) Wall Functions

Scalable (SCA) Wall Function

Non-equilibrium (NON) Wall Functions

3.5.1 Standard (STD) Wall Functions

The current standard wall function was proposed by Launder and Spalding (Launder et al., 1974). It works reasonably well and has been most widely used in wall-bounded turbulent flows.

1) Momentum

The wall-law of mean velocity can be expressed using the dimensionless velocity U^* and distance from the wall y^* by:

$$U^* = \begin{cases} y^* & (y^* \le 11.225) \\ \frac{1}{\kappa}\ln\left(Ey^*\right) & (y^* > 11.225) \end{cases} \tag{3.92}$$

κ: von Karman constant, 0.4187

E: empirical constant, 9.793

$$U^* = \frac{UC_\mu^{1/4}k^{1/2}}{\tau_w / \rho} \tag{3.93}$$

U: fluid mean velocity at the near-wall node

k: fluid turbulent kinetic energy at the near-wall node

τ_w: wall shear stress

$$y^* = \frac{\rho C_\mu^{1/4}k^{1/2}y}{\mu} \tag{3.94}$$

y: distance from the wall to the near-wall node

2) Energy

Similar with the momentum logarithmic law, the temperature boundary layers in thermal transfer in the near-wall region can also be classified as different layers. The innermost is the thermal viscous sub-layer in which the conduction plays a dominant role and the outermost is the fully turbulent region where the thermal conduction obeys the logarithmic-law (ANSYS, 2012). Generally speaking, the thicknesses of the sub-layers

are different from fluid to fluid. As for the thickness of the thermal viscous sub-layer, it roughly obeys:

$$\frac{\delta}{\delta_T} \approx \sqrt{\Pr} \tag{3.95}$$

δ : thickness of the momentum viscous sub-layer

δ_T : thickness of the thermal viscous sub-layer

$\Pr$: molecular Prandtl number

$$\Pr = \frac{\mu c_p}{k_f} \tag{3.96}$$

c_p : fluid specific heat

k_f : fluid thermal conductivity

The wall-law of temperature can be expressed as:

$$T^* \equiv \frac{(T_w - T)\rho c_p C_\mu^{1/4} k^{1/2}}{\dot{q}} \quad (3.1)$$

$$= \begin{cases} \Pr y^* + \dfrac{1}{2}\rho \Pr \dfrac{C_\mu^{1/4} k^{1/2}}{\dot{q}} U^2 & (y^* \le y_T{}^*) \\ \Pr_t \left[\dfrac{1}{\kappa} \ln(E y^*) + P \right] + \dfrac{1}{2}\rho \dfrac{C_\mu^{1/4} k^{1/2}}{\dot{q}} \left[\Pr_t U^2 + (\Pr - \Pr_t) U_c{}^2 \right] & (y^* > y_T{}^*) \end{cases} \tag{3.97}$$

T^* : dimensionless temperature

T_w : wall temperature

T : fluid mean temperature at the near-wall node

$\dot{q}$: wall heat flux

$\Pr_t$: turbulent Prandtl number (=0.85 at the wall)

P : sub-layer resistance function

$$P = 9.24 \left[\left(\frac{\Pr}{\Pr_t} \right)^{3/4} - 1 \right] \left[1 + 0.28 e^{-0.007 \Pr / \Pr_t} \right] \tag{3.98}$$

U_c : mean velocity magnitude when $y^* = y_T{}^*$

y_T^*: dimensionless thermal sub-layer thickness

Once the molecular Prandtl number is computed, y_T^* could be computed by letting the linear and log-profile of T^* be equal at the intersection point.

Depending on the thermal boundary type specified at the wall, T_w or $\dot{q}$ could be then computed.

3) Species

The species transport in the near-wall region is assumed to behave similarly as that of heat (ANSYS, 2012):

$$Y^* \equiv \frac{\left(Y_{i,w} - Y_i\right)\rho C_\mu^{1/4} k^{1/2}}{J_{i,w}} \tag{3.99}$$

$$= \begin{cases} Scy^* & (y^* \le y_S^*) \\ Sc_t\left[\frac{1}{\kappa}\ln\left(Ey^*\right) + P_S\right] & (y^* > y_S^*) \end{cases} \tag{3.100}$$

$Y_{i,w}$: mass fraction of species i on the wall

Y_i: mass fraction of species i at the near-wall node

$J_{i,w}$: diffusion flux of species i on the wall

Sc: Schmidt number

$$Sc = \frac{\mu}{\rho D}$$

D: molecular diffusivity

Sc_t: turbulent Schmidt number

$$Sc_t = \frac{\mu_t}{\rho D_t} \tag{3.101}$$

D_t: turbulent diffusivity

P_S and y_S^* are computed similarly to P and y_T^*, with Prandtl numbers substituted by Schmidt numbers.

4) Turbulence

In the whole domain, the transport equation of k would be solved with the following boundary condition imposed on the wall:

$$\frac{\partial k}{\partial n} = 0 \tag{3.102}$$

n: normal coordinate to the wall

However, the terms in the transport equation of k would be modified in the wall-adjacent cells (ANSYS, 2012):

$$G_k \approx \tau_w \frac{\partial U}{\partial y} = \tau_w \frac{\tau_w}{\kappa \rho C_\mu^{1/4} k^{1/2} y} \tag{3.103}$$

$$\varepsilon = \frac{C_\mu^{3/4} k^{3/2}}{\kappa y} \tag{3.104}$$

The transport equation of ε would not be solved in the near-wall cells, with equation (3.104) instead.

It should be noted that the deviation of k and ε is based on the assumptions of the constant-shear and local equilibrium. As a result, the computation results would be compromised for the near-wall flows with severe pressure gradients or strong non-equilibrium.

3.5.2 Scalable (SCA) Wall Function

In general, the numerical results would deteriorate with uncontrollable error if the refinement of the grid exerted normal to the wall for the standard wall function. As a result, it is necessary to locate the first mesh node outside the buffer layer ($y^* \approx 5 \sim 30$) but within the log-law layer ($y^* \approx 30 \sim 300$). This would be very difficult to be ensured especially in complex wall flows. To remedy this, a limiter is introduced for y^*:

$$\tilde{y}^* = \max(y^*, 11.225)$$

By forcing the usage of log-law in the near-wall region, the scalable wall function produces consistent results for arbitrary refinement (ANSYS, 2012).

3.5.3 Non-equilibrium (NON) Wall Functions

As mentioned above, the deviation of k and ε is based on the assumptions of the constant-shear and local equilibrium. This would restrict the universality of the standard wall function in the near-wall flows with severe pressure gradients or strong non-equilibrium. In non-equilibrium wall functions, a pressure-gradient term is introduced to compute the mean velocity in the near-wall region:

$$\frac{\tilde{U}C_{\mu}^{1/4}k^{1/2}}{\tau_w/\rho}=\frac{1}{\kappa}\ln\left[E\frac{\rho C_{\mu}^{1/4}k^{1/2}y}{\mu}\right] \tag{3.105}$$

$$\tilde{U}=U-\frac{1}{2}\frac{dp}{dx}\left[\frac{y_{\upsilon}}{\rho\kappa\sqrt{k}}\ln\left(\frac{y}{y_{\upsilon}}\right)+\frac{y-y_{\upsilon}}{\rho\kappa\sqrt{k}}+\frac{y_{\upsilon}^{2}}{\mu}\right] \tag{3.106}$$

$$y_{\upsilon}\equiv\frac{\mu y_{\upsilon}^{*}}{\rho C_{\mu}^{1/4}k^{1/2}} \tag{3.107}$$

$$y_{\upsilon}^{*}=11.225 \tag{3.108}$$

The two-layer concept is introduced and the turbulence parameters k and ε are computed using their cell-averaged values. The two-layer concept assumes that the wall-adjacent cells are separated into viscous sub-layer and turbulent layer with the following profiles:

$$\tau_t=\begin{cases}0, & y<y_{\upsilon}\\ \tau_w, & y>y_{\upsilon}\end{cases} \tag{3.109}$$

$$k=\begin{cases}\left(\frac{y}{y_{\upsilon}}\right)^2 k_p, & y<y_{\upsilon}\\ k_p, & y>y_{\upsilon}\end{cases} \tag{3.110}$$

$$\varepsilon = \begin{cases} \dfrac{2\nu k}{y^2}, & y < y_\upsilon \\ \dfrac{k^{3/2}}{\kappa C_\mu^{-3/4} y}, & y < y_\upsilon \end{cases} \tag{3.111}$$

Then the volume-averaged values of G_k and ε are substituted into the transport equation of k (Equation 3.53, 3.59 or 3.80) to obtain the k in the near-wall cells. The volume-averaged ε is used as the near-wall cells value.

The mean temperature and species in the near-wall region are computed similarly with in the standard wall functions.

Through such treatments, the non-equilibrium wall functions account for the pressure gradients and thus improvements can be obtained to predict the wall-bounded flows with separation and reattachment (ANSYS, 2012).

3.6 Discrete Phase Model (DPM)

In diesel engine combustion process, the liquid fuel oil is injected into the combustion chamber with high velocity through very small holes in injector. Figure 3.5 schematically shows a typical diesel spray diagram under engine conditions. In the near nozzle region, a liquid core region exists and the aerodynamic breakup, namely primary atomisation happens in this region. Even though its existence is still debated (Dam, 2007), we would rather include this region for the consideration of the model tested. In the disperse region, the droplets would experience break-up, collision and finally evaporate from liquid into vapour. In the evaporation region, the vapour would mix with the surrounding gas and the combustion commences if the conditions are met.

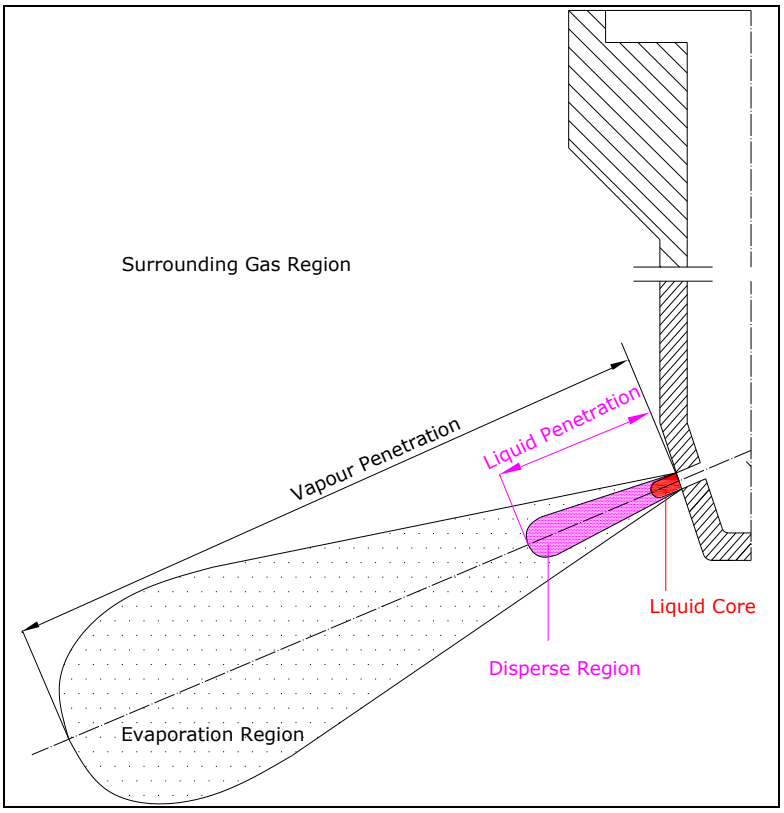

Figure 3.5 A typical diesel spray diagram under engine conditions

In the engine combustion simulation, it is critical to predict the diesel droplets and spray. Generally, there are two approaches to deal with the two phase flows:

1) Euler-Euler Approach

The essential idea of Euler-Euler modelling is to treat the liquid droplets and the gas phase as continuum (Iyer et al., 2005). In Euler-Euler approach, the tracking of individual droplets is avoided and the transport properties of the discrete phase would be defined.

2) Euler-Lagrange Approach

In Euler-Lagrange approach, the discrete phase is treated as spherical particles dispersed in the gas phase and the particles are tracked in a Lagrangian reference frame. In order to reduce the computational cost, the concept "parcel" is introduced to represent the droplets of the same properties. The coupling of the droplets and the gas phase would impact the trajectories of the particles as well as the heat and mass transfer between them (ANSYS, 2012).

In general, these two approaches are equivalent, but the Euler-Lagrange approach is the most popular one by far because of its amenable physical interpretation and numerical advantages (Iyer et al., 2005). In Euler-Lagrange approach, the calculation is limited in the spray domain and the ordinary differential equations controlling the particle motions are relatively simple to solve. In contrast with this, in Euler-Euler approach, the entire computation domain should be encompassed and more time consuming partial differential equations are solved. The Euler-Lagrange DPM approach is the adopted scheme in this dissertation.

3.6.1 Particle Motion Equations

In Cartesian coordinates, the force balance in x-direction on individual particle is expressed by the following equation:

$$\frac{du_p}{dt} = F_D\left(u - u_p\right) + \frac{g_x\left(\rho_p - \rho\right)}{\rho_p} + F_x \tag{3.112}$$

u_p : the particle velocity

u : the gas phase velocity

$F_D\left(u - u_p\right)$: the drag force per unit particle mass

$$F_D = \frac{18\mu}{\rho_p d_p^2}\frac{C_D \mathrm{Re}}{24} \tag{3.113}$$

μ : the molecular viscosity of the gas phase

ρ : the density of the gas phase

ρ_p : the density of the particle

d_p : the diameter of the particle

C_D : the drag coefficient.

For smooth spherical particles:

$$C_D = a_1 + \frac{a_2}{\mathrm{Re}} + \frac{a_3}{\mathrm{Re}^2} \tag{3.114}$$

a_1, a_2 and a_3 are given over the ranges of Reynolds number in Table 3.1 (Morsi et al., 1972).

Table 3.1 Constants of drag coefficient at different Reynolds numbers

a_1	a_2	a_3	Re
0	24.0000	0	Re＜0.1
3.6900	22.7300	0.0903	0.1＜Re＜1.0
1.2220	29.1667	-3.8889	1.0＜Re＜10
0.6167	46.5000	-116.6700	10＜Re＜100
0.3644	98.3300	-2778.0000	100＜Re＜1000
0.3570	148.6200	-47500.0000	1000＜Re＜5000
0.4600	-490.5460	5.7870×10^5	5000＜Re＜10000
0.5191	-1662.5000	5.4167×10^6	10000＜Re＜50000

Re : the relative Reynolds number:

$$\mathrm{Re} = \frac{\rho d_p \left| u_p - u \right|}{\mu} \tag{3.115}$$

g_x : the gravity in x-direction

F_x : the additional force, such as the "virtual mass" force which accelerates the fluid surrounding the particle:

$$F_x = \frac{1}{2}\frac{\rho}{\rho_p}\frac{d}{dt}\left(u - u_p\right) \tag{3.116}$$

and the pressure gradient force:

$$F_x = \frac{\rho}{\rho_p} u_{pi} \frac{\partial u}{\partial x_i} \tag{3.117}$$

The set of the factors given in Table 3.1 is only applicable to the smooth spherical particles, which assumes that the droplets would remain spherical throughout the evaporation process. It would not be the case for that the initial spherical droplet would distort significantly under large Weber numbers. The dynamic drag model would take the distortion of the particles into consideration. The drag coefficient can be modelled using the following formula:

$$C_D = \begin{cases} 0.424\left(1 + 2.632y\right) & \mathrm{Re} > 1000 \\ \dfrac{24}{\mathrm{Re}}\left(1 + 2.632y\right)\left(1 + \dfrac{1}{6}\mathrm{Re}^{\frac{2}{3}}\right) & \mathrm{Re} \le 1000 \end{cases} \tag{3.118}$$

y is the distortion of the particle. The value of y ranges from 0 (no distortion) to 1 (flat disk) (Liu et al., 1993).

3.6.2 Turbulent Dispersion on Particles

Due to the turbulence in the gas phase, the trajectories of the injected liquid particles would be affected by such turbulent fluctuations. In this research, the adopted method is the stochastic Discrete Random Walk Model (ANSYS, 2012). This model is a mathematical expression for a succession of random paths. It can be used to describe a

stochastic activity as molecule traveling in a fluid, or a drunkard's walk, an animal's foraging path. Through this stochastic method, the Discrete Random Walk Model could simulate the effect of instantaneous velocity fluctuations in the fluid phase on the trajectories of the particles. The turbulent dispersion on particles can be included by using the gas phase velocity $u = \bar{u} + u'$ in equation (3.112). In Discrete Random Walk Model, the random velocity fluctuations u', v' and w' are sampled by assuming that they obey a Gaussian probability distribution during the eddy life time τ_e:

$$u' = \zeta\sqrt{\overline{u'^2}} \tag{3.119}$$

$$v' = \zeta\sqrt{\overline{v'^2}} \tag{3.120}$$

$$w' = \zeta\sqrt{\overline{w'^2}} \tag{3.121}$$

ζ is a normally distributed random number.

In $k-\varepsilon$ turbulence models:

$$u' = v' = w' = \zeta\sqrt{\overline{u'^2}} = \zeta\sqrt{\overline{v'^2}} = \zeta\sqrt{\overline{w'^2}} == \zeta\sqrt{\frac{2k}{3}} \tag{3.122}$$

To get the turbulent dispersion on particles trajectories, the time spent in the turbulence motion along the particle path, T_L, should be firstly determined. Match the particle diffusivity to the turbulent scalar diffusion rate in one direction (e.g. x-axis):

$$\overline{u'^2}T_L = \frac{\mu_t}{\rho} \tag{3.123}$$

In $k-\varepsilon$ turbulence models:

$$\overline{u'^2} = \frac{2}{3}k \tag{3.124}$$

$$\frac{\mu_t}{\rho} = C_\mu \frac{k^2}{\varepsilon} \tag{3.125}$$

Thus:

$$T_L = \frac{3}{2}C_\mu \frac{k}{\varepsilon} \approx 0.15\frac{k}{\varepsilon} \tag{3.126}$$

The eddy life time is defined as:

$$\tau_e = T_L \log\left(\frac{1}{r}\right) \approx 0.15\frac{k}{\varepsilon}\log\left(\frac{1}{r}\right) \tag{3.127}$$

r is a uniform stochastic number between 0 and 1.

The particle-eddy interacting time, t_{cross} is defined as:

$$t_{cross} = \min\left(-\tau \ln\left[1-\left(\frac{L_e}{\tau\left|u-u_p\right|}\right)\right],\ \tau_e\right) \tag{3.128}$$

τ : the particle relaxation time

L_e : the eddy length scale

$\left|u-u_p\right|$: the relative velocity magnitude

The fluctuating velocity components are piecewise constant functions of time and the value is constant over the particle-eddy interacting time.

3.6.3 Droplet Collision Model

For the collision and breakup modelling, the concept “parcel” is introduced, which represents a number of droplets with the same characteristics. In droplet collision simulations, the widely used O’Rourke model (O'Rourke, 1981) is based on the assumption that two parcels would collide if they are in the same cell. The introduction of this assumption and “parcel” makes the collision simulation possible, but the O’Rourke assumption would cause grid-dependent artefacts. Even though such grid-dependent artefacts can be reduced by using a finer mesh, however, the required mesh number makes the accurate spray collision prediction prohibitive. As a result, the droplet collision effect would not be included in the model test.

3.6.4 Droplet Breakup Models

1) WAVE Breakup Model

The WAVE breakup model is applicable to high Weber number sprays (ANSYS, 2012). It assumes that the droplets breakup is induced by the relative velocity between the gas and liquid phases. The fastest growing Kelvin-Helmholtz instability would finally decide the breakup time point and the child droplet size. The mass of the child parcel would be accumulated from the initial parcel at certain rate until the shed mass equates 5% of the parent parcel.

Based on the work of Reitz (1987), the radius of the newly-formed children droplets r can be determined by the following formulas:

$$r = 0.61\Lambda \tag{3.129}$$

The change rate of the parent parcel droplet radius is calculated by:

$$\frac{da}{dt} = -\frac{a-r}{\tau} \quad (r \le a) \tag{3.130}$$

Λ is the wavelength of the fastest growing surface wave on the parent droplet and is determined by:

$$\Lambda = 9.02a\frac{\left(1+0.45Oh^{0.5}\right)\left(1+0.4Ta^{0.7}\right)}{\left(1+0.87We_2^{1.67}\right)} \tag{3.131}$$

a is the radius of the injector orifice.

τ is the breakup time and is given by:

$$\tau = \frac{3.726B_1a}{\Lambda\Omega} \tag{3.132}$$

Ω is the maximum growth rate of the corresponding wavelength:

$$\Omega = \frac{\sigma}{\rho_1 a^3}\frac{\left(0.34+0.38We_2^{1.5}\right)}{\left(1+Oh\right)\left(1+1.4Ta^{0.6}\right)} \tag{3.133}$$

$$Oh = \frac{\sqrt{We_1}}{\mathrm{Re}_1} \tag{3.134}$$

$$Ta = Oh\sqrt{We_2} \tag{3.135}$$

$$We_1 = \rho_1 \frac{U^2 a}{\sigma} \tag{3.136}$$

$$We_2 = \rho_2 \frac{U^2 a}{\sigma} \tag{3.137}$$

$$\mathrm{Re}_1 = \frac{Ua}{\nu_1} \tag{3.138}$$

ρ_1 is the liquid density and ρ_2 is the gas phase density.

σ is the surface tension.

B_1 is the breakup time constant. It determines how quickly the parcel would lose its mass. A larger value means that it would last longer to lose certain mass. According to the injector property, the value of B_1 can range from 1 to 60. A value of 1.73 is recommended by Liu et al.(1993).

2) KHRT Breakup Model

When the droplets are injected, they would not only experience the Kelvin-Helmholtz shear stress instability due to relative velocity, but also experience the Rayleigh-Taylor instability as well. Due to the deceleration, the droplets would be flattened and waves would be created on the backside. KHRT model would include both mechanisms by tracking the fastest growing instabilities of them (ANSYS, 2012).

KHRT model assumes the existence of the liquid core near the nozzle outlet with a certain length. Within the liquid core, the Kelvin-Helmholtz effect is the dominant and only the aerodynamic breakup is considered. Then the child droplets are subjected to deceleration and the Rayleigh-Taylor instability dominates. The KH and RT effects would be considered outside the liquid core and the new parcel would be produced only if the accumulated parcel mass is over 5% of the parent parcel mass in both cases. The KH effect would be computed similarly as the previous WAVE model. The RT breakup would occur if the lasting time of RT wave exceeds the breakup time defined as:

$$\tau_{RT} = \frac{C_\tau}{\Omega_{RT}} \tag{3.139}$$

C_τ is the constant, 0.5

$$\Omega_{RT} = \sqrt{\frac{2\left(-g_t\left(\rho_l - \rho_g\right)\right)^{\frac{3}{2}}}{3\sqrt{3\sigma}\left(\rho_l + \rho_g\right)}} \tag{3.140}$$

g_t is the acceleration in the droplet traveling direction.

The radius of the newly produced child droplets is given by:

$$r_c = \pi C_{RT}\sqrt{\frac{3\sigma}{-g_t\left(\rho_l - \rho_g\right)}} \tag{3.141}$$

C_{RT} is the constant, 1.0.

3) Stochastic Secondary Droplet (SSD) Breakup Model

SSD breakup model assumes the child droplets randomly distributed over a range (ANSYS, 2012). The newly formed droplet diameters follow an analytical solution of a probability distribution (ANSYS, 2012).

SSD model defines the critical radius and the breakup time as:

$$r_c = \frac{We_{cr}\sigma_l}{\rho_g u_{rel}^2} \tag{3.142}$$

$$t_{bu} = B\sqrt{\frac{\rho_l}{\rho_g}}\frac{r}{\left|u_{rel}\right|} \tag{3.143}$$

We_{cr} : the critical Weber number (=6).

B : the breakup const (=1.73).

When the droplet size of a parcel is larger than the defined critical radius, the breakup time would be calculated. If the breakup time is longer than the critical breakup time, then the parcel would breakup into the randomly distributed secondary parcels. The

distribution of the diameters of the secondary parcels would obey the following equation:

$$P(r) = \frac{1}{\sqrt{0.2\pi \ln \frac{We}{We_{cr}}}} \exp\left[\frac{-\left(\ln(r) - \ln(r_0) - C\right)^2}{0.2 \ln \frac{We}{We_{cr}}} \right] \tag{3.144}$$

C : constant (= -0.1)

3.6.5 Evaporation Models

1) Diffusion Controlled Model

The Diffusion Controlled model is applied to the situations that the evaporation is slow and the evaporation rate is controlled by the gradient of the vapour concentration. The molar vapour flux can be expressed as:

$$N = k_c \left(\frac{p_{sat}(T_p)}{RT_p} - X \frac{p}{RT} \right) \tag{3.145}$$

N : the molar flux of the vapour

k_c : the mass transfer coefficient

$p_{sat}(T_p)$: the saturated vapour pressure at the droplet temperature

X : the local mole fraction of the vapour

The mass transfer coefficient can be obtained by:

$$k_c = \frac{D}{d}\left(2 + 0.6\,\mathrm{Re}_d^{0.5}\, Sc^{1/3}\right) \tag{3.146}$$

D : the diffusion coefficient of the vapour

d : the diameter of the droplet

Re_d : the Reynolds number of the droplet

Sc : the Schmidt number

$$Sc = \frac{\mu}{\rho D}$$

Thus, the evaporated droplet mass can be computed according to:

$$m(t+\Delta t) = m(t) - NSM_w \Delta t \tag{3.147}$$

S: the droplet surface area

M_w: the molecular weight of the evaporated species

2) Convection/Diffusion Controlled Model

The Convection/Diffusion Controlled evaporation model is suitable for high evaporation rate in which the convection becomes important. In such situation, the evaporation rate can be computed by:

$$\frac{dm}{dt} = k_c S \rho \ln\left(\frac{1-Y}{1-Y_s}\right) \tag{3.148}$$

k_c: the mass transfer coefficient and is computed similarly as (3.146)

Y: the local mass fraction of the vapour

Y_s: the mass fraction of the vapour at the droplet surface

3.6.6 Coupling of the Discrete and Continuous Phases

As the discrete droplets pass through the control volume of the continuous phase, the mass, energy and momentum would be transferred in equilibrium. The mass gained by the continuous phase can be computed through the loss of the droplets. By solving such equations of the discrete phase and continuous phase alternately, the coupling of the discrete and continuous phases can be considered. The momentum transfer should be equal with the change of the droplets momentum and the heat exchange can be determined by calculating the thermal energy change of the droplets.

3.7 Combustion Models

Species Transport Models

Each chemical species experiencing convection, diffusion and chemical reaction can be tracked by the conservation equations in the control volume. In species transport models, the local mass fraction of each species Y_i could be solved through the following convection-diffusion equation:

$$\frac{\partial}{\partial t}\left(\rho Y_i\right)+\nabla\bullet\left(\rho\vec{v}Y_i\right)=-\nabla\bullet\vec{J}_i+R_i+S_i \tag{3.149}$$

$\vec{J}_i$ is the mass diffusion flux of species i, given by the following equation:

$$\vec{J}_i=-\left(\rho D_{i,m}+\frac{\mu_t}{Sc_t}\right)\nabla Y_i \tag{3.150}$$

$D_{i,m}$: diffusion coefficient of species i

Sc_t: turbulent Schmidt number (=0.7)

R_i: net production rate of species i through chemical reaction

S_i: creation rate of species i from the discrete phase or any other source

The chemical reaction rate R_i can be computed by the following four methods (ANSYS, 2012):

1) Laminar Finite-Rate model: the reaction rates are computed using Arrhenius expression and the turbulent fluctuations effect is completely neglected.

2) Eddy-Dissipation model: the reaction rates are controlled by turbulence.

3) Finite-Rate/Eddy-Dissipation (FRED) model: the reaction rates are controlled by the minimum value of the Arrhenius chemical reaction rate and turbulent eddy dissipation rate.

4) Eddy-Dissipation-Concept (EDC) model: detailed element chemical kinetics controlled by Arrhenius law interacts with the turbulence. If the combustion system

involves many species, every species transport equation would be solved in each control volume. The expensive computational cost makes this model completely prohibitive. As a result, this model is out of the scope of the current thesis research.

3.7.1 Laminar Finite-Rate Model

In Laminar Finite-Rate model, the chemical reaction rate is obtained by summing the Arrhenius reaction rate in every reaction that the species i involved:

$$R_i = M_{w,i} \sum_{r=1}^{N_R} \hat{R}_{i,r} \tag{3.151}$$

$M_{w,i}$: the molecular weight of species i

$\hat{R}_{i,r}$: the molar creation/destruction rate of species i

For reaction r involves species i:

$$\sum_{i=1}^{N} \nu'_{i,r} M_i \underset{k_{b,r}}{\overset{k_{f,r}}{\rightleftharpoons}} \sum_{i=1}^{N} \nu''_{i,r} M_i \tag{3.152}$$

the molar rate of creation/destruction of species i can be obtained by (ANSYS, 2012):

$$\hat{R}_{i,r} = \left(\nu''_{i,r} - \nu'_{i,r}\right)\left[k_{f,r} \prod_{j=1}^{N} \left(C_{j,r}\right)^{\eta'_{j,r}} - k_{b,r} \prod_{j=1}^{N} \left(C_{j,r}\right)^{\nu''_{i,r}} \right] \tag{3.153}$$

N: total number of chemical species

$\nu'_{i,r}$: stoichiometric coefficient for reactant i in reaction r

$\nu''_{i,r}$: stoichiometric coefficient for product i in reaction r

M_i: reactant or product i

$C_{j,r}$: molar concentration of species j in reaction r

$\eta'_{j,r}$: rate exponent of species j as reactant in reaction r

$k_{f,r}$: forward reaction rate constant in reaction r

$$k_{f,r} = A_r T e^{-E_r / RT} \tag{3.154}$$

A_r : pre-exponential factor

E_r : reaction activation energy

$k_{b,r}$: backward reaction rate constant in reaction r

$$k_{b,r} = \frac{k_{f,r}}{K_r} \tag{3.155}$$

K_r : equilibrium constant:

$$K_r = \exp\left(\frac{\Delta S_r^0}{R} - \frac{\Delta H_r^0}{RT}\right)\left(\frac{p_{atm}}{RT}\right)^{\sum_{i=1}^{N}\left(\nu''_{i,r}-\nu'_{i,r}\right)} \tag{3.156}$$

$$\frac{\Delta S_r^0}{R} = \sum_{i=1}^{N}\left(\nu''_{i,r} - \nu'_{i,r}\right)\frac{S_r^0}{R} \tag{3.157}$$

$$\frac{\Delta H_r^0}{RT} = \sum_{i=1}^{N}\left(\nu''_{i,r} - \nu'_{i,r}\right)\frac{h_r^0}{RT} \tag{3.158}$$

S_r^0 : standard-state entropy

h_r^0 : standard-state enthalpy

3.7.2 Eddy-Dissipation Model

For engine combustion, fuels would burn quickly. The combustion reaction rate would be determined by the mixing rate. As a result, the complex chemical kinetics would be ignored in the combustion modelling (Magnussen et al. 1977). In reaction r, the reaction rate of species i can be computed as:

$$R_{i,r} = \min\left[\nu'_{i,r}M_{w,i}A\rho\frac{\varepsilon}{k}\min_R\left(\frac{Y_R}{\nu'_{R,r}M_{w,R}}\right),\quad \nu'_{i,r}M_{w,i}AB\rho\frac{\varepsilon}{k}\frac{\sum_P Y_P}{\sum_j^N \nu''_{j,r}M_{w,j}}\right] \tag{3.159}$$

Y_R : mass fraction of every reactant R

Y_P : mass fraction of every product P

A: constant (=4.0)

B: constant (=0.5)

3.7.3 FRED Model

In FRED model (ANSYS, 2012), the reaction rates are controlled by the Arrhenius rate and turbulence. Before the flame is ignited, the Arrhenius rate is the smaller value and the overall reaction rate is determined by the kinetics rate. Once the flame begins to combust, the reaction rate predicted by ED model would be smaller than Arrhenius rate. Thus, the Arrhenius rate model in FRED can be considered as the ignition switch which determines the ignition start point.

Compared with the Laminar Finite-Rate model, FRED model takes the turbulence effect into account. The neglecting of turbulence in Laminar Finite-Rate model would introduce error. Compared with Eddy-Dissipation model, FRED presents superiority for that it accounts for the ignition period controlled by the Arrhenius rate. Considering the features of the internal combustion engine environment and the application range of the species transport models, we adopt the FRED combustion model as the only test case in species transport models.

3.7.4 Non-Premixed Combustion Models

During the combustion of diesel internal combustion engines, the diesel fuel and oxidizer enter the combustion cylinder in different streams. Such feature makes the diesel engine combustion process can be modelled using the non-premixed scheme. The non-premixed method is elegant for that every element is conserved during the combustion process. As a result, the modelling of the combustion is reduced to the solving of a mixing problem and the individual species transport equations would not be solved. The mixture fraction is defined as the mass fraction of burnt and unburnt fuel stream elements in the combustion system:

$$f = \frac{Z_i - Z_{i,ox}}{Z_{i,\,fuel} - Z_{i,ox}} \tag{3.160}$$

Z_i: element mass fraction of i

$Z_{i,ox}$: element mass fraction of i at the oxidizer inlet

$Z_{i,\,fuel}$: element mass fraction of i at the fuel stream inlet

The introduction of the mixture fraction makes the complex closing of the non-linear kinetics reaction reduced into the solving of a single parameter. The concentration of every species can be obtained from the mixture fraction fields. According to the mixture fraction results, the related thermochemistry of the reactions can be looked up from the pre-processed table which includes the corresponding relation of them. The assumed Probability Density Function (PDF) is used to account for the interaction of turbulence and chemistry. Through this way, the intermediate species or radical can be elegantly solved without the trouble of huge computational cost increase. The model of dissociation effects and the highly non-linear turbulence-chemistry coupling is simplified as well.

Transport Equations of Mixture Fraction

The diffusion coefficients of all the species could be assumed to be equal in turbulent flow. The turbulent convection would overwhelm the molecular diffusion. Thus, the density-averaged mixture fraction equation can be constructed as (ANSYS, 2012):

$$\frac{\partial}{\partial t}\left(\rho \bar{f}\right) + \nabla \bullet \left(\rho \vec{v} \bar{f}\right) = \nabla \bullet \left(\frac{\mu_t}{\sigma_t} \nabla \bar{f}\right) + S_f \tag{3.161}$$

$$\bar{f} = f - f' \tag{3.162}$$

S_f: mass transfer from the fuel stream into the gas phase

In order to close the turbulence-chemistry model, the transport equation of mixture fraction variance $\overline{f'^2}$ should be solved by:

$$\frac{\partial}{\partial t}\left(\rho \overline{f'^2}\right) + \nabla \bullet \left(\rho \vec{v} \overline{f'^2}\right) = \nabla \bullet \left(\frac{\mu_t}{\sigma_t} \nabla \overline{f'^2}\right) + C_g \mu_t \left(\nabla \bar{f}\right)^2 - C_d \rho \frac{\varepsilon}{k} \overline{f'^2} \tag{3.163}$$

σ_t : constant (=0.85)

C_g : constant (=2.86)

C_d : constant (=2.00)

Turbulence-Chemistry Interaction Modelling

The turbulence-chemistry interaction determines the averaging process from the instantaneous values to the mean values. Herein, the β-PDF is used to account for the interaction of turbulence and chemistry. The probability function $p(f)$ can be used to present the time fraction of the fluid staying at f with a range of Δf. As a result, the shape of $p(f)$ determines the turbulence-chemistry interaction. β-PDF is considered as good an approximation of the actual observed shape:

$$p(f) = \frac{f^{\alpha-1}(1-f)^{\beta-1}}{\int f^{\alpha-1}(1-f)^{\beta-1} df} \tag{3.164}$$

$$\alpha = \bar{f}\left[\frac{\bar{f}(1-\bar{f})}{\overline{f'^2}} - 1\right] \tag{3.165}$$

$$\beta = (1-\bar{f})\left[\frac{\bar{f}(1-\bar{f})}{\overline{f'^2}} - 1\right] \tag{3.166}$$

According to the chemical reaction features, the non-premixed model can be applied in three distinct schemes:

1) Non-Premixed Equilibrium Model

The diesel engine combustion processes can be assumed to be composed of a serial of chemical equilibrium states as the chemical reaction time scales are usually much faster compared with the crank rotational speed (Oppenauer et al, 2011). As a result, the related thermochemistry could be obtained directly from equilibrium reactions of the diesel combustion. To simulate the chemical non-equilibrium in the rich regions, a Rich Flammability Limit (RFL) could be used to consider the rich regions as the mixing of

unburnt diesel fuel and leaner equilibrium burnt flame (ANSYS, 2012).

In the current non-adiabatic diesel engine combustion simulation, only one mixture fraction would be solved. The instantaneous thermochemical scalars as density, species fraction and temperature are solely related with the mixture fraction in equilibrium combustion:

$$\phi_i = \phi_i\left(f, H\right) \tag{3.167}$$

ϕ_i: instantaneous thermochemical scalars as density, species fraction and temperature

H: instantaneous enthalpy

Then the density-averaged mean scalars as species fraction and temperature can be calculated:

$$\bar{\phi}_i = \int_0^1 p(f)\phi_i(f, \bar{H})df \tag{3.168}$$

And the mean time-averaged density can be calculated as:

$$\frac{1}{\bar{\rho}} = \int_0^1 \frac{p(f)}{\rho(f, \bar{H})} df \tag{3.169}$$

$\bar{H}$ is the mean enthalpy and it can be obtained by solving:

$$\frac{\partial}{\partial t}\left(\rho\bar{H}\right) + \nabla\bullet\left(\rho\vec{v}\bar{H}\right) = \nabla\bullet\left(\frac{k_t}{c_p}\nabla\bar{H}\right) + S_h \tag{3.170}$$

S_h: heat exchanges with walls or the discrete phase

For non-premixed equilibrium combustion model, the equilibrium look-up table is generated before the whole domain iterations. The generation of the look-up table needs the equilibrium thermochemistry of the fuel under every non-adiabatic condition:

$$Y_i\left(f, \bar{H}\right) \tag{3.171}$$

$$T\left(f, \bar{H}\right) \tag{3.172}$$

$$\rho\left(f, \bar{H}\right) \tag{3.173}$$

Then the mean scalars can be obtained from its integration with probability density function. For every specific species, the mean mass fraction is three-dimensional. So are the mean temperature and density:

$$\bar{Y}_i\left(\bar{f},\ \overline{f'^2},\ \bar{H}\right) \tag{3.174}$$

$$\bar{T}\left(\bar{f},\ \overline{f'^2},\ \bar{H}\right) \tag{3.175}$$

$$\bar{\rho}\left(\bar{f},\ \overline{f'^2},\ \bar{H}\right) \tag{3.176}$$

The generated three-dimensional look-up table would be saved for later tracking. The transport equations would be then solved through the whole domain to determine the mixture fraction, which could get the means scalars by looking up the saved table. Through this way, the mixture fraction field correlates with the thermochemistry elegantly.

2) Non-Premixed Steady Flamelet Model

In non-premixed steady flamelet model (ANSYS, 2012), the chemical non-equilibrium induced by aerodynamic straining in turbulent diffusion flames could be included. The stretching effect is accounted through the counterflow diffusion flame which represents the flamelet in turbulent flow. The steady flamelet model is subjected to the restriction of fast reaction. It is suitable to simulate non-equilibrium effects induced by fast aerodynamic strain from turbulence but is not recommended for slow-chemistry flames simulation.

The introduction of the concept “flamelet” makes the non-premixed steady flamelet model capable of considering the non-equilibrium effect induced by aerodynamic strain. It assumes that the turbulent flame can be presented by an ensemble of flamelet in counterflow diffusion flames. Thus, the complex chemistry can be described by the mixture fraction and the strain rate. The strain rate can be represented using the scalar

dissipation defined as:

$$\chi = 2D\left|\nabla f\right|^2 \tag{3.177}$$

D: diffusion coefficient

The scalar dissipation with the dimension of s^{-1} can be regarded as the inverse of diffusion time. Generally, to consider the varying stains in turbulent flames, multiple flamelets include a range of strain rates should be generated. The values of the scalar dissipation can be determined by:

$$\chi_i = \begin{cases} 10\chi_{i-1} & \left(\chi_{i-1} < 1\,s^{-1}\right) \\ \chi_{i-1} + \Delta\chi & \left(\chi_{i-1} \geq 1\,s^{-1}\right) \end{cases} \tag{3.178}$$

For any specific flamelet, the strain rate can be related with the stoichiometric scalar dissipation χ_{st} at the stoichiometric mixture fraction f_{st} (Kim et al., 1997):

$$\chi_{st}\left(f_{st}\right) = \frac{v}{8\pi d}\frac{3\left(\sqrt{\frac{\rho_\infty}{\rho}}+1\right)^2}{2\sqrt{\frac{\rho_\infty}{\rho}}+1}\exp\left[-\frac{0.5\pi}{\left(\int_{2f_{st}}^{\infty} e^{-t^2}dt\right)^2}\right] \tag{3.179}$$

v: relative velocity magnitude of the fuel and oxidizer nozzles

d: distance of the fuel and oxidizer nozzles

ρ_∞: initial density of the oxidizer

The detailed chemical mechanism of the fuel is needed. Using the detailed chemical mechanisms of the diesel fuel, the flamelet can be generated by solving the equations of species mass fractions and temperature:

$$\rho\frac{\partial Y_i}{\partial t} = \frac{\rho\chi_{st}}{2}\frac{\partial^2 Y_i}{\partial f^2} + S_i \tag{3.180}$$

$$\rho\frac{\partial T}{\partial t} = \frac{\rho\chi_{st}}{2}\frac{\partial^2 T}{\partial f^2} - \frac{1}{c_p}\sum_i H_i S_i + \frac{\rho\chi_{st}}{2c_p}\left[\frac{\partial c_p}{\partial f} + \sum_i c_{p,i}\frac{\partial Y_i}{\partial f}\right]\frac{\partial T}{\partial f} \tag{3.181}$$

S_i: reaction rate of species i

H_i: specific enthalpy of species i

c_p: mixture-averaged specific heat

$c_{p,i}$: specific heat of species i

For non-adiabatic flamelets, the heat gain and loss is assumed to have a negligible effect on the species mass fraction to make the problem simpler, thus:

$$Y_i = Y_i\left(f, \chi_{st}\right) \tag{3.182}$$

$$T = T\left(f, \chi_{st}, \bar{H}\right) \tag{3.183}$$

$$\rho = \rho\left(f, \chi_{st}, \bar{H}\right) \tag{3.184}$$

The density-averaged mean scalar values can be obtained by:

$$\bar{\phi} = \iint \phi\left(f, \chi_{st}\right) p\left(f, \chi_{st}\right) df\, d\chi_{st} \tag{3.185}$$

Considering that f and χ_{st} being assumed statistically independent:

$$p\left(f, \chi_{st}\right) = p_f\left(f\right) p_\chi\left(\chi_{st}\right) \tag{3.186}$$

$p_f\left(f\right)$ can be assumed to obey β PDF and $p_\chi\left(\chi_{st}\right)$ to obey the Dirac Delta function as the fluctuations of χ_{st} are neglected. Thus, the look-up PDF table can be generated with the following dimensions:

$$\bar{Y}_i = \begin{cases} \bar{Y}_i\left(\bar{f}, \overline{f'^2}, \bar{\chi}_{st}\right) & \left(\bar{\chi}_{st} \neq 0\right) \\ \bar{Y}_i\left(\bar{f}, \overline{f'^2}, \bar{H}\right) & \left(\bar{\chi}_{st} = 0\right) \end{cases} \tag{3.187}$$

$$\bar{T} = \bar{T}\left(\bar{f}, \overline{f'^2}, \bar{\chi}_{st}, \bar{H}\right) \tag{3.188}$$

$$\bar{\rho} = \bar{\rho}\left(\bar{f}, \overline{f'^2}, \bar{\chi}_{st}, \bar{H}\right) \tag{3.189}$$

After the flamelet and the look-up PDF table being generated, the transport equations would be then solved through the whole domain to determine the mean mixture fraction,

mixture fraction variance and the mean enthalpy. By solving the equations of turbulence and mixture fraction variance, the scalar dissipation can be determined by:

$$\bar{\chi}_{st} = 2\overline{f'^2}\frac{\varepsilon}{k} \tag{3.190}$$

Using these obtained values, the mean values of chemistry can be tracked in the PDF look-up table.

More critical reviews and analyses about non-premixed steady flamelet combustion model can be found in Dixon-Lewis (1991) and Bray et al. (1994).

3) Non-Premixed Unsteady Flamelet Diesel Model

The non-premixed unsteady flamelet diesel model is specifically designed for the prediction of compression-ignition diesel engine combustion. The slow-forming of the products (NO_x), ignition and extinction during diesel engine combustion would make the related reaction far from chemical equilibrium. The unsteady flamelet diesel model can capture such deep non-equilibrium effects with substantial running time saved over the detailed finite rate EDC approach.

Similar with the steady flamelet combustion model, the detailed chemical mechanism of the fuel oil is required as well in unsteady flamelet diesel combustion model. But the flamelet and look-up PDF table in unsteady flamelet diesel combustion model are not pre-processed as that happened in steady flamelet model. The species mass fractions, temperature and the flow field would be solved simultaneously. With the solution of the flow field, the flamelet and the look-up PDF table are generated similarly as in non-adiabatic steady flamelet at the end of every time step. Then the former stored flamelet and look-up PDF table would be used for flow solution during this time step.

Different from the initially started combustion condition in steady flamelet combustion models, the initial flamelet in unsteady flamelet diesel model is in the mixed but unburnt state. The flamelet solver derives the mean values of scalar dissipation, pressure and

temperature from the flow solver. To simulate the compression ignition process, the energy equation includes an additional term to represent the volume-averaged pressure rise:

$$\rho \frac{\partial T}{\partial t} = \frac{\rho \chi_{st}}{2} \frac{\partial^2 T}{\partial f^2} - \frac{1}{c_p} \sum_i H_i S_i + \frac{\rho \chi_{st}}{2 c_p} \left[\frac{\partial c_p}{\partial f} + \sum_i c_{p,i} \frac{\partial Y_i}{\partial f} \right] \frac{\partial T}{\partial f} + \frac{1}{c_p} \frac{\partial p}{\partial t} \qquad (3.191)$$

More detailed description of the non-premixed unsteady flamelet diesel model can be found in Barths et al. (1998).

3.8 Closure

In this chapter, the computational models involved in the CFD simulation of a large 2-stroke marine engine combustion processes are summarised. For the reason that the computations are based on the software ANSYS FLUENT, this summary is more than inclusive of the more general computational models. Some of the constants and expressions are based on the combinations used in ANSYS FLUENT. Table 3.2 summarises the discretisation parameters in the corresponding physical models.

Table 3.2 Summary of the parameters discretised in different physical models

Physical Models	Discretisation Parameters
RANS Equations	Reynolds averaged velocities $\bar{u}_i$ of continuous phase
k-ε Turbulence Models	turbulent kinetic energy *k*, turbulence dissipation rate ε
EOS	pressure p, temperature t and volume v of continuous phase
DPM	particle velocity v_p, particle diameter r, particle temperature and particle position
LFR	Arrhenius reaction rate
ED	mixing rate
FRED	Arrhenius reaction rate and mixing rate
Non-Premixed Equilibrium	density-averaged mixture fraction $\overline{f}$, variance of mixture fraction $\overline{f'^2}$, mean enthalpy $\bar{H}$
Non-Premixed Flamelet	density-averaged mixture fraction $\overline{f}$, variance of mixture fraction $\overline{f'^2}$, mean enthalpy $\bar{H}$, stoichiometric scalar dissipation $\overline{\chi}_{st}$

In the following chapters, the detailed techniques would not be presented. More detailed theory and background can be found in ANSYS (2012).

Chapter 4 Basic Cases Tests

In this chapter, three basic cases tests (compressible turbulent mixing layers, heat transfer in the boundary layer of a pipe expansion and droplet breakup of n-heptane spray) would be carried out to determine the turbulence model, wall function, mesh size and droplet breakup models to prepare for the modelling of the large 2-stroke marine diesel engine.

4.1 Compressible Turbulent Mixing Layers

High speed turbulent mixing dominates the flow field during the engine scavenging and mixing process. Therefore, it is critical to predict the velocity and turbulence profiles to locate the involved species and the corresponding states, which would finally affect the combustion performance. In view of lack of conclusive evidence or experimental data to characterise the scavenging process, the 2D turbulent mixing layer benchmark case (Goebel, 1991) is used to investigate the velocity and turbulent kinetic energy distribution in mixing and shearing flows. Then the tested setup is used to calculate the engine pressure to validate results against the shop test data.

4.1.1 Geometry and Setup

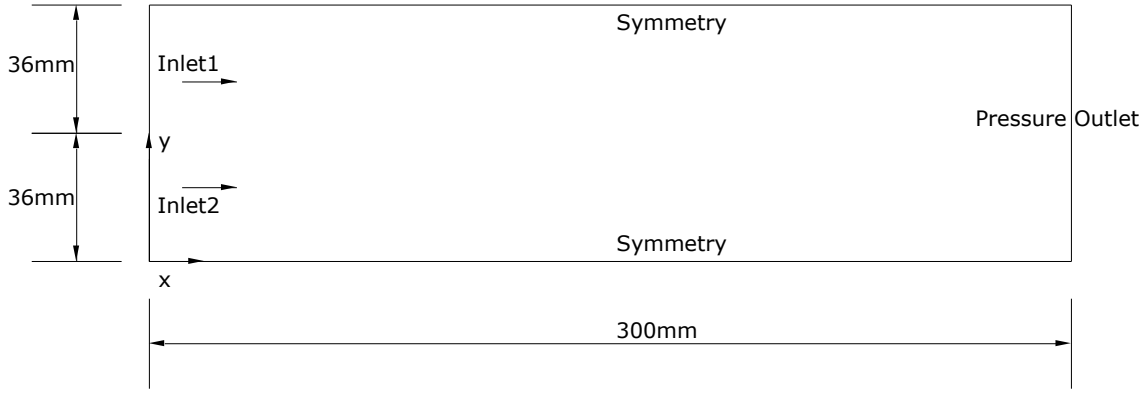

Figure 4.1 Geometry and boundary conditions of the mixing layers

The geometry and the boundaries are presented in Figure 4.1. The boundary conditions of Inlet1 and Inlet2 are specified as:

Inlet1:

Total Pressure:	487	kPa
Static Pressure:	36	kPa
Total Temperature:	360	K
Mach Number:	2.35	
Turbulent Kinetic Energy:	74	m^2/s^2
Turbulent Dissipation Rate:	62300	m^2/s^3

Inlet2:

Total Pressure:	38	kPa
Static Pressure:	36	kPa
Total Temperature:	290	K
Mach Number:	0.36	
Turbulent Kinetic Energy:	226	m^2/s^2
Turbulent Dissipation Rate:	332000	m^2/s^3

4.1.2 Tested Cases and Results

The profiles of turbulent kinetic energy and axial velocity from simulation and measurement are compared. Standard (STD), RNG and Realisable (REA) *k*-ε turbulence models are calculated and the tested positions are selected at x=0.01m, 0.025m, 0.05m, 0.1m, 0.125m, 0.15m and 0.175m. Comparison is demonstrated in Figure 4.2.

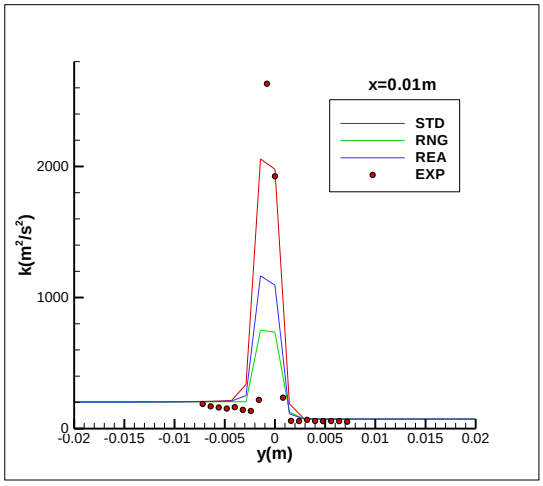

(a) Profile of *k* at x=0.01m

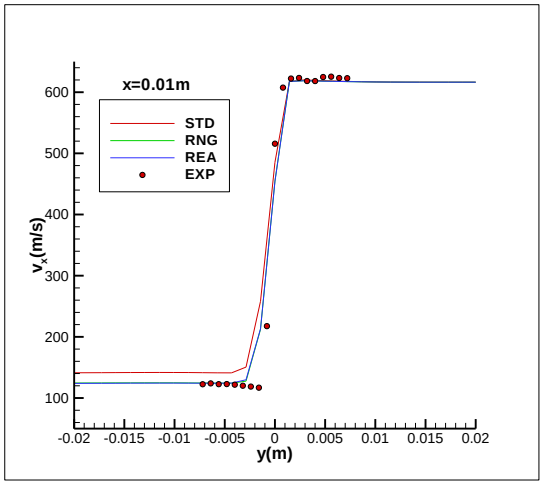

(b) Profile of V_x at x=0.01m

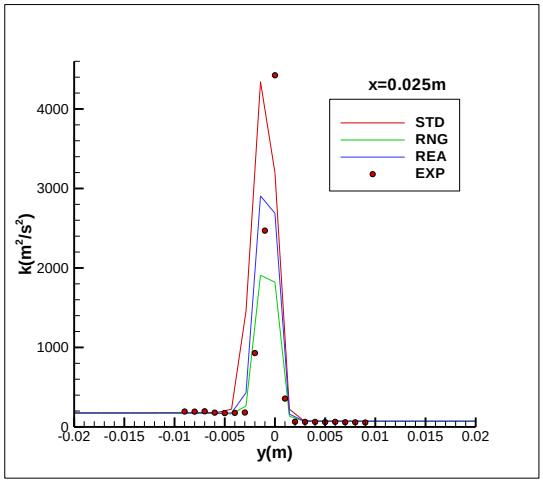

(c) Profile of *k* at x=0.025m

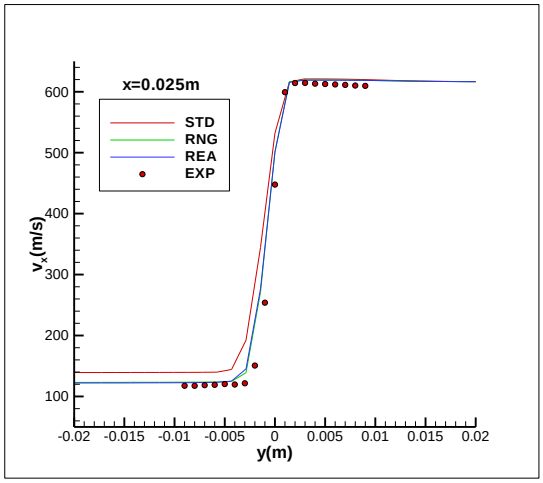

(d) Profile of V_x at x=0.025m

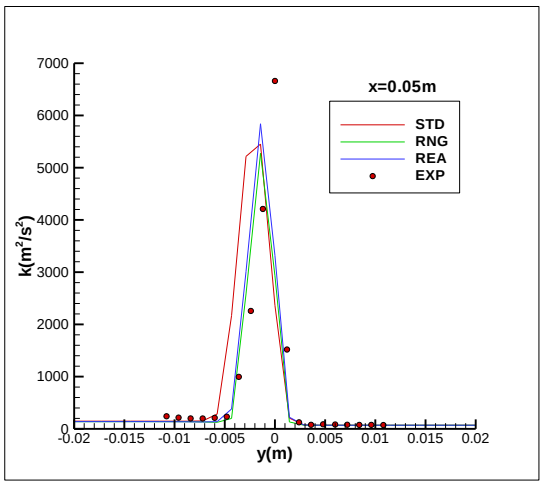

(e) Profile of k at x=0.05m

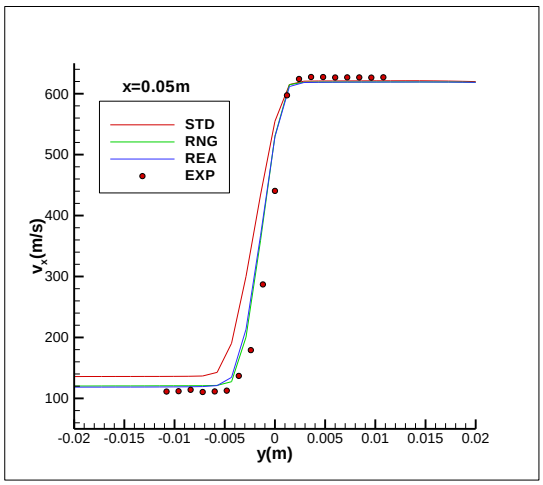

(f) Profile of V_x at x=0.05m

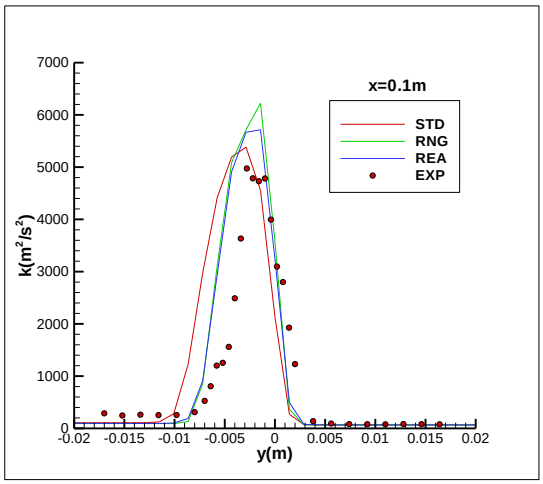

(g) Profile of k at x=0.1m

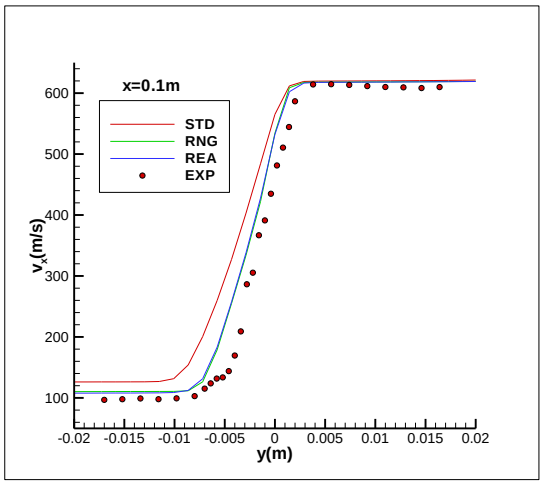

(h) Profile of V_x at x=0.1m

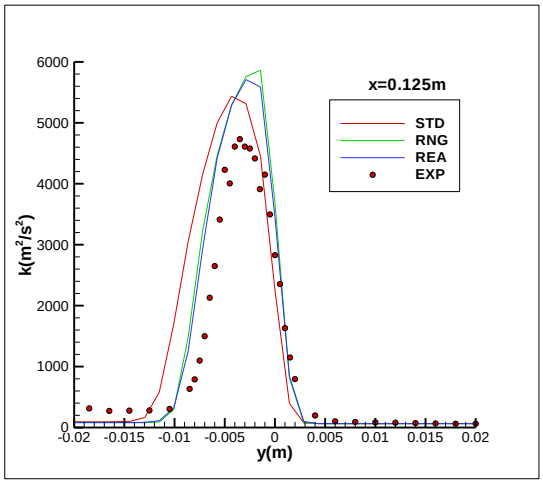

(i) Profile of k at x=0.125m

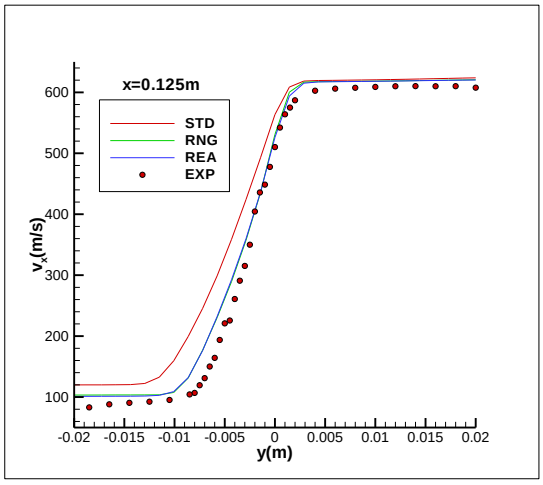

(j) Profile of V_x at x=0.125m

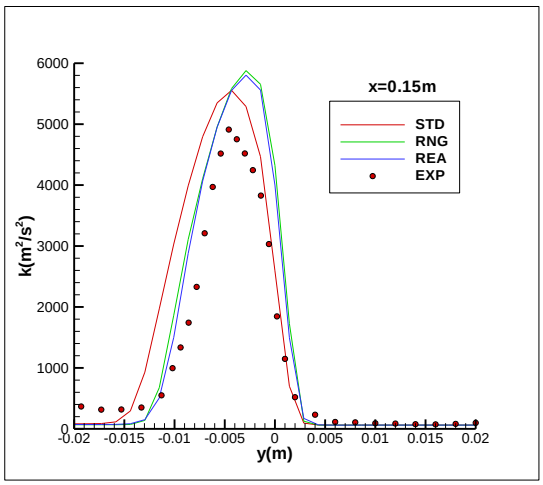

(k) Profile of k at x=0.15m

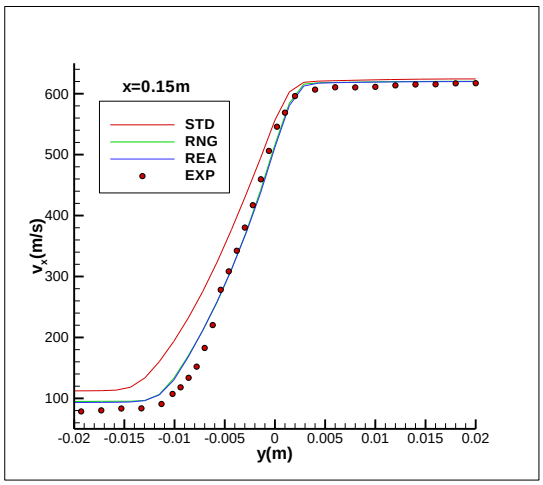

(l) Profile of V_x at x=0.15m

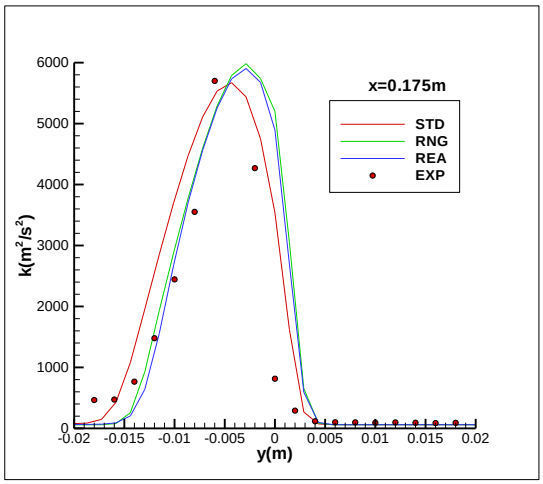

(m) Profile of k at x=0.175m

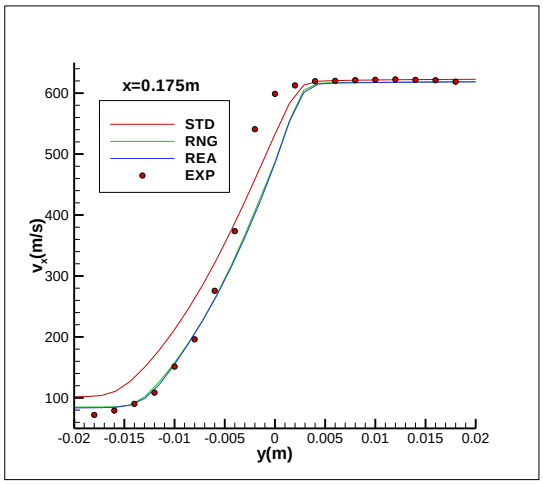

(n) Profile of V_x at x=0.175m

Figure 4.2 Comparison of the profiles of k and Vx at different positions using STD, RNG and REA k-ε turbulence models

4.1.3 Conclusions and Discussion

From comparison of the profiles in Figure 4.2, it can be concluded that:

1) At different positions, STD, RNG and REA k-ε turbulence models can predict acceptable accuracy for k profile.

2) RNG and REA k-ε turbulence models can predict more accurate axial velocity profiles than the Standard k-ε turbulence model.

Considering the fact that the RNG k-ε turbulence model is still the most widely used turbulence closure scheme and the Realisable k-ε turbulence model does not show any superiority over the RNG model, the RNG k-ε turbulence model was chosen as the turbulence closure method in the following complete cycle engine simulations.

4.2 Heat Transfer in the Boundary Layer of a Pipe Expansion

To guarantee the engine works smoothly out of the risk of being overheated, the piston, cylinder cover and liner would be cooled by water or oil. The heat taken away by the water and oil would ensure that the engine components operate within the safe temperature range. However, this cooling process also transfers the in-cylinder effective heat to the water and air through the cylinder walls. Thus, to accurately capture the in-cylinder pressure, it is necessary to take this part of heat loss into account. In the current engine shop test, such heat transfer data is not available. As a result, the heat transfer in the boundary layer of a pipe expansion is modelled and validated against the experimental data (Baughn et al., 1984), through which, the most appropriate heat transfer modelling wall function is determined.

4.2.1 Geometry and Setup

The selected computation case is an axisymmetric pipe expansion with the geometry and boundary conditions presented in Figure 4.3.

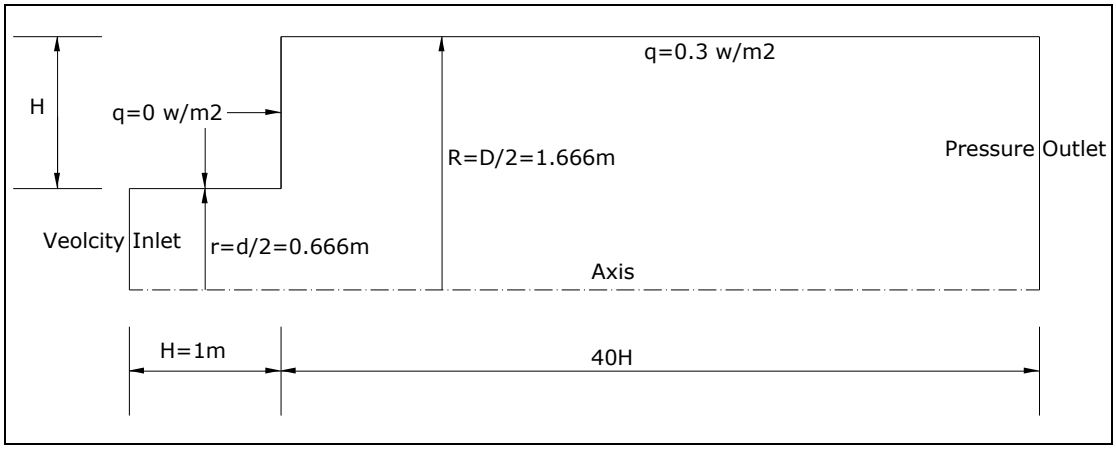

Figure 4.3 Geometry and boundary conditions of the pipe expansion

The fluid properties are listed as follows:

Density ρ:	1	kg/m^3
Viscosity μ:	10^{-4}	Pa-s
Thermal Conductivity k:	10^{-4}	W/m-K
Specific Heat c_p:	0.7	J/kg-K

The velocity inlet conditions are specified using profile data from fully developed turbulent formulas. The mass flow rate $\dot{m}$ is about 10.64kg/s and the Reynolds number can be computed as:

$$\mathrm{Re} = \frac{4\dot{m}}{\pi\mu D} \approx 40750 \tag{4.1}$$

The Prandtl number equates:

$$\mathrm{Pr} = \frac{c_p \mu}{k} = 0.7 \tag{4.2}$$

The Nusselt number is used to quantify the amount of heat transfer. The local Nusselt number is defined as the ratio of the heat transfer due to convection and conduction and can be computed as:

$$Nu = \frac{hD}{k} \tag{4.3}$$

h : the local heat transfer coefficient

$$h = \frac{q}{T_{wall} - T} \tag{4.4}$$

q : the local heat flux

T_{wall} : the wall temperature

T : the local temperature

$$T = \frac{4xq}{\mathrm{Re}\,\mu c_p} + 273 \tag{4.5}$$

The fully turbulent Nusselt number can be computed using the Dittus-Boelter equation

as:

$$Nu_{DB} = 0.023\,\mathrm{Re}^{0.8}\,\mathrm{Pr}^{0.4} = 97.24 \tag{4.6}$$

In the following section, the ratio of local Nusselt number and Dittus-Boelter Nusselt number Nu/Nu_{DB} from the simulation and measurement is compared.

4.2.2 Test Cases and Results

The height of the first layer grid would influence the distribution of Y*, which finally determines the working range of wall functions. The definition of Y* is:

$$Y^* = \frac{\rho C_\mu^{0.25} k^{0.5} y}{\mu} \tag{4.7}$$

Five different first-wall-mesh heights (0.1m, 0.05m, 0.02m, 0.01m and 0.005m) are tested using Standard wall function (STD), Scalable wall function (SCA) and Non-Equilibrium wall function (NON). RNG k-ε turbulence model is adopted to model the fully developed turbulence. The distribution of Y* and Nu/Nu_{DB} are demonstrated in Figure 4.4.

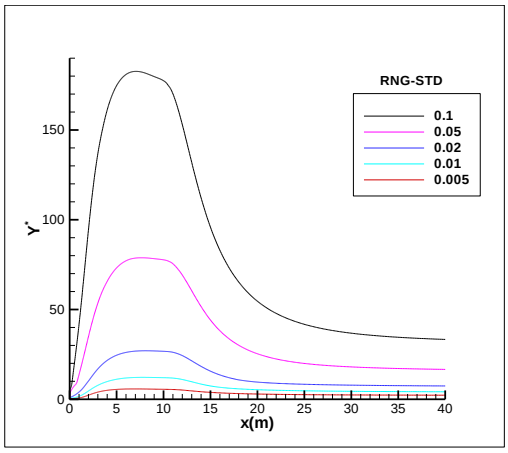

(a) Y* distribution using RNG-STD

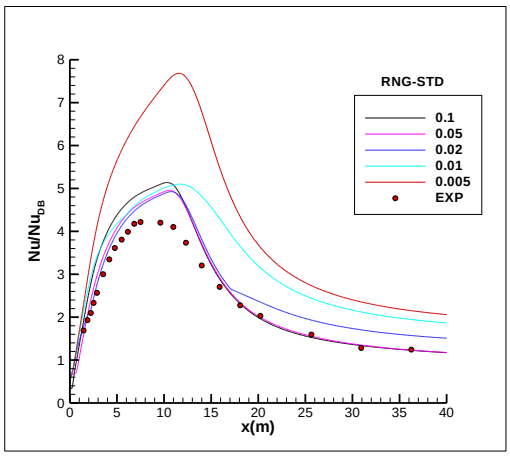

(b) Nu/Nu_{DB} distribution using RNG-STD

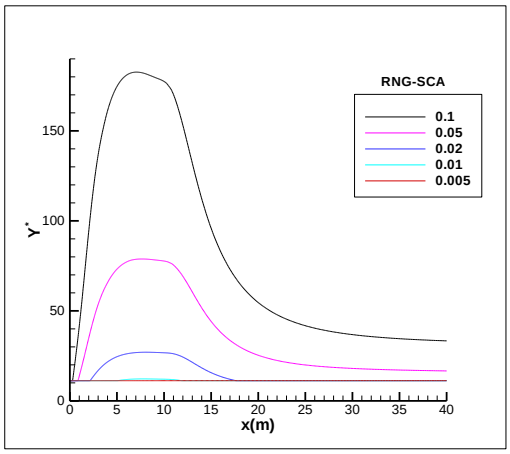

(c) Y* distribution using RNG-SCA

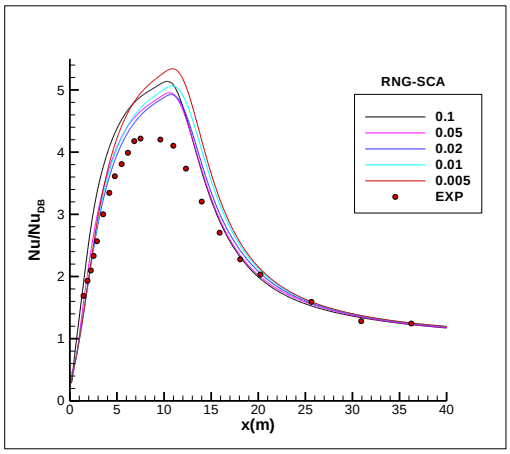

(d) Nu/Nu_{DB} distribution using RNG-SCA

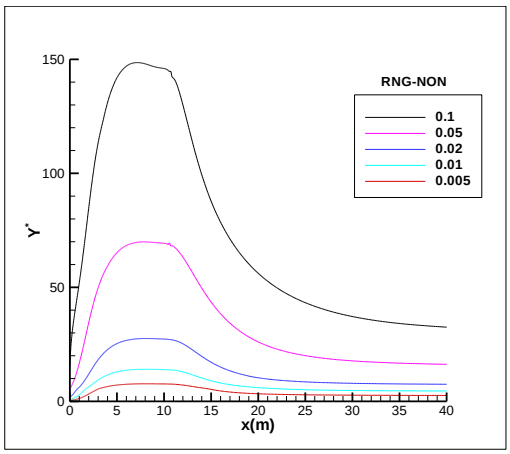

(e) Y* distribution using RNG-NON

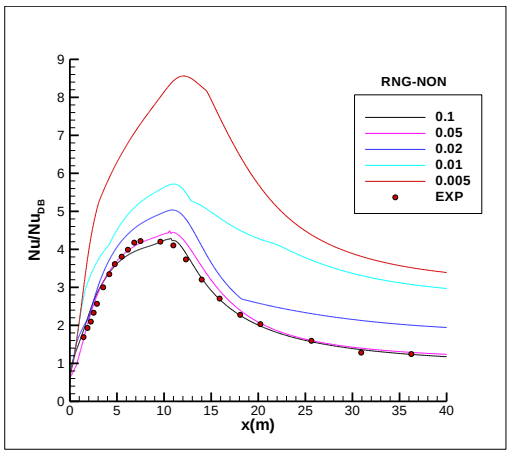

(f) Nu/Nu_{DB} distribution using RNG-NON

Figure 4.4 Y* and Nu/ Nu_{DB} distribution using STD, SCA and NON wall functions with five different wall mesh heights

By analysing the presented results, the following conclusions can be obtained:

1) For STD wall function if Y*<30, the predicted Nu/Nu_{DB} distribution obviously deviate from the measured data. This means that STD wall function would be most appropriate for Y*>30 in the whole wall domain.

2) For SCA wall function, Y* is specified as the maximum of 11.225 and the local Y*. This makes the predicted Nu/Nu_{DB} distribution much more stable compared with STD wall function.

3) For NON wall function if Y*<30, the predicted Nu/Nu_{DB} distribution presents obvious deviations from the measured result. If Y*>30, the predicted Nu/Nu_{DB} distribution gives the best coincidence with the experimental data.

As a result, 0.1m is adopted as the first layer mesh height for its computed Y* is greater than 30, from which the wall function starts to work properly. Figure 4.5 presents the comparison of Nu/Nu_{DB} distribution using different wall functions with the first layer mesh height 0.1m.

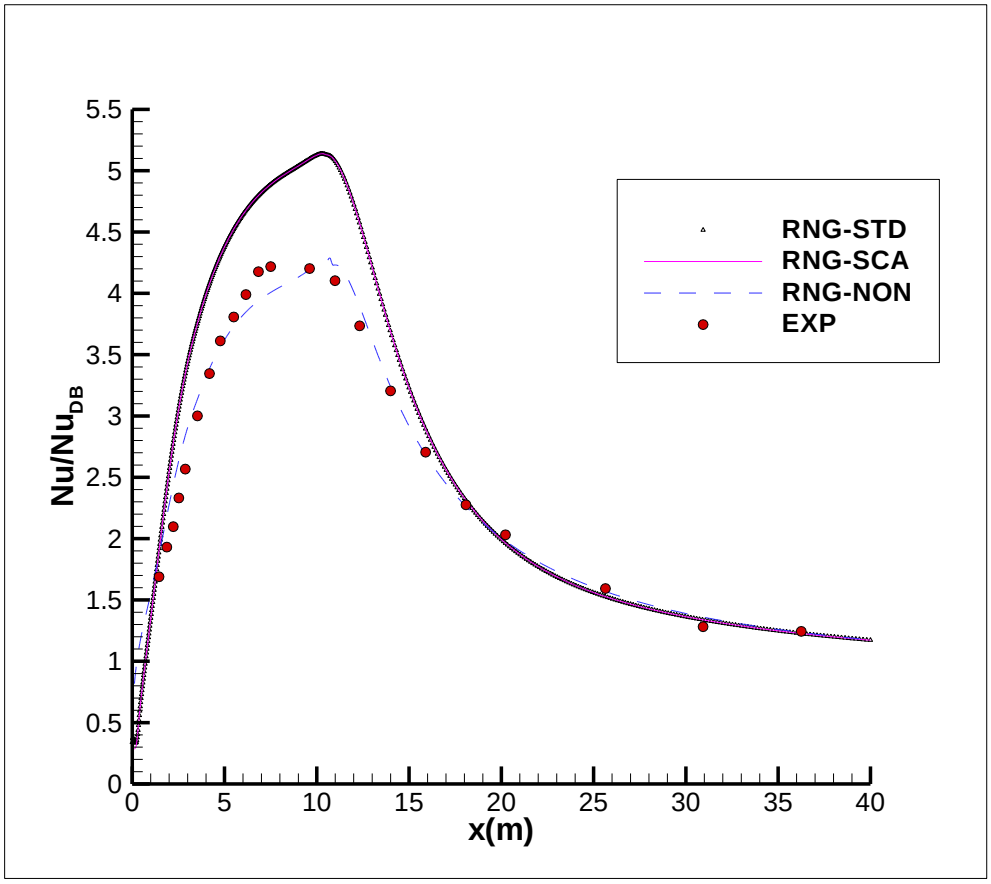

Figure 4.5 Comparison of Nu/ Nu_{DB} using different wall functions with the wall mesh height 0.1m

As it is seen from Figure 4.5, it can be concluded that Non-Equilibrium wall function predicts the best wall heat transfer compared with Standard and Scalable wall functions.

In order to get the combination effects of the turbulence model and Non-Equilibrium wall function, Standard (STD), RNG and Realisable (REA) *k-ε* turbulence models are combined with Non-Equilibrium wall function. The result is plotted in Figure 4.6.

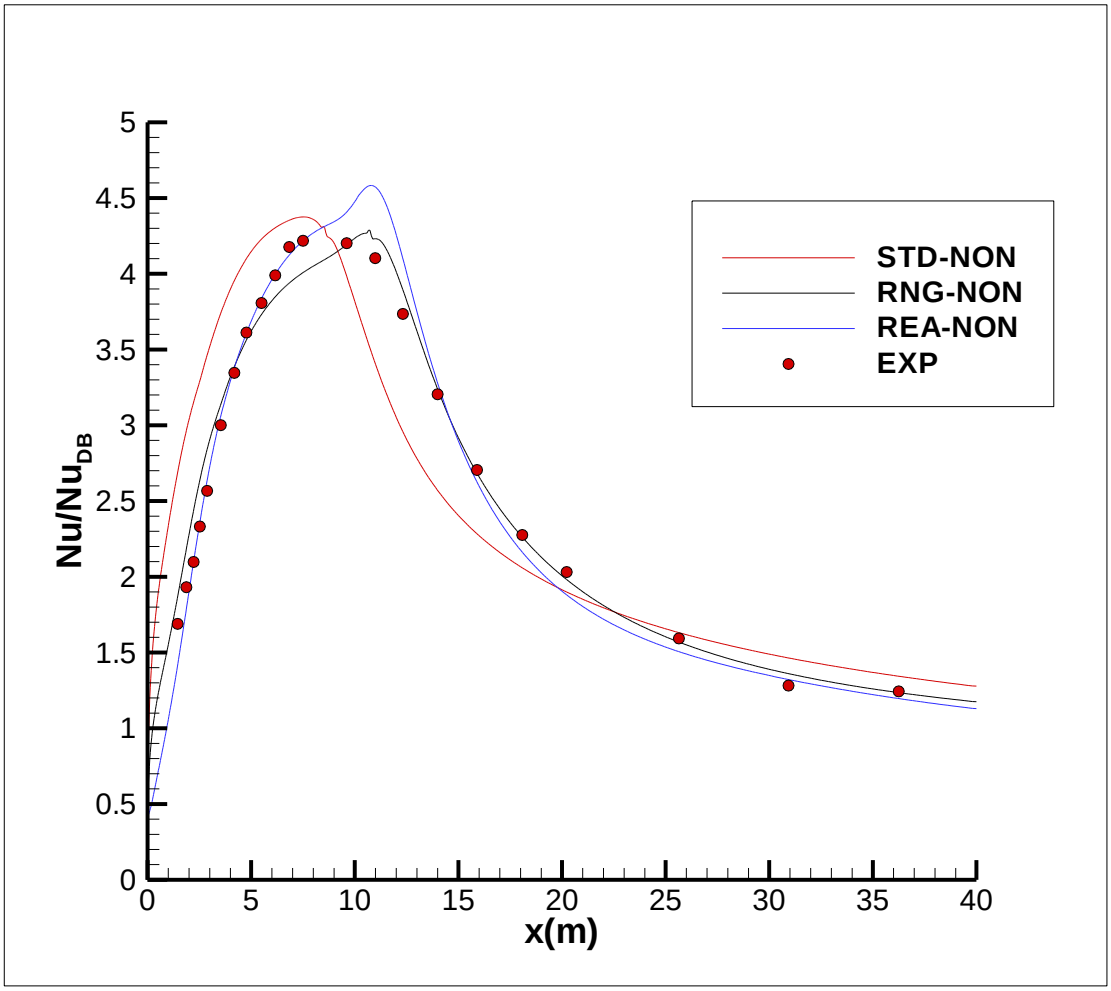

Figure 4.6 Comparison of Nu/ Nu_{DB} using different turbulence models combined with Non-Equilibrium wall function

As it is seen from Figure 4.6, it can be concluded that RNG and REA *k*-*ε* turbulence models combined with Non-Equilibrium wall function can predict similarly better wall heat transfer results than the Standard *k*-*ε* turbulence model.

4.2.3 Conclusions and Discussions

To sum up, to obtain accurate heat transfer results in the numerical simulation:

1) Y* should be greater than 30 to make sure the wall function works properly.

2) RNG or Realisable k-ε turbulence model show superiority over Standard k-ε turbulence model.

3) Non-Equilibrium wall function is recommended for its consideration on the non-equilibrium effect in the near wall region.

As a result, in the following engine combustion simulations, only the Non-Equilibrium wall function is adopted and the Y* is limited larger than 30. Compared with RNG or Realisable k-ε turbulence models, Standard k-ε turbulence model would not be recommended.

4.3 Droplet Breakup of N-heptane Spray

In Eulerian coordinates, an appropriate mesh with adequate accuracy and acceptable computational cost can be obtained by making the grids finer and finer. However, that is not the case for the Eulerian-Lagrangian approach mainly for the following reasons:

1) The Eulerian-Lagrangian approach is based on the fundamental assumption that the liquid phase occupies a fairly low volume fraction, generally less than 10%-12% of the grid volume (ANSYS, 2012). If the liquid volume fraction exceeds such limit, the assumption of Eulerian-Lagrangian approach is violated and would also induce numerical instability (Dam, 2007).

2) If the mesh size is reduced too small, the droplets in each parcel would be limited. This would make the stochastic approach invalid (Dam, 2007).

3) The droplet diameters are always very small. Very fine meshes resolving the physical scales of the droplets would make the determining of the appropriate mesh impossible.

For such reasons, it was inferred by Dam (2007) that the numerical independent mesh cannot be obtained. However, this should never be the reason to induce uncertain viewpoint and drop the efforts to minimise such uncertainties. For the reason that the spray-mesh interaction would introduce the major uncertainty for the spray simulation, it is necessary to determine the best mesh which would be able to accurately resolve the gas phase development near the nozzle Lucchini et al. (2011). The numerical investigations to obtain an appropriate mesh which fulfils the following requirements should be carried out:

1) Adequate accuracy.
2) Acceptable computational cost.

3) Abidance of the Eulerian-Lagrangian assumption, thus low fluid volume fraction.

4) Stochastic effect is valid or rooted out.

To validate the injection process and finally obtain the guidelines for the modelling of the large 2-stroke marine engine spray, the SANDIA constant combustion chamber (ECN, 2014) test is numerically investigated with different mesh scales.

4.3.1 SANDIA Combustion Chamber

The geometry of the SANDIA combustion chamber is shown in Figure 4.7. It is a bored cube with the dimension of 105mm. The fan is used to mix the ambient air in the chamber uniformly at the time of injection. The fuel spray is evaporated without combustion, thus the spark plugs are not working.

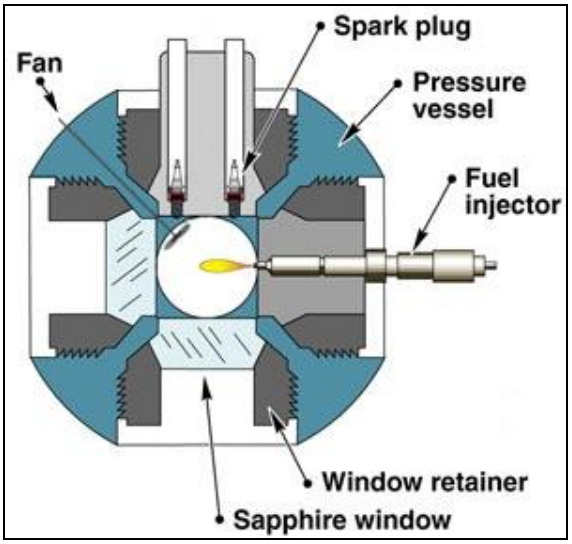

(a) Cross-section of the combustion vessel

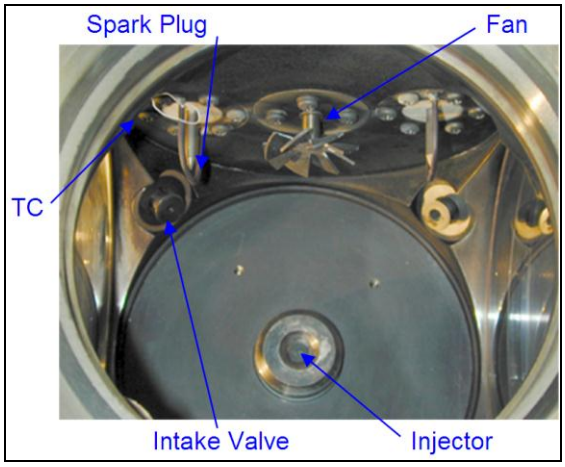

(b) Inside of the combustion vessel

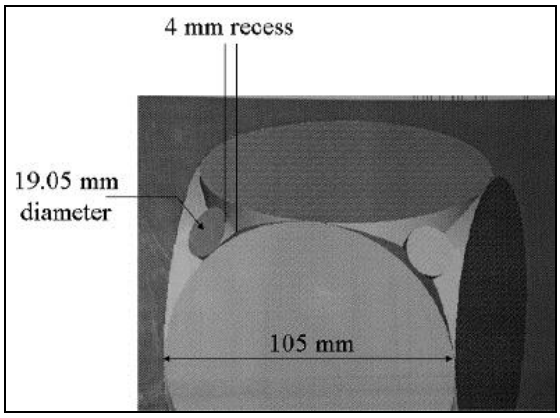

(c) Outside of the combustion vessel

Figure 4.7 Geometry of SANDIA combustion chamber

The injector with a 0.1mm orifice is installed at the centre of one port as shown in Figure 4.7(b). The injected fuel oil is 100% n-heptane (C_7H_{16}) with the density of 613kg/m^3 and the temperature of 373K. The injection profile is given in Figure 4.8. The composition of the bulk gas at diesel injection time is listed in Table 4.1. Table 4.2 summarises the bulk gas initial conditions and the fuel nozzle working conditions (ECN, 2014).

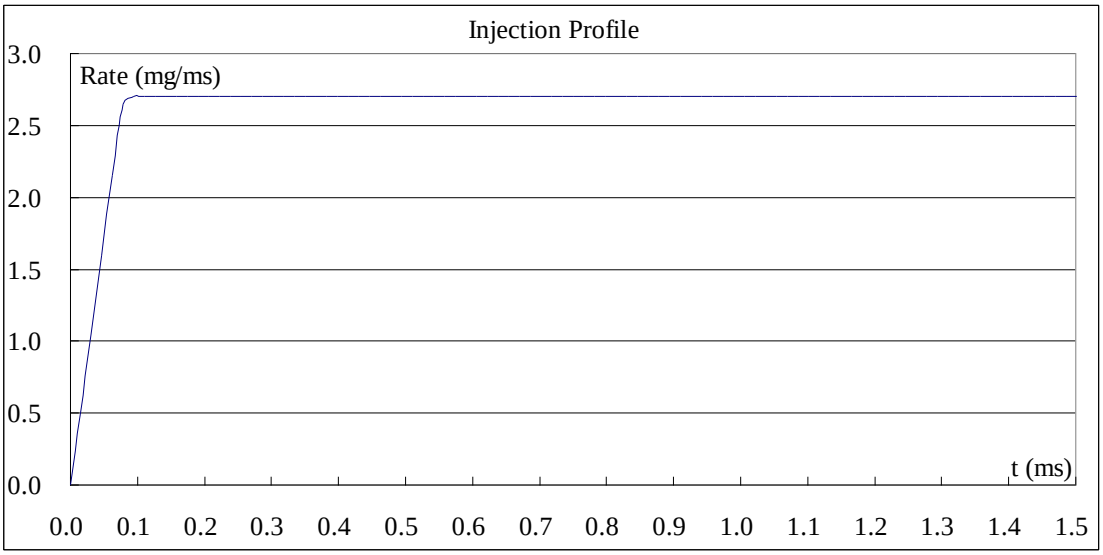

Figure 4.8 Injection profile

Table 4.1 Composition of the bulk gas at the time of injection

Species	O_2	N_2	CO_2	H_2O
Percentage (%)	0	89.71	6.52	3.77

Table 4.2 Bulk gas and the fuel nozzle setups

bulk gas temperature (K)	976.85
bulk gas density (kg/m^3)	14.80
pressure difference between injector and ambient gas (MPa)	150.00
ambient pressure (MPa)	4.33
discharge coefficient C_d	0.80
area contraction coefficient C_a	0.86

4.3.2 Mesh Configurations

To make the geometry simpler, the computation domain can be modelled as a cube with the effective dimensions of 108mm considering the recessing of the windows (ECN, 2014). Referring to the mesh schemes and the corresponding results in Lucchini et al. (2011), three different meshes with scales ranging from 2mm to 0.5mm are generated using the local adaptive refinement. The coarsest mesh is uniform with the scale of 2mm and the median one with the adapted scale of 1mm from the former uniform mesh. The finest mesh is adapted with 0.5mm scale from the adapted 1mm scale mesh. Figure 4.9 displays the cross sections of three meshes at the injection direction. The mesh numbers of them are listed in Table 4.3.

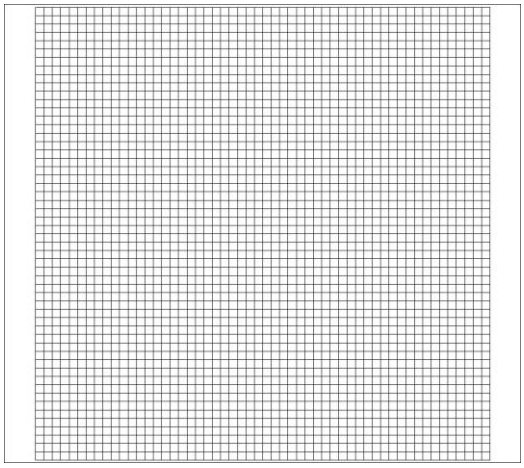

(a) Uniform 2mm scale mesh (Mesh 1)

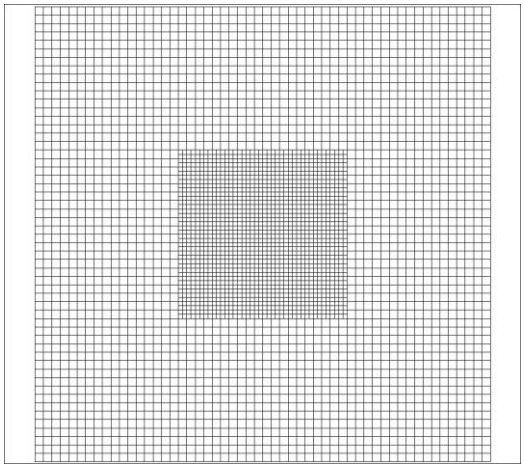

(b) Adapted 1mm scale mesh (Mesh 2)

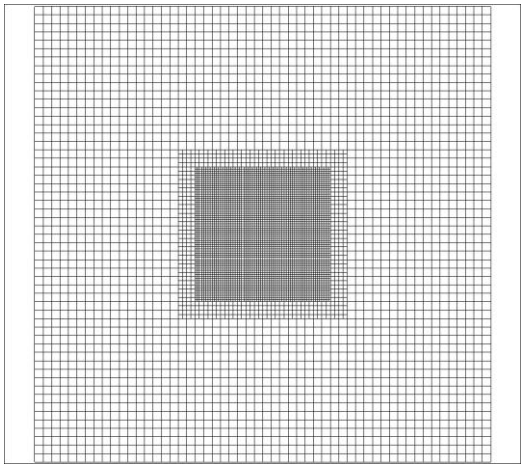

(c) Adapted 0.5mm scale mesh (Mesh 3)

Figure 4.9 Cross structures of three different meshes

Table 4.3 Minimum mesh size and corresponding mesh number

Mesh	Minimum Size	Mesh Number
1	2	157,464
2	1	308,664
3	0.5	1,082,808

In this case, smaller scale, as 0.25mm is not used to generate the finer meshes for the reason that the diameter of the nozzle is only 0.1mm. If 0.25mm scale mesh is used, the Eulerian-Lagrangian assumption would be violated for the high droplet volume fraction. The results produced by the 0.25mm scale mesh in Lucchini et al. (2011) confirm such consequence.

4.3.3 Solver Setup

The simulation starts at 0 ms and ends at 1.5 ms. The time step size is specified as 5×10^{-4}ms, the same as that used in Lucchini et al. (2011). In the mesh test calculations, the coalescence of the droplets is not considered and the breakup is computed using KHRT model (B0=0.61, B1=10). The setups of the solver in mesh test calculations are summarised in Table 4.4. Table 4.5 lists the injection properties.

Table 4.4 Solver configurations

Turbulence	Turbulence Model	RNG k-ε
	RNG Option	Differential Viscosity Model
	Near-Wall Treatment	Non-Equilibrium Wall Function
Discrete Phase Model	Drag Law	Dynamic Drag
	Coalescence	Off
	Breakup	KHRT (B0=0.61 B1=10)
Equation Of State	Real Gas Peng-Robinson	
Droplet Vaporisation Model	Diffusion-Controlled	

Table 4.5 Injection properties

Injection Type	Solid Cone
Particle Streams	20
Initial Particle Diameter (mm)	0.10
Initial Particle Velocity (m/s)	650.75*
Solid Cone Half Angle (degree)	15.00
Inner Cone Radius (mm)	0.05
Mass Flow Rate (mg/ms)	As shown in Figure 4.8

* The velocity coefficient:

$$C_v = \frac{C_d}{C_a} = \frac{U}{\sqrt{\frac{2\left(P_{inj} - P_{amb}\right)}{\rho_l}}} = \frac{U}{\sqrt{\frac{2\times150\times10^6}{613}}} = \frac{0.80}{0.86} \tag{4.8}$$

The values of C_d and C_a were tested by ECN (2014).

Thus, the velocity of the injected droplets U would be 650.75m/s.

4.3.4 Mesh Test Results

The calculated liquid penetrations with different mesh scales are summarised in Figure 4.10 and compared with the experimental data. The liquid penetrations reach constant values for all three different mesh scales because of evaporation. It can be noticed that the liquid penetrations predicted with these three mesh scales give very good coincidence（≈3-4 mm), even though the predicted results present some discrepancy compared with the experimental data 9 mm. Compared with the 1 mm and 0.5 mm scale meshes results, the 2 mm scale mesh presents the tiny unstable behaviour at the initial injection stage. It can be concluded that for the prediction of the liquid penetration, any of the currently used three mesh scales is appropriate.

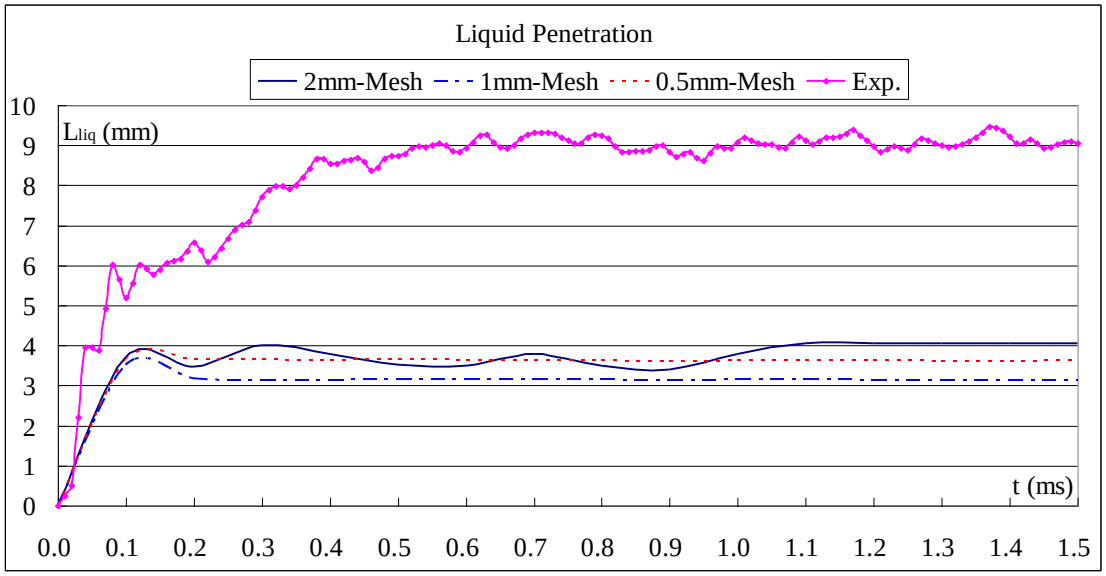

Figure 4.10 Comparison of computed liquid penetrations using three mesh scales and experimental data

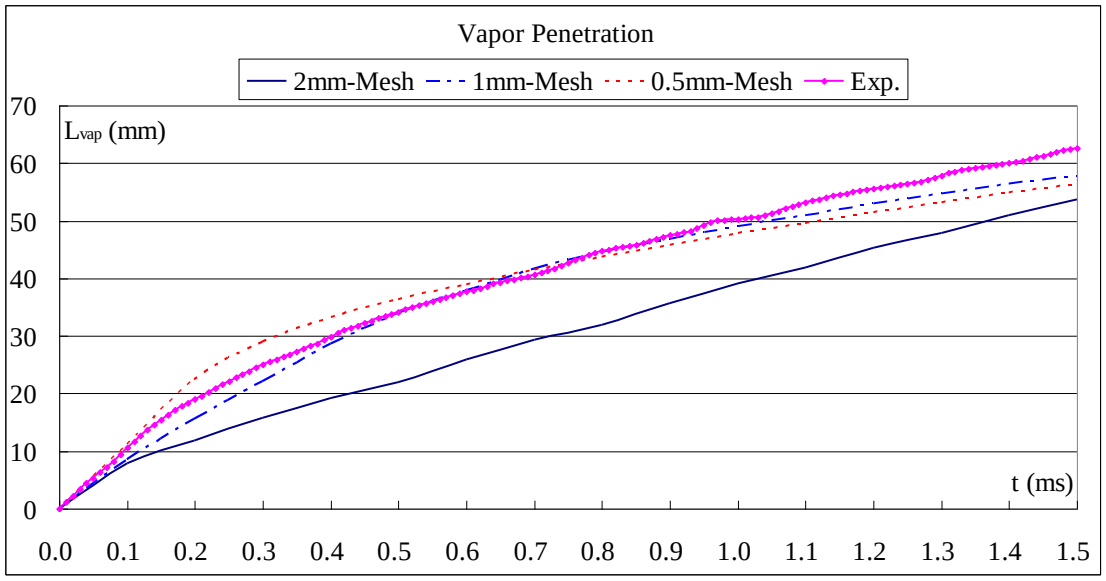

Figure 4.11 Comparison of computed vapour penetrations using three mesh scales and experimental data

Figure 4.11 compares the computed vapour penetrations with three different mesh scales and the experimental data. It can be seen that the predicted vapour penetration length of

2mm-Mesh presents obvious discrepancy compared with the experimental data. On the contrary, the predicted vapour penetration lengths using 1mm-Mesh and 0.5mm-Mesh give very good coincidence with the measured data. Considering the fact that the computation time of 0.5mm-Mesh is much longer than that of 1mm-Mesh, the 1mm-Mesh is finally adopted as the appropriate mesh for the following model tests.

4.3.5 Numerical Investigation of Different Breakup Models

A summary work has been carried out by Hawkes (2011) based on the n-heptane spray CFD simulations by nine groups from 5 different countries. It was shown that these groups adopted the different definitions for the liquid and vapour penetration lengths. Even though the reasonable agreements were obtained, it is still concluded that it is necessary to carry out the parametric studies to better expose what is not working rather to simply demonstrate that the models can work with tuning (Hawkes, 2011). In this respect, the different breakup models and their prediction performances for the droplets and vapour distribution was investigated. For WAVE and KHRT models, the parameter B1 was changed from the original recommended value 1.73 to the default value 10 to find its specific effect. The test cases included the following 6 schemes:

1) Off (No breakup model is activated.)
2) WAVE-B1=1.73 (WAVE breakup model with B0=0.61 and B1=1.73)
3) WAVE-B1=10 (WAVE breakup model with B0=0.61 and B1=10)
4) KHRT-B1=1.73 (KHRT breakup model with B0=0.61 and B1=1.73)
5) KHRT-B1=10 (KHRT breakup model with B0=0.61 and B1=10)
6) SSD (Stochastic Secondary Droplet model)

The initially injected particle diameter is set as 0.1mm. The coalescence between the droplets is not included considering its unreasonable assumption that two droplets located in the same cell would collide with each other. According to the recommendations proposed in Hawkes (2011), the liquid penetration length is defined as

a level of 0.15% local liquid volume fraction and the vapour penetration is defined as a mixture fraction of 0.001.

Figure 4.12 presents the comparison of computed liquid penetrations with the breakup models and the measurement. Figure 4.13 gives the droplets distribution predicted by different breakup models at 1.5ms. The following conclusions can be obtained from Figure 4.12:

1) It seems that none of the current test models could predict the liquid penetration very accurately.

2) Only the Off model (the breakup model is switched off) gets the unsteady liquid penetration length in the later injection stage and the predicted liquid penetration would be obviously overestimated. This is understandable for that the droplets would not break into small pieces and would not be evaporated into vapour in a short distance from the injector.

3) For the other breakup models, the predicted liquid penetrations reach the steady length, which is the same as that of the measured feature. This proves that it is necessary to include the droplet breakup for the liquid penetration prediction.

The droplets distribution predicted by deactivating the breakup models is demonstrated in Figure 4.13(a). It can be found that the injected droplets occupy a large number of the meshes in the computation domain. This verifies the overestimated liquid penetration in Figure 4.12.

For the WAVE-B1=1.73 and KHRT-B1=1.73 cases, the liquid penetrations predicted by these two models present very similar results, which is confirmed by Figure 4.13(b) and Figure 4.13(c) as well. However, the liquid penetration lengths calculated using WAVE-B1=10 and KHRT-B1=10 models show obvious discrepancy, which can be

noticed in Figure 4.13(d) and (e) as well.

From Figure 4.12, we can notice that the predicted liquid penetration with SSD model gives much better result compared with that of WAVE-B1=10 and KHRT-B1=10 models. WAVE and KHRT models can certainly give very good results by tuning the value of B1. B1 is the constant controlling how quickly the parcel will loose mass. Depending on the feature of the injector, the value of B1 can range between 1 and 60 (ANSYS, 2012). However, it is not planned to do so considering the generality of the conclusion and specificity of the following used large 2-stroke marine diesel engine nozzle. Figure 4.13(f) presents the droplets distribution predicted by SSD model at 1.5ms. It can be noticed that the droplets distribution gives no regular law as those of WAVE and KHRT models. Because of the introduction of the stochastic effects in SSD model, the droplet distribution presents random characteristics. In the nearby of the injector, small diameter droplets exist but the larger size droplets are dominant. In the far field, the small size droplets are overwhelming but some larger size droplets appear as well. Compared with the other breakup models, SSD model presents its generality and rationality in the prediction of the liquid phase behaviour.

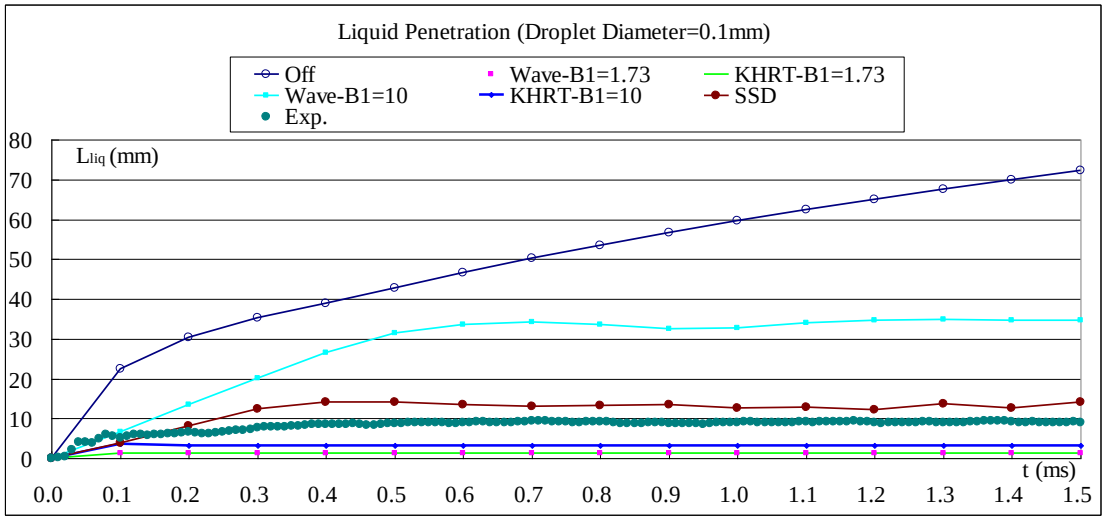

Figure 4.12 Comparison of computed liquid penetrations using different breakup models and experimental data

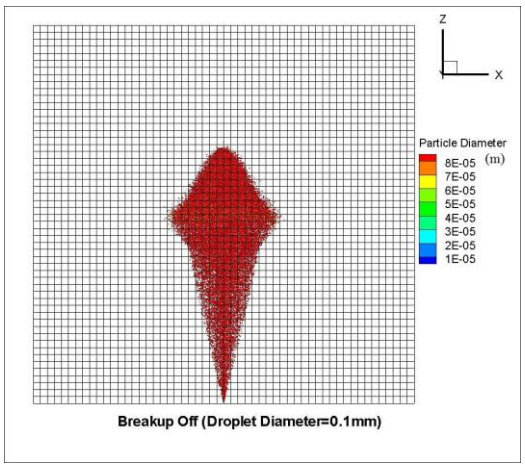

(a) Breakup Off

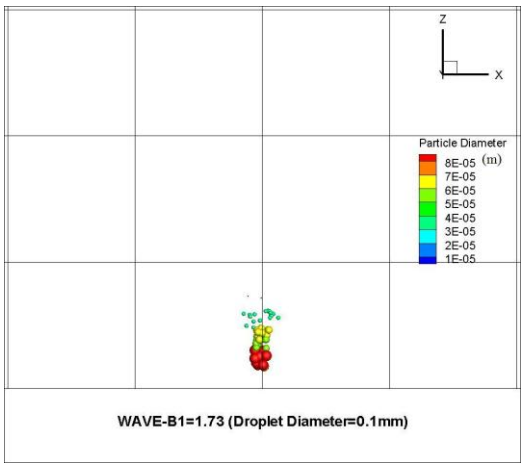

(b) WAVE-B1=1.73

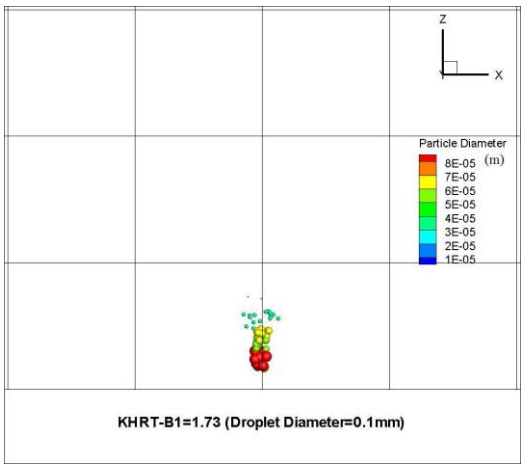

(c) KHRT-B1=1.73

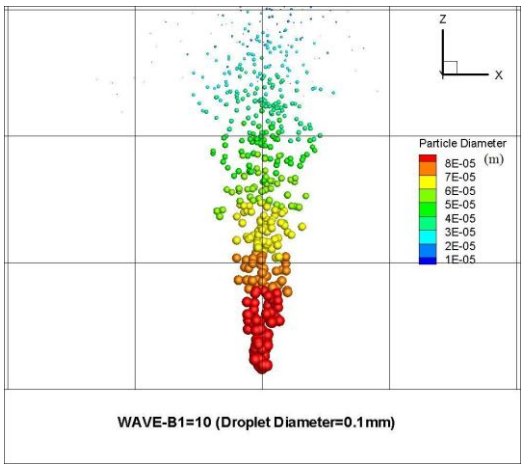

(d) WAVE-B1=10

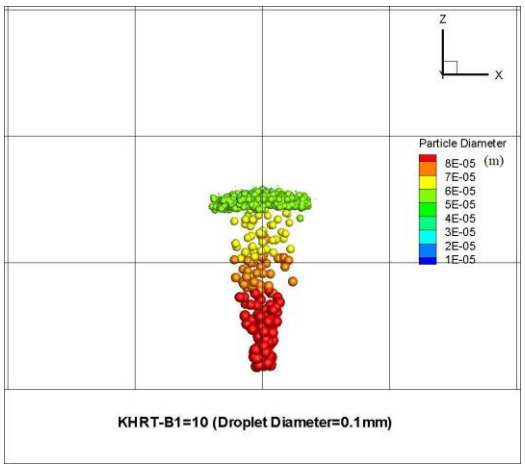

(e) KHRT-B1=10

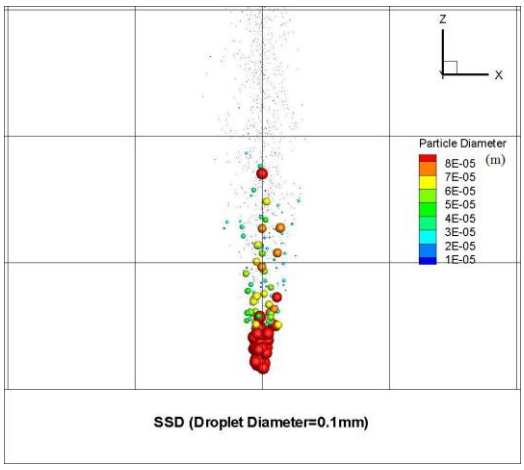

(f) SSD

Figure 4.13 Droplets distribution predicted by different breakup models at 1.5ms

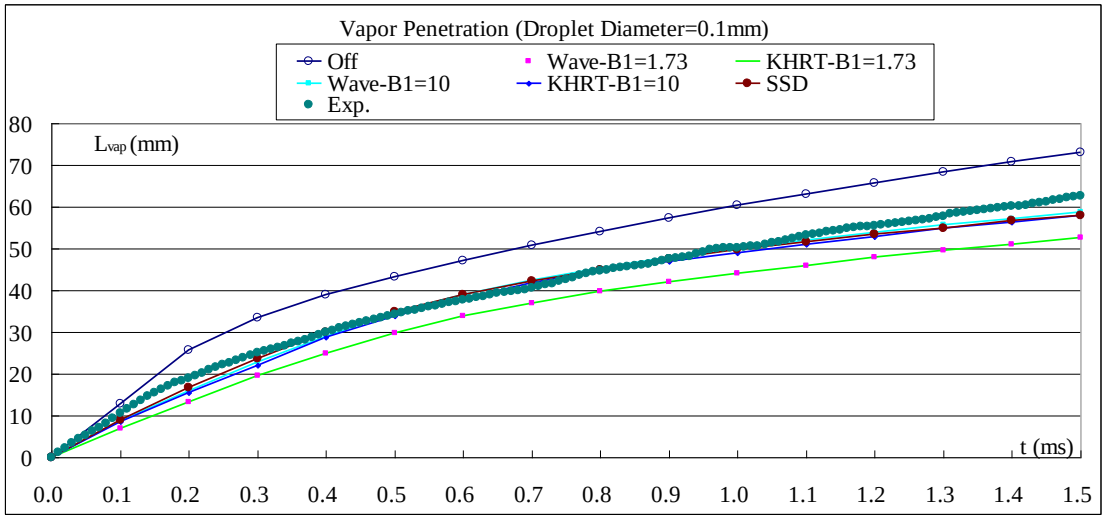

Figure 4.14 Comparison of computed vapour penetrations with different breakup models and experimental data

Figure 4.14 presents the comparison of computed vapour penetrations with the breakup models and the measurement. If no breakup model is activated, the vapour penetration would be overestimated obviously since the very initial injection stage. As to the vapour penetration under WAVE-B1=1.73 and KHRT-B1=1.73 cases, the predicted results of them almost coincide with each other, both of which underestimate the vapour penetration length compared with the measure data. For SSD, WAVE-B1=10 and KHRT-B1=10 cases, the predicted vapour penetrations present very similar results, all of which almost coincide with the experimental data.

For the diesel engine combustion simulations, it is critical to get the predicted diesel vapour well in place. Figure 4.15 presents more detailed comparison of the predicted and measured mixture fraction of C_7H_{16} at 3 different positions, namely for distances 20, 30 and 40 mm from the injector. Off model gives the mostly underestimated results. It is understandable for that the droplets would bear the C_7H_{16} mass and less vapour is produced. The other obvious discrepancy appears at the 40 mm position predicted by KHRT-B1=1.73 model which underestimates the C_7H_{16} vapour mixture fraction. This

means that the prediction results are not improved for this case, even the more complicated breakup mechanism is included. Except for these two obviously visible deviations, the other 4 models demonstrate almost the same acceptable accuracy.

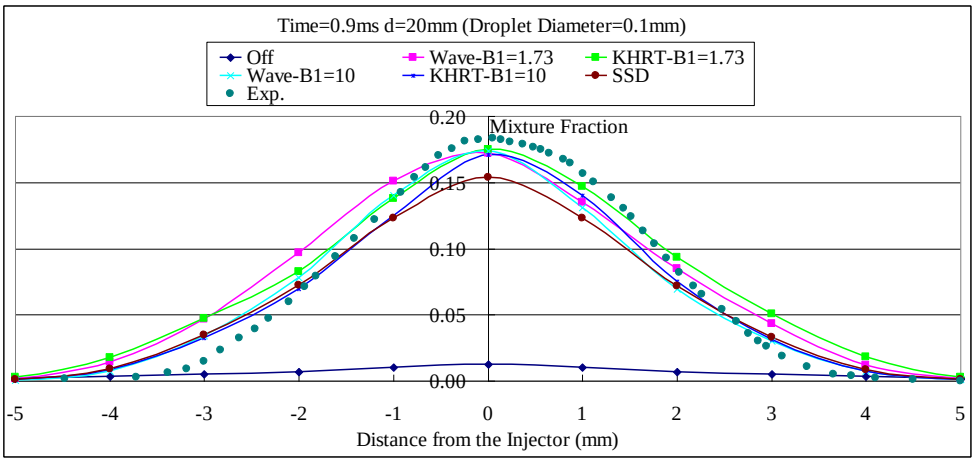

(a) d=20mm

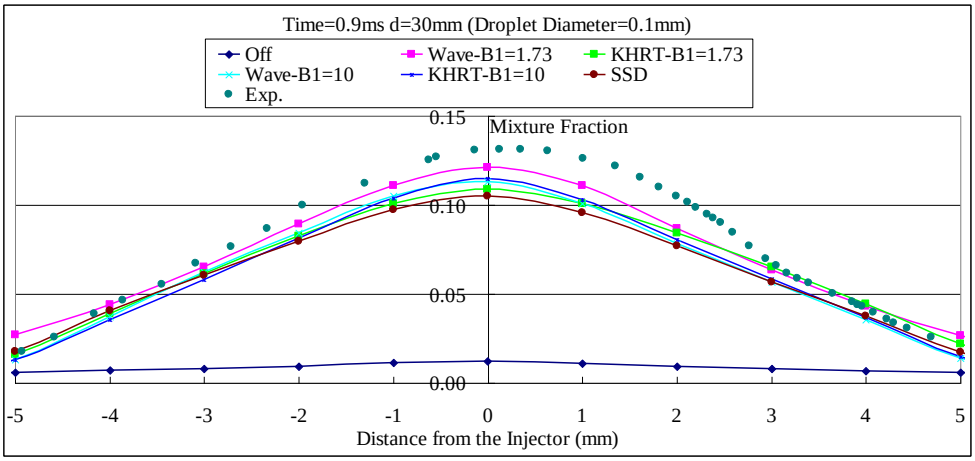

(b) d=30mm

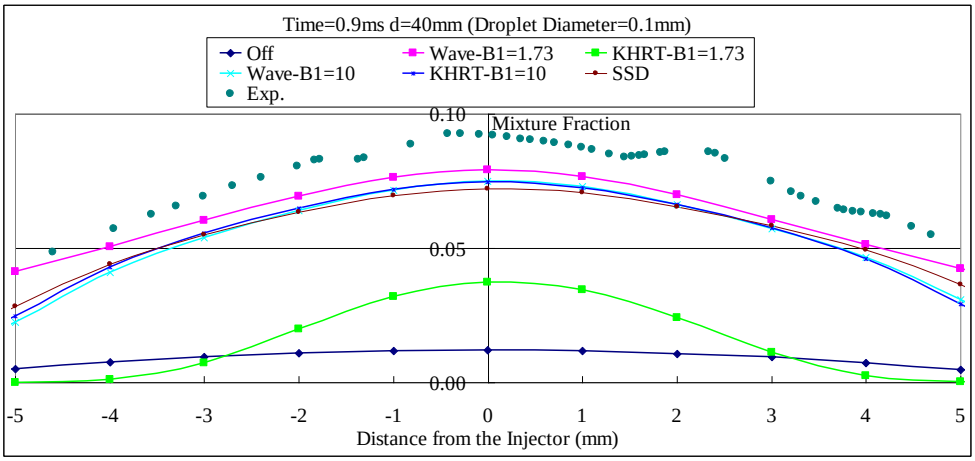

(c) d=40mm

Figure 4.15 Comparison of mixture fraction of C_7H_{16} at three different positions

4.3.6 Conclusions

In this section, the numerical investigation of the spray-mesh interaction and the droplet breakup models were carried out. Based on the presented results and analysis, the following conclusions can be obtained:

1) In view of the fulfilment of the basic assumption and computational cost, a mesh scale equates 10 times nozzle diameter would be appropriate for Eulerian-Lagrangian droplet and vapour prediction.

2) The breakup effect should be considered for the spray flow prediction.

3) None of the current test models could predict the liquid penetration very well.

4) Even though the selection of different breakup models would influence the distribution of the droplets, however, most of the tested models can get acceptable accuracy for the mixture fraction of n-heptane vapour.

5) Considering its generality, rationality and acceptable precision in the prediction of the liquid phase and vapour mixture fraction, SSD model would be a recommended breakup scheme for the prediction of spray flows.

4.4 Closure

In this chapter, to prepare for the modelling of the large 2-stroke marine diesel engine, three cases (compressible turbulent mixing layers, heat transfer in the boundary layer of a pipe expansion and droplet breakup of n-heptane spray) were calculated to determine the turbulence model, wall function, mesh size and droplet breakup models.

To sum up:

1) The mesh size with about 10 times of the injector diameter can be regarded to be appropriate for the prediction of the droplet and evaporated vapour.

2) The RNG k-ε turbulence model is accurate enough to model the turbulence in compressible mixing flows.

3) The Non-Equilibrium wall function can predict satisfactory heat transfer between the wall and the in-cylinder gases.

4) The SSD breakup model gives very good breakup predictions for its generality and rationality.

As a result, in the following engine combustion simulations, the afore tested best models would be applied.

Chapter 5 Scavenging Simulation

Based on the conclusions obtained in the heat transfer and mixing flow cases, the RNG k-ε turbulence model is combined with non-equilibrium wall function to deal with the mass, momentum and energy transports in the fully developed turbulent region and the near wall transition. As to the mesh height next to the wall, a scale of 1 cm guarantees Y* (defined in 4.2.2) greater than 30, which makes the non-equilibrium wall function keep working effectively for heat transfer. Most importantly, the mesh scale of 5-10 mm is proven to be appropriate to capture the spray breakup and evaporation.

5.1 Geometry and Setup

Accurate geometry modelling is the essential prerequisite for the whole simulation process. Figure 5.1 shows the geometry of the head and the scavenging ports of the cylinder of a large 2-stoke marine diesel engine MAN B&W S60MC-C6. For simplicity, the exhaust manifold is cut ahead of the exhaust valve housing. As a result, hexahedral meshes can be generated over the whole computational domain. The mid-plane of the cylinder and the corresponding meshes at Top Dead Centre (TDC) and the scavenging ports meshes are presented in Figure 5.2. The maximum mesh length scale is 1cm in large part of the cylinder region. The 0.5cm mesh scale is used in the scavenging ports to increase the numerical accuracy during the scavenging process. The same fine length scale is used in the combustion chamber to capture the injected fuel droplets and the corresponding convection, mixing, evaporation and combustion processes. Near the exhaust valve, 0.5cm fine scale meshes are also used to ensure numerical stability and precision in the computation, given that very strong heat and mass transfers exist during the exhaust process in this region. In order to ensure that the layering approach of the dynamic mesh model in ANSYS FLUENT working smoothly when the exhaust valve reaches the valve seat, a 0.717 mm gap between the valve and the seat is used to deal

with zero distance, i.e. when they are in contact.

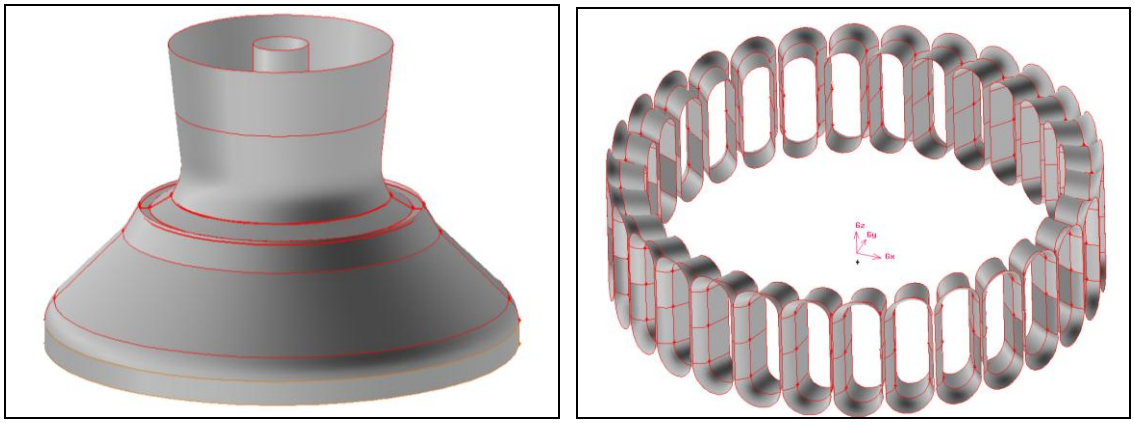

Figure 5.1 Geometry of cylinder head and scavenging ports of MAN B&W S60MC-C6

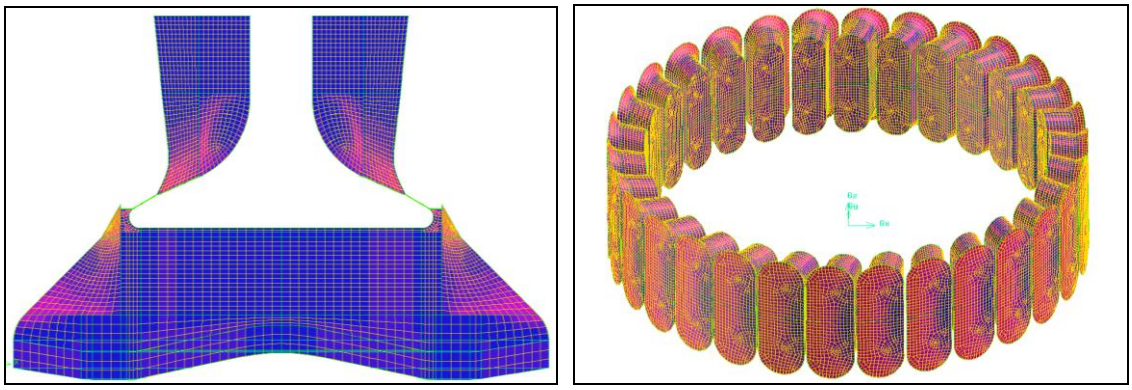

Figure 5.2 Meshes at the mid-plane and scavenging ports

Table 5.1 General engine data of MAN B&W S60MC-C6

Parameters		Unit
Cylinder Bore Diameter	0.6	m
Piston Stroke	2.4	m
Connecting Rod Length	2.46	m
Cycle Period	360	degrees
Exhaust Valve Opening/Closing Timing	112 CAD/286 CAD	degrees
Scavenge Ports Opening/Closing Timing	142 CAD/218 CAD	degrees
Crank Shaft Speed (100% MCR)	100.5	rpm
Crank Shaft Speed (75% MCR)	91.3	rpm
Crank Shaft Speed (50% MCR)	79.8	rpm
Crank Shaft Speed (25% MCR)	63.3	rpm

Table 5.1 presents the engine particulars. The piston moves from TDC (0 Crank Angle Degree (CAD)) down to BDC (180 CAD). Then it moves up from BDC to TDC (360 CAD) to complete a whole cycle with two strokes. The exhaust valve opens at 112 CAD and closes at 286 CAD. When, the piston moves down to the BDC, the scavenge ports open at 142 CAD and when it moves up to close them at 218 CAD. This process is known as scavenging, during which the exhausted gas is expelled out and the fresh air is drawn in.

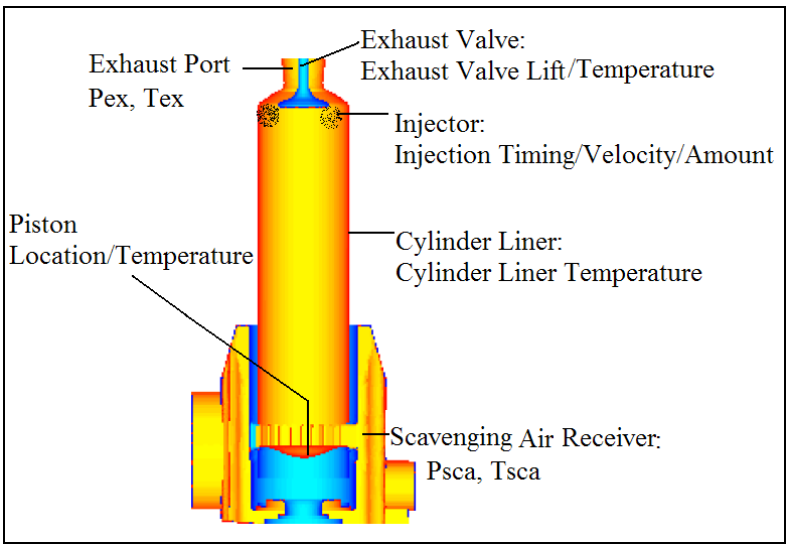

Figure 5.3 Working conditions of MAN B&W S60MC-C6

Figure 5.3 demonstrates the working conditions of MAN B&W S60MC-C6. The corresponding boundary conditions and operating data are applied to the built computation model.

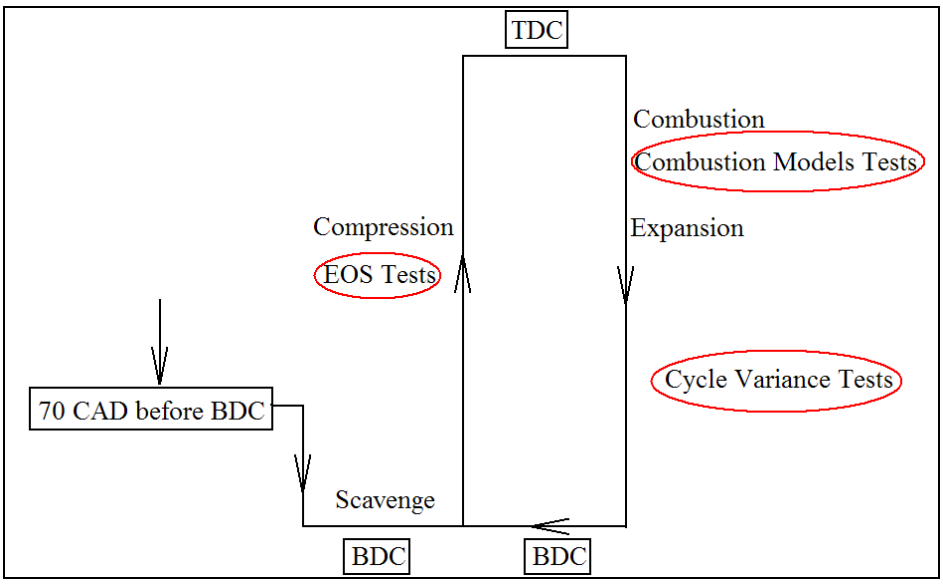

Figure 5.4 Workflow of numerical investigations

Figure 5.4 plots the workflow of the numerical investigations in the following chapters. The CFD simulation of the scavenging process ranges from 110 CAD at which the

exhaust valve has not opened yet to 290 CAD, where the exhaust valve has just closed. To save computation time, the scavenging ports would be activated at 141 CAD and deactivated at 219 CAD and the exhaust port is activated at 111 CAD and deactivated at 287 CAD. It should be pointed out that when the exhaust valve has just opened and closed, a time step of 0.01 CAD/Δt is used for 2 CAD (111 CAD-113 CAD, 285 CAD-287 CAD) to stabilise the solution process, given the very high pressure gradient between the cylinder and the exhaust port. With the exception of this, the time step size of 0.1 CAD/Δt is used to achieve a balance between numerical stability and computational cost. The same treatment was also adopted by Kim et al. (2001).

Table 5.2 Initial and boundary conditions at four different loads

MCR Load (%)	100	75	50	25
Inlet Absolute Pressure (Pa)	393800	314800	231900	153900
Inlet Temperature (K)	315	307	302	305
Outlet Absolute Pressure (Pa)	375800	297800	221900	143900
Outlet Temperature (K)	683	623	603	553
Absolute Cylinder Pressure at 110 CAD (Pa)	997788	781500	592206	379189
Temperature at 110 CAD (K)	1100	1100	1050	950

Table 5.2 lists the initial and boundary conditions at four engine loads (100%, 75%, 50% and 25%) obtained from shop tests with the exception of temperature at 110 CAD , as these were not available. As it can be seen from the results of the later combustion simulations, the temperature values at 110 CAD in Table 5.1 are very well estimated.

To make the current scavenging process simulation results usable for the following combustion simulation, the FRED combustion model is used to transport the species. It is proven that 10 inner iterations within every time step are enough for convergence of transient results in the scavenging process simulation.

5.2 Results and Analysis

5.2.1 Effect of Real and Ideal Gas Model during Scavenging

Enlightened by the analysis of Lamas et al. (2012), the ideal gas model and the Peng-Robinson (PR) real gas model are both adopted to close EOS during the scavenging process for investigating the difference between them. Figure 5.5 illustrates the comparison of calculated pressure traces using ideal gas model and PR real gas model, from which it can be noticed that the two lines almost coincide. Table 5.3 lists the corresponding values of pressure, temperature and gas mass at the start and the end of the scavenge calculation. Seeing from the deviations, one can find that the initialisation would introduce negligible mass difference at 110 CAD. At the end of the scavenge process, the deviations of the values calculated using these two models can also be neglected. The result obtained from real gas model does not present obvious superiority over that from ideal gas model due to the fact that states during this process are far from the critical point.

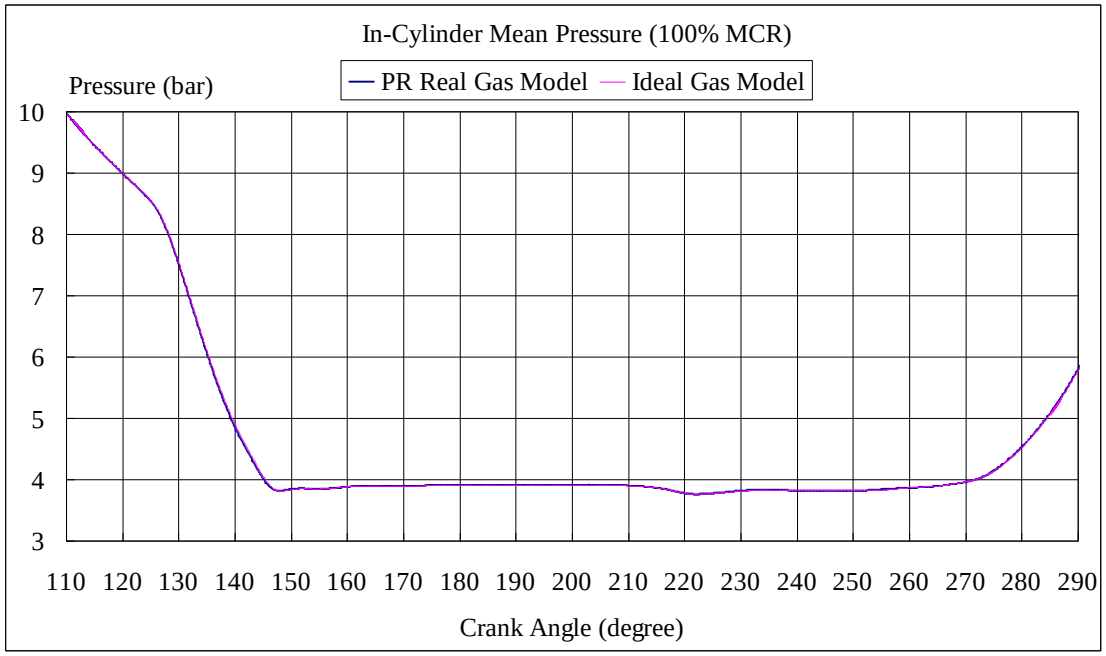

Figure 5.5 Pressure traces using ideal and real gas model during scavenging

Table 5.3 Comparison of ideal and real gas models at 110 and 290 CAD

	110 CAD			290 CAD		
	P (bar abs)	T (K)	Mass (kg)	P (bar abs)	T (K)	Mass (kg)
Ideal Gas	9.97788	1100	1.780	5.77876	408	1.639
Peng-Robinson	9.97788	1100	1.776	5.77813	403	1.657
Deviation (%)	0.00	0.00	0.25	0.01	1.16	-1.09

However, it should be noticed that the time consumed for real gas calculations is much longer than for the ideal gas model, nearly triple the latter. This result can be attributed to the use of more complex equations for the real gas model. The related properties like density, pressure and temperature need to be updated in all other equations. Thus, the whole computational cost is correspondingly increased. To make the current scavenge simulation results usable for the following more critical investigations during compression, the Peng-Robinson real gas model results are adopted to validate against the shop test data.

5.2.2 Validation of the Scavenging Process at Different Loads

The computed pressure traces at four different loads (100% MCR, 75% MCR, 50% MCR and 25% MCR) are validated against the corresponding measured data in shop tests. Figure 5.6 to Figure 5.9 present the comparison of the computed and measured in-cylinder pressure at four tested conditions. From the in-cylinder pressure, it can be concluded that the experimental data is relatively unstable during the scavenging process, given the oscillations on the pressure trace lines. However, in CFD calculations, the scavenging air pressure at the inlet and exhaust gas pressure at the outlet are set as constant values as presented in these figures. This would be one source of numerical error as mentioned in Lamas et al. (2012). In addition, the error of measuring facilities would be another source of uncertainty during the tests.

With the exception of the oscillations in the pressure traces, an obvious pressure decrease, which is also captured by CFD calculations, can be observed near 220 CAD. This decrease is caused by the closing of the scavenge ports at 218 CAD. However, the predicted pressure traces do not show the same reduction as that of the test data. Nevertheless, it can be concluded that the precision of the obtained results based on the adopted models in CFD are satisfactory.

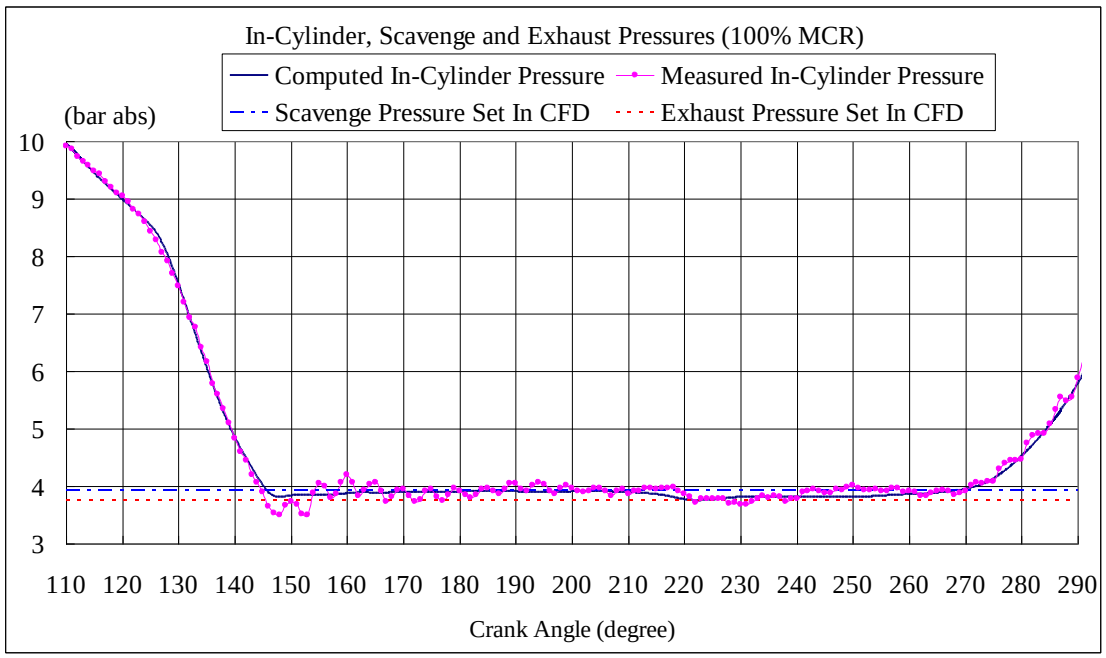

Figure 5.6 Comparison of in-cylinder, scavenge and exhaust pressure at 100% MCR

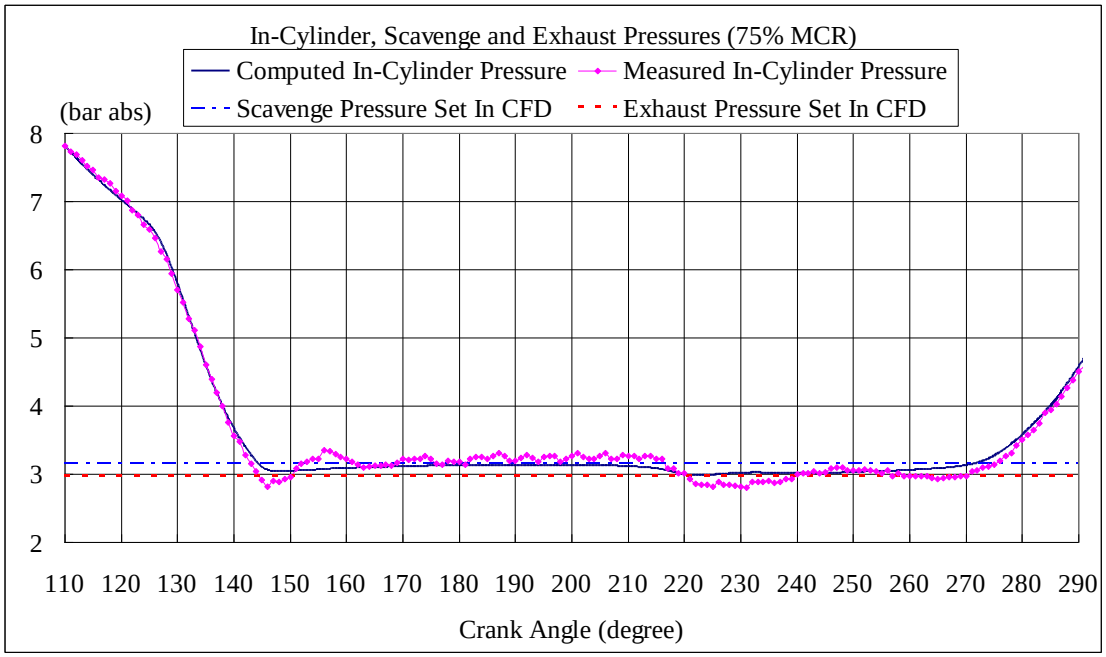

Figure 5.7 Comparison of in-cylinder, scavenge and exhaust pressure at 75% MCR

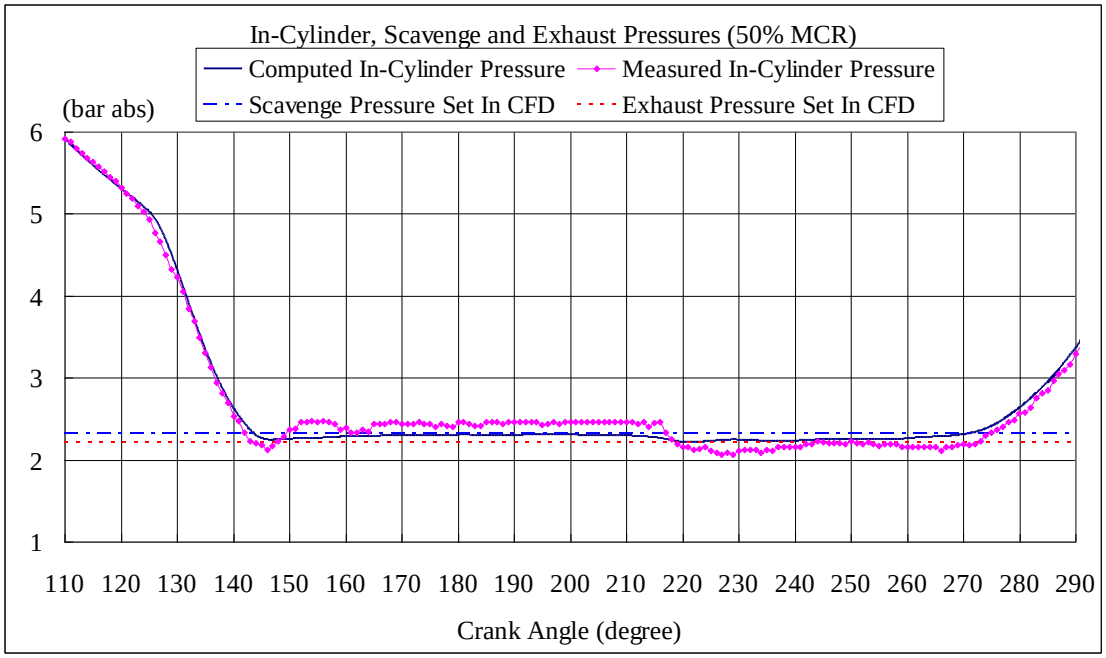

Figure 5.8 Comparison of in-cylinder, scavenge and exhaust pressure at 50% MCR

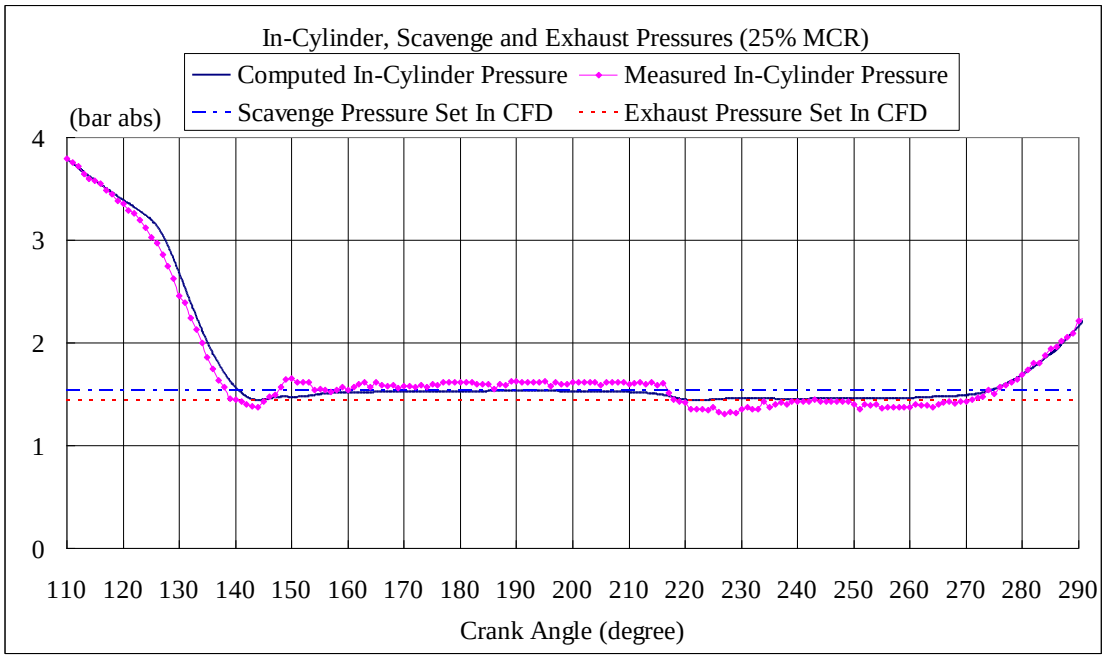

Figure 5.9 Comparison of in-cylinder, scavenge and exhaust pressure at 25% MCR

5.2.3 Analysis of the Mass Flow Rates and Velocity Fields

Figure 5.10 to Figure 5.13 show the mass flow rates through the inlet ports and outlet exhaust valve at four tested loads. The negative values in these figures represent the flow out rates. It can be seen that the flowing out through the exhaust port experiences the maximum peak before the scavenge ports are opened (near 142 CAD). As a result, the total mass, pressure and heat undergo an obvious decrease period. As the opening of the scavenge ports, reverse flow from the in-cylinder to the scavenge air receiver occurs at 100%, 75% and 50% MCR loads. However, such reverse does not exist at 25% MCR load. The reversed flow is caused by the pressure differences between the in-cylinder and the scavenge air receiver. The in-cylinder pressures at 143 CAD in 100%, 75% and 50% MCR loads are higher than the scavenging pressure. As a result, the reversed flow exists at 100%, 75% and 50% MCR loads but this is not the case for the engine load at 25% MCR. The streamlines at 145 CAD for 100% MCR and 25% MCR are presented in Figure 5.14.

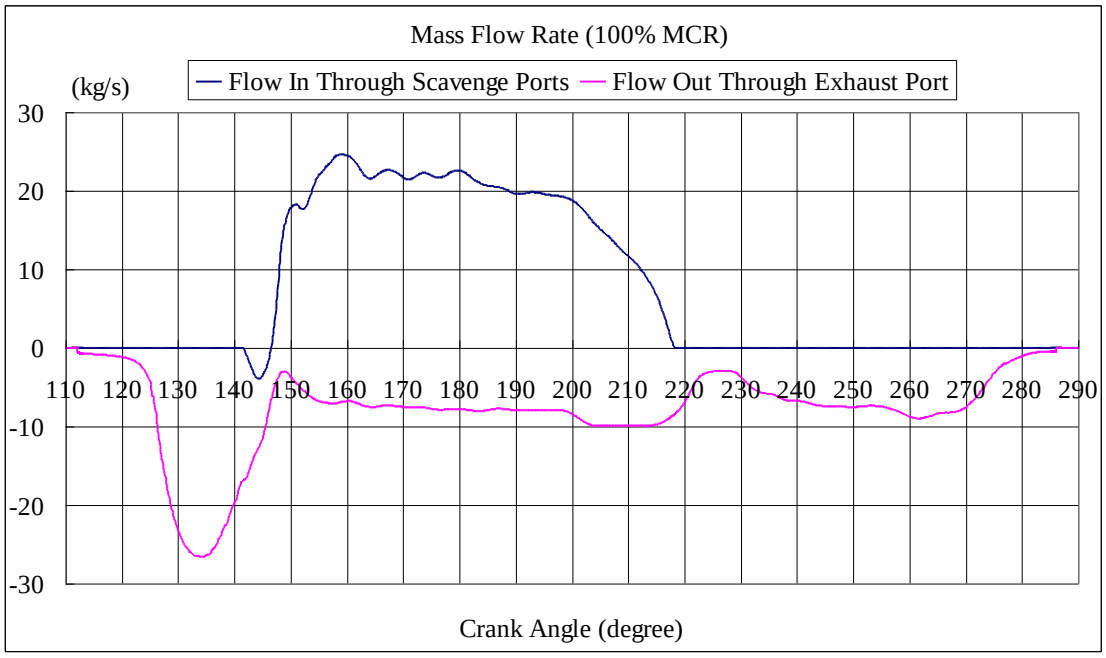

Figure 5.10 Mass flow rates at the inlet and outlet at 100% MCR

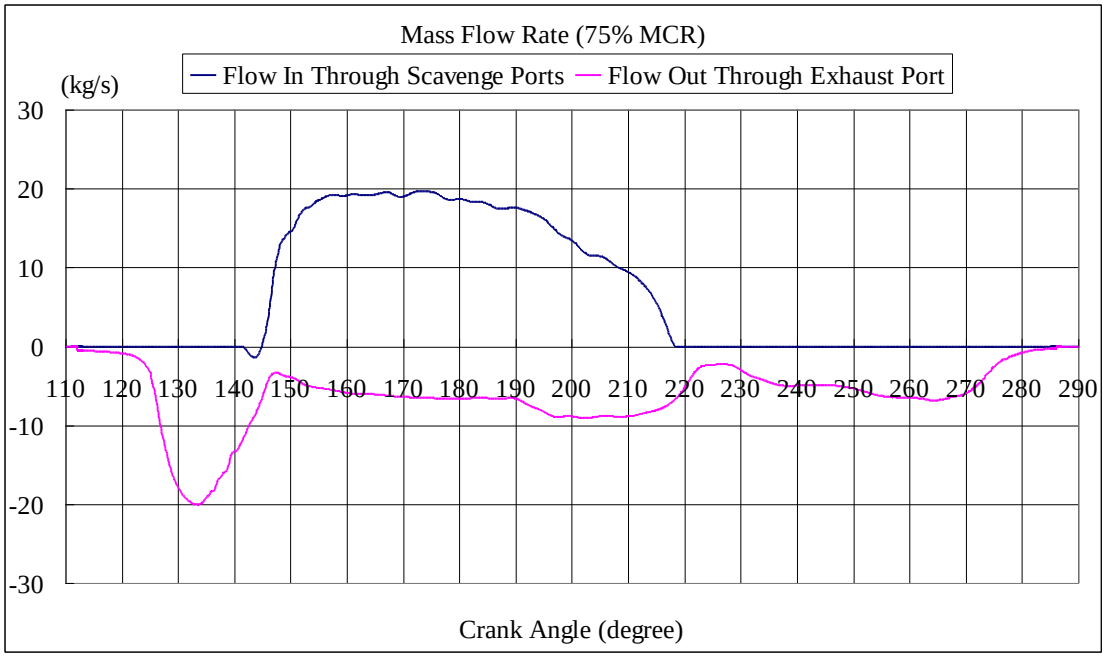

Figure 5.11 Mass flow rates at the inlet and outlet at 75% MCR

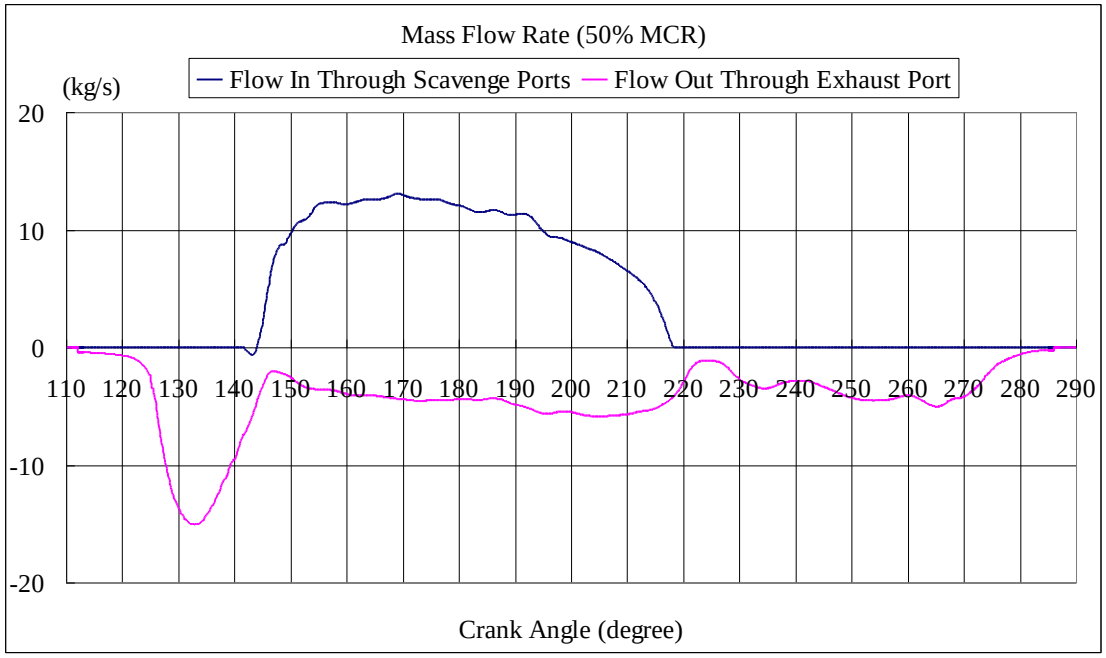

Figure 5.12 Mass flow rates at the inlet and outlet at 50% MCR

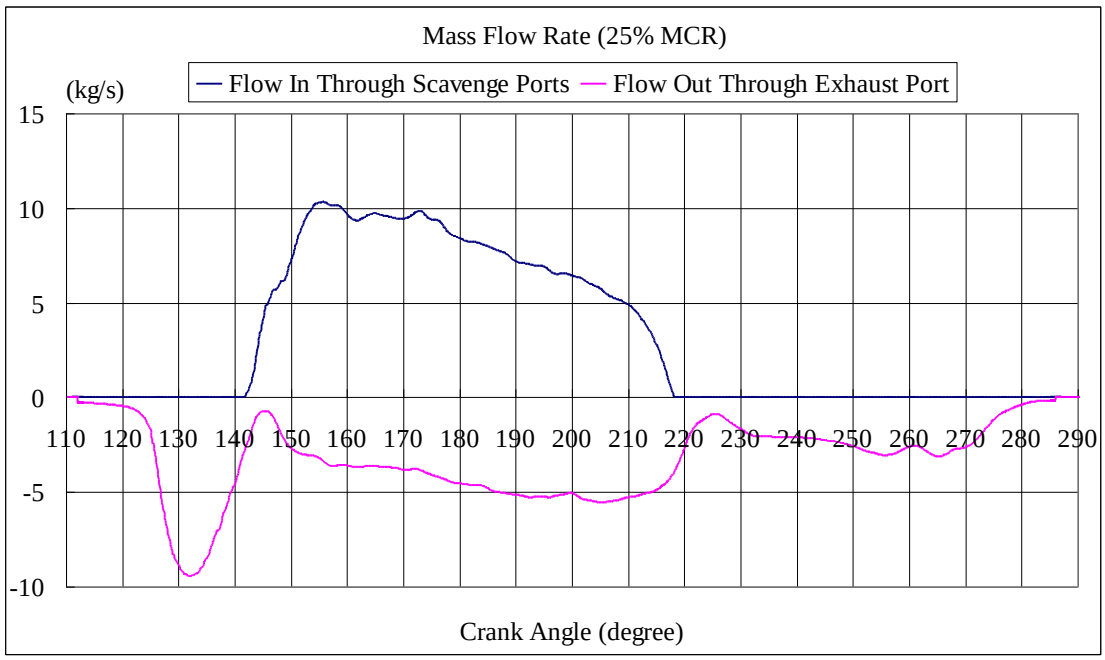

Figure 5.13 Mass flow rates at the inlet and outlet at 25% MCR

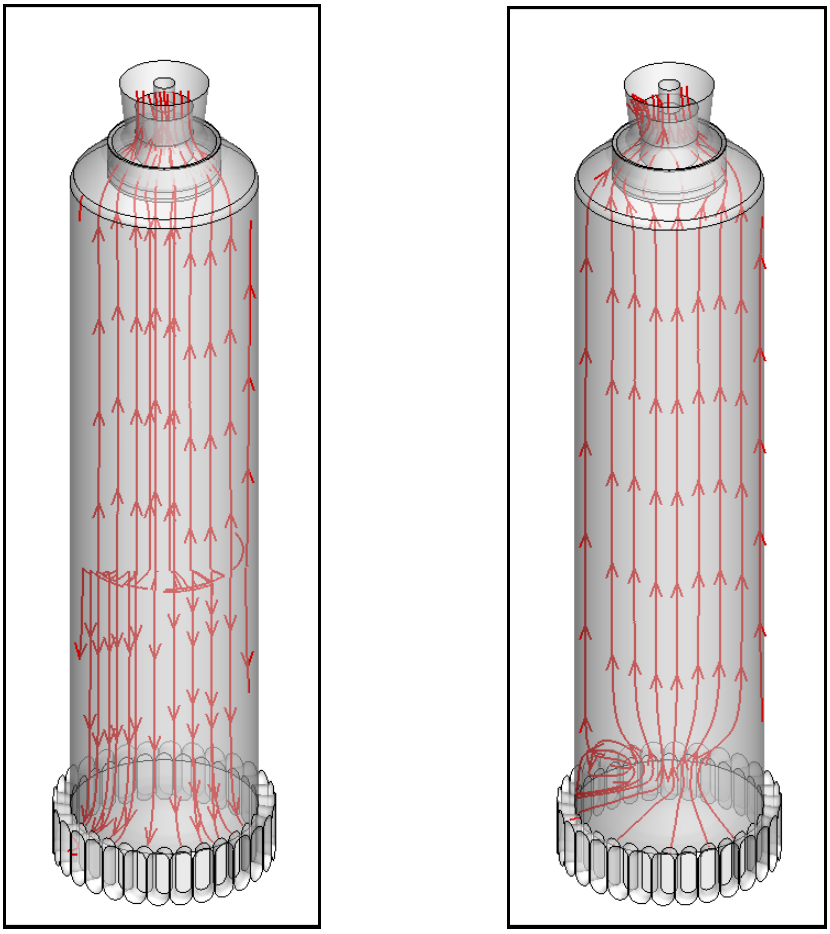

(a) 100% MCR (b) 25% MCR

Figure 5.14 Streamlines at 145 CAD for 100% MCR and 25% MCR

The streamlines of representative crank angle degrees (160 CAD, 180 CAD and 220 CAD) are displayed in Figure 5.15(a), Figure 5.15(b) and Figure 5.15(c), respectively. The strong swirling flows can be observed from the bottom of the cylinder. The swirling flow is generated by the scavenging ports, which are designed with an obliquity angle of 18° in radial directions. Such design would expel the residual gas efficiently and minimise its mixing with the inducted fresh air.

Figure 5.16 to Figure 5.18 display the flow fields at the selected three cross sections coloured in Figure 5.15(d). It can be noticed that at the initial scavenging stage, the upper flow field is nearly not disturbed by the inflow. The upper air is expelled out

without being induced in the cross directions. However, with more and more swirl flows generated, the undisturbed flows are expelled out from the exhaust port. At the final scavenging stage, the whole cylinder is completely dominated by the strong swirl flows.

The temperature variations during the scavenging process at different loads are shown in Figure 5.19. After the scavenging, the temperature of the in-cylinder air becomes slightly higher than the scavenging air temperature due to the heat transfer from the hot wall. This reflects to some extent that the scavenging efficiency is good for all cases.

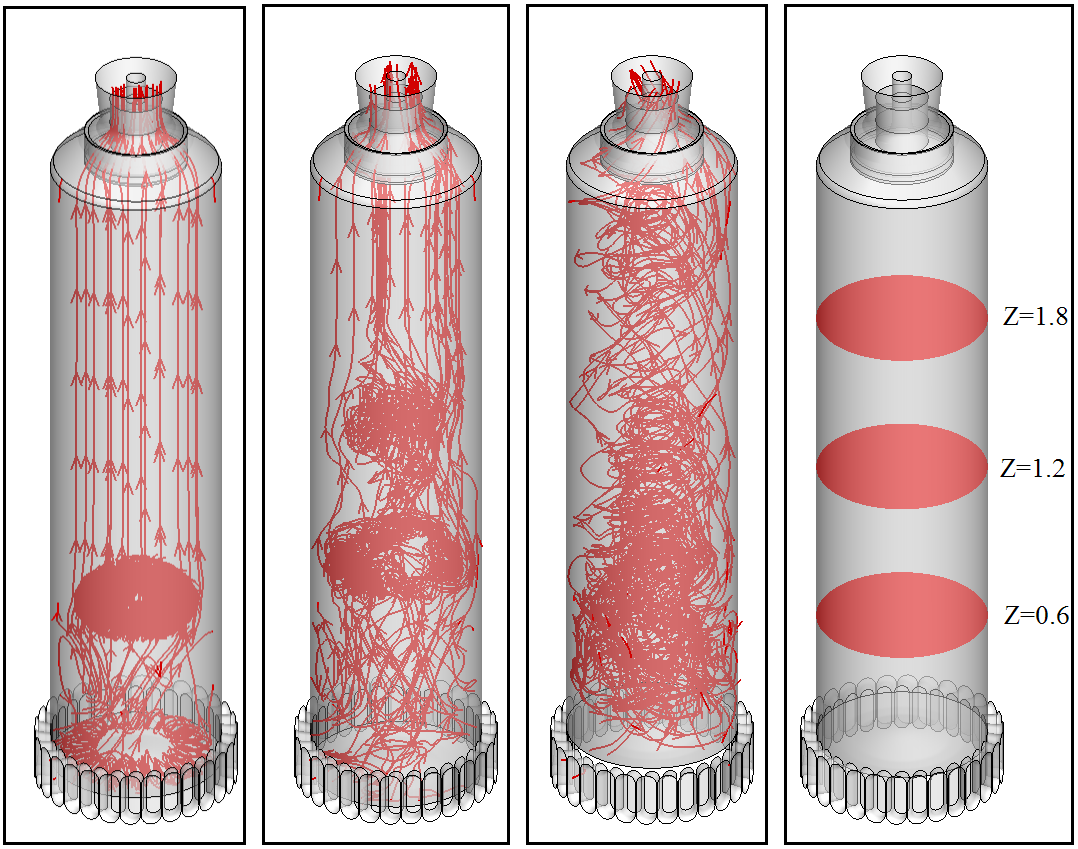

(a) 160 CAD (b) 180 CAD (c) 220 CAD (d)

Figure 5.15 Streamlines of representative crank angle degrees (160 CAD, 180 CAD and 220 CAD) and the selected cross sections to present the velocity

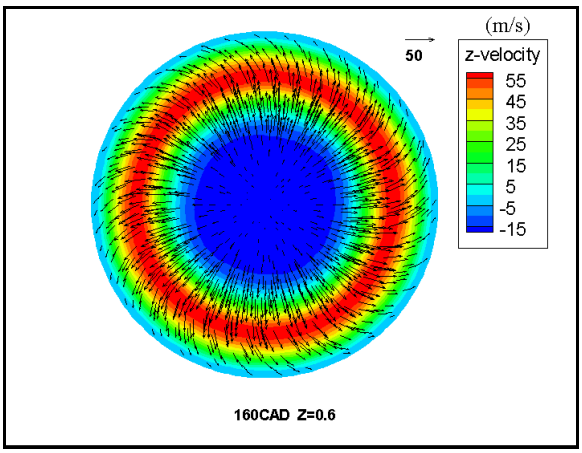

(a) Z=0.6

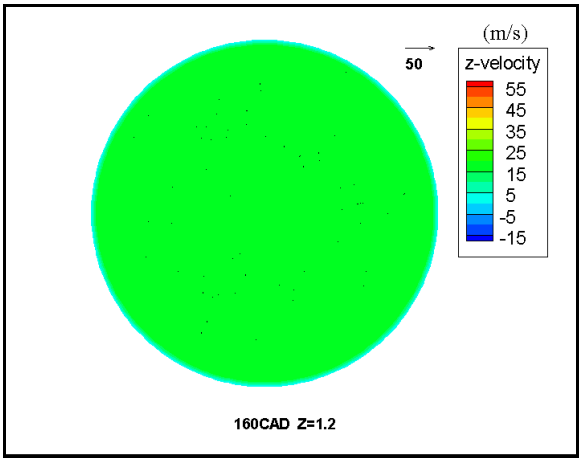

(b) Z=1.2

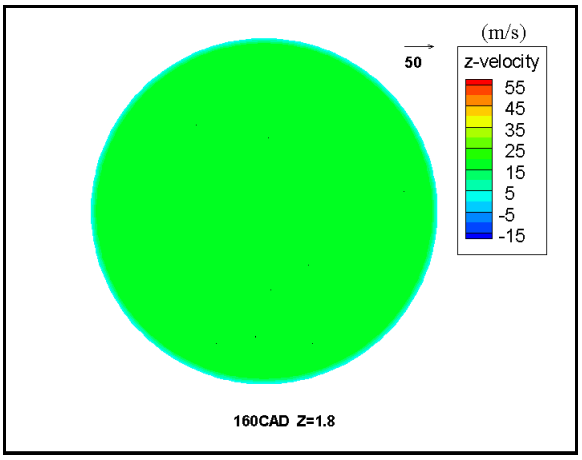

(c) Z=1.8

Figure 5.16 Flow field at three selected cross sections at 160 CAD

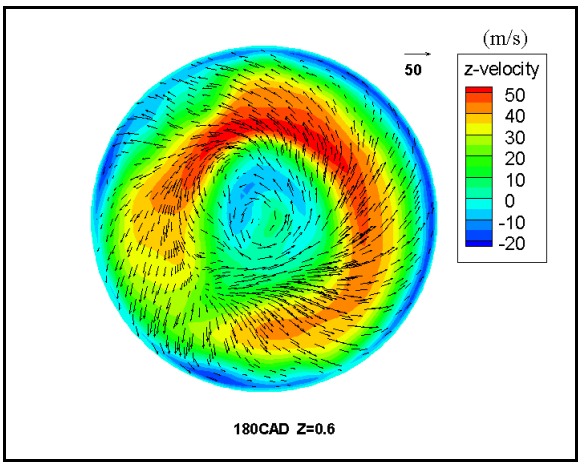

(a) Z=0.6

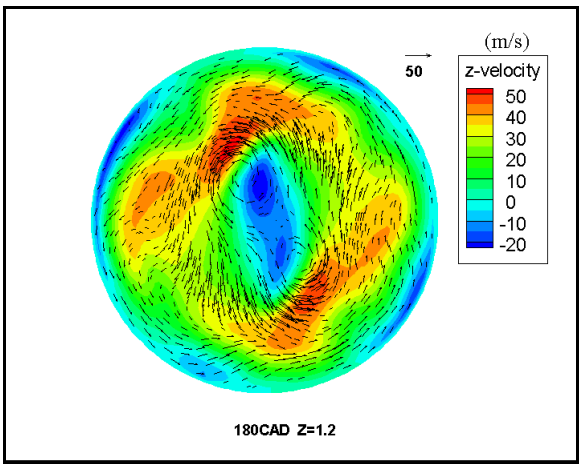

(b) Z=1.2

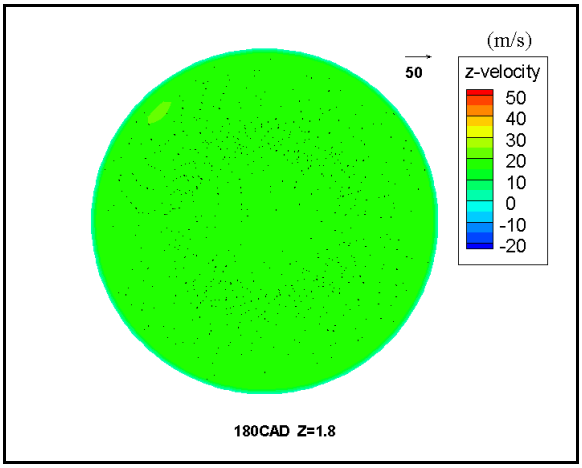

(c) Z=1.8

Figure 5.17 Flow field at three selected cross sections at 180 CAD

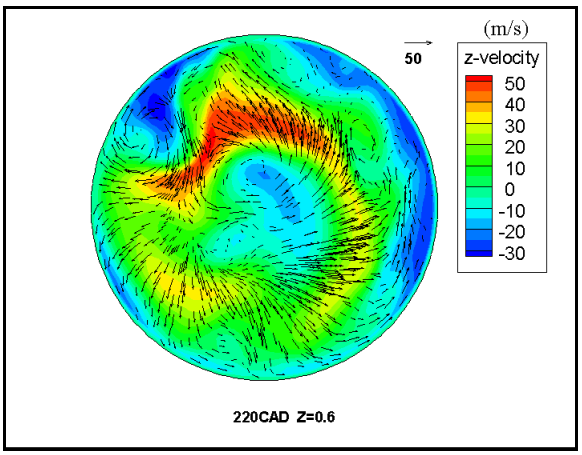

(a) Z=0.6

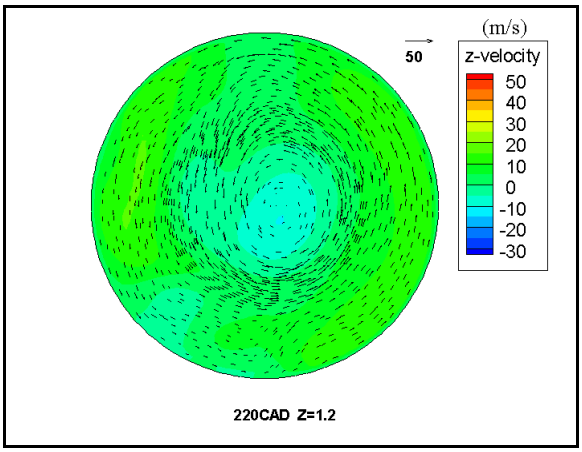

(b) Z=1.2

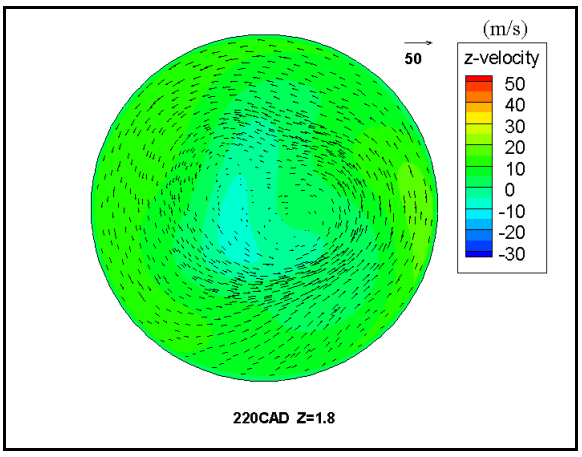

(c) Z=1.8

Figure 5.18 Flow field at three selected cross sections at 220 CAD

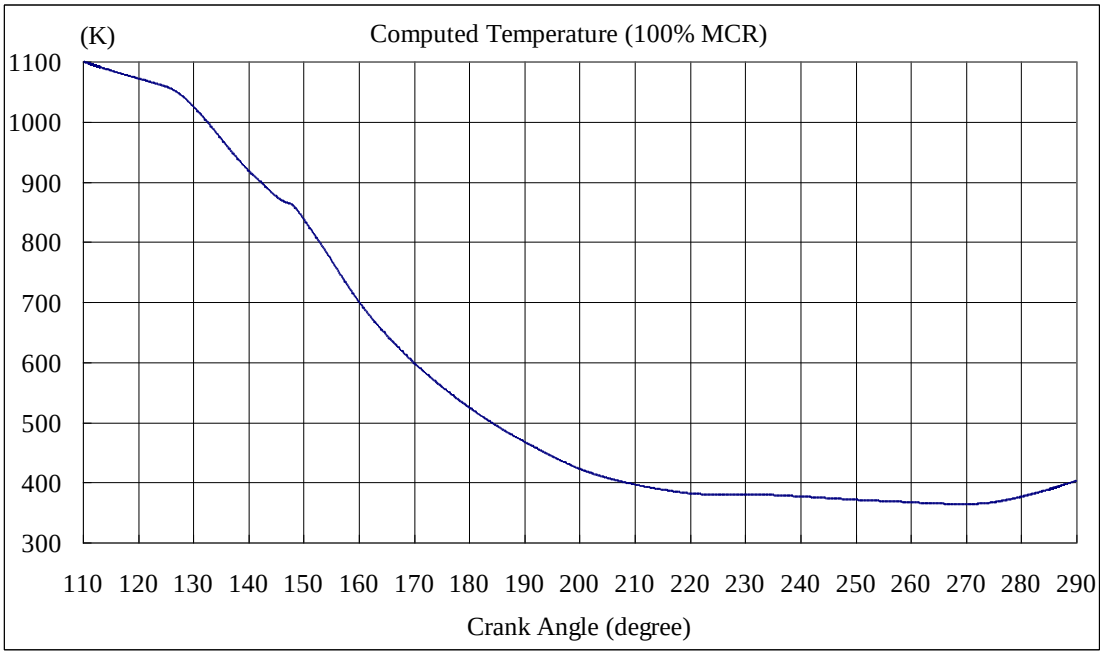

(a) 100% MCR

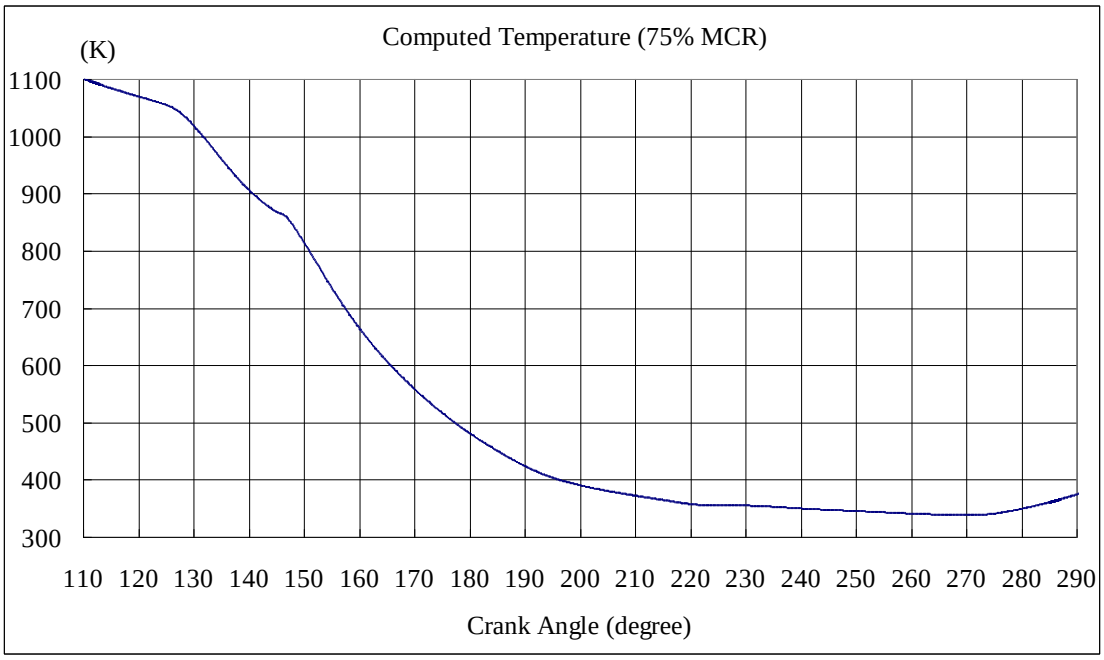

(b) 75% MCR

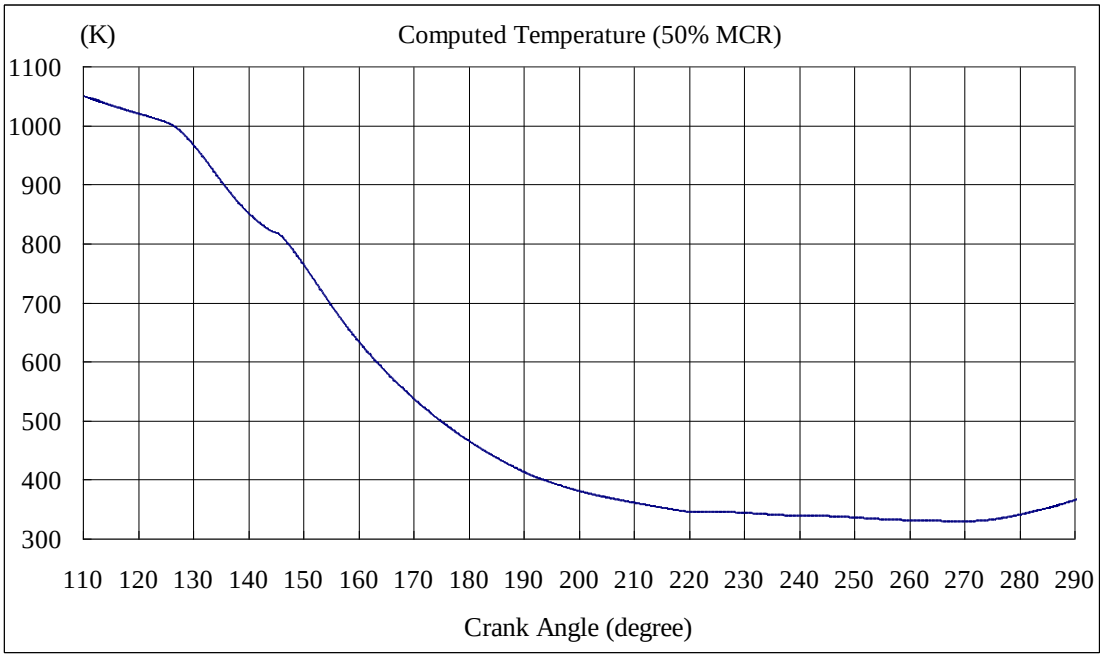

(c) 50% MCR

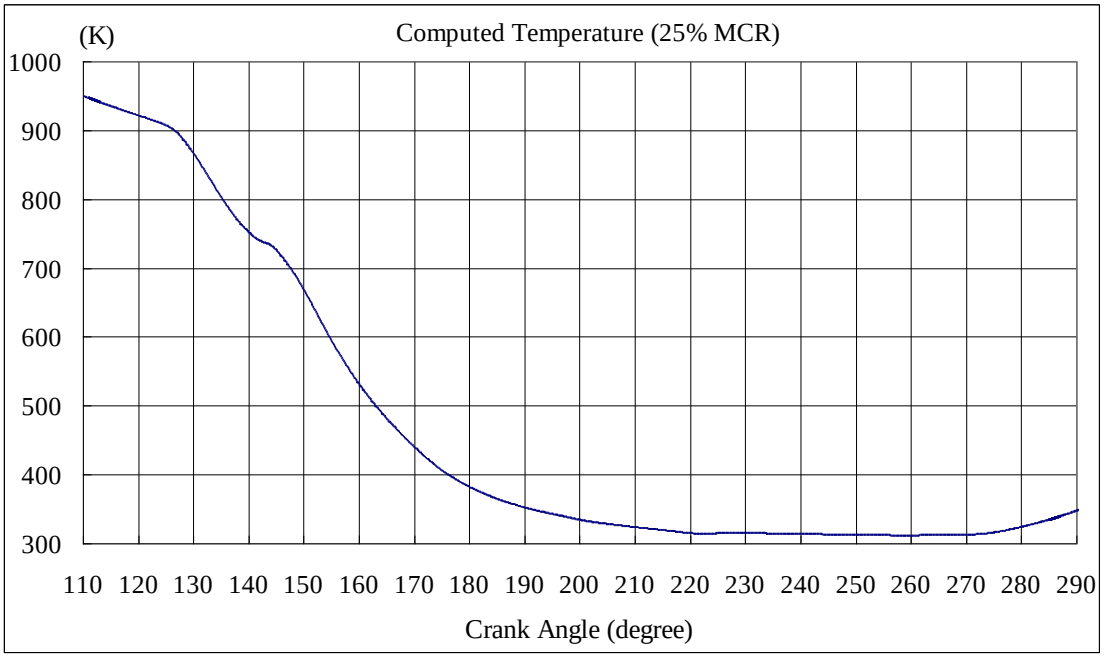

(d) 25% MCR

Figure 5.19 Temperature variations during the scavenging process at different loads

It should be noted that the data used in Chapter 5 were based on the initial tests, which

means that the non-combusted air is used and the primary assumed temperature is initialised.

5.2.4 Conclusions

The RNG k-ε turbulence model is selected to calculate the scavenging process of MAN B&W S60MC-C6. The piston and exhaust valve were controlled by the dynamic layering mesh and the scavenging transferring between the cylinder and scavenging air receiver was achieved using the mesh interface approach. The prediction results are compared with the shop test data at four different loads. It is found that:

1) During the scavenging process, the real gas model does not present any superiority over the ideal gas model. However, the computation time consumed in real gas simulation is much longer than that in the ideal gas case.

2) Even though the specifications of the scavenging and exhaust pressures are averaged, the results predicted by the developed computation model are satisfactory.

3) The robustness of the CFD prediction makes it possible to use these as an optimisation tool for the geometries and operating conditions. It also paves the way for using CFD to address the whole combustion process.

Chapter 6 Combustion Simulation

For the combustion simulations, the combustion model is very important because it controls the combustion process. Depending on the treatment for turbulence, flame structure and chemical kinetics, the combustion models can be classified into different brackets. For example, in the Eddy-Dissipation model (Magnussen et al., 1976), the burning rate is assumed to be controlled by the mixing rate. Whereas, in flamelet models, the turbulent combustion is assumed to be an ensemble of laminar flamelets and the stretching effect is accounted through the counterflow diffusion flame which represents the flamelet in turbulent flow. The turbulence in flamelet models would control the flame surface area. As for the chemical kinetics models, the reaction is assumed to be controlled by the chemical mechanisms (Lakshminarayanan et al., 2010).

For the prediction performance of the combustion models, Lakshminarayanan et al. (2010) made the conclusion that none of the combustion models can perform equally well over the entire range of the engine conditions. Each model has its application ranges. In this context, in order to compare the combustion models performance during the engine combustion simulations, FRED, Non-Premixed Equilibrium, Non-Premixed Steady Flamelet and Non-Premixed Unsteady Flamelet Diesel combustion models are investigated at different engine loads. A simplified C_7H_{16} reaction mechanism (Patel et al., 2004) which includes 52 reactions and 29 species is used to generate the flamelet structures for both of the Flamelet models. The mechanism was validated by Patel et al. under both the constant-volume and engine conditions and the predicted results presented adequate coincidence with a comprehensive mechanism which involves 179 species and 1642 reactions (Patel et al., 2004).

6.1 Compression

6.1.1 Effect of Real and Ideal Gas Model during Compression

Before the combustion calculations, it is necessary to validate the state at TDC. As a result, it is critical to investigate the EOS in advance. Four real gas models (Peng-Robinson (PR), Redlich-Kwong (RK), Aungier-Redlich-Kwong (ARK), Soave-Redlich-Kwong (SRK)) and ideal gas model are used to close equations of state during the compression stoke of 100% load MCR. The in-cylinder pressure at four loads (100%, 75%, 50% and 25% MCR) needs to be validated against the measured data from shop tests to provide baselines for the following combustion simulations.

The compression calculation ranges from 290 CAD to 360 CAD. To initialise the properties at 290 CAD similarly for all real gas models and ideal gas model, the computation results of 290 CAD using PR real gas model would be used as the starting point for all the models. It can be seen from Table 6.1 that the initial states of all the tested models coincide very well. The minor difference is induced by the inevitable numerical error.

Table 6.1 Initial properties of the real gas models and ideal gas model

290 CAD	PR	RK	ARK	SRK	Ideal Gas
Mean Pressure (bar abs)	5.7781	5.7781	5.7781	5.7781	5.7781
Mean Temperature (K)	402.9938	402.9953	402.9957	402.9971	403.0030
Mass (kg)	1.6574	1.6576	1.6573	1.6551	1.6582

The in-cylinder mean pressure and temperature traces computed using the real gas models and ideal gas model are illustrated in Figure 6.1 and Figure 6.2. It can be noticed that the in-cylinder pressure predicted by the real gas models presents very good agreement with the measured data. As for the ideal gas model, the predicted pressure and temperature gradually separate with the results predicted by the real gas models as

reaching TDC. Table 6.2 lists the properties at TDC predicted by the real and ideal gas models. It can be inferred that even though the mass predicted by ideal gas coincides very well with that of real gas models, the pressure predicted by ideal gas model presents obvious discrepancy with the experimental data. This means that the ideal gas model can conserve the mass even the gas goes beyond the critical point.

Considering its robustness and good precision, PR real gas model is determined as the closure EOS model in the following validations and combustion modelling.

Table 6.2 Properties at TDC predicted by the real gas models and ideal gas model

360 CAD	PR	RK	ARK	SRK	Ideal Gas
Mean Pressure (bar abs)	145.7727	145.3841	145.4527	146.4664	138.2140
Mean Temperature (K)	960.5394	961.1297	961.0830	960.0082	946.7994
Mass (kg)	1.6565	1.6567	1.6564	1.6542	1.6573

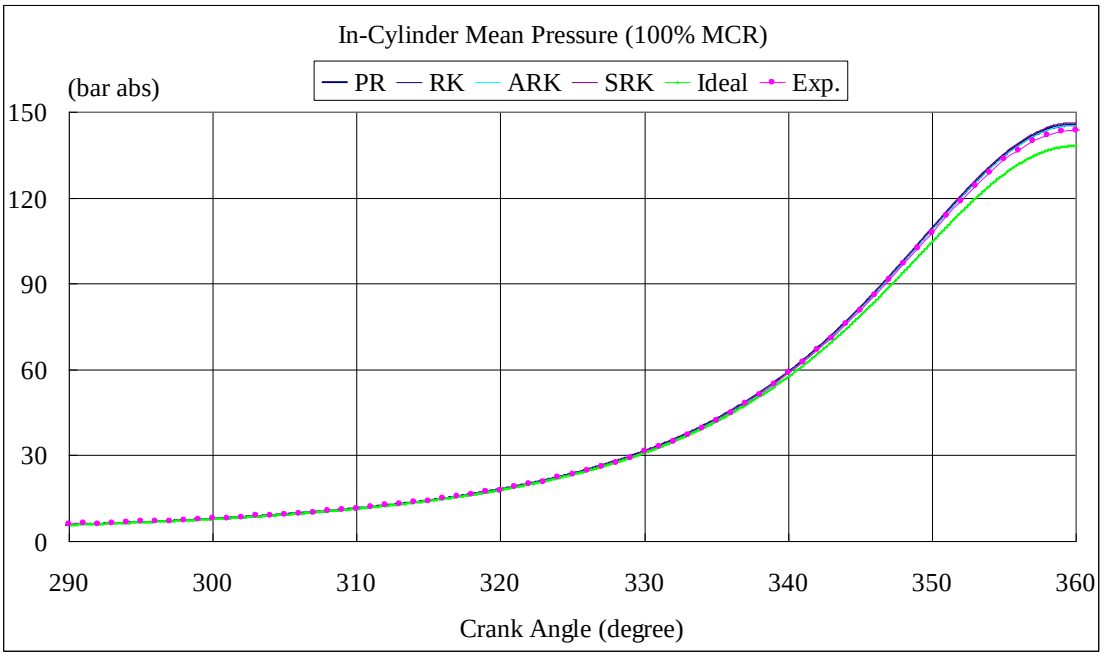

Figure 6.1 Comparison of in-cylinder mean pressure at 100% MCR

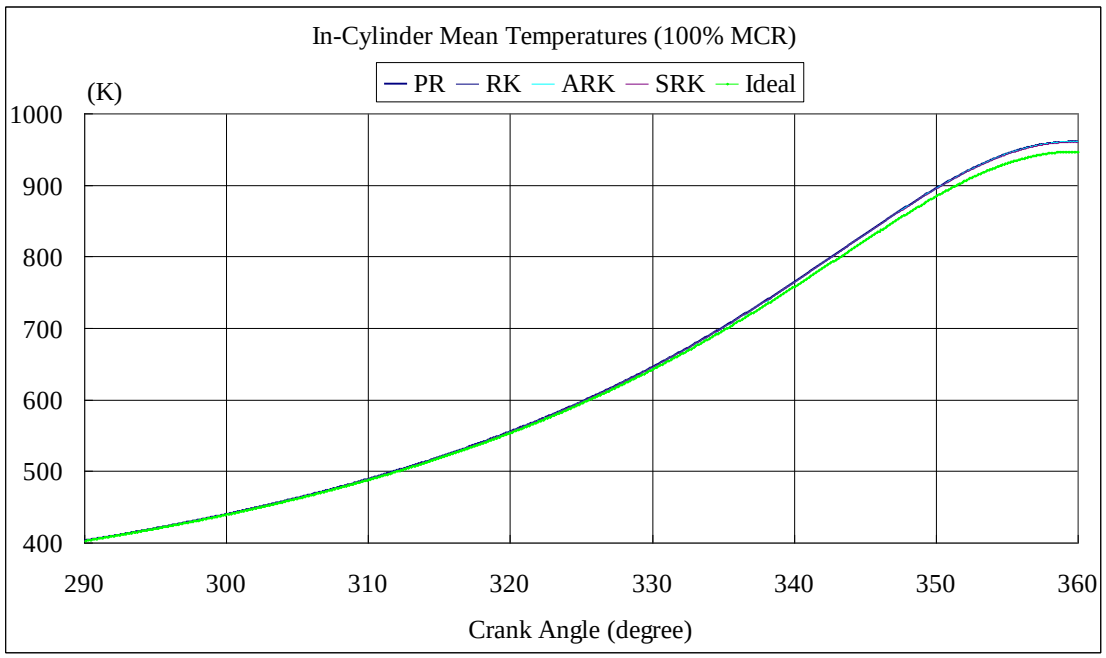

Figure 6.2 Comparison of in-cylinder mean temperature at 100% MCR

6.1.2 Comparison of Results during Compression

Figure 6.3 presents the comparison of the pressure traces at four tested loads. The error percentages of the predicted in-cylinder mean pressure at TDC for the tested loads are listed in Table 6.3. Considering the fact that this is only the first cycle calculation, the predicted results are acceptable and can be used for the following combustion simulations. Figure 6.4 presents the comparison of the temperature traces at four tested loads. In the compression stroke, the temperature would be higher for increasing of the engine load.

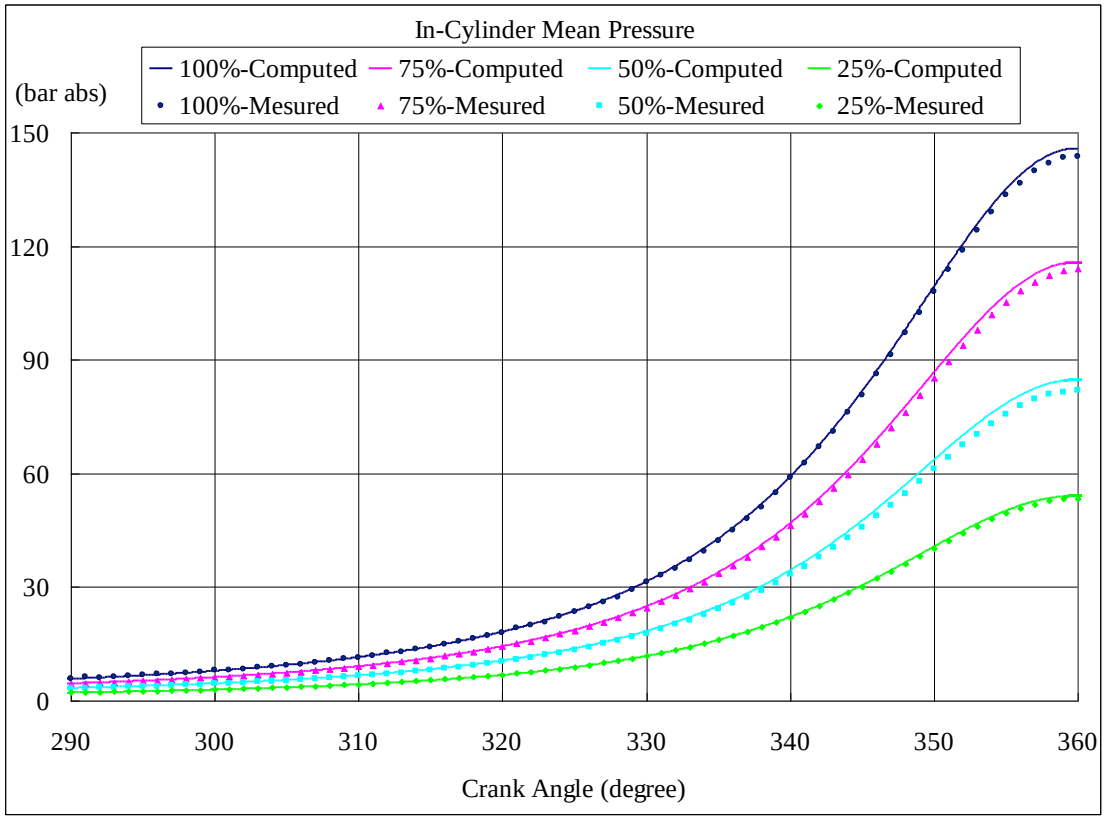

Figure 6.3 In-cylinder mean pressure traces at four tested loads during compression

Table 6.3 Comparison of in-cylinder mean pressure at TDC

MCR (%)	100	75	50	25
CFD (bar abs)	145.7727	115.5822	84.6911	54.0747
Measured (bar abs)	143.7973	114.0595	81.8850	53.4413
Error (%)	1.37	1.33	3.43	1.19

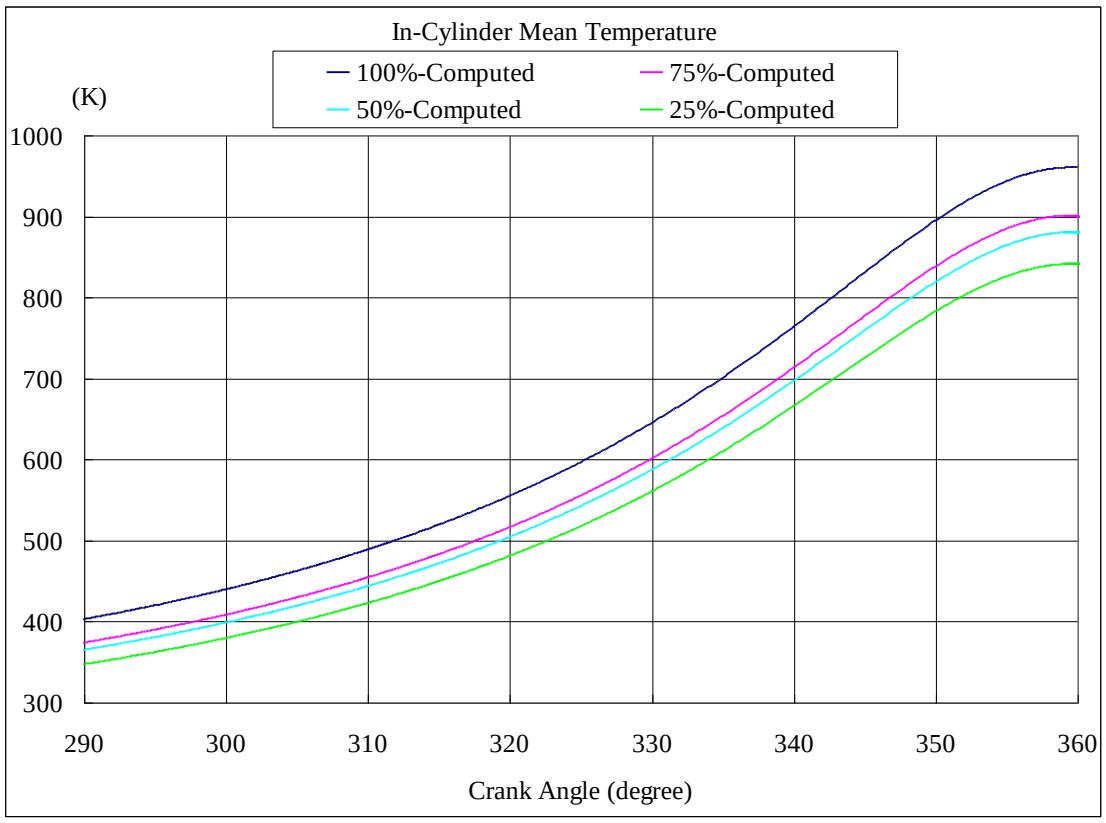

Figure 6.4 In-cylinder mean temperature traces at four tested loads during compression

6.2 Injection

6.2.1 Setup

The controlling of the diesel spray plays a critical role on the engine performance and emissions. It is known that the internal nozzle flow controls the downstream discrete spray. The internal nozzle flow undergoes strong wall bounded shear, and induces strong turbulent vortex and cavitation (Dam, 2007). Such complex flow is dependent on the nozzle geometry and the operating process. As a result, the fuel injector is strictly manufactured following the design drawings and operated on the well-tuned working conditions. The currently used two nozzles in each cylinder of MAN B&W S60MC-C6 engine are mounted on the opposite sides of the cylinder cover. Each nozzle has five

holes, which are distributed at different positions on the nozzle to produce the best mixing with the scavenged fresh air. In the CFD simulations, it is necessary to setup every hole position and direction against the injector design diagrams to make sure that the fuel sprays injected from the holes are strictly the same with that of the shop tests.

Except for the injection position and direction, the velocity and profile of the fuel oil injected from every hole are also the key and critical parameters for the engine performance. For the present shop tests, the velocity and profile of the injected fuel are unavailable. However, the injection pressure in the nozzle and the fuel oil consumption can be used to determine the velocity and injection mass flow rate profiles.

The Bernoulli velocity can be computed as:

$$U_b = \sqrt{2\frac{P_{inj} - P}{\rho_f}} \tag{6.1}$$

U_b : Bernoulli velocity

P_{inj} : the injection pressure

P : the pressure of the nozzle exit

ρ_f : the density of the fuel oil

As to the velocity coefficient, the experimental data (C_v=0.96) provided in Dam (2007) can be referred for that the tested nozzle S0003 works with the similar diameter and injection pressure with the current nozzle. Then the injection mass flow rate, which is assumed to have the same profile with that of the velocity, can be then computed using the nozzle exit diameter and tested fuel consumption rate SFOC during the injection.

6.2.2 Fuel Oil Transferring

For large 2-stroke marine diesel engine, marine gas oil and heavy fuel oil can both be used and they can be changed during operation. During the voyage of the ship, the heavy fuel oil is used to reduce the operation cost. However, before the engine leaving the factory, the shop tests generally should be done using marine gas oil in the presence of representatives of ship yard, ship owner, Classification Society and the engine manufacturer.

The marine gas oil is produced from the fractional distillation of crude oil. It is a mixture of hydrocarbons and the chemical composition would be different depending on the production place. In CFD simulations, different average chemical formulas are used to represent the marine gas oil. In the present calculations, C_7H_{16} is selected as the chemical type of marine gas oil since the simplified reaction mechanisms of C_7H_{16} are regarded as a smart substitute for much more complex comprehensive mechanism. The density, viscosity and the other properties of C_7H_{16} are changed into the same properties of the marine gas oil used in the shop test, as shown in Table 6.4.

Table 6.4 Marine gas oil specification used in the shop test

Brand	SHANGLIAN
Type	0#
Lower Heating Value (kJ/kg)	42600
Density (g/cm^3) (20℃)	840
Viscosity (kg/(m.s)) (20℃)	0.000409

However, the Lower Heating Value (LHV) of C_7H_{16} is not same as that of diesel oil. As a result, it is necessary to ascertain that the released heat amounts of them are equal. Considering the combustion reaction:

$$C_7H_{16}+11O_2 \rightarrow 7CO_2+8H_2O \quad (6.2)$$

The Standard State Enthalpy (SSE) values are list in Table 6.5 (ANSYS, 2012):

Table 6.5 SSE values of the involved species

	SSE (kJ/mol)
C_7H_{16}	-187.8000
O_2	0.0000
CO_2	-393.5324
H_2O	-241.8379

And the latent heat of liquid C_7H_{16} is 320.096 kJ/kg. Then the LHV of liquid C_7H_{16} can be computed as:

$$\frac{7\times(393.5324)+8\times(241.8379)-(187.8+320.096\times 0.100204)(kJ/mol)}{0.100204(kg/mol)} = 44604.5577(kJ/kg) \tag{6.3}$$

The LHV of the diesel fuel oil used in shop test is 42600 kJ/kg. As a result, to make sure the released heat amounts of C_7H_{16} and diesel fuel oil are same, the correction factor C should be multiplied to the injection flow rate of C_7H_{16}:

$$C = \frac{42600(kJ/kg)}{44604.55772(kJ/kg)} = 0.955 \tag{6.4}$$

6.3 FRED and Non-Premixed Manipulations

6.3.1 Difference between FRED and Non-Premixed Model

Prior to the combustion model tests, it is necessary to check the computation accuracy of FRED and Non-Premixed model at TDC. The FRED and Non-Premixed Equilibrium models are both used to calculate the scavenging and compression process, thus from 110 CAD to 360 CAD. The initialisation data at 110 CAD of FRED and Non-Premixed

Equilibrium models is the same as listed in Table 6.6. After the scavenging and compression calculations, the in-cylinder mean pressure, temperature and gas mass are finally compared at TDC in Table 6.6. It can be observed that the deviations of the properties predicted by FRED and Non-Premixed Equilibrium combustion models are within 1%. It can be concluded that there is very good coincidence of FRED and Non-Premixed Equilibrium models. This means that the FRED and Non-Premixed combustion models are standing at the same starting line for the following combustion tests.

Table 6.6 Comparison of initial and final results computed by FRED and Non-Premixed Equilibrium models

	Pressure (bar abs)		Temperature (K)		Gas Mass (kg)	
	110	360	110	360	110	360
FRED	9.9779	145.77	1100	960.54	1.7756	1.6565
Non-Premixed Equilibrium	9.9779	145.80	1100	969.34	1.7750	1.6421
Deviation (%)	0.00	-0.02	0.00	-0.91	0.04	0.88

6.3.2 Starting the Non-Premixed Calculations from FRED Results

The non-premixed calculations can be switched from the previously convergent FRED results as the starting point. This would save a lot of time for the settings and calculations. The incompatible configurations from FRED combustion model will be disabled by ANSYS FLUENT during this process. The property input that conflicts with the non-premixed models would be ignored. During the current combustion model tests, the FRED model calculations are firstly carried out. Then the convergent FRED results are switched to non-premixed Equilibrium model before the TDC. The non-premixed Steady Flamelet model is then switched from the non-premixed Equilibrium model before the TDC as well. Finally, the non-premixed Unsteady Flamelet Diesel model is obtained from the Steady Flamelet model. Such switches would save the most time-consuming cycle stabilising iterations. Most importantly, these switches would

guarantee the almost seamless data passing from one to another, which is the prerequisite for comparison.

Moreover, it should be noted that for FRED model, the density under-relaxation factor of 1.0 and 10 iterations are enough in every time step. However, for Non-Premixed combustion models, the default density under-relaxation factor of 1.0 would make the iterations non-converging. Thus the density under-relaxation factor is set as 0.5 and 20 inner iterations are carried out in every time step. This makes the Non-Premixed models more time-consuming than FRED model. During the combustion process simulations, small time step size (0.01 CAD/Δt) and more inner iterations (20 iterations for FRED model and 40 for Non-Premixed combustion models) are used to minimise the numerical errors.

6.4 Cycle Variance

Even though the initial conditions are specified appropriate values according to the measured data at the onset of the calculation, it would inevitably induce discrepancies of the corresponding spatial quantities as those in the shop test. Thus, it is necessary to carry out the cycle variance test to stabilise the calculation results and eliminate the error introduced in the setup and convergence stages. Following the previously presented test results, three complete working cycles are calculated at 100% MCR to test the cycle variance. Figure 6.5 presents the cylinder pressure traces calculated in three continuous cycles. It is noticed that the computed pressure traces in three cycles almost coincide.

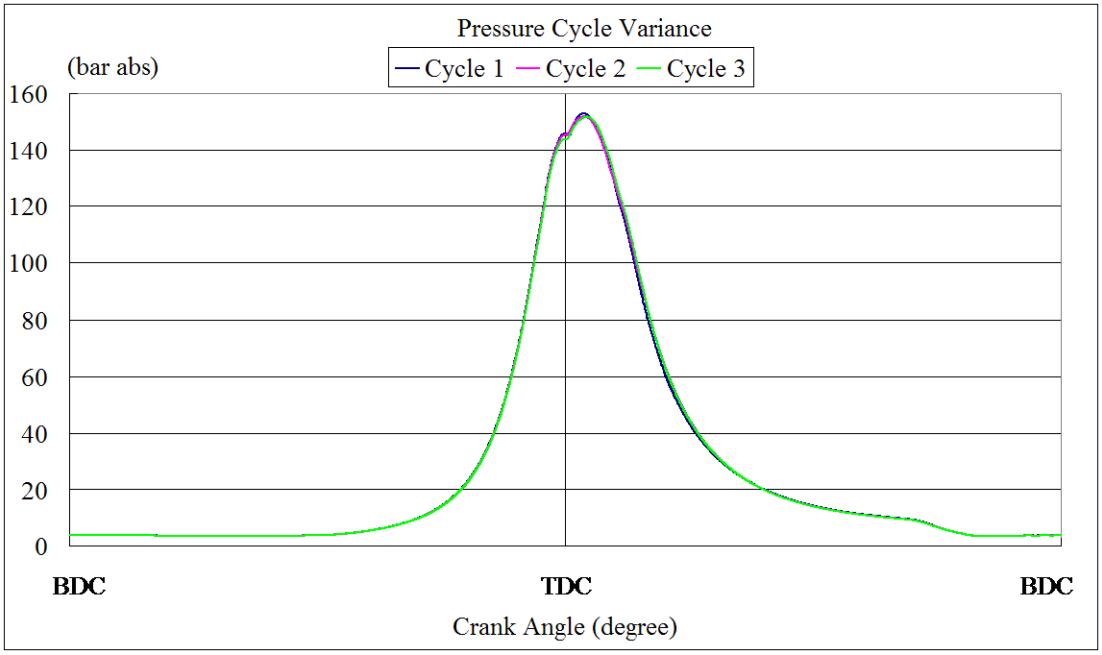

Figure 6.5 In-cylinder mean pressure at different cycles

To scrutinise the transient data as volume-averaged pressure, mass-averaged temperature, and the total gas mass, mass fraction of C_7H_{16}, O_2 and CO_2, and mass flow rates through the scavenging ports and exhaust port are summarised in Table 6.7. The selected 6 crank angles are 110 CAD where the calculation starts, 180 CAD (BDC), 290 CAD, 360 CAD (TDC), 380 CAD and 400 CAD. It can be noted that the species mass fractions of cycle 2 and cycle 3 coincide very well. As a result, it is concluded that the cycle variance could be excluded after the initial cycle calculation.

Table 6.7 Transient values at different cycles

CAD	Cycle	P (bar abs)	T (K)	Gas Mass (kg)	Mass Fraction			Mass Flow Rate	
					C_7H_{16} (%)	O_2 (%)	CO_2 (%)	In (kg/s)	Out (kg/s)
110	1 (110)	9.98	1100	1.78	0.00	23.30	0.31	0.00	0.00
	2 (470)	11.11	1258	1.72	0.02	8.74	11.97	0.00	0.00
	3 (830)	10.97	1248	1.71	0.02	8.37	12.25	0.00	0.00
180	1 (180)	3.91	524	1.82	0.00	23.30	0.16	22.60	7.78
	2 (540)	3.92	559	1.70	0.00	16.56	5.55	22.82	6.89
	3 (900)	3.91	584	1.63	0.00	15.17	6.67	22.84	6.67
290	1 (290)	5.78	403	1.66	0.00	23.30	0.02	0.00	0.00
	2 (650)	5.77	404	1.65	0.00	22.43	0.72	0.00	0.00
	3 (1010)	5.74	410	1.62	0.00	22.25	0.86	0.00	0.00
360	1 (360)	145.92	962	1.66	0.00	23.30	0.02	0.00	0.00
	2 (720)	145.37	962	1.65	0.00	22.52	0.64	0.00	0.00
	3 (1080)	143.93	974	1.61	0.00	22.35	0.78	0.00	0.00
380	1 (380)	119.97	1507	1.72	1.91	11.25	9.54	0.00	0.00
	2 (740)	121.40	1531	1.71	1.86	10.44	10.19	0.00	0.00
	3 (1100)	123.25	1586	1.67	1.74	9.96	10.61	0.00	0.00
400	1 (400)	52.16	1536	1.72	0.75	9.30	11.37	0.00	0.00
	2 (760)	54.32	1604	1.71	0.53	8.54	12.02	0.00	0.00
	3 (1120)	54.00	1628	1.67	0.52	8.29	12.22	0.00	0.00

It is noticed that the selection of the computation starting point is very important for the required cycles to stabilise the variance. The computation starting point is selected at the compression stroke by Jin et al. (2013) and it needs three cycles to get the stable results. The relative amount of NO_x and heat release rate are used as the convergence criterion in the work of Imamori et al. (2004), who concluded that three cycles iterations are required at least. The starting point of the calculation of Imamori et al. was selected during the scavenging process. The current calculation selects 110 CAD as the starting point and only two cycles are needed. The reason should be that the current selected point would then experience the scavenging process, which has an obvious readjusting effect for the initial specified conditions. In the case of Jin et al. (2013), the inaccurate specification of the initial conditions would be enlarged in the following combustion. As a result, one more cycle is needed to stabilise the variance. By specifying accurate initial conditions and the appropriate starting point, one cycle and the corresponding

computation time could be possibly saved. It should be noted that the data used in Figure 5.6 and Table 6.7 were obtained from a separated test, which does not relate with the following sections tests.

After the cycle variance being largely removed, the comparison of the in-cylinder mean pressure at TDC is summarised in Table 6.8. Generally, the currently obtained TDC conditions are accurate enough for the following combustion process calculations.

Table 6.9 lists the injection timings at different load conditions.

Table 6.8 Comparison of in-cylinder mean pressure at TDC without cycle variance

MCR (%)	100	75	50	25
CFD (bar abs)	143.9305	114.3242	84.4310	54.0377
Measured (bar abs)	143.7973	114.0595	81.8850	53.4413
Error (%)	0.09	0.23	3.11	1.12

Table 6.9 Injection periods at different loads

MCR (%)	Injection Timing
100	360.0 CAD - 378.7 CAD
75	359.1 CAD - 375.1 CAD
50	359.8 CAD - 371.8 CAD
25	361.0 CAD - 369.0 CAD

6.5 Results and Analysis

6.5.1 Validation of the In-Cylinder Pressure and HRR

Figure 6.6 illustrates the comparison of the computed in-cylinder mean pressure and the corresponding heat release rate with the shop test data during the combustion process at 100% engine load. The tested combustion models included the Finite-Rate / Eddy-Dissipation (FRED), the Non-Premixed Equilibrium model (NP-Equilibrium), the Non-Premixed Steady Flamelet model (NP-Flamelet) and the Non-Premixed Unsteady Flamelet Diesel model (NP-Diesel). It can be found that all the tested models adequately predict good trends of the cylinder pressure as well as heat release rate. However, for the NP-Diesel model, the pressure is slightly overestimated in the region before and after reaching the maximum pressure. And NP-Diesel model presents very obvious numerical instability during the combustion process simulation. Most importantly, the NP-Diesel model would update the PDF table and flamelet files at the end of every time step, and this results in considerably increasing of computation time. Thus, NP-Diesel model would be excluded from the following tests.

For the FRED model, the pressure is underestimated before the peak pressure point, while it is overestimated after that. In this test, the NP-Equilibrium and the NP-Flamelet models presented the best prediction results as well as computation stability.

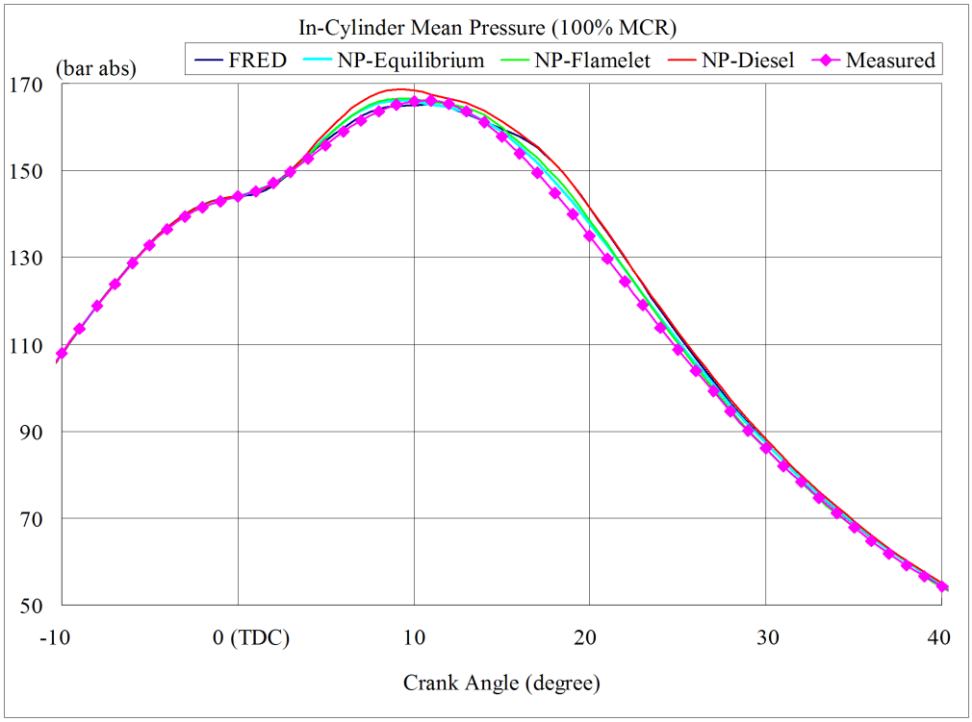

(a) Comparison of in-cylinder mean pressure at 100% MCR

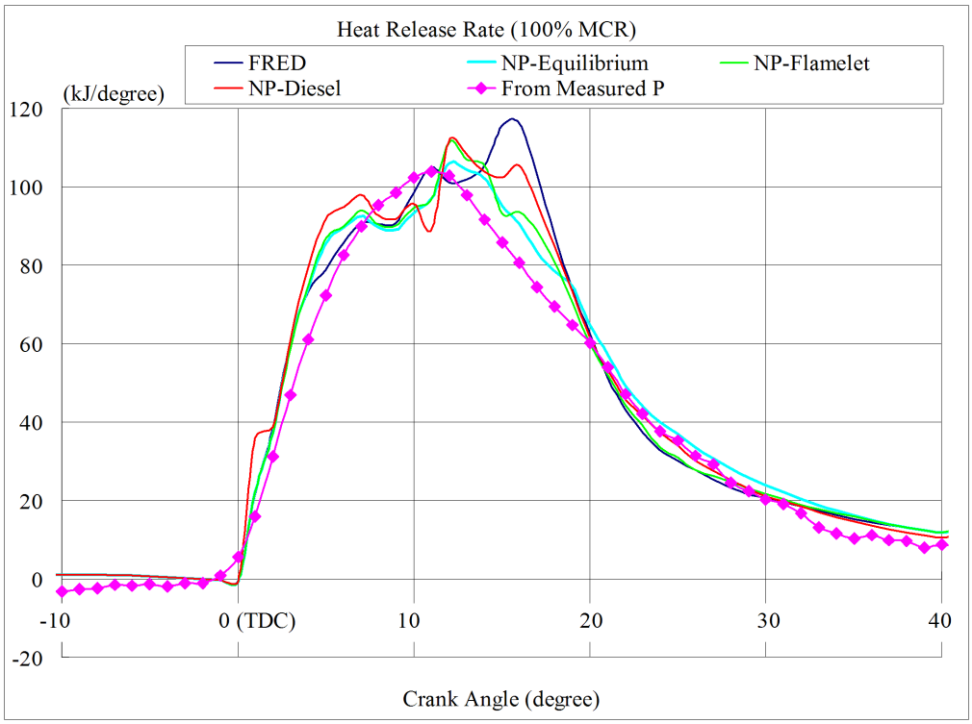

(b) Comparison of HRR at 100% MCR

Figure 6.6 Comparison of pressure and HRR at 100% MCR

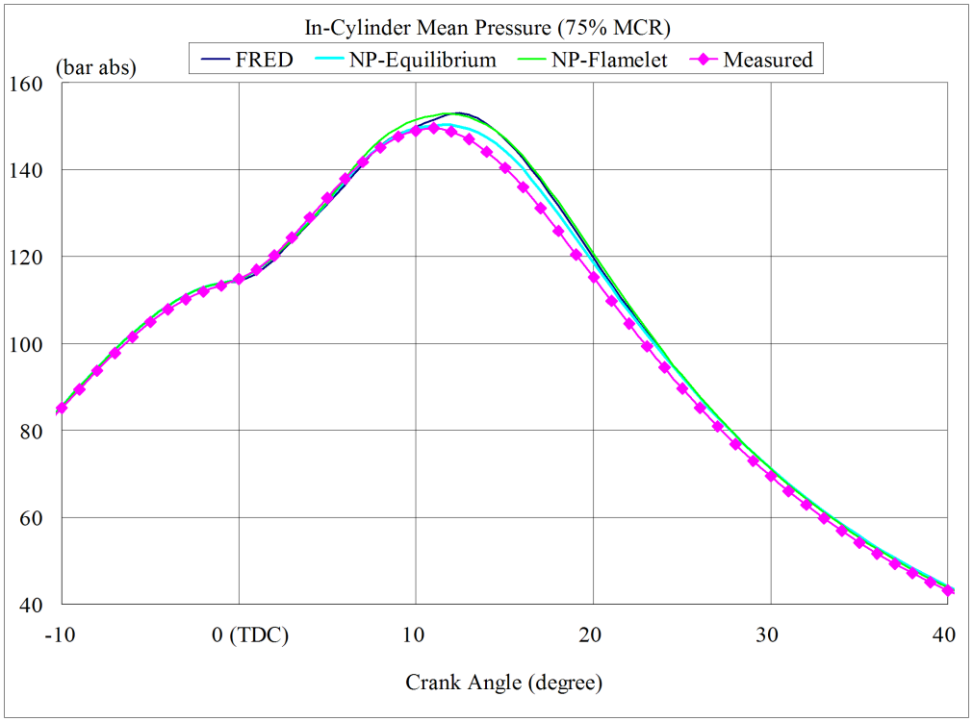

(a) Comparison of in-cylinder mean pressure at 75% MCR

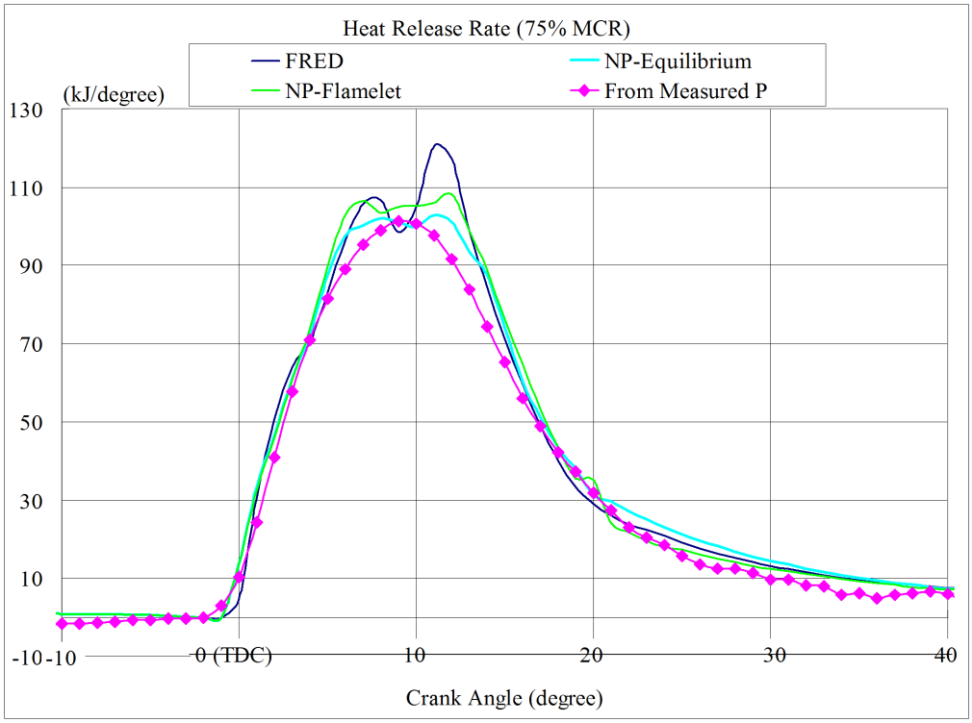

(b) Comparison of HRR at 75% MCR

Figure 6.7 Comparison of pressure and HRR at 75% MCR

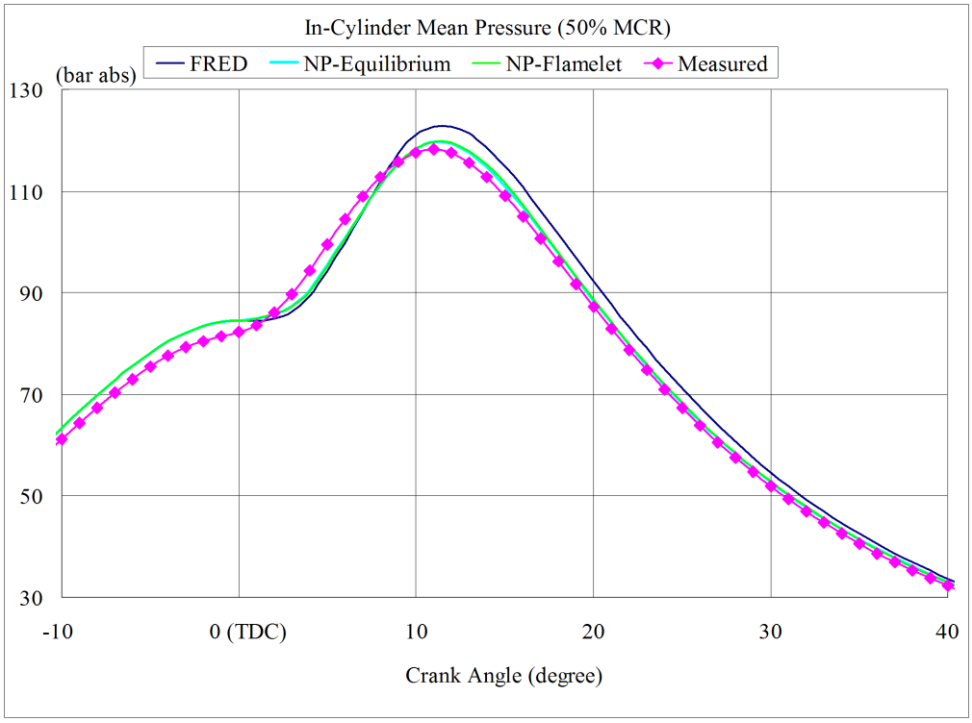

(a) Comparison of in-cylinder mean pressure at 50% MCR

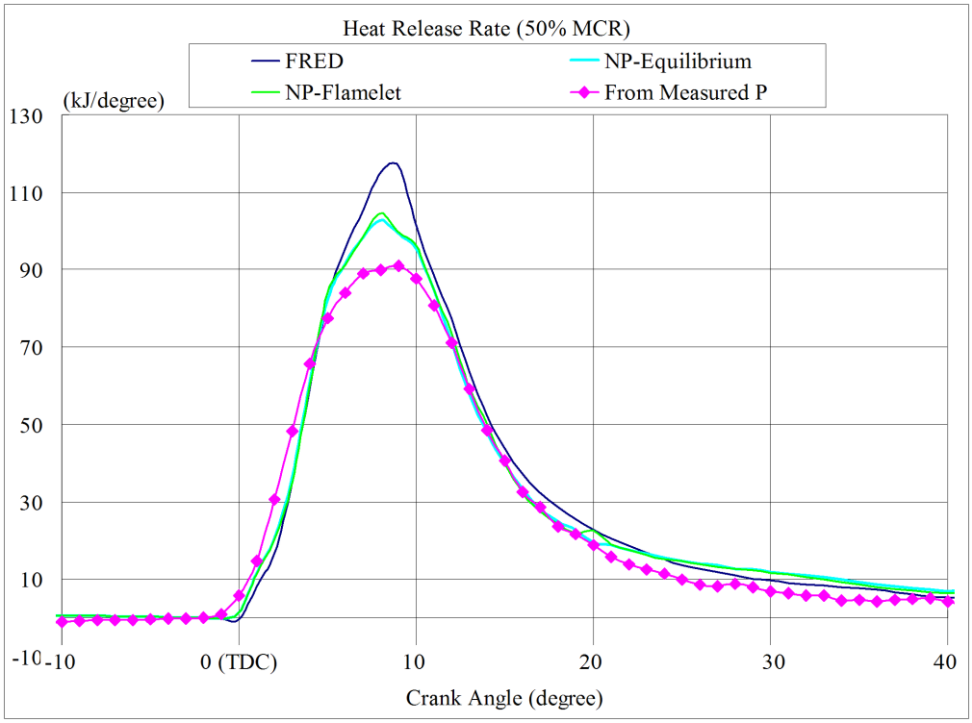

(b) Comparison of HRR at 50% MCR

Figure 6.8 Comparison of pressure and HRR at 50% MCR

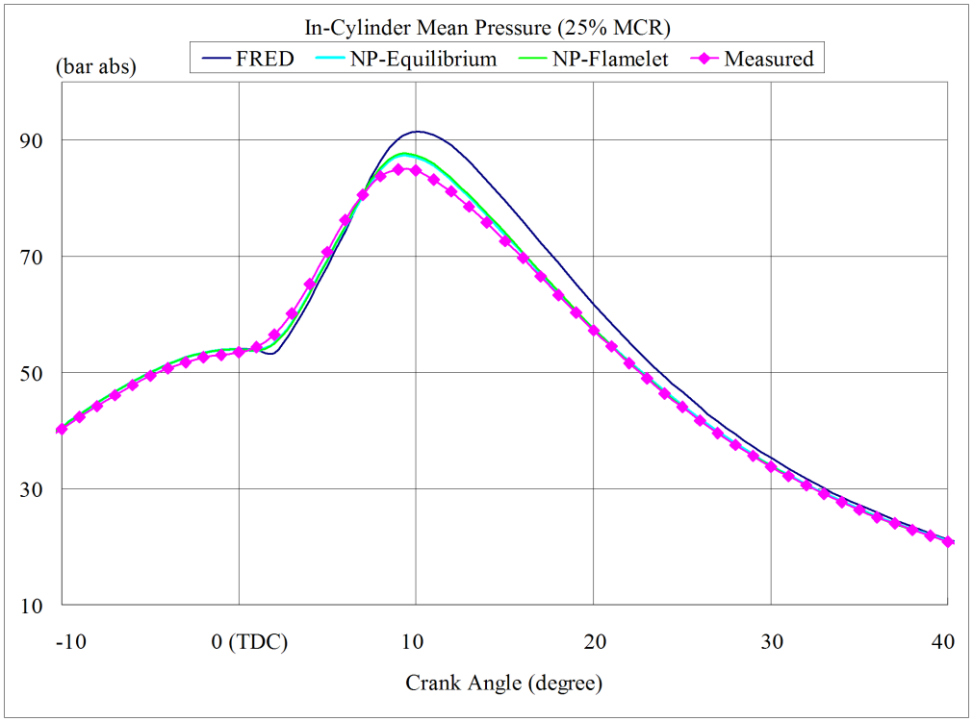

(a) Comparison of in-cylinder mean pressure at 25% MCR

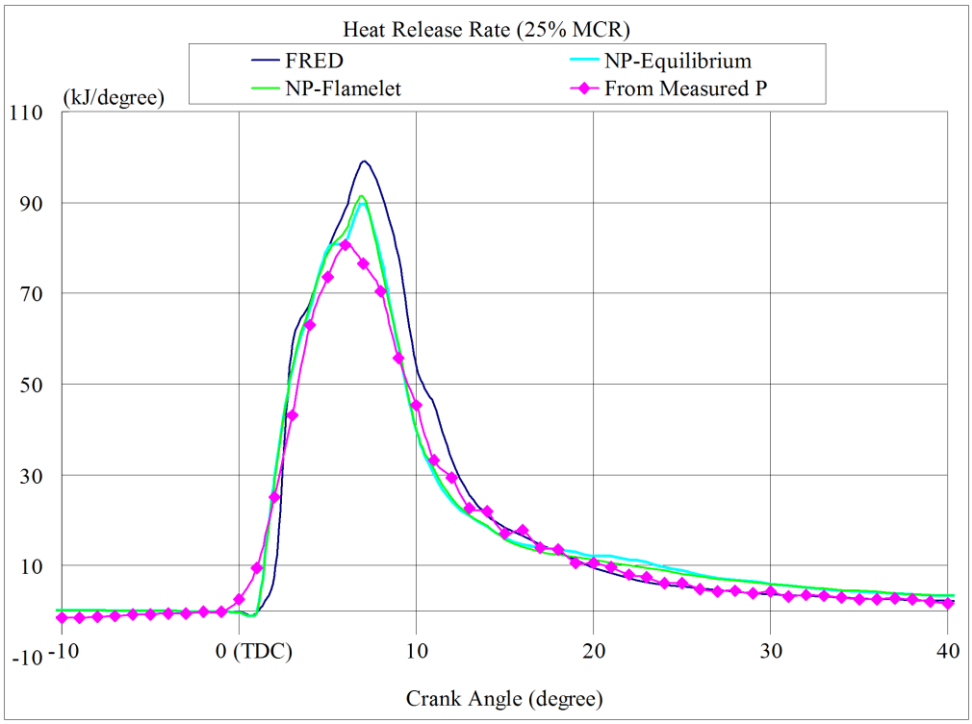

(b) Comparison of HRR at 25% MCR

Figure 6.9 Comparison of pressure and HRR at 25% MCR

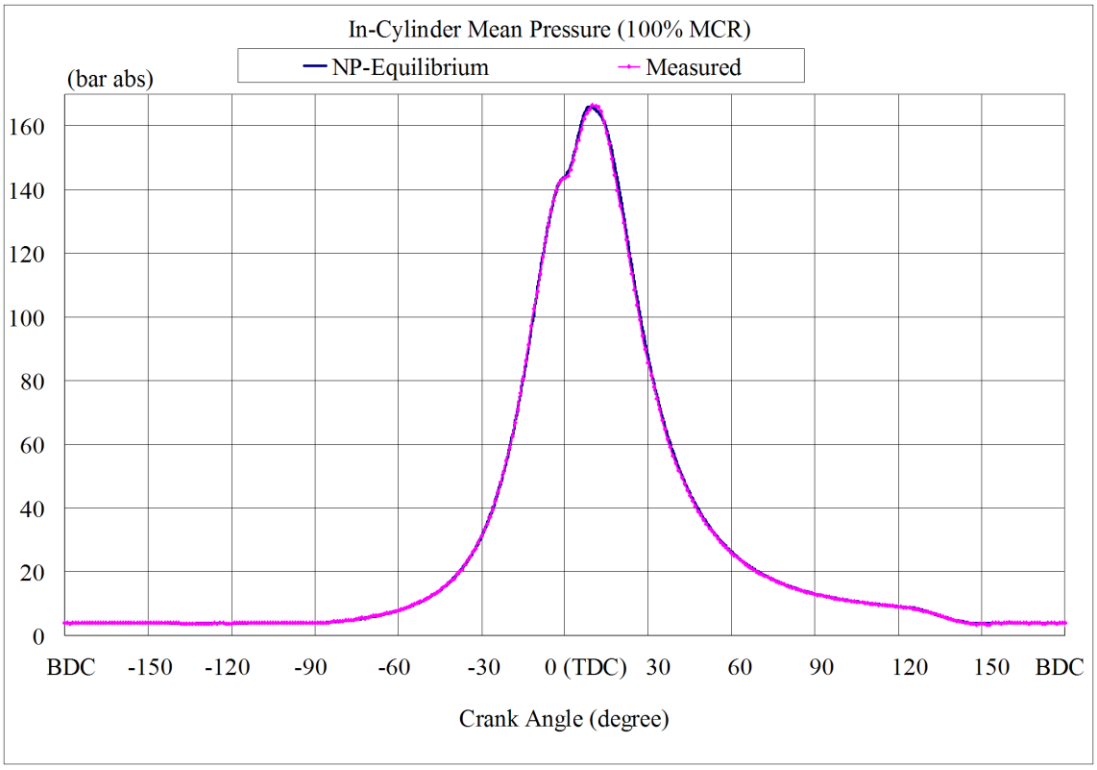

Figure 6.10 Comparison of pressure at 100% MCR

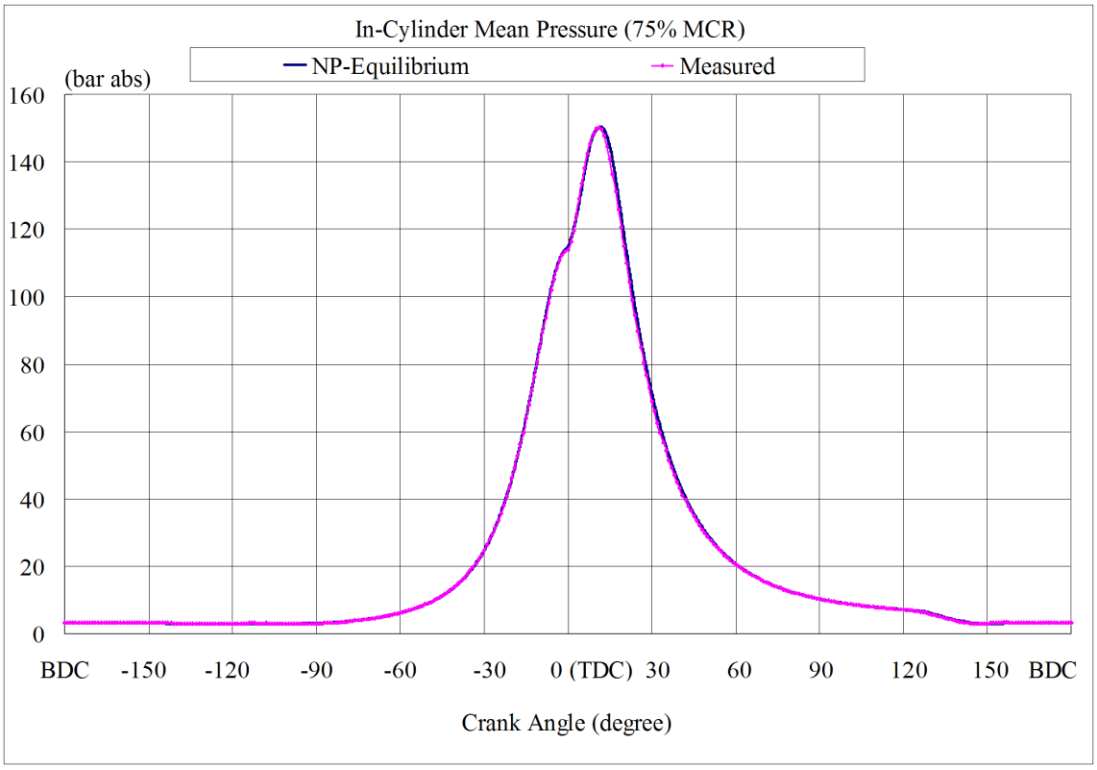

Figure 6.11 Comparison of pressure at 75% MCR

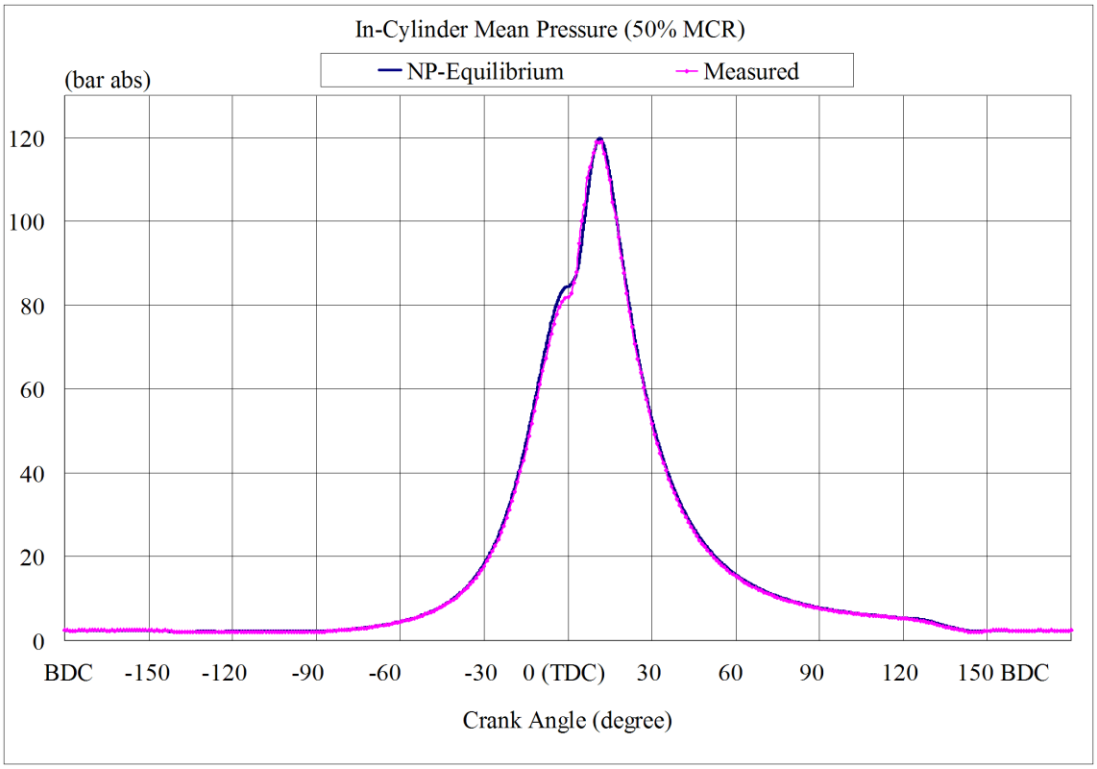

Figure 6.12 Comparison of pressure at 50% MCR

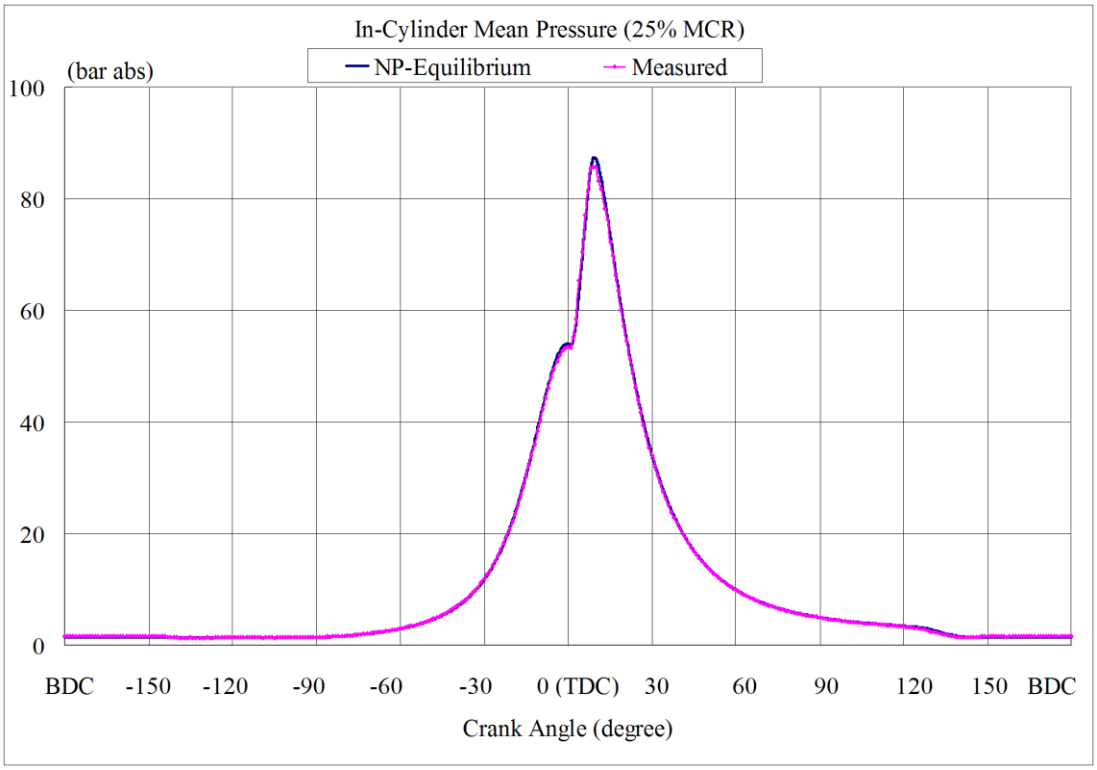

Figure 6.13 Comparison of pressure at 25% MCR

Figure 6.7 to Figure 6.9 present the predicted in-cylinder mean pressure and heat release rate of three combustion models at 75%, 50% and 25% loads, respectively. Similarly with the result in 100% MCR, FRED over predicts the heat release rates at all loads. At 75% load condition, FRED and NP-Flamelet models overestimated the pressure at about 10 CAD after TDC. However, at 50% and 25% load conditions, NP-Equilibrium and NP-Flamelet models produced almost the same pressure and heat release rate traces. Even though the chemical mechanisms of NP-Equilibrium and NP-Flamelet models are different, however, both of them gave very good coincidence for the combustion process results. As it is referred to all the comparison, NP-Equilibrium model gave the best agreement combustion process results. Thus, it can be concluded that chemical equilibrium is a good assumption at different load conditions for the present large 2-stroke marine diesel engine combustion.

The predicted full cycle in-cylinder pressure by Non-Premixed Equilibrium combustion model at four loads is compared with the measured data as shown in Figure 6.10 to Figure 6.13. It can be concluded that very good pressure data can be obtained using the adopted computation models.

6.5.2 Analysis of the Predicted In-Cylinder Properties

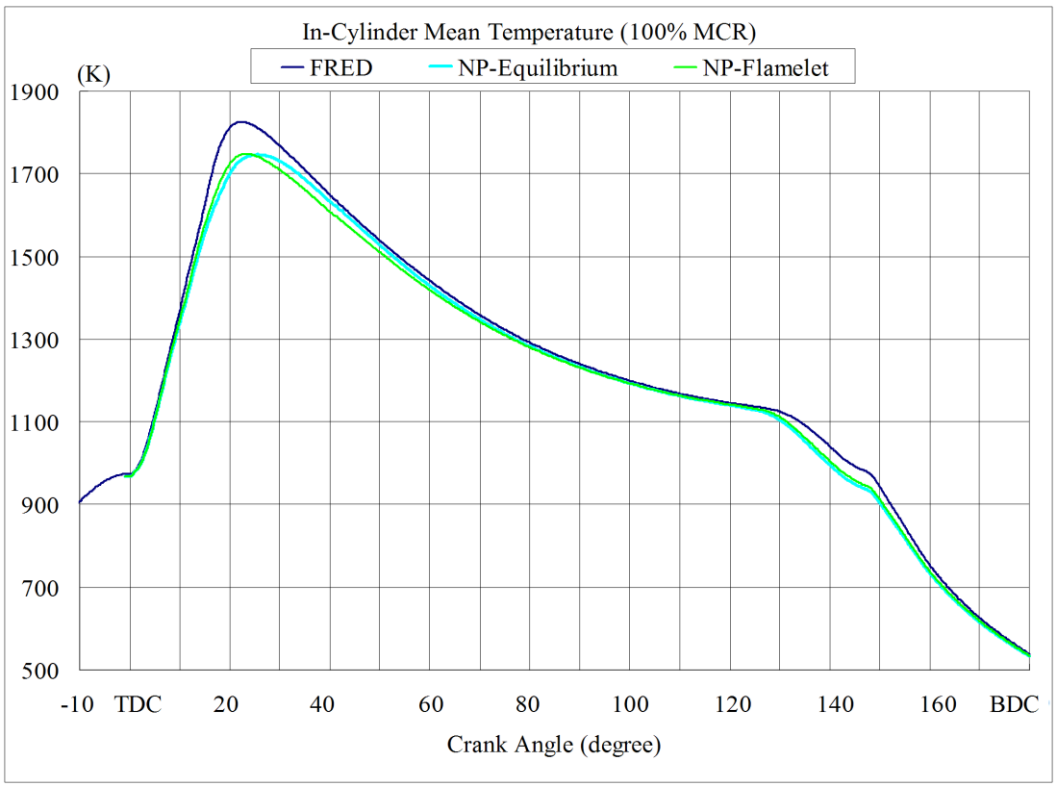

Figure 6.14 Calculated mean temperature at 100% MCR

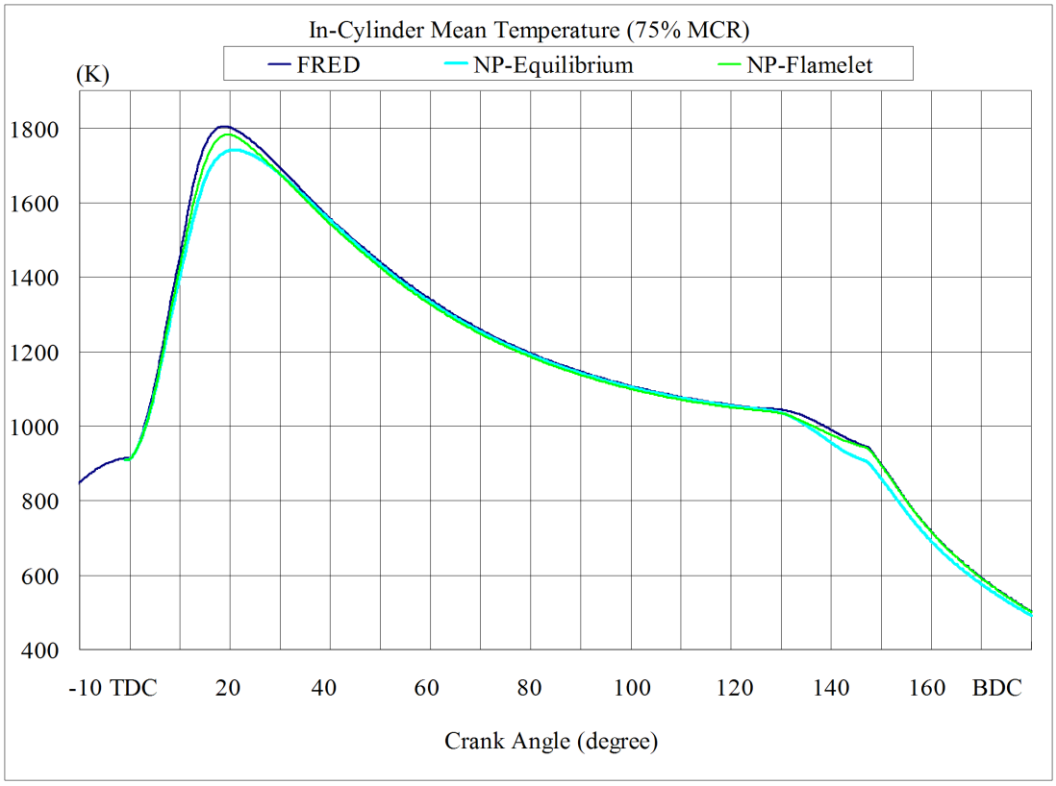

Figure 6.15 Calculated mean temperature at 75% MCR

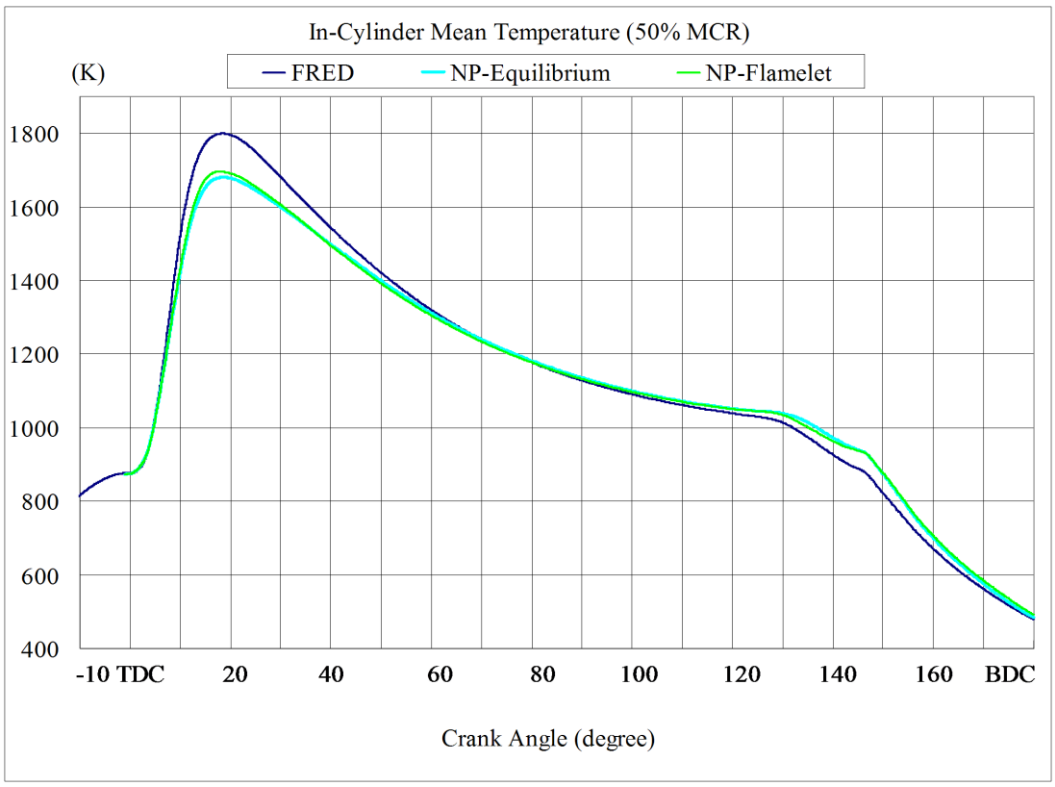

Figure 6.16 Calculated mean temperature at 50% MCR

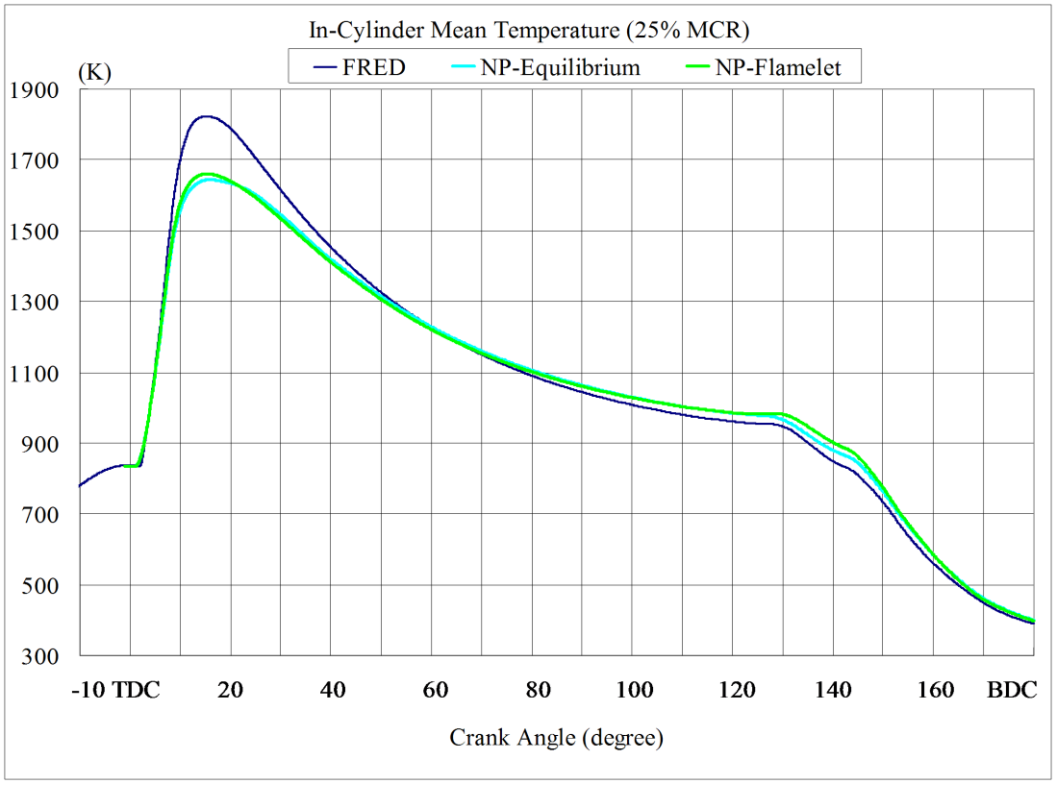

Figure 6.17 Calculated mean temperature at 25% MCR

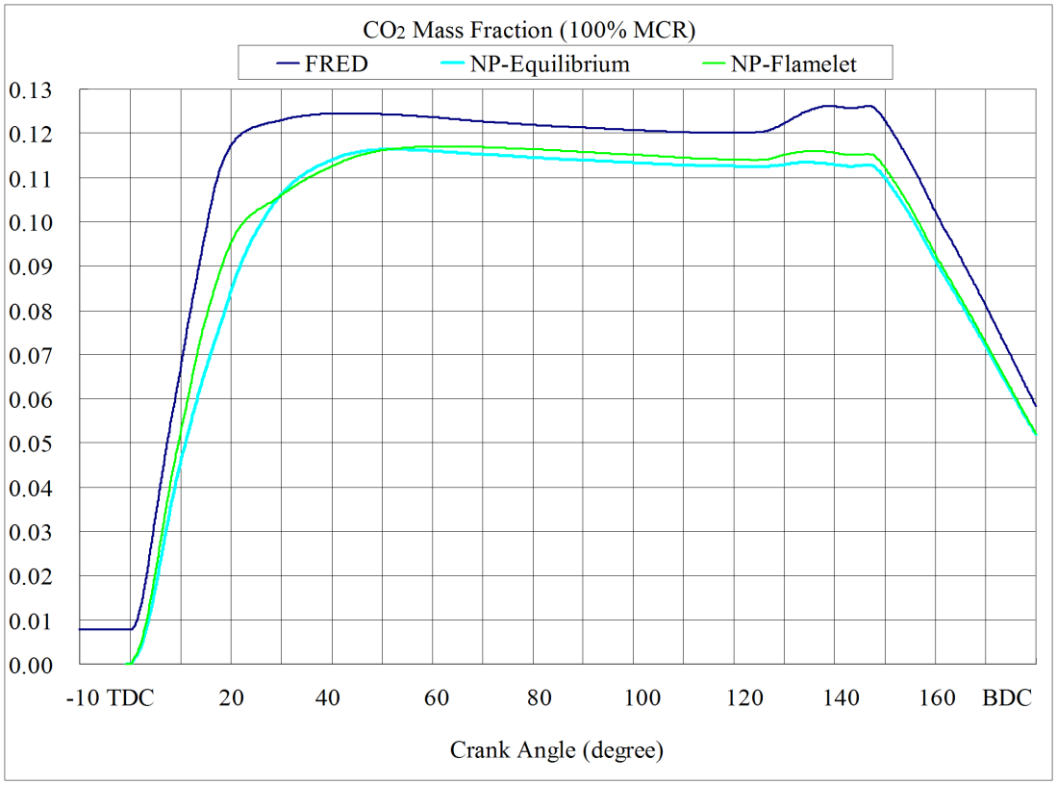

Figure 6.18 Calculated CO_2 mass fractions at 100% MCR

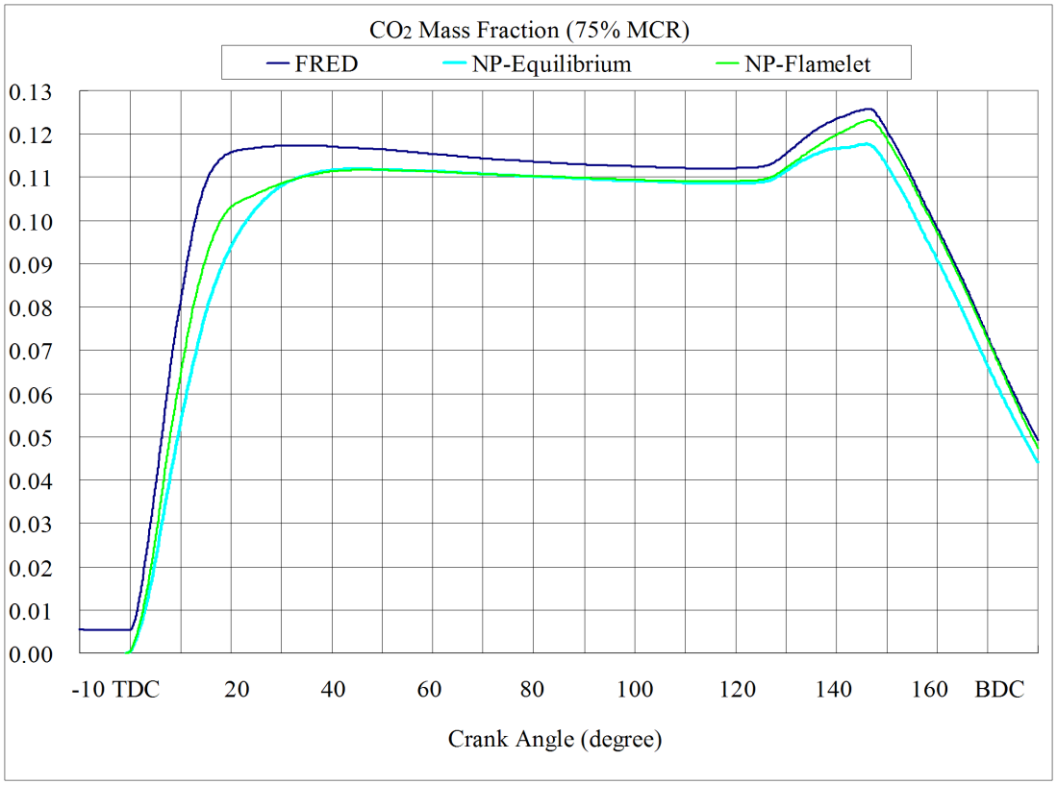

Figure 6.19 Calculated CO_2 mass fractions at 75% MCR

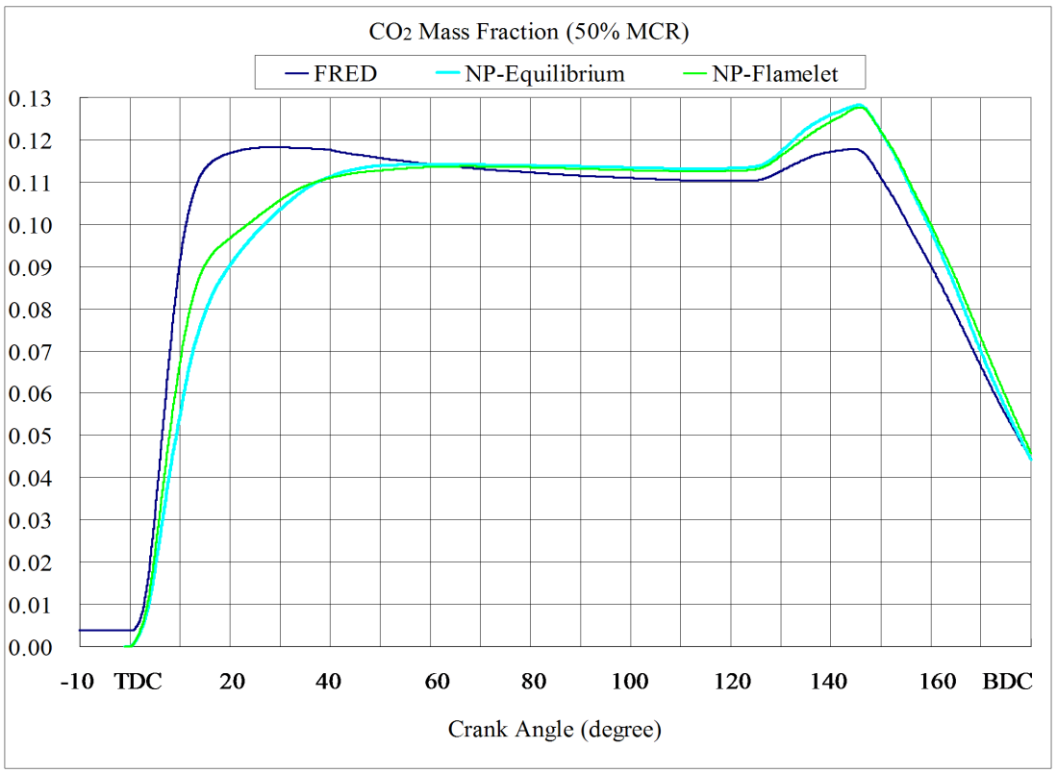

Figure 6.20 Calculated CO_2 mass fractions at 50% MCR

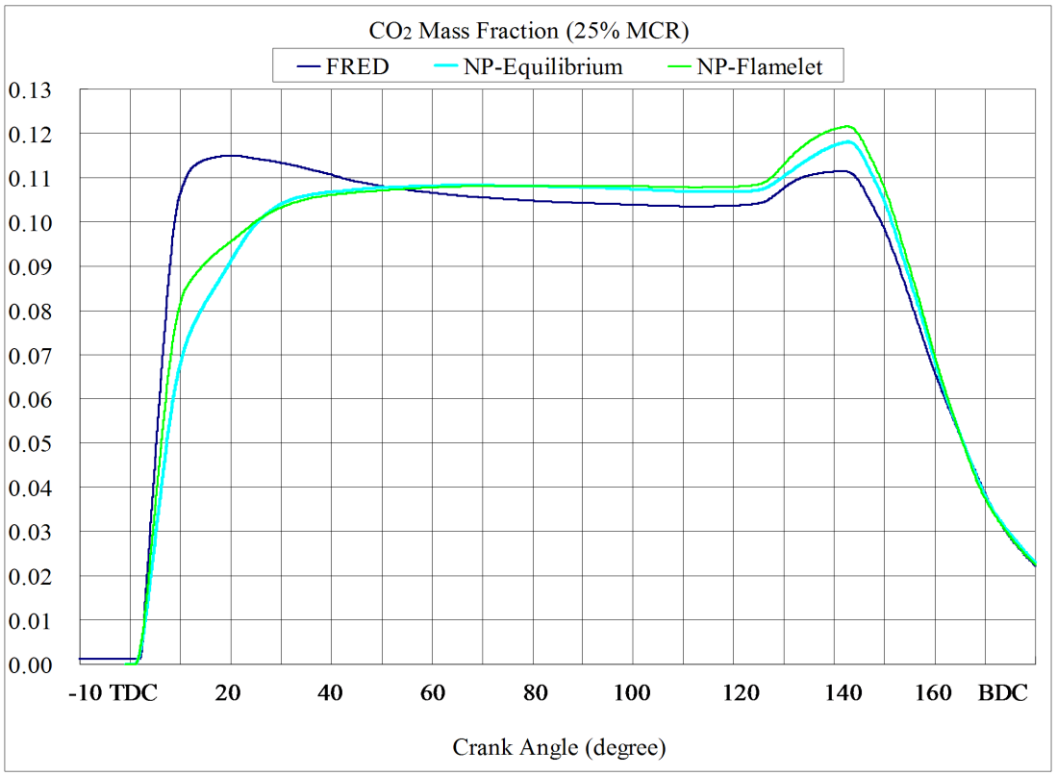

Figure 6.21 Calculated CO_2 mass fractions at 25% MCR

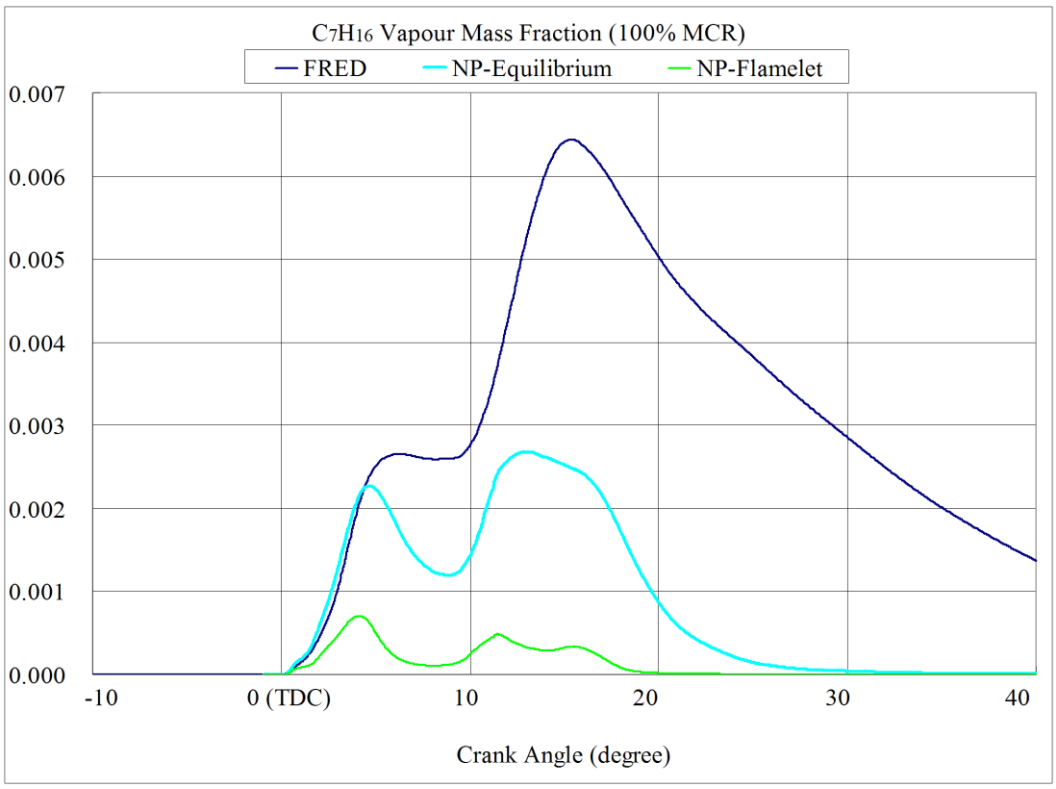

Figure 6.22 Calculated C_7H_{16} mass fractions at 100% MCR

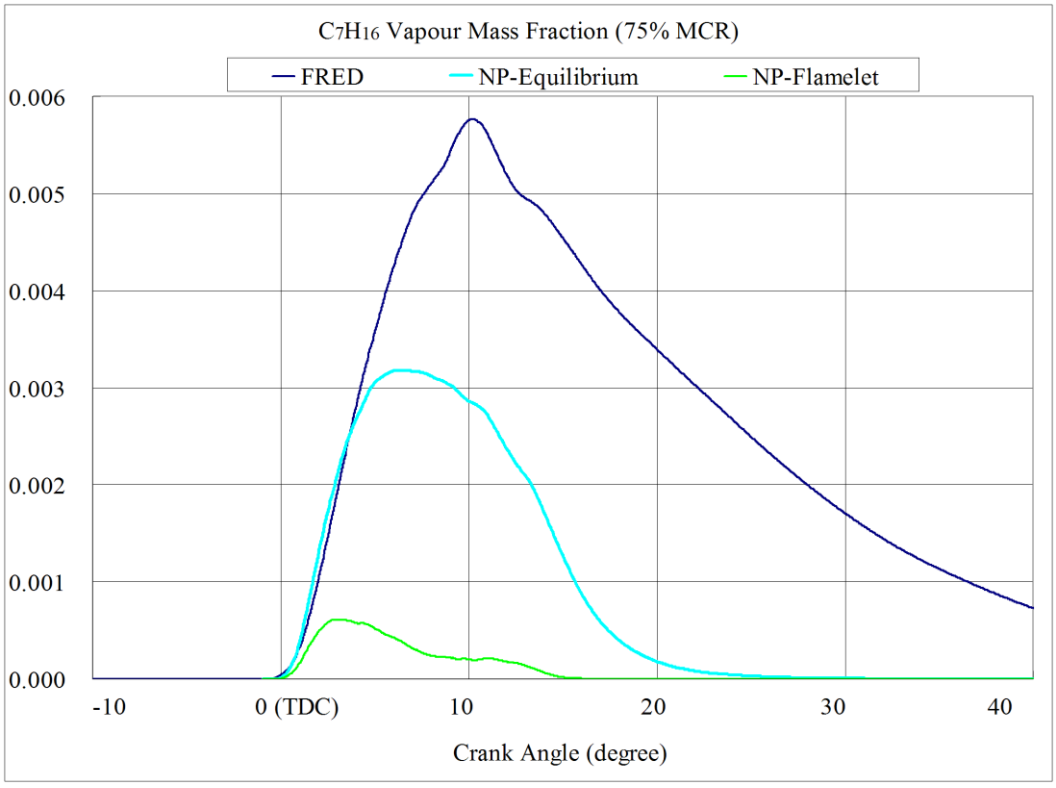

Figure 6.23 Calculated C_7H_{16} mass fractions at 75% MCR

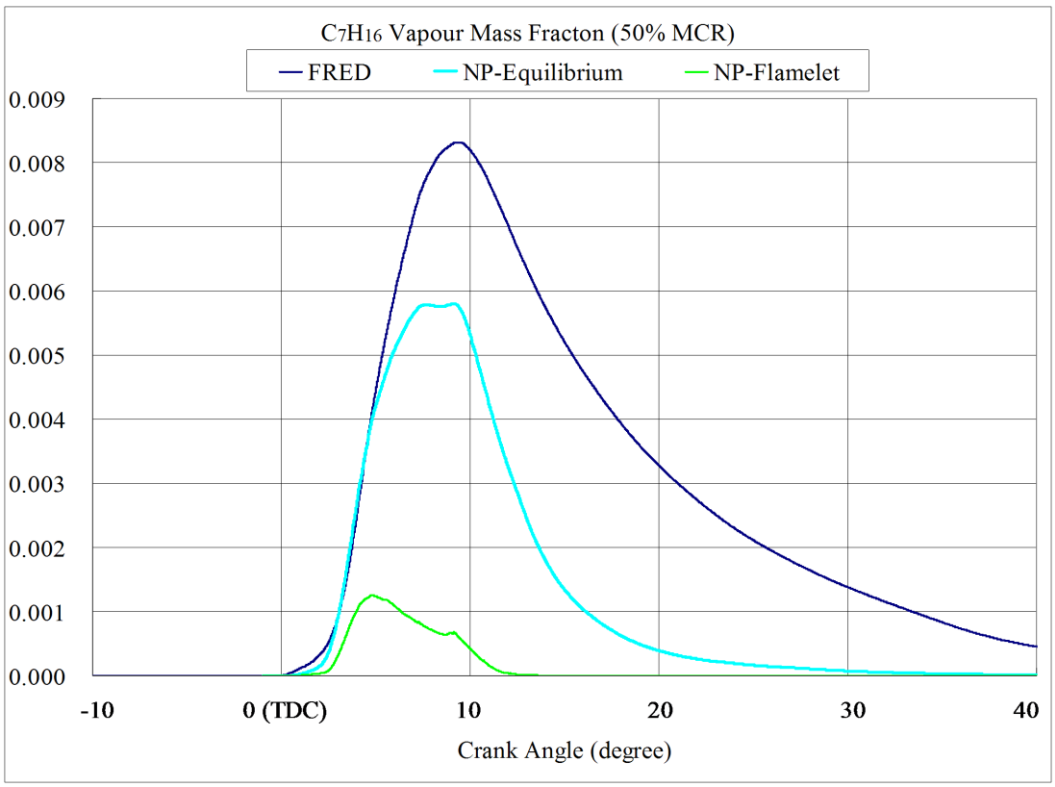

Figure 6.24 Calculated C_7H_{16} mass fractions at 50% MCR

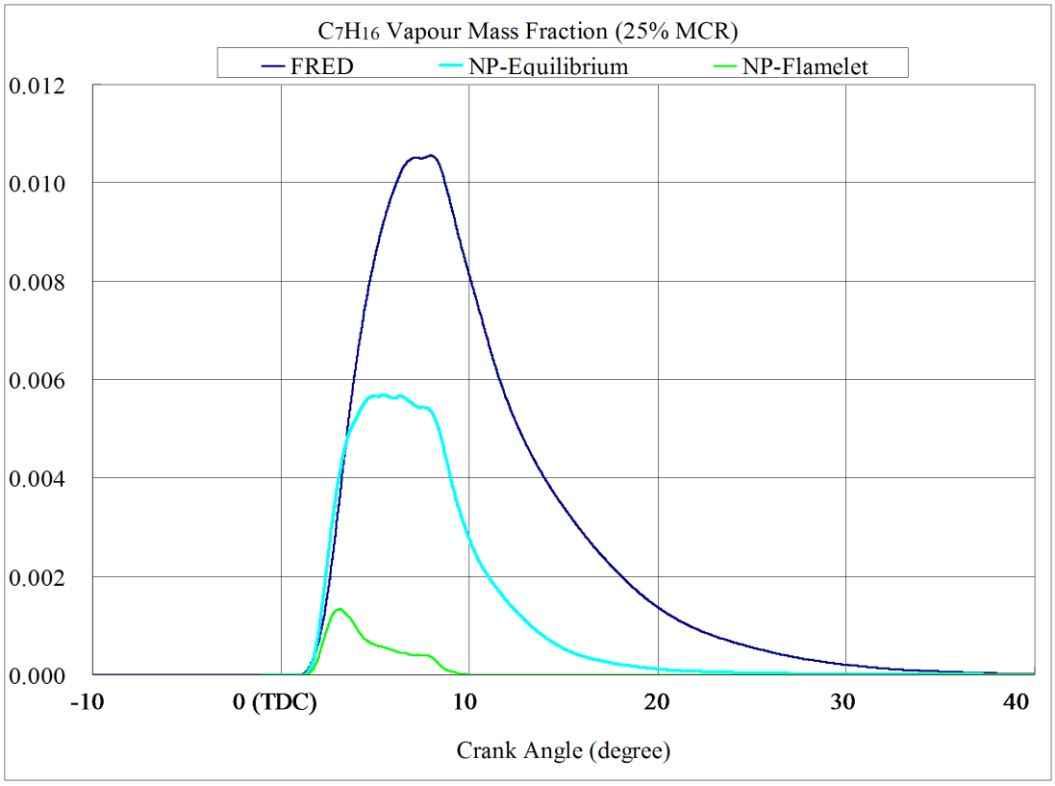

Figure 6.25 Calculated C_7H_{16} mass fractions at 25% MCR

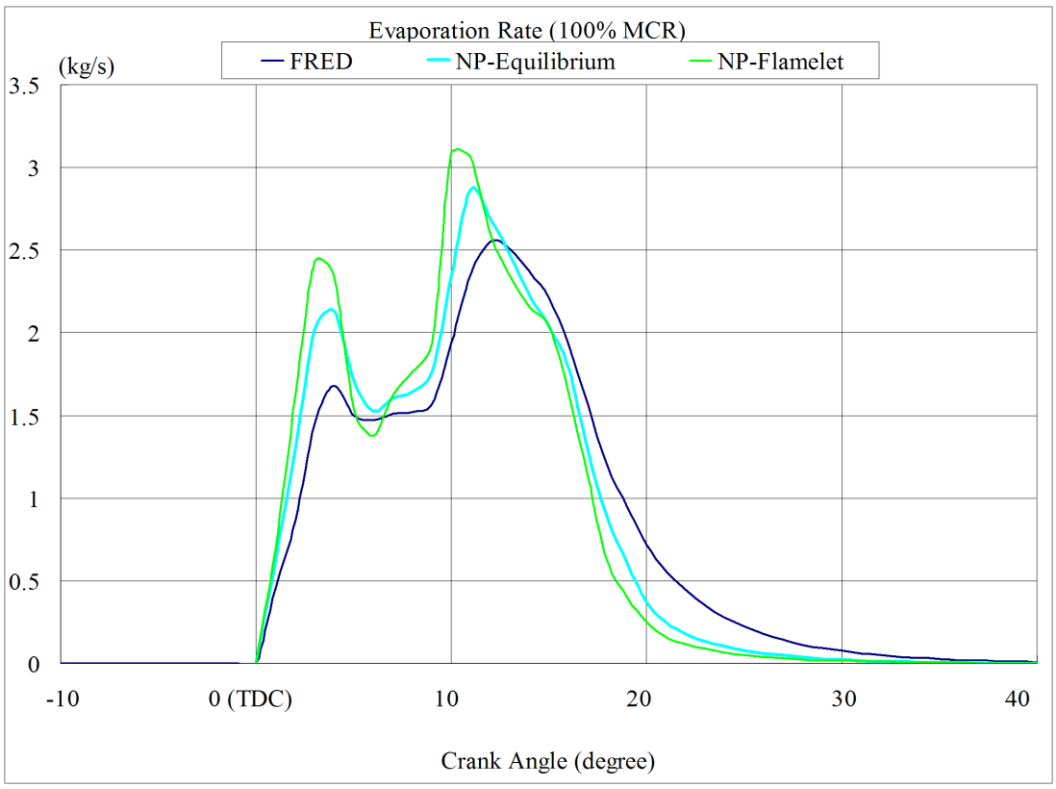

Figure 6.26 Calculated evaporation rates at 100% MCR

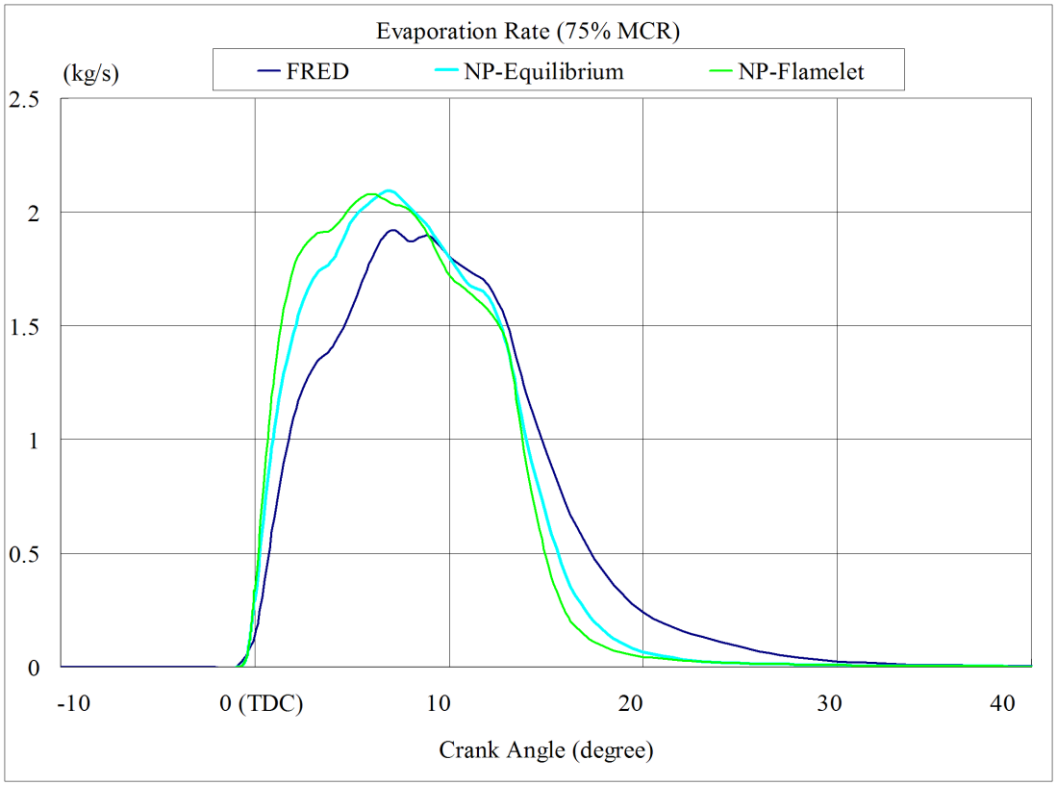

Figure 6.27 Calculated evaporation rates at 75% MCR

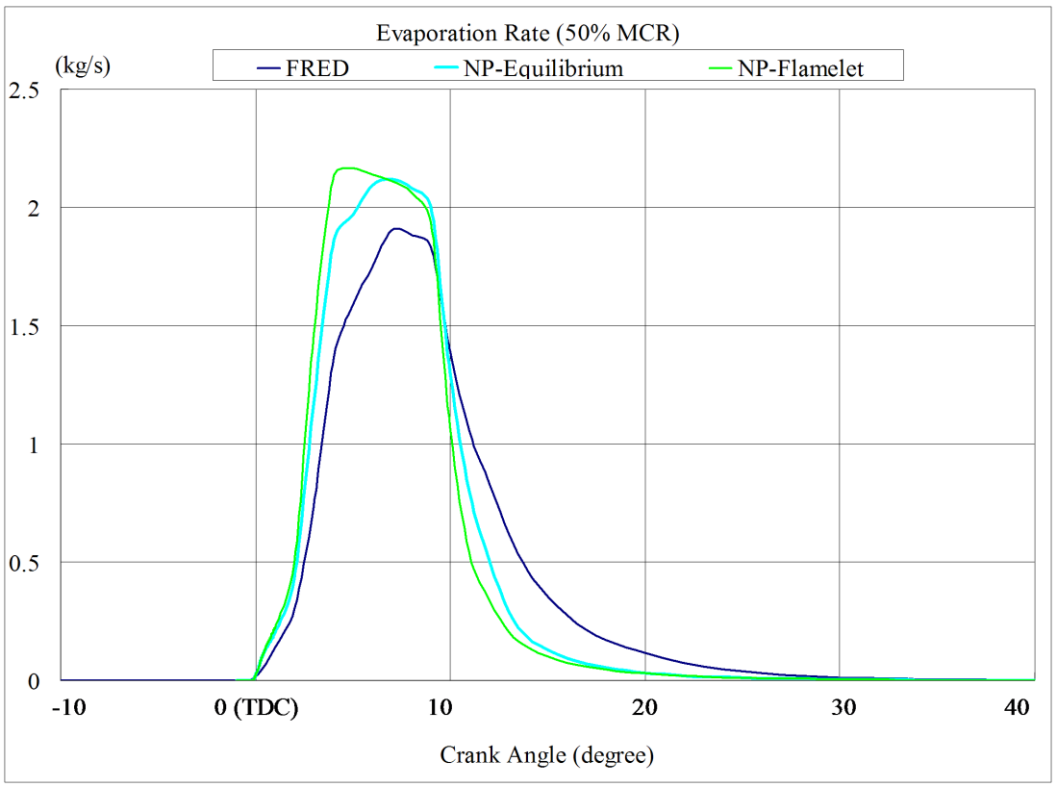

Figure 6.28 Calculated evaporation rates at 50% MCR

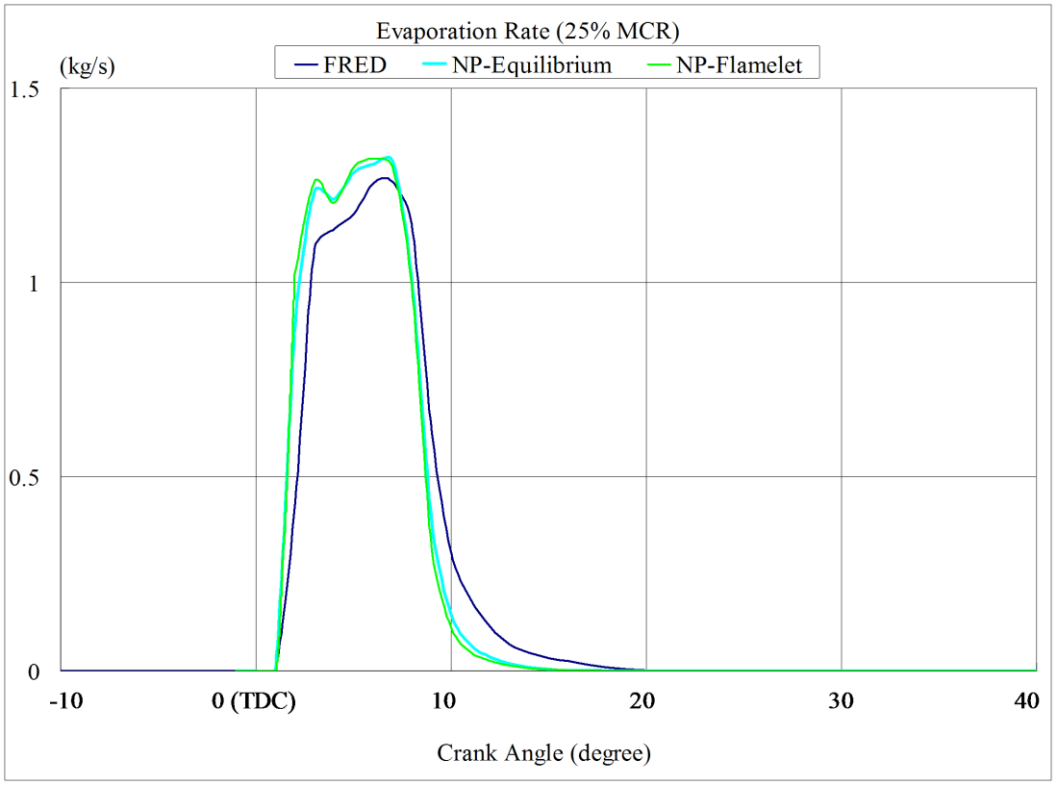

Figure 6.29 Calculated evaporation rates at 25% MCR

Figure 6.14 to Figure 6.17 present the calculated mean temperature at 100%, 75%, 50% and 25% engine loads. The temperature predicted by FRED model is obviously higher than the prediction of the other two combustion models during the combustion process. After the combustion process, the predicted temperature by the three combustion models almost follows the same trace. Generally, the highest temperature appears at about 4-6 CAD after the injection process.

The calculated CO_2 mass fractions by three combustion models at four loads are presented in Figure 6.18 toFigure 6.21. It should be noted that a minor error was introduced at the TDC when the FRED model cases were transferred to Non-Premixed combustion model cases for the incompatible data transferring. Neglecting the introduced error, the CO_2 fractions predicted by FRED are higher than those predicted by the other two Non-Premixed combustion models. This is because of the fact that the C element would directly be burnt into CO_2 in the FRED model. In the Non-Premixed combustion models, the intermediate species containing C element would make the production of CO_2 slower than that of FRED model. The CO_2 mass fractions predicted by FRED experience a decreasing at about 30 CAD after TDC. This decrease is caused by the increase of the evaporated but unburnt C_7H_{16} vapour. After the end of the combustion, the mass fractions of CO_2 predicted by FRED model still undergo a slight decrease. This may be induced by the inevitable numerical error in FRED model. During the scavenging process, the predicted mass fractions of CO_2 increase slightly because of the fact that the upper part of the cylinder, the region outside combustion, is mainly occupied by lower CO_2 concentration as shown in Figure 6.31. When the upper lower CO_2 concentration species are removed from the exhaust port, the mass fraction of CO_2 becomes higher.

The calculated C_7H_{16} vapour mass fraction plots at different loads are presented in Figure 6.22 Figure 6.25. The combustion model has significant influence to the mass fraction of C_7H_{16}. The predicted vapour C_7H_{16} mass fractions of for the Non-Premixed cases are much lower than the respective FRED ones. This means that the C_7H_{16} vapour

would be burnt much faster in the Non-Premixed combustion models. This also reflects the fact that the Non-Premixed combustion models are only suitable for fast combustion predictions (ANSYS, 2012).

From the predicted evaporation rates in Figure 6.26 Figure 6.29, it can be found that the evaporation rates are mainly controlled by the injection rates. However, the in-cylinder conditions would also affect the evaporation process.

6.5.3 Analysis of the In-Cylinder Flow Fields at 100% MCR

For simplicity, the flow fields predicted by Non-Premixed Equilibrium at 100% MCR are graphically presented.

Figure 6.30 shows the predicted temperature and density distribution at the longitudinal section. It can be found that the higher temperature positions coincide very well with the lower density regions. This is reasonable for that the combustion would release the chemical energy to the expansion of the gases. As a result, lower density is induced.

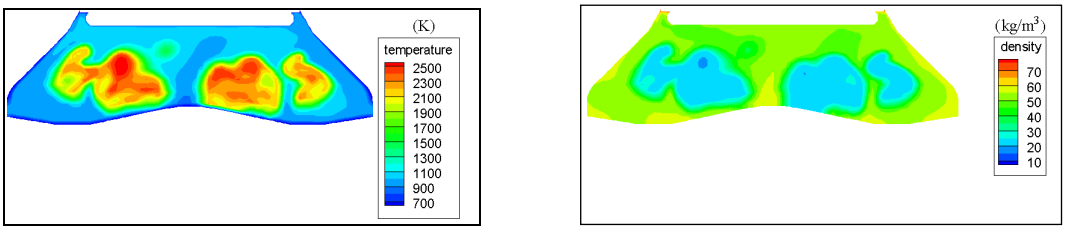

(a) 5 CAD after TDC

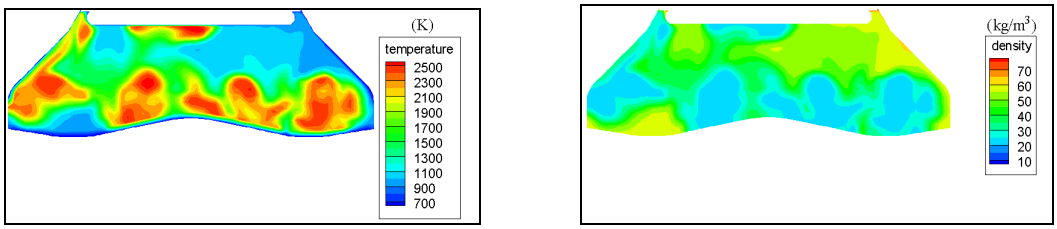

(b) 10 CAD after TDC

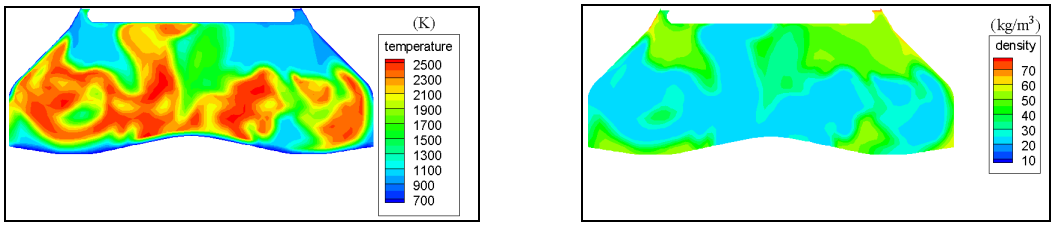

(c) 15 CAD after TDC

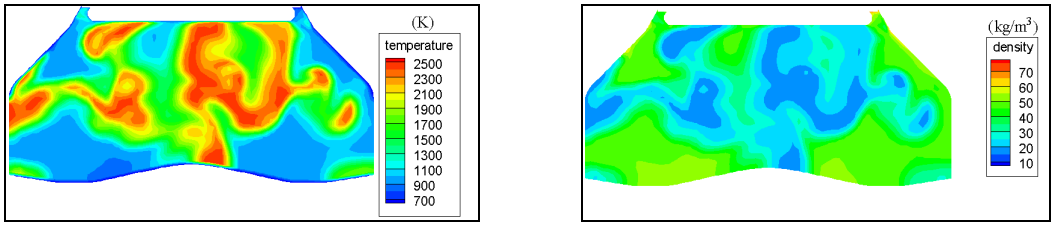

(d) 20 CAD after TDC

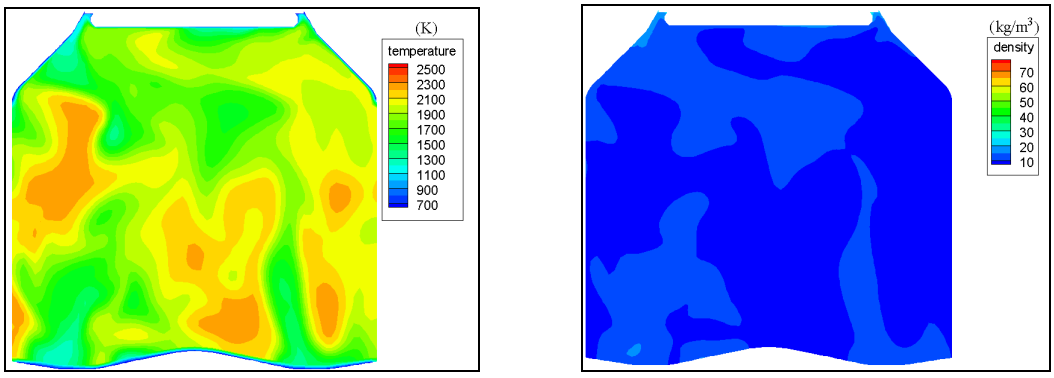

(e) 40 CAD after TDC

Figure 6.30 Calculated temperature (left) and density (right) by Non-Premixed equilibrium model at different positions of 100% MCR

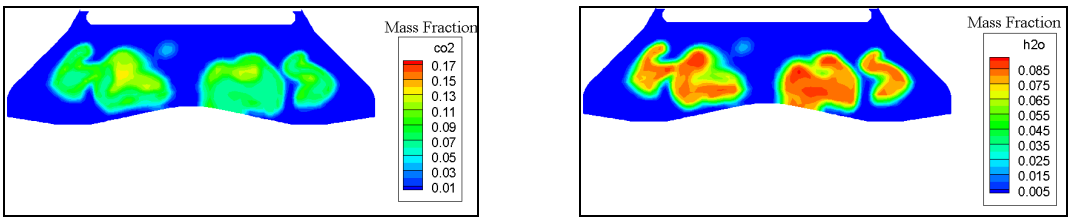

(a) 5 CAD after TDC

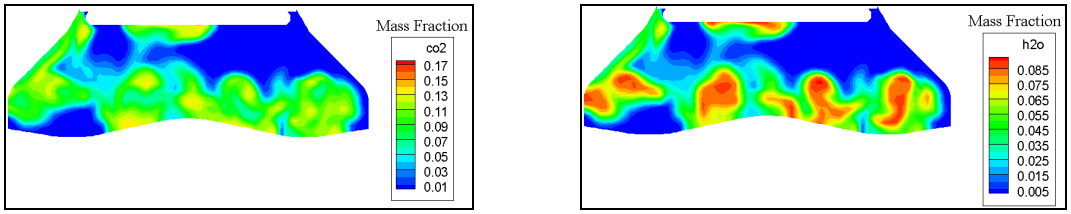

(b) 10 CAD after TDC

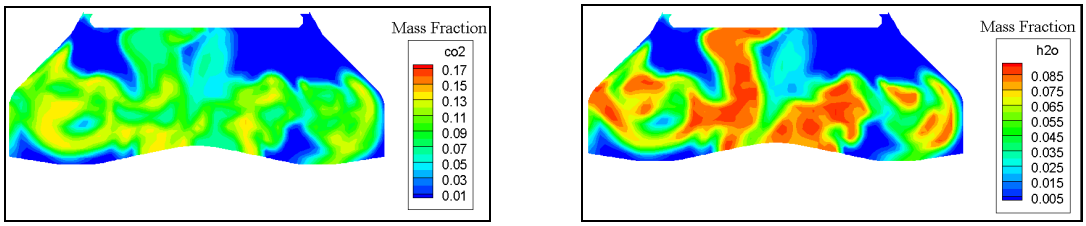

(c) 15 CAD after TDC

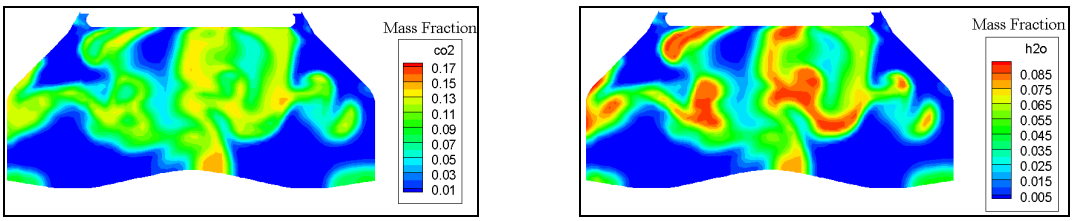

(d) 20 CAD after TDC

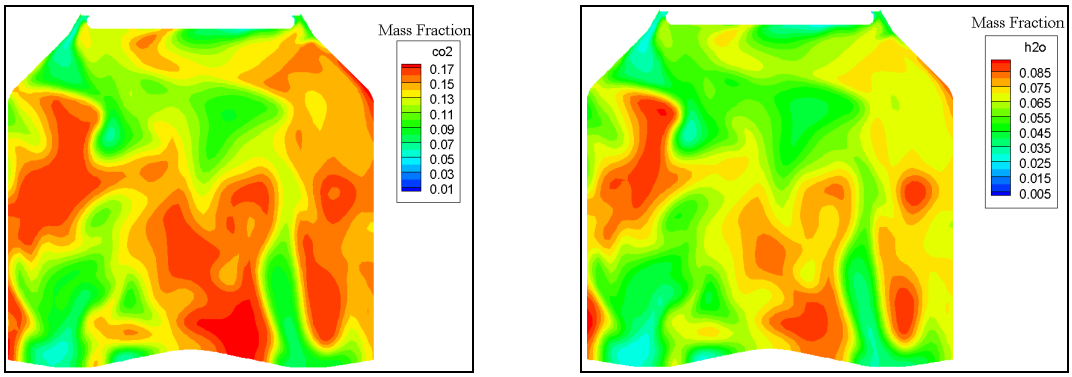

(e) 40 CAD after TDC

Figure 6.31 Calculated mass fractions of CO_2 (left) and H_2O (right) by Non-Premixed equilibrium model at different positions of 100% MCR

Figure 6.31 demonstrates the predicted mass fractions of CO_2 and H_2O during the combustion process. Generally, the products CO_2 and H_2O go hand in hand during this process. And because of the direction of the fuel injection, the products occupy the lower part of the combustion chamber because of the injection direction. The density and temperature distributions are influenced by such feature as well.

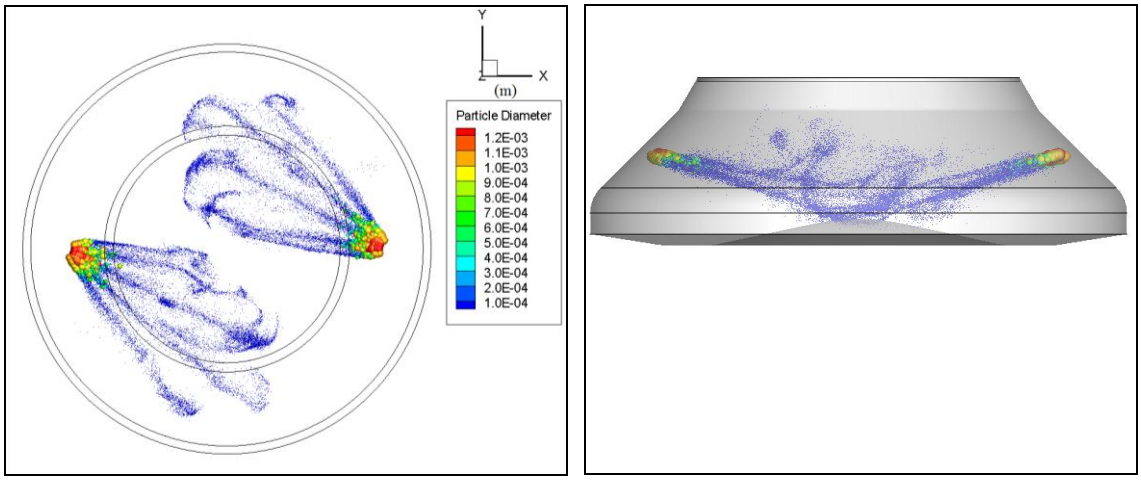

(a) 5 CAD after TDC

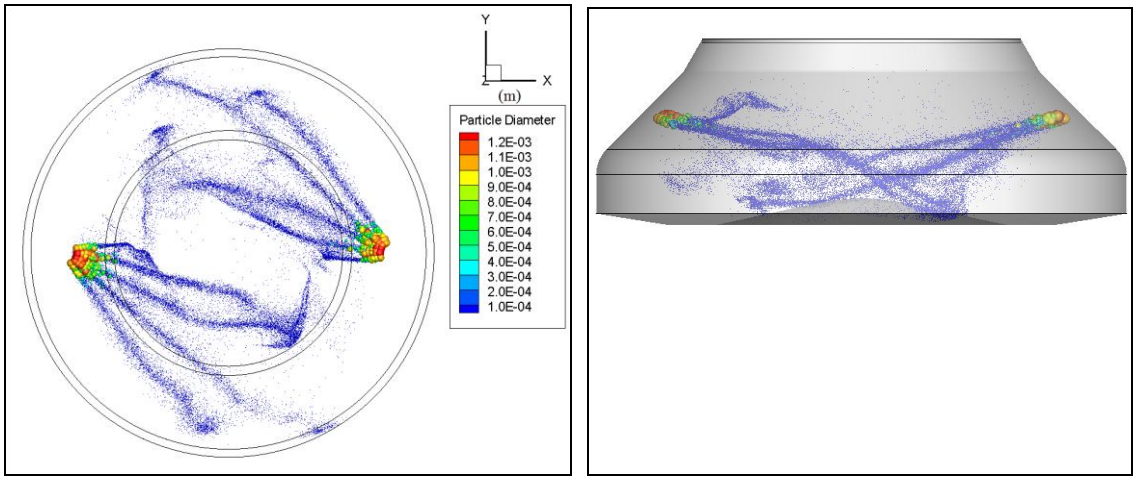

(b) 10 CAD after TDC

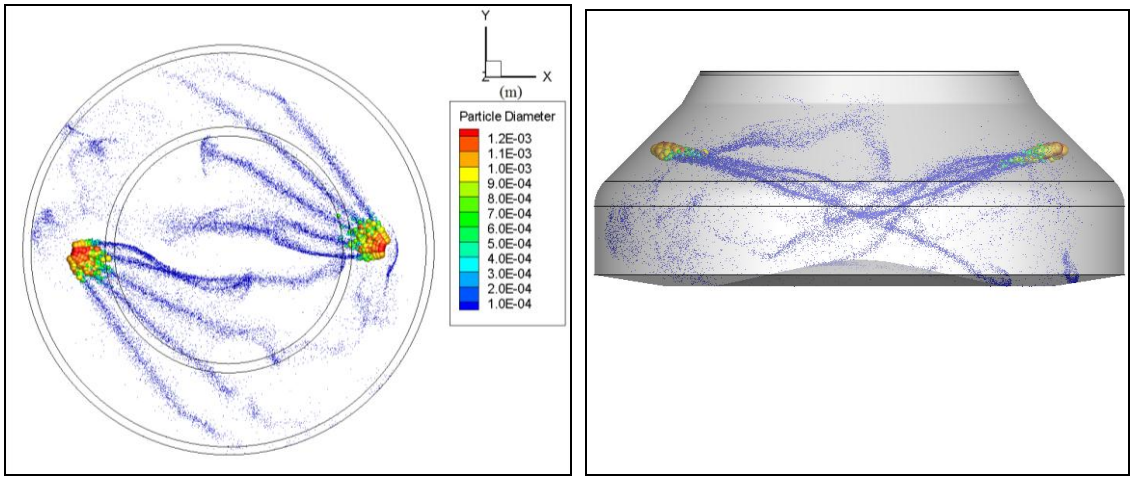

(c) 15 CAD after TDC

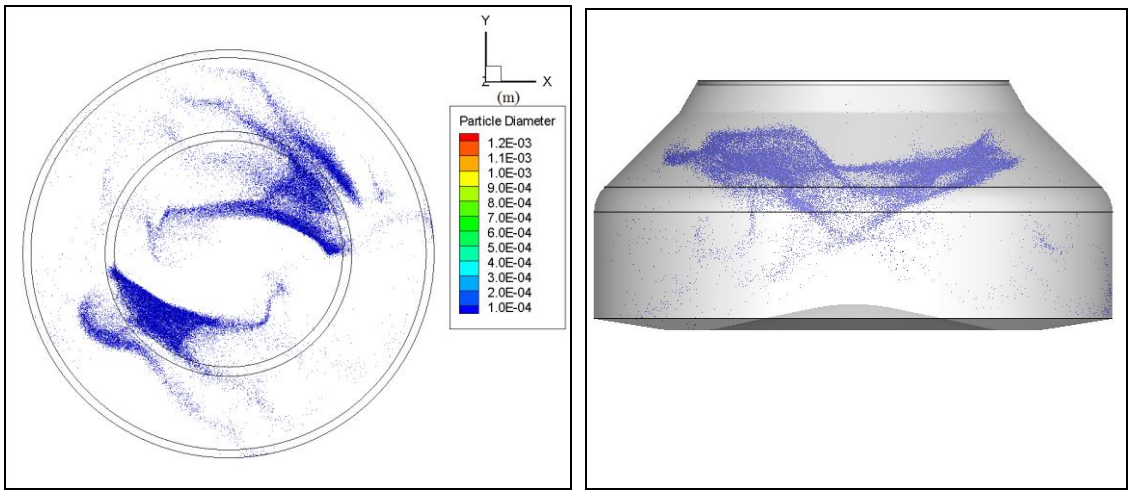

(d) 20 CAD after TDC

Figure 6.32 Calculated droplet diameters by Non-Premixed equilibrium model at different positions of 100% MCR (left: cross view; right: longitudinal view)

Figure 6.32 presents the calculated droplet diameters development during the combustion process. It can be found that at the injector outlet, the diameter of the droplet is similar with the hole diameter. However, such large diameter droplets would break into very small children droplets very quickly. In a very short distance from the injector exit, the diameter of the droplets becomes only 1/10 of the initial scale. As it is ovserved from the curved traces, the paths of the injected droplets are affected by the in-cylinder swirl flows generated throughout the scavenging process. Very few droplets collide with the cylinder wall and piston, and this would induce the carbon deposit in reality.

However, in the current computations, such effects are not included for simplicity. The droplets collide with the wall would be reflected back and involved into the following evaporation.

The temperature distribution in the cylinder is shown in Figure 6.33. The higher temperature appears at the combustion regions outside the droplet sprays where the fuel is evaporated. At the end of the injection, the high temperature gas occupies large part of the combustion chamber.

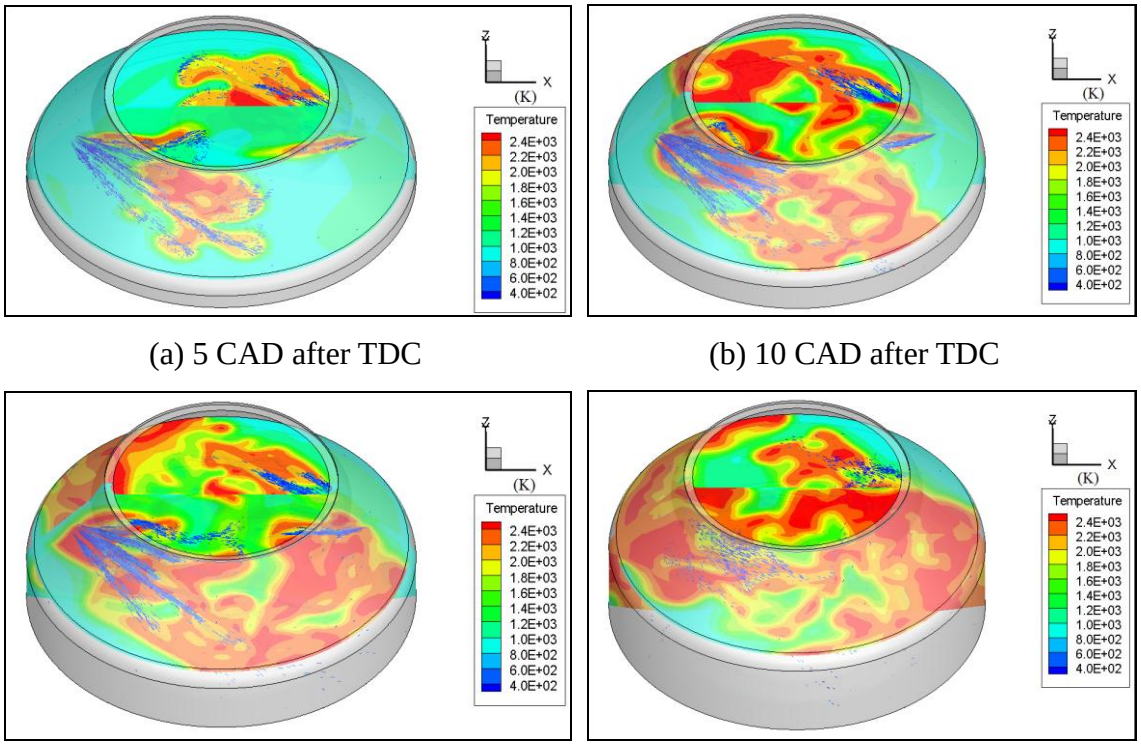

(a) 5 CAD after TDC (b) 10 CAD after TDC

(c) 15 CAD after TDC (d) 20 CAD after TDC

Figure 6.33 Calculated in-cylinder temperature by Non-Premixed equilibrium model at different positions of 100% MCR

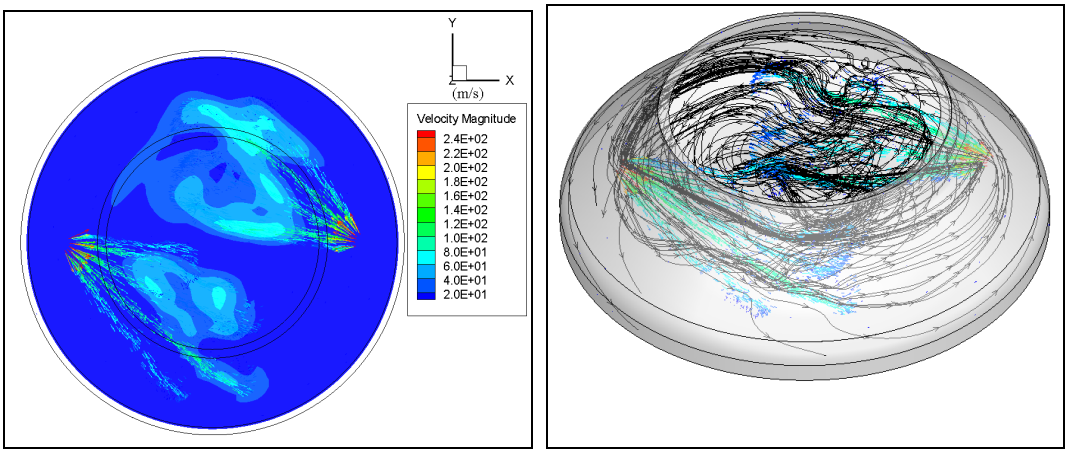

(a) 5 CAD after TDC

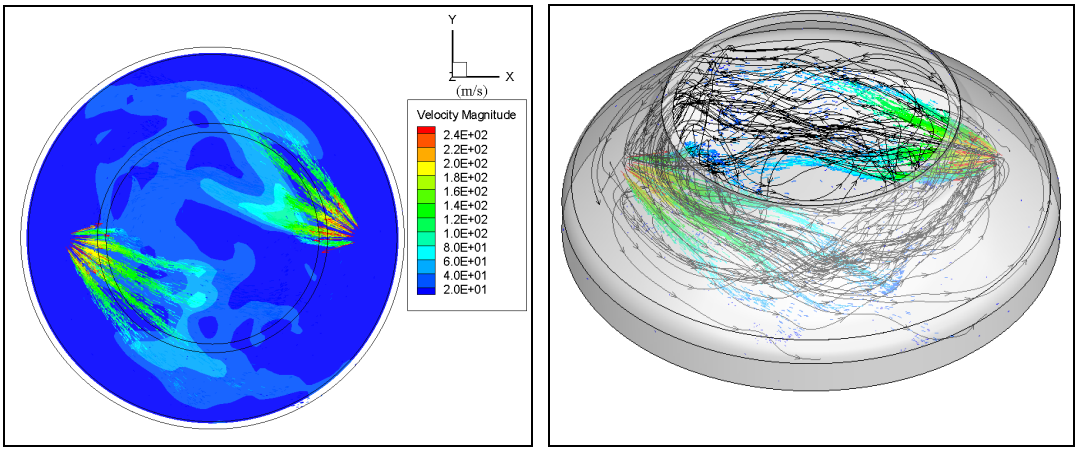

(b) 10 CAD after TDC

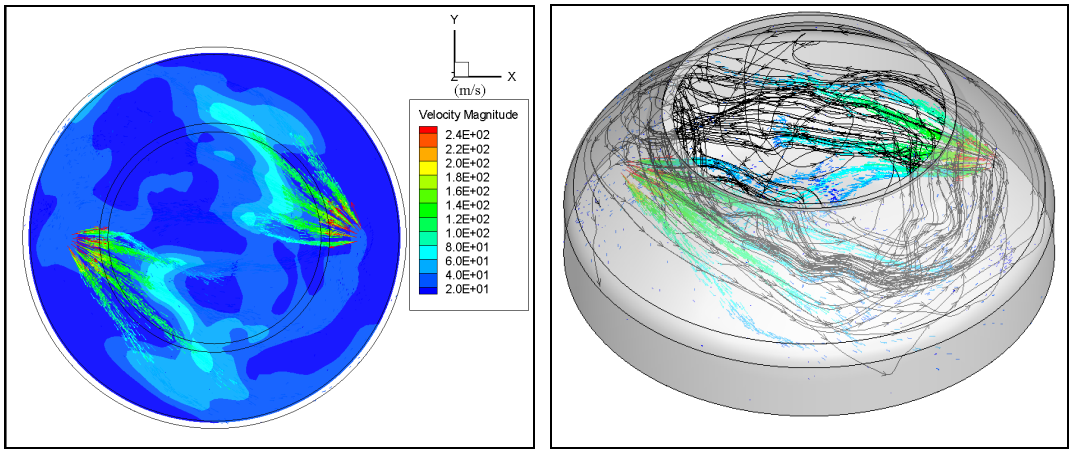

(c) 15 CAD after TDC

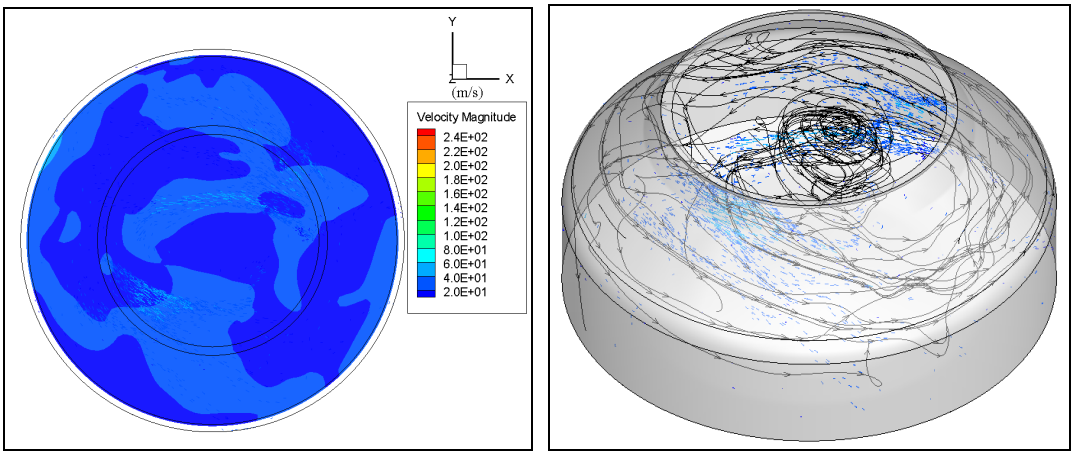

(d) 20 CAD after TDC

Figure 6.34 Calculated in-cylinder velocities (left) and streamlines (right) by Non-Premixed equilibrium model at different positions of 100% MCR

The in-cylinder flow fields are presented in Figure 6.34. The high speed droplets would induce the gas to be accelerated and finally, the whole combustion chamber is completely dominated by such strong swirl flows. The strong swirls make sure the good mixing of the fuel vapour with the compressed air. Thus, the combustion quality would be improved as well.

6.6 Conclusions

The compression and combustion process of large 2-stroke marine diesel engine MAN B&W S60MC-C6 was simulated using CFD solver ANSYS FLUENT. RNG k-ε turbulence model was combined with non-equilibrium wall function to deal with the fully developed turbulent and the near wall transition regions. SSD breakup model was used to simulate the droplet breakup process. The conclusions are summarised as:

1) Real gas model is required for engine combustion process simulations as the reaching of the critical point. For the currently tested real gas models, all of them can predict the satisfactory results.

2) At least two cycles preliminary calculation is needed to stabilise the species fractions, velocity field and fluid state.

3) All the tested combustion models can predict very good trends for pressure and heat release rate traces.

4) Even though more dedicated non-equilibrium effects are considered, NP-Diesel model does not present more accurate results. On the contrary, NP-Diesel model is not so stable during the combustion process simulation.

5) The chemical mechanisms of NP-Equilibrium and NP-Flamelet models are different. But they give very good coincidence for the combustion process results. NP-Equilibrium model predicts the best combustion accuracy at different load conditions for the present large 2-stroke marine diesel engine combustion process.

Chapter 7 Discussion and Conclusions

7.1 Summary Remarks

The present research aims at the validation of the physical models related with the CFD simulation of the combustion processes of large 2-stroke marine diesel engines.

Chapter 1 outlined the history and the latest development of large 2-stroke marine diesel engines, and is followed by the detailed literature reviews in chapter 2. The key EU supported projects and the open published results on large 2-stroke marine diesel engines were critically reviewed. The conclusion is that efforts are being involved to improve the engine efficiency and to reduce the pollutant emissions. The research and development would not only be focused on the optimisation of the engine itself but also on the whole propulsion system. As a powerful development tool, CFD is highly relied on to support the research and development of large 2-stroke marine diesel engines considering the obtained accuracy. To obtain further insights into the in-cylinder processes, more sophisticated facilities and critical measured data are still needed, and based on which, more intensive and extensive investigations of the existing and new CFD models are necessarily to enable applications to general cases.

Chapter 3 summarised the most promising and widely used computational models involved in the CFD simulation of large 2-stroke marine engine combustion processes. All such complex models were implemented and exist in various codes and commercial software. More and more applications of these existing tools is confirming the gradual maturity of CFD as a potential means to solve the problems of the large 2-stroke marine engines.

In chapter 4, three basic cases (compressible turbulent mixing layers, heat transfer in the boundary layer of a pipe expansion and droplet breakup of n-heptane spray) were tested

to validate the adopted mesh size, turbulence models, wall functions and breakup models, for the lack of the directly measured data from the large 2-stroke marine diesel engines. Based on the comparison and analysis, we draw the conclusions as:

1) The mesh size with about 10 times of the injector diameter can be regarded to be appropriate for the prediction of the droplet and evaporated vapour distribution.

2) The RNG k-ε turbulence model is accurate enough to model the turbulence in compressible shearing and mixing flows, which are prevalent in engine working process.

3) The Non-Equilibrium wall function can predict satisfactory heat transfer between the wall and the in-cylinder gases.

4) The SSD breakup model gives acceptable breakup predictions for its generality and rationality.

In chapter 5 and 6, the afore validated best models were applied to the working processes simulation of a large 2-stroke marine diesel engine MAN B&W S60MC-C6 at four engine loads (25%, 50%, 75% and 100% MCR). The piston and exhaust valve were controlled by the dynamic layering mesh and the scavenging transferring between the cylinder and scavenging box was achieved using the mesh interface approach. The positions and directions of the nozzle holes were strictly specified as described according to the design diagrams to make sure the agreement of the measurement and calculations. The diesel fuel oil used in shop test was transferred into the equivalent C_7H_{16}. The prediction results were compared with the shop test data at four different loads. It is found that:

1) During the scavenging process, the real gas model does not present any superiority over the ideal gas model. However, the computation time consumed in real gas simulation is much longer than that in the ideal gas case.

2) Even though the scavenging and exhaust pressure is averaged, the results predicted by the developed computation model are satisfactory.

3) Real gas model is necessary for engine combustion process simulations as the reaching of the critical point. For the currently tested real gas models, all of them can predict the satisfactory results.

4) At least two cycles preliminary calculation is needed to stabilise the species fractions, velocity field and fluid state.

5) All the tested combustion models can predict good trends for pressure and heat release rate traces. All the calculated pressure traces coincide very well with the measure data in shop tests.

6) Even though more dedicated non-equilibrium effects are considered, NP-Diesel model does not present more accurate results. On the contrary, NP-Diesel model is not so stable during the combustion process simulation.

7) Even though the chemical mechanisms of NP-Equilibrium and NP-Flamelet models are different, however, they give very good coincidence for the pressure traces. NP-Equilibrium model predicts the best combustion accuracy at different load conditions for the present large 2-stroke marine diesel engine combustion process.

Considering the satisfactory agreement and the reasonable in-cylinder graphic results, the currently built model is reliable. These derived conclusions can be used as guidelines for the following CFD simulations of large 2-stroke marine diesel engines working processes. It also provides the starting point for the following engine optimisation to increase the engine efficiencies and to reduce the pollutant emissions.

7.2 Key Contributions of the Research

The present work contributes the following points on the CFD simulation of large 2-stroke marine diesel engine working processes:

1) The physical models involved in the full cycle CFD simulation of the large 2-stroke marine diesel engine working processes were systematically validated.

In some of the previous researches, only the incomplete investigations were carried out for the CFD simulation of the large 2-stroke marine diesel engine. Dam (2007) dedicated to spraying. Obeidat et al (2010), Haider (2011), Lamas et al (2012) and Hemmingsen et al (2013) focused only on scavenging. Rasmussen (2011) gave the contributions to the flows past exhaust valve. Bolla et al (2012) and Endo et al (2001) only gave their efforts on injection and combustion for the closed cycle. This thesis includes the complete cycle simulation and systematic investigations. For the lack of the directly measured data from the large 2-stroke marine diesel engines, the turbulence models, the heat transfer models and discrete phase breakup models were validated against the basic flows with the similar flow characteristics with those in the large 2-stroke marine diesel engines working processes. Then the tested best models were used to the simulation of the large 2-stroke marine diesel engine. Investigations of every step were based on former accurate results to make the validation processes systematic.

2) The critical strategies for CFD simulation of large 2-stroke marine diesel engine were obtained, which include the guidelines for the configuration of mesh size and clearance of the cycle variance.

Dam (2007) advanced a criterion for the absolute maximum grid size for achieving reasonable momentum transfer from liquid to the gas. In this thesis, the author also advanced a guideline for the grid size for engine sprays. The mesh size of the full cycle

simulation should be determined by the diameter of the injector. Based on the results of the interaction of the mesh and the n-heptane spray, a mesh size of 10 times of the injector diameter was finally determined in the full cycle simulation of the large 2-stroke marine diesel engine injection process. It is proven that such configuration is reasonable.

Endo et al (2001) concluded that three cycles' calculations are necessary to stabilise the initial and boundary conditions. In this thesis, the author pointed out that two cycles' preliminary calculation is enough to stabilise the species fractions, velocity field and fluid state. For the difficulty to initialise the initial and boundary conditions, several cycles' preliminary calculation is proven to be valid and efficient to solve this problem. The best computation starting point should be before the scavenging process to make the preliminary cycles stabilising calculations less.

3) The best physical models in CFD simulation of large 2-stroke marine diesel engine were obtained. It is recommended to use the following models combination in the CFD calculations of the large 2-stroke marine diesel engine working processes:

- RNG k-ε turbulence model
- Non-Equilibrium wall function
- SSD breakup model
- Real gas model
- Non-Premixed Equilibrium combustion model

7.3 Recommendations for Further Research

Concerning the CFD simulation itself, the currently presented processes can be still largely improved based on the following steps:

1) More critical validations should be carried out during the scavenging.
For the lack of the experimental data with the similar characteristics of the real engine scavenging process, the currently adopted test case, compressible mixing layers, includes only the shearing and mixing phenomena during this stage. To make the validations more reasonable and reliable, a test case which includes the strong swirling flow field data is ideal. The data generated in the improved DTU swirl rig (Hemmingsen et al., 2013) should be a better reference.

2) Injection validations could also be improved with similar engine configurations.
In this research, the adopted validation test nozzle hole diameter is a typical automobile engine size. Even though there are some published results confirmed that some extent similarities exist for the small and large size nozzle injection, it should be stricter to validate the injection models against the similar injector configurations as that of the large 2-stroke marine diesel engines. In this aspect, the ETH spray combustion chamber (Schulz et al., 2013) data would be much more plentiful and closer with the injection of the large 2-stroke marine diesel engines.

3) Stricter numerical investigations should be applied on the droplet development.
During the tests of the injection breakup, the collision and the coalescence effects were not included. The continuous injection would be separated into very small time step sizes. Even though the time step is set to be 0.01 CAD/Δt considering the trade-off of precision and computational cost, it should be more appropriate to get the best compromise between them. Last but not least, the SSD breakup model itself cannot capture the liquid penetration very accurately. This is another aspect that needs to be

improved or substituted by more general but powerful breakup approaches.

4) The combustion processes could be further validated.

In the final combustion investigations, only the pressure traces were used as the reference data to validate the combustion models. However, pressure data is only the macroscopic result, without monitoring and evaluating of the microscopic reaction processes. The influence of the in-cylinder conditions before the combustion, as swirling, turbulence, temperature, evaporation and so on should also be included to make more intensive investigations. As a result, more critical measured data would be needed to make the validation processes stricter. The ETH spray combustion chamber (Schulz et al., 2013) and the MAN B&W optical engine (Mayer et al., 2013) are considered as the most promising facilities to provide such data.

5) The wall heat transfer validation should also be supported under the engine conditions.

Even though the Non-Equilibrium wall function is capable of the heat transfer in the 2D expansion case, the engine working conditions would be different from such simple and steady situation and thus more complex and accurate models should be built and validated to strictly consider the influence of the heat transfer.

6) Advanced mesh adaptation techniques should be introduced to make the whole simulation processes efficient and robust.

Because of the inclusion of the droplet prediction, the mesh size would be determined by the injector hole diameter to fulfil the Lagrangian-Eulerian assumptions. As a result, the mesh number and the consumed time would be largely increased. However, the application of adaptation mesh is conflict with the adopted In-Cylinder dynamic mesh in the presently employed software ANSYS FLUENT 14.0. The software STAR CD and CONVERGE would be the smarter choice.

References

Andreadis, P., Zompanakis, A., Chryssakis C., Kaiktsis, L., 2011. Effects of the fuel injection parameters on the performance and emissions formation in a large-bore marine diesel engine. International Journal of Engine Research, 12, 14-29.

ANSYS, 2012. ANSYS FLUENT Theory Guide.

Assael,M. J., Trusler, J. P. M., Tsolakis, T. F., 1996. Thermophysical Properties of Fluids. Imperial College Press, London.

Aungier, R. H., 1995. A Fast, Accurate Real Gas Equation of State for Fluid Dynamic Analysis Applications. Journal of Fluids Engineering, 117(2), 277-281.

Barths, H., Antoni, C., Peters, N., 1998. Three-Dimensional Simulation of Pollutant Formation in a DI Diesel Engine Using Multiple Interactive Flamelets. SAE Technical Paper 982459.

Baughn, J. W., Launder, B. E., Hoffman, M. A., Takahashi, R. K., 1984. Local Heat Transfer Downstream of an Abrupt Expansion in a Circular Channel With Constant Wall Heat Flux, Journal of Heat Transfer, 106(4), 789-796.

Bolla, M., Cattin, M. A., Wright, Y. M., Boulouchos, K., Schulz, R., 2012. 3D-CFD Lagrangian Spray Simulations for Large Two Stroke Marine Diesel Engines Compared with Experimental Data of A Spray Combustion Chamber. Proceedings of the ASME 2012 Internal Combustion Engine Division Spring Technical Conference, Torino, Piemonte, Italy.

Bolla, M., Srna, A., Wright, Y. M., Von Rotz, B., Herrmann, K., Boulouchos, K., 2014. Influence of Injector Diameter (0.2-1.2 mm range) on Diesel Spray Combustion: Measurements and CFD Simulations. SAE Technical Paper 2014-01-1419.

Borkowski, T., 2007. The effect of cylinder process variation on total nitrogen oxides emission for large bore slow speed marine engines. Paper NO.: 183, CIMAC Congress 2007, Vienna.

Bray, K. N., Peters, N., 1994. Laminar Flamelets in Turbulent Flames. Turbulent

Reacting Flows, Academic Press, 63-114.

Chryssakis, C., Kaiktsis, L., Frangopoulos, A., 2010(1). Computational Investigation of In-Cylinder NO_x Emissions Reduction in a Large Marine Diesel Engine Using Water Addition Strategies. SAE Technical Paper 2010-01-1257.

Chryssakis, C., Pantazis, K., Kaiktsis, L., 2010(2). Combustion Modelling with Heavy Fuel Oil for Large Marine Diesel Engine Applications. Paper NO.: 236, CIMAC Congress 2010, Bergen.

Dam, B. S., 2007. Experimental and Numerical Investigations of Sprays in Two Stroke Diesel Engines. PhD thesis, Technical University of Denmark.

Dixon-Lewis, G., 1991. Structure of Laminar Flames. Symposium (International) on Combustion 23(1), 305-324.

Durbin, P. A., 1993. A Reynolds Stress Model for Near-wall Turbulence. Journal of Fluid Mechanics, 249, 465-498.

ECN,2014. http://www.sandia.gov/ecn/

Endo, H., Oda, Y., Okabe, M., Sakaguchi, K., 2001. The Three Dimensional Combustion Simulation for Low Speed Two Stroke Diesel Engine. CIMAC Congress 2001, Hamburg.

Frisch, U., 1995. Turbulence: The Legacy of A. N. Kolmogorov. Cambridge University Press.

Gatski, T. B., Hussaini, M. Y., Lumley, J. L., 1996. Simulation and modelling of turbulence flows. Oxford University Press.

Goebel, S. G., Dutton, J. C., 1991. Experimental Study of Compressible Turbulent Mixing Layers. AIAA Journal, 29(4), 538-546.

Haider, S., 2011. Experimental and Numerical Study of Swirling Flow in Scavenging Process for 2-Stroke Marine Diesel Engines. PhD Thesis, Technical University of Denmark.

Hawkes E.,R., 2011. Baseline n-heptane, NCW Workshop, California.

Hemmingsen, C. S., Ingvorsen, K. M., Walther, J. H., Mayer, S., 2013. Swirling Flow in a Two-Stroke Marine Diesel Engine. Proceedings of the 26th Nordic Seminar on Computational Mechanics, Oslo.

Herrmann, K., Schulz, R., Weisser, G., 2007. Development of a Reference Experiment for Large Diesel Engine Combustion System Optimisation. Paper NO.: 98, CIMAC Congress 2007, Vienna.

Herrmann, K., Von Rotz, B., Schulz, R., Weisser, G., Boulouchos, K., Schneider, B., 2010. Reference Data Generation of Spray Characteristics in Relation to Large 2-Stroke Marine Diesel Engines Using a Novel Spray Combustion Chamber Concept. ILASS-Europe 2010, 23rd Annual Conference on Liquid Atomisation and Spray Systems, Brno, Czech Republic.

Herrmann, K., Von Rotz, B., Schulz, R., Weisser, G., Schneider, B., Boulouchos, K., 2011. A "Spray Combustion Chamber" Facility for Investigations in Relation to Large 2-Stroke Marine Diesel Engine Combustion System Optimisation. Proceedings of the International Symposium on Marine Engineering, Kobe, Japan.

Heywood, J. B., 1988. Internal Combustion Engine Fundamentals, McGrwa-Hill, Inc.

Hill, T. L., 1960. An Introduction to Statistical Thermodynamics, Addison-Wesley.

Hwang, S. S., Liu, Z., Reitz, R. D., 1996. Breakup Mechanisms and Drag Coefficients of High-Speed Vaporising Liquid Drops. Atomisation and Spray, 6, 353-376.

Imamori, Y., Endo, H., Sakaguchi, K., Yanagi, J., 2004. Development of combustion system in low speed two-stroke diesel engine using CFD. Paper NO.: 208, CIMAC Congress 2004, Kyoto.

IMO, 2009. Revised MARPOL Annex VI and NO_x Technical Code.

Iyer, V., Abraham, J., 2005. Two-fluid modelling of spray penetration and dispersion under diesel engine conditions. Atomisation and Sprays, 15, 249-269.

Jin, W., Vassalos, D., 2013. Energy Modelling of Large 2-Stroke Marine Diesel Engine using CFD. In: Proceedings of International Conference on Technologies, Operations, Logistics and Modelling for Low Carbon Shipping, London, September 2013.

Kim, J. S., Williams, F. A., 1997. Extinction of diffusion flames with nonunity Lewis numbers. Journal of Engineering Mathematics, 31 (2-3), 101-118.

Kim, S. C., Lee, D. H., Cho, Y. S., 2001. The Comparison about CFD-Simulation & Measurement Result of Large Two-Stroke Diesel Engine. CIMAC Congress 2001,

Hamburg.

Kindt, S., 2013. State-of-the-art MAN B&W Two-stroke Super-long-stroke Engines. Paper NO.: 71, CIMAC Congress 2013, Shanghai.

Kyriakides, N., Chryssakis, C., Kaiktsis, L., 2009. Influence of Heavy Fuel Properties on Spray Atomisation for Marine Diesel Engine Applications. SAE Technical Paper 2009-01-1858.

Kyrtatos, N. P., 2012. HERCULES A-B-C, A 10-Year Major R&D Effort Towards the Next Generation Large Marine Diesel Engines. Procedia - Social and Behavioral Sciences, 48, 1068-1077.

Kyrtatos, N., Hellberg, L., Poensgen, C., 2013. Ten Years After: Results from the Major Programme HERCULES A-B-C on Marine Engine R&D. Paper NO.: 18, CIMAC Congress 2013, Shanghai.

Lakshminarayanan, P. A., Aghav, Y. V., 2010. Modelling Diesel Combustion, Springer Science+Business Media B. V.

Lamas, M. I., Videl, C. G. R., 2012. Computational Fluid Dynamics Analysis of the Scavenging Process in the MAN B&W 7S50MC Two-Stroke Marine Diesel Engine. Journal of Ship Research, 56(3), 154-161.

Larmi, M., Rantanen, P., Tiainen, J., Kiijärvi, J, Tanner, F. X., Stalsberg-Zarling, K., 2002. Simulation of Non-Evaporating Diesel Sprays and Verification with Experimental Data, SAE Technical Paper 2002-01-0946.

Larmi, M., Tiainen, J., 2003. Diesel Spray Simulation and KH-RT Wave Model, SAE Technical Paper 2003-01-3231.

Launder, B. E., Spalding, D. B., 1974. The Numerical Computation of Turbulent Flows. Computer Methods in Applied Mechanics and Engineering, 3(2), 269-289.

Litke, B., 1999. The influence of inlet angles in inlet ports on the scavenging process in two-stroke uniflow-scavenged engine. 3rd International Conference on Marine Technology (ODRA 99), SZCZECIN, POLAND, 247-252.

Liu, A. B., Mather, D., Reitz, R. D., 1993. Modelling the Effects of Drop Drag and Breakup on Fuel Sprays. SAE Technical Paper 930072.

Lucchini, T., D'Errico, G., Ettorre, D., 2011. Numerical Investigation of the

Spray–Mesh–Turbulence Interactions for High-Pressure, Eevaporating Sprays at Engine Conditions. International Journal of Heat and Fluid Flow, 32, 285-297.

Magnussen, B. F., Hjertager, B. H., 1977. On mathematical models of turbulent combustion with special emphasis on soot formation and combustion. Symposium (International) on Combustion 16(1), 719-729.

Marzi, J., Hollwedel, M., Atlar, M., Tsichlis, P., Mermiris, G., Lightfoot, M., 2011. Energy efficiency TARGETS. In: Proceedings of International Conference on Technologies, Operations, Logistics and Modelling for Low Carbon Shipping, Glasgow, June 2011. Glasgow: University of Strathclyde, 3-12.

Mayer, S., Hult, J., Nogenmyr, K. J., Clausen, S., 2013. Advanced optical development tools for two-stroke marine diesel engines. Paper NO.: 53, CIMAC Congress 2013, Shanghai.

Mermiris, D., Vassalos, D., Dodworth, K., Sfakianakis, D., Mermiris, G., 2011. Dynamic energy modelling – a new approach to energy efficiency and cost effectiveness in shipping operations. In: Proceedings of International Conference on Technologies, Operations, Logistics and Modelling for Low Carbon Shipping, Glasgow, June 2011. Glasgow: University of Strathclyde, 13-22.

Morsi, S. A., Alexander, A. J., 1972. An investigation of particle trajectories in two-phase flow systems. Journal of Fluid Mechanics, 55(2), 193-203.

Nakagawa, H., Kato, S., Tateishi, M., Adachi, T., Tsujimura, H., Nakashima, M., 1990. Airflow in the Cylinder of a 2-Stroke Cycle Uniflow Scavenging Diesel Engine During Compression Stroke. JSME International Journal, 33(3), 591-598.

Nobelprize.org, 2014, http://www.nobelprize.org/nobel_prizes/themes/physics/karlsson/index.html

Obeidat, A., Haider, S., Ingvorsen, K. M., Meyer, K. E., Walther, J. H., 2010. Influence of Piston Displacement on the Scavenging and Swirling Flow in Two-Stroke Diesel Engines. 23rd Nordic Seminar on Computational Mechanics, Stockholm.

Oppenauer, K. S., Alberer, D., Re, L., 2011. Simplified Calculation of Chemical Equilibrium and Thermodynamic Properties for Diesel Combustion. SAE Technical Paper 2011-24-0020.

O'Rourke, P. J., 1981. Collective Drop Effects on Vaporising Liquid Sprays. PhD thesis, Princeton University, Princeton, New Jersey.

Owczarek, I., Blazej, K., 2003. Recommended Critical Temperatures. Part I. Aliphatic Hydrocarbons. Journal of Physical and Chemical Reference Data, 32(4), 1411-1427.

Owczarek, I., Blazej, K., 2006. Recommended Critical Pressures. Part I. Aliphatic Hydrocarbons. Journal of Physical and Chemical Reference Data, 35(4), 1461-1474.

Patel, A., Kong, S., Reitz, R., 2004. Development and Validation of a Reduced Reaction Mechanism for HCCI Engine Simulations, SAE Technical Paper 2004-01-0558.

Peng, D. Y., Robinson, D. B., 1976. A New Two-Constant Equation of State. Industrial and Engineering Chemistry Fundamentals. 15(1), 59-64.

Pergolesi, F., 2009. Scavenging Flow in a Model Of a Two-Stroke Diesel Engine. Master Thesis, Technical University of Denmark.

Poling, B. E., Prausnitz, J. M., O'Connell, J. P., 2007. The properties of Gases and Liquids. McGraw-Hill, International Edition, 5th edition.

Rasmussen, J. H., 2011. Numerical Simulation of the Flow Past an Exhaust Valve in a Two-Stroke Diesel Engine. Master Thesis, Technical University of Denmark.

Redlich, O., Kwong, J. N. S., 1949. On the Thermodynamics of Solutions. V. An Equation of State. Fugacities of Gaseous Solutions. Chemical Reviews, 44(1), 233-244.

Reitz, R. D., 1987., Mechanisms of Atomisation Processes in High-Pressure Vaporising Sprays. Atomisation and Spray Technology, 3, 309-337.

Richardson, L. F., 1922. Weather Prediction by Numerical Process. Cambridge University Press.

Rodatz, P., Weisser, G., Tanner, F. X., 2000. Assessment of CFD Methods for Large Diesel Engines Equipped with a Common Rail Injection System. SAE Technical Paper, 2000-01-0948.

Rosten, O. J., 2012. Fundamentals of the exact renormalization group. Physics Reports, 511(4), 177-272.

Schulz, R., Hensel, S., Von Rotz, B., Schmid, A., Herrmann, K., Weisser, G., 2013. Development of Spray and Combustion Simulation Tools and Application to Large Two-Stroke Diesel Engine Combustion Systems. Paper NO.: 259, CIMAC Congress 2013, Shanghai.

Schulz, R., Herrmann, K., Von Rotz, B., Hensel, S., Seling, F., Weisser, G., Wright, Y. M., Bolla, M., Boulouchos, K., 2010. Assessing the Performance of Spray and Combustion Simulation Tools against Reference Data Obtained in a Spray Combustion Chamber Representative of Large Two-Stroke Diesel Engine Combustion Systems. Paper NO.: 247, CIMAC Congress 2010, Bergen.

Sencic T., 2010. Analysis of Soot and NO_x Emissions Reduction Possibilities on Modern Low Speed, Two-Stroke, Diesel Engines. Strojarstvo, 52(5), 525-533.

Sher, E., 1990. Scavenging the Two-Stroke Engine. Progress in Energy and Combustion Science, 16(2), 95-124.

Sher, E., Hossain, I., Zhang, Q., Winterbone, D. E., 1991. Calculations and Measurements in the Cylinder of a Two-Stroke Uniflow-Scavenged Engine Under Steady Flow Conditions. Experimental Thermal and Fluid Science, 4, 418-431.

Shih, T. H., Liou, W. W., Shabbir, A., Yang, Z., Zhu, J., 1995. A New k-e Eddy-Viscosity Model for High Reynolds Number Turbulent Flows - Model Development and Validation. Computers Fluids, 24(3), 227-238.

Sigurdsson, E., Ingvorsen, K. M., Jensen, M. V., Matlok, S., Mayer, S., Walther,J . H., 2014. Numerical Analysis of the Scavenge Flow and Convective Heat Transfer in Large Two-Stroke Marine Diesel Engines. Applied Energy, 123, 37-46.

Sladkov, I. B., 2001. Physicochemical Properties of Methyl-and Ethylhalosilanes. Russian Journal of Applied Chemistry, 74(11), 1801-1805.

Smith, A. L., 1994. Family Plots for Evaluating Physical Properties of Organosilicon Compounds. AIChE Journal 40(2), 373-377.

Soave, G., 1972. Equilibrium Constants from a modified Redlich-Kwong equation of State. Chemical Engineering Science. 27(6), 1197-1203.

Somayajulu, G. R., 1989. Estimation Procedures for Critical Constants. Journal of Chemical and Engineering Data, 34(1), 106-120.

Sreenivasan, K. R., Stolovitzky, G., 1995. Turbulent Cascades, Journal of Statistical Physics, 78(1-2), 311-333.

TARGETS, 2010. Targeted Advanced Research for Global Efficiency of Transportation Shipping Annex I - Description of Work. Seventh Framework Programme.

Taylor, D. A., 1996. Introduction to Marine Engineering, 2nd Edition, Elsevier Butterworth-Heinemann.

Von Rotz, B., Herrmann, K., Weisser, G., Cattin, M., Bolla, M., Boulouchos, K., 2011. Impact of Evaporation, Swirl and Fuel Quality on the Characteristics of Sprays typical of Large 2-Stroke Marine Diesel Engine Combustion Systems. ILASS-Europe 2011, 24th Annual Conference on Liquid Atomisation and Spray Systems, Estoril, Portugal.

Wang, Y., Ge, H. W., Reitz, R. D., 2010. Validation of Mesh- and Timestep- Independent Spray Models for Multi-Dimensional Engine CFD Simulation. SAE Technical Paper 2010-01-0626.

Wärtsilä, 2014. http://www.wartsila.com/en/investors/markets/market-shares

Weisser, G., Schulz, R., Boulouchos, K., 2004. Progress in Computational Fluid Dynamics (CFD) Applications for Large Diesel Engine Development. Paper NO.: 211, CIMAC Congress 2004, Kyoto.

Weisser, G., Tanner, F. X., Boulouchos, K., Kramer, J., Holtbecker, R., 1998. Integrating CRFD-Simulations into the Development Process of Large Diesel Engines: A Status Report. CIMAC Congress 1998, Copenhagen.

Wilcox, D. C., 1998. Turbulence Modelling for CFD. DCW Industries, Inc., La Canada, California.

Wilson, K. G., 1975. Renormalization Group Methods. Advances in Mathematics, 16(2), 170-186.

Woodyard, D., 2009. Pounder's Marine Diesel Engines and Gas Turbines, 9th Edition, Elsevier Butterworth-Heinemann.

Yakhot, V., Orszag, S. A., 1986. Renormalisation Group Analysis of Turbulence: I.Basic Theory. Journal of Scientific Computing, 1(1), 3-51.